APERTURE SYNTHESIS OF INTERSTELLAR NEUTRAL HYDROGEN IN ABSORPTION

Thesis by

Eric Winslow Greisen

In Partial Fulfillment of the Requirements

for the Degree of

Doctor of Philosophy

California Institute of Technology

Pasadena, California

1973

(Submitted July 31, 1972)

ACKNOWLEDGEMENTS

To acknowledge all those who have assisted me through the many years required to complete this thesis is an impossible task. This thesis would not have been possible without the patient understanding, guidance, and advice provided by my advisor Professor Marshall Cohen. I am also most grateful to Gordon Stanley, Director of the Owens Valley Radio Observatory, not only for the considerable fund of computing and observing time made available to me, but also for his suggestion of the noise diode calibration procedure. I wish to thank Professor Alan Moffet for suggesting the project and Dr. Richard B. Read for constructing the equipment needed for the noise diode calibration and assisting with numerous other equipment problems.

The observations could not have been made without the wholehearted cooperation and assistance of the observatory staff, in particular Chuck Spencer, Ron Allen, and Wayne Hutton. Ms. Carol Walton provided skilled assistance taking the data as did Drs. George Seielstad and Leonid Weliachew and fellow students Seth Shostak, Ka Bing Yip, J. C. Pigg, Bill Wright, and John Bieging.

I also wish to thank Dr. David Rogstad for providing the Fourier inversion procedure, Dr. William Quirk for assisting with the physical interpretation of the data, and Dr. G. Seth Shostak for many useful discussions. V. Radhakrishnan, A. R. Thompson, and R. S. Colvin provided some of their results prior to publication. Dr. Barney Rickett helped rescue some of the data by providing a computer program and computing time at the University of California at San Diego.

Through most of my tenure at the California Institute of Technology I was a recipient of a National Science Foundation Graduate Fellowship. Financial assistance has also been generously provided through several Graduate Research Assistantships. Research at the Owens Valley Radio Observatory is supported by the National Science Foundation under grant GP30400-X and by the Office of Naval Research under Contract N00014-67-A-0094-0019.

This thesis is dedicated to all those who have the patience to read it.

ABSTRACT

The Owens Valley Radio Observatory interferometer has been used to carry out a program of aperture synthesis in the interstellar neutral hydrogen line. Maps having resolutions of 1 KHz and about 1.3 arc minutes have been produced using a novel Fourier inversion procedure which is discussed in some detail. The equipment, observing procedure, noise, and gaussian analysis of spectra are also treated.

The Perseus arm feature in the spectrum of Cygnus A is of low optical depth but reveals considerable spatial structure. The data suggest that the hydrogen is located in a thin shell expanding at 2 km/sec, with a radius around 9.7 parsecs and a total mass of 175 solar masses. The Perseus arm feature in the spectrum of Cassiopeia A contains very large amounts of hydrogen with extremely complicated spatial structure. The results may be explained qualitatively by the two-arm spiral shock model of the Galaxy. The principal component in the spectrum of the Crab Nebula is found to show a considerable velocity gradient across the source and appears to contain several condensations within a large, less dense cloud. The absorption feature in the spectrum of 3C353 appears to have

a gradient in the dispersion of one component. If real, this result suggests scale lengths in the interstellar hydrogen as small as 0.14 parsecs. The absorption spectra of W12, 3C147, Cygnus A (local arm), and 3C123 are also discussed briefly.

Upper limits to the temperature as low as 50° K are found for some of the spectral components although upper limits between 80 and 160° K are more common. Hydrogen clouds with diameters about 1 parsec and densities on the order of 100 cm^{-3} are shown to be common. The implications of these results for the two-phase model of the interstellar medium are discussed.

TABLE OF CONTENTS

Table of Contents (continued)

Table of Contents (continued)

INTRODUCTION

The 21-cm line arising from the ground state hyperfine transition in neutral hydrogen has become a sensitive tool for studying the interstellar medium and for mapping the structure of galaxies. The possibility of detecting this line was first suggested by Van de Hulst (1945). After discussion by a number of authors (e.g. Schklovsky 1949 and Spitzer and Savidoff 1950), the line was observed in emission on March 25, 1951 by Ewen and Purcell (1951) at Harvard followed closely by Muller and Oort (1951) in the Netherlands and Pawsey (1951) in Australia. Soon thereafter extensive surveys were begun which revealed the spiral nature of the Galaxy. The results of these surveys are presented in Kerr, Hindman, and Gum (1959), Van de Hulst, Muller, and Oort (1954), Muller and Westerhout (1957), and accompanying articles. In the past decade, Westerhout and co-workers (Westerhout 1967) have prepared an atlas of hydrogen emission profiles within one degree of the Galactic plane and with resolutions of 7 KHz and 10 minutes of arc. In addition, numerous workers (e.g. Heiles 1967 and Kepner 1970) have studied limited regions within the Galaxy.

The 21-cm line was first detected in absorption by Hagen and McClain (1954) and by Williams and Davies (1954).

More certain and correct results were soon reported by many workers including Hagen, Lilley, and McClain (1955), Williams and Davies (1956) and Muller (1957). These papers were among the first to discuss a difficulty which affects all attempts to measure hydrogen line absorption profiles using a single-dish telescope. This problem arises because a single-dish telescope responds not only to the background source with its absorbed spectrum, but also to the emission of all the Galactic hydrogen within the beam of the telescope. To obtain the true spectrum of the source it is necessary to subtract from the measured spectrum an estimate of the spectrum which would have been received in the absence of the source. This estimate or "expected profile" is commonly obtained by averaging observations taken around the source approximately one beamwidth away. The uncertainties in the expected profile exceed the antenna temperatures generated by all but the strongest radio sources. The magnitude of this problem has been pointed out by Radhakrishnan and co-workers (see Radhakrishnan, et al 1972a, b, c and Goss, et al 1972) who have compared absorption profiles obtained with this single-dish technique to those obtained with an interferometer. Their results for two sources are illustrated in Figures 1.

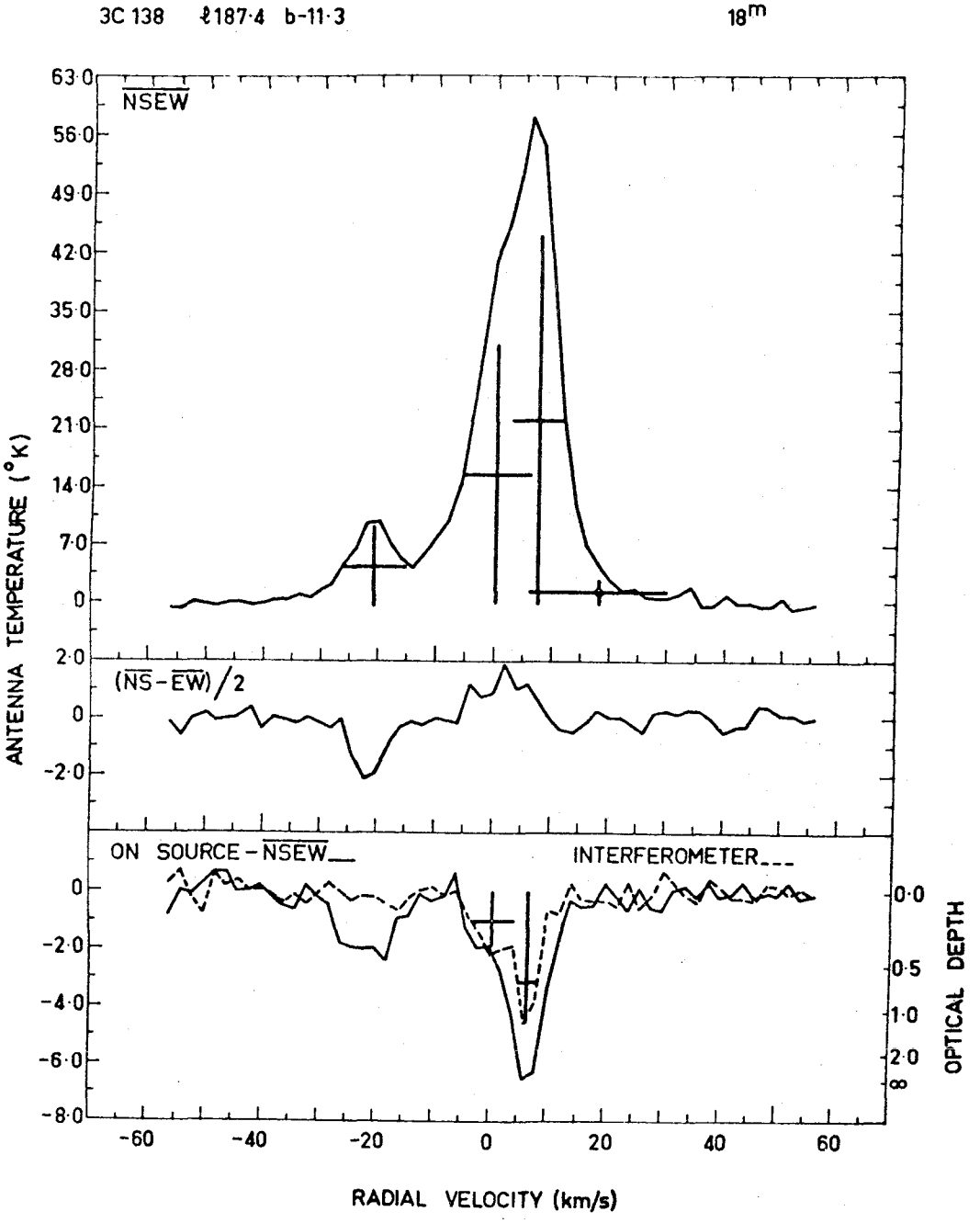

Figure 1a. Absorption and associated emission spectra of 3C138. The middle part gives one-half the difference of the average of emission profiles north and south of the source and east and west of the source. From Radhakrishnan, et al (1972d).

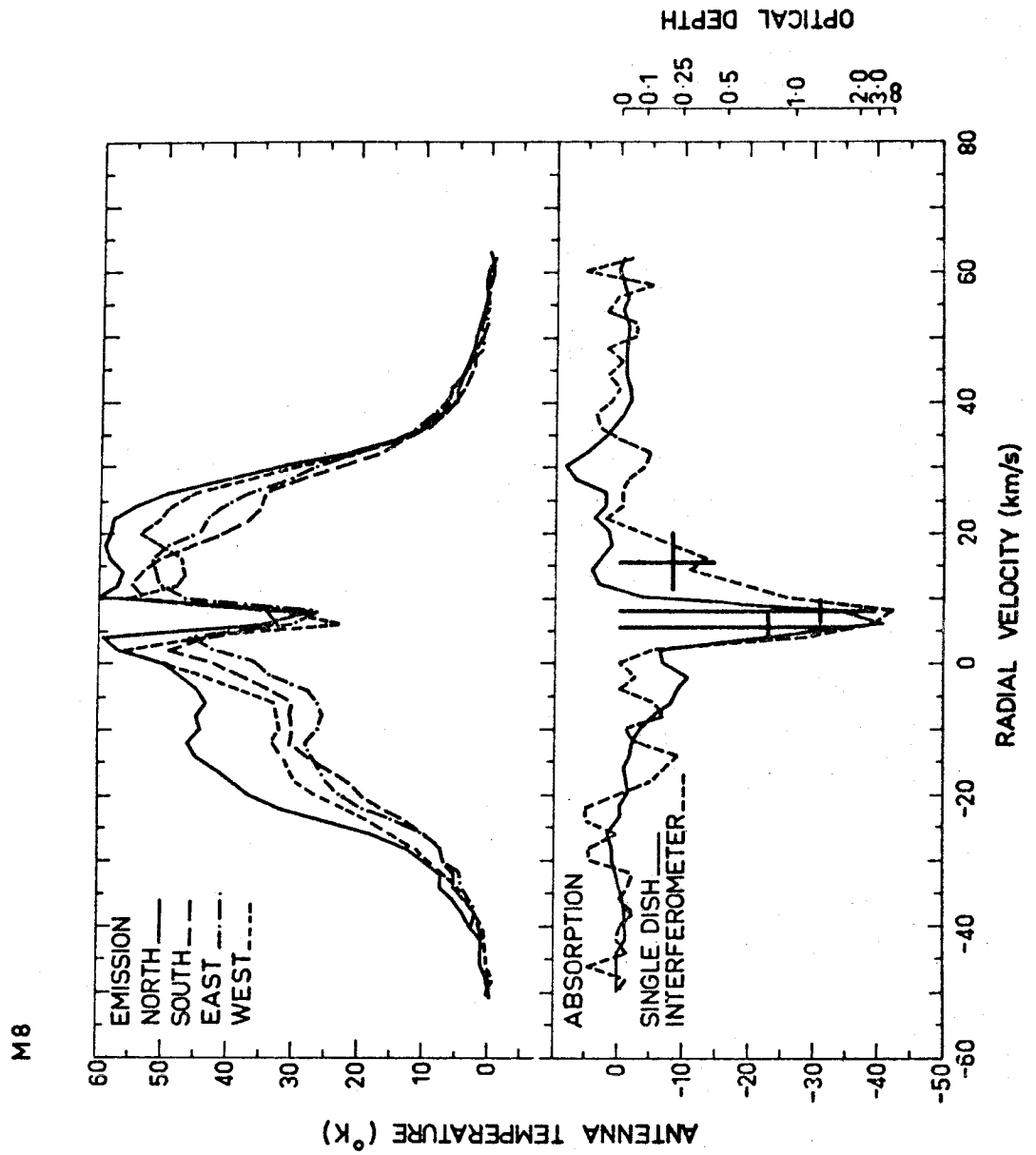

Figure 1b. Absorption and associated emission spectra of M8. From Radhakrishnan, et al (1972c).

There are two approaches which remove most, if not all, of the uncertainty associated with the expected profile. One of these, first suggested by Heiles and Verschuur (1969), uses the variations in intensity of the background source to determine the true absorption profile. This technique has only been successfully used for pulsars (see de Jager, Lyne, Pointon, and Ponsonby 1968 and Gordon and Gordon 1970 and references). The pulsar observations have uncovered a surprising lack of significant absorption in the spectra of a considerable fraction of the sources observed. If some of these pulsars are as distant as is suggested by their dispersion measures, then their lack of absorption suggests that the neutral hydrogen is very sparsely distributed in small, very dense clouds. This result is in apparent conflict with the fact that absorption features are found in the spectra of most quasi-stellar sources.

Interferometry provides the second approach which can remove the difficulties associated with the expected profile. In essence, an interferometer responds only to sources which are smaller than the fringe spacing. Thus, at a sufficient interferometer baseline, the contribution to the fringe amplitude from the general hydrogen emission will be reduced to a negligible amount. This statement

is strictly true only if the general emission has no structure on a scale comparable to the size of the sources we wish to observe. In such a case, there would be little problem with the expected profile. Fortunately, the many small-scale emission features within the beam of the antennas of the interferometer will contribute to the fringe amplitude with random phases. As a result, the interferometer should show little or no response to the general emission.

An interferometer was first used to measure absorption profiles by Clark, Radhakrishnan, and Wilson (1962). Clark (1965) measured the absorption profiles of a number of sources and found evidence for spatial structure in the absorbing medium. Hughes, Thompson, and Colvin (1971) have recently published a catalogue of the absorption spectra of northern sources observed with an interferometer. They find no evidence for effects of the general hydrogen emission at interferometer spacings greater than 300 wavelengths. Radhakrishnan, et al (1972a, b, c, d) and Goss, et al (1972) have also recently published the results of a survey of the absorption spectra of southern sources some of which were observed with an interferometer.

With the first measurements of absorption profiles came the realization that neutral hydrogen does not lie in a uniform medium within the spiral arms of the Galaxy. Absorption profiles are uniformly found to be narrower and different in shape than corresponding emission profiles. Two models of the interstellar medium have been advanced to explain this observation. In the discrete cloud model, the absorption profile is understood to result from the small number of clouds directly along the line of sight to the source while the emission profile derives from the large number of clouds within the main beam of the antenna (Hagen, Lilley, and McClain 1955). The average cloud was felt to have a diameter about 18 parsecs, a density around 1.5 cm^{-3}, and a velocity width around 5 km/sec (Van de Hulst 1958). More recently the two-phase model of the interstellar medium has become popular. In this model, discrete clouds having temperatures less than or around 100° K are in pressure equilibrium with a diffuse medium having temperatures in excess of 7000° K. Both phases would contribute to the hydrogen emission profiles, but only the cool clouds would be seen in absorption (see Appendix B). This model is well understood theoretically. A number of authors have calculated the heating of a two-

phase medium from low energy cosmic rays and find their results in substantial agreement with observation (see Spitzer and Scott 1969, Goldsmith, Habing, and Field 1969, and Field, Goldsmith, and Habing 1969). Recently Shu, et al (1972) have extended the calculations of these authors to take into account the effects of a revised estimate of the abundance of iron and the effects of the density wave (or spiral shock wave) pattern in the Galaxy.

The observational evidence for the two-phase model is in a considerably more uncertain state. Clark (1965) was one of the first observers to feel that the observations indicated a preference for the two-phase model. He felt the model would best explain the observation of hydrogen self-absorption (see the emission spectrum of Figure 1b). It is the case, however, that one near-by cloud with $T \approx 20°K$ is sufficient to account for the self-absorption, independent of the general model. Clark pointed out that the gaussian spectral components found in absorption by Shuter and Verschuur (1964) gave apparent temperatures significantly lower than the 125°K peak brightness temperature commonly seen in emission. This would require that the absorbing material is cooler than the average material as would the fact that gaussian components fit to emission

spectra are on average wider than those fit to absorption spectra. However, Shuter and Verschuur's data were obtained using the basic single-dish technique and their guassians do not describe their profiles within any reasonable estimate of noise. Moreover, since emission profiles are obtained with larger bandwidths (and larger effective beamwidths) than absorption profiles, it is not surprising that they should contain wider gaussian components. Clark also noted that the dispersions of the gaussians were usually on the order of, or greater than, the velocity of sound in hydrogen clouds and the escape velocities from the clouds. This would suggest that an external source of pressure such as a hot inter-cloud medium is required in order to maintain the stability of the clouds. However, it could also mean that the dispersions each represent the blend of several clouds which could not be resolved with Clark's signal-to-noise ratios and his frequency and spatial resolutions.

Shuter (1967) has pointed out that if the differences in emission and absorption profiles are due solely to differences of angular resolution, then the dispersions of the gaussian components fit to absorption profiles should show a smooth increase with increasing angular

diameter of the background source. Plotting results taken from Clark (1965), he finds that the widths do not depend on source diameter. However, he fails to point out the fundamental limitations of Clark's data. Clark estimated that about 40 percent of his components listed as single are actually double. In addition, a disturbingly large fraction of the components found by Clark had dispersions equal to or less than Clark's bandwidth. Also, the poor signal-to-noise ratio obtained by Clark on all but a few of the smaller sources in his study made any determination of gaussian components highly uncertain. Hughes, Thompson, and Colvin (1971) have assumed the two-phase model in conducting a statistical analysis comparing observed emission brightness temperatures with corresponding absorption optical depths. Unfortunately, due to a large scatter in the data, the fit to the model depends on only a few data points. This fit is particularly unconvincing, not only because of the large variance, but also because it implies an average hydrogen density at least a factor of ten lower than normally accepted values.

Radhakrishnan, et al (1972d) discuss observations of the absorption and associated emission profiles for a number of high-galactic latitude, extra-galactic radio

sources. They find that the absorption and emission profiles do share similar gaussian components having physical temperatures in the range 20 to 200° K. However, the emission profiles invariably also contain a wide component (full width at half-maximum around 20 to 40 km/sec) not seen in the corresponding absorption profiles. These authors feel that this observation constitutes a direct proof of the two-phase model. However, their arguments depend on the assumption, which is not supported by their data, that resolution effects may be ignored at high galactic latitudes. Most discussions of the two-phase model depend on the gaussian analysis of spectral features. The severe difficulties with such analysis, especially in the presence of inadequate frequency or spatial resolution, will be discussed throughout this thesis.

It is clear that the angular sizes, temperatures, peak optical depths, and dispersions of neutral hydrogen clouds are important to the understanding of the interstellar medium. Accurate measurements of absorption profiles with good frequency and spatial resolution are necessary if gaussian analysis is to be considered at all meaningful. Clark (1965) attempted such measurements

at the Owens Valley Radio Observatory (OVRO), but was severely hampered by equipment limitations. Since that time the OVRO has decreased the system temperature by a factor of ten, increased the number of narrowband channels from one to twenty-three and converted to digital data recording and processing. In addition, narrower filter widths have become available, the side band rejection has been improved by about 20 db, and aperture synthesis observations have become routine. As a result of these developments, it has been possible to improve considerably on Clark's measurements.

CHAPTER 1

THE CHOICE OF SOURCES AND EQUIPMENT

This chapter will discuss how the source list was chosen and why the particular sets of baselines and filters were selected. The first observing session was, as is common for graduate students, a disastrous failure. The reasons for this failure and the observations and tests undertaken to correct the difficulties will also be discussed.

Table I gives the source list together with position and flux information. The principal source, Cassiopeia A (3C461), was chosen because it is an extremely strong source with a well-known structure and with no confusing sources nearby (Ryle, Elsmore, and Neville 1965). Furthermore it is at a declination which allows the rotation of the earth to be used to synthesize a nearly circular antenna. The hydrogen identified with the Perseus arm of the Galaxy causes a deep, complicated, and much-studied absorption line in the spectrum of this source (from Hagen, Lilley, and McClain 1955; Muller 1957 to de Jager 1970). Magnetic fields of 11 and 18 micro-gauss have been reported from the Zeeman splitting of this line (see Verschuur 1970 and references). That the projected

TABLE I: SYNTHESIS SOURCES

SOURCE	RIGHT ASCENSION (1950.0)	DECLINATION (1950.0)	FLUX	GALACTIC LONGITUDE	GALACTIC LATITUDE
3C461	23 21 09.0	+58 32 45	2200	111 44.3	-02 07.5
3C405	10 57 45.0	+40 35 46	1550	76 11.4	+05 45.2
3C144	05 31 31.2	+21 59 17	880	184 33.1	-05 46.9
3C353	17 17 55.3	-00 55 44	57.3	21 12.4	+19 38.4
3C147.1	05 39 11.0	-01 55 29	64.6	206 31.8	-16 21.3

magnetic field can have such high values raises some interesting questions about the spatial structure of the absorbing hydrogen. Clark (1965) established that this structure is indeed complicated, but, for reasons previously stated, was unable to carry out a full synthesis.

Since a source may be observed for a maximum of eight hours each day with the Owens Valley interferometer, three additional sources were selected for observation. The sampling theorem required that the supplementary sources have angular sizes comparable to 3C461. Cygnus A (3C405) was chosen, although it conflicts in observing time with Cassiopeia A, because, in contrast with Cassiopeia A, the absorption feature due to hydrogen associated with the Perseus arm is narrow, shallow, and apparently simple. This source was made a definite member of the source list after short-spacing observations established the presence of measurable spatial structure in the absorbing medium. The Crab Nebula (Taurus A, 3C144) and 3C353 were chosen to fill out the observing day, although neither source is at a favorable declination for aperture synthesis. The absorption feature of the Crab Nebula was known to have a complicated frequency structure, but was reported to show no spatial structure (Clark 1965,

Radhakrishnan et al 1972c). The radio galaxy 3C353 is at relatively high galactic latitude and is considerably weaker than the other sources in the source list. These two sources, then, posed a challenge to the observing techniques, but held only slight promise of producing interesting results. The HII region 3C147.1 (W12, NGC2024) was originally part of the source list. A deep absorption line showing spatial structure was discovered in the spectrum of this source (see Chapter 8). However, a proper synthesis of the source was not possible because of its declination, large size, and low flux.

The choice of baselines is guided by the sampling theorem derived in Appendix A which states that to map an area six minutes of arc on a side one must take samples of the complex visibility function at intervals less than 573 wavelengths. This interval is 397 feet at 21.1 cm wavelength which is conveniently close to the set of integral multiples of 400-foot baselines available at the OVRO. The six-minute area is sufficient to cover all sources on the source list. The 90-foot telescopes at the OVRO can only observe sources at hour angles between -4 and +4 hours. As a result, to obtain good coverage of the (u, v) plane, both north-south and east-west baselines

are required. The spacings used in this program were 200 feet east-west and 400, 800, and 1200 feet both east-west and north-south. The 1600-foot spacings available at the OVRO were not used, at the insistence of the Scheduling Committee, for reasons of economy in observing time.

The filter banks at the OVRO contain filters of widths 1, 4, 50, and 100 KHz. The shape of a line broadened solely by random thermal motions is given by

$$\exp(-mv^2/2kT)$$

or, for the hydrogen line,

$$T = 0.9734\ (\Delta\nu)^2$$

where $\Delta\nu$ is the full width at half maximum expressed in KHz. De Jager and Neven (1966) have shown that a line profile cannot be restored if its width is less than twice the instrumental width. In other words, the minimum apparent temperatures which can be measured by the four available filter banks are 4, 62, 2440, and 9734° K , respectively. These minimum temperatures can only be measured with a detailed deconvolution of the instrumental profile from the observed line profile. Such a deconvolution cannot be reasonably performed in this experiment. As a result, the true minimum apparent temperatures must

be a factor of four or so greater than those given above. On theoretical grounds, interstellar hydrogen clouds are predicted to have temperatures ranging from 25 to 200° K (Shu, et al 1972). Narrow spectral features have been observed with apparent temperatures less than 30° K (Verschuur 1969, Verschuur and Knapp 1971 and Riegel and Jennings 1969). Thus, the 1-KHz filters are the natural choice.

The interferometer at the OVRO used for this program consists of two fully-steerable, 90-foot diameter paraboloids. The telescopes may be moved along railroad tracks between sets of fixed mounting piers. The signals are received at the prime focus where they are amplifed by parametric amplifiers followed by tunnel diode amplifiers. The resulting system temperatures ranged from 125 to 150° K during the early stages of the program, but were reduced to 90° K by the installation of new paramps in the fall of 1970. The RF amplifiers are followed by an RF filter tuned to the line frequency, the mixer, and the first IF amplifiers. Further IF amplification is provided in the base of the telescopes. The IF signals from both telescopes are carried by buried cable through the delay system to a central observing room where they receive further

amplification and are split between the full "broadband" channel and the filter banks. The outputs from the filters for one telescope are multiplied by the outputs from the corresponding filters for the other telescope. The multiplied outputs after some DC amplification are recorded on magnetic tape at five-second intervals. This regular sampling interval is made possible by an analogue phase rotator which removes the natural fringe rate and adds a 1/60 Hz fringe. The amount of the phase rotation as well as the time and channel number are recorded with each data point.

The filter bank consists of 23 pairs of crystal filters each having a bandwidth of 1 KHz; the separation between adjacent central frequencies is 2 KHz. Thus to obtain one-KHz resolution on a feature of width 46 KHz it is necessary to use two distinct local oscillator settings. Since few hydrogen absorption features are as narrow as 46 KHz, it was in fact necessary to use more than two such settings. The local oscillator settings (or "frequency shifts") used on the principal sources are listed in Table II where the frequency shifts are expressed in KHz from the Local Standard of Rest for the central channel of

TABLE II: FREQUENCY SHIFTS FOR THE PRINCIPAL SOURCES

3C461	3C405	3C144	3C353
+370 c	+540 c	+125 c	+130 c
+260	+430 *	+020	+018
+231	+428	-003	-005
+226	+423 *	-026	-028
+217	+403	-049	-140 c
+192	+384 *	-072	
+171	+382	-180 c	
+146	+377 *		
	+260 c		

* 200' East-West only

c continuum frequency shift

the filter bank. Those frequency shifts used to observe the background source in the continuum are identified by the letter c.

The initial observing session of this program was a disastrous, but educational, failure. The narrowband calibrations were seriously in error as a result of absorption features in the spectra of the calibration sources. The measured fluxes of the strong sources were significantly lower than those measured by Fomalont (1967). Detector law failure and the overloading of the IF amplifiers were suspected as the causes of this difficulty. The measured flux at the bottom of the deep line of 3C461 was higher than that reported in the literature (Clark 1965 and references). Problems with the wings of the narrow filters and with incomplete sideband rejection were suspected. Finally, the gains and phases of the narrowband channels relative to those of the broadband channel varied as a group with time. Variations in the shape of the wings of the IF amplifier passband were blamed for this difficulty.

The problem revealed the necessity of knowing the location of the absorption features in the spectra of the calibration sources. To this end an observing session was

conducted at 800 feet east-west (8/29/69 to 9/4/69) using the 4-Khz filter bank. The spectrum obtained for 3C123 is shown in Figure 2, but the other spectra obtained will not be presented here since better spectra of comparable frequency resolution have been published by Hughes, Thompson, and Colvin (1971). The spectra obtained by these authors were used well in advance of publication to help determine what frequencies should be avoided in observing calibration sources.

A noise diode was also used as a strong calibration source, but only for the relative gains and phases of the narrowband channels. The noise diode was placed midway between the two antennas and was connected to both receivers through cables and 20 db directional couplers. There was no serious difficulty in treating the noise diode as a celestial source, since the noise diode has a natural fringe rate of zero which is essentially equivalent to a source at the North Pole.

In December, 1969 the frequency response of a few of the narrow filters and the detector law of the broadband channel were measured. The problem of detector law is complicated and, hence, is deferred to Appendix C. Samples of the filter responses are shown in Figures 3a and 3b.

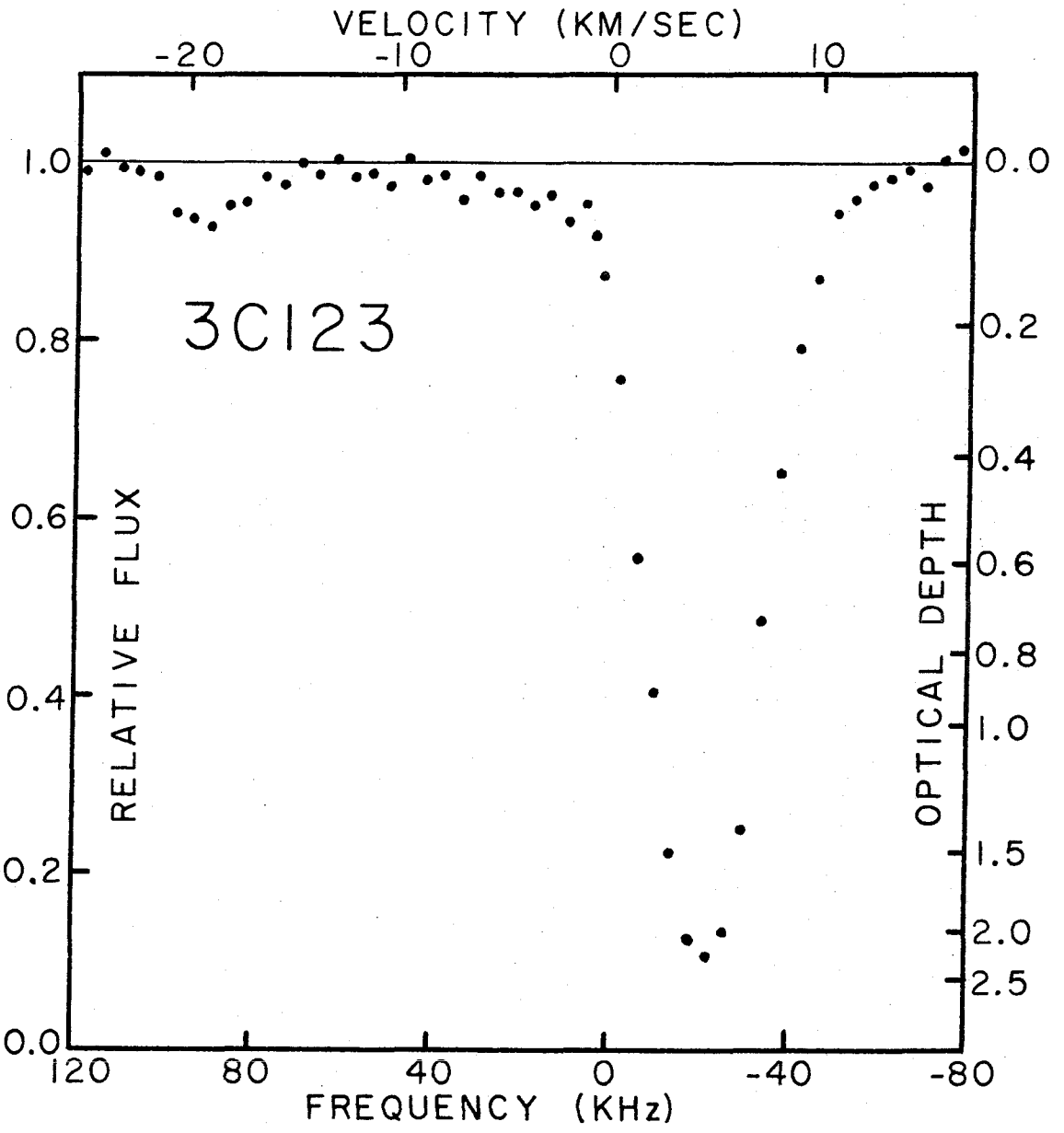

Figure 2. Spectrum of 3C123 obtained at 800 feet east-west using 4 KHz filters with about 165 minutes integration.

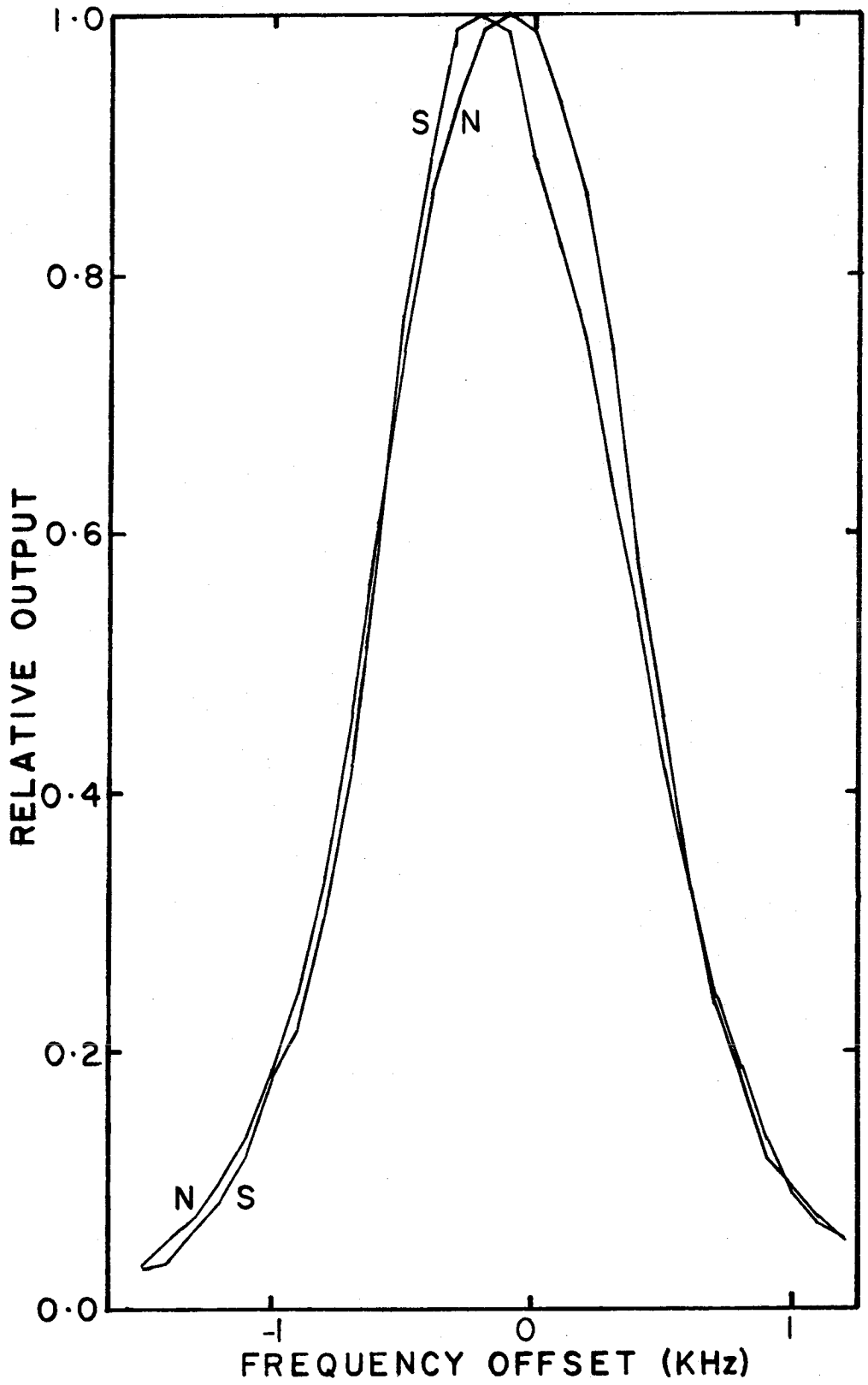

Figure 3a. Response of filter as a function of frequency.
Formal frequency center = 9.989 MHz

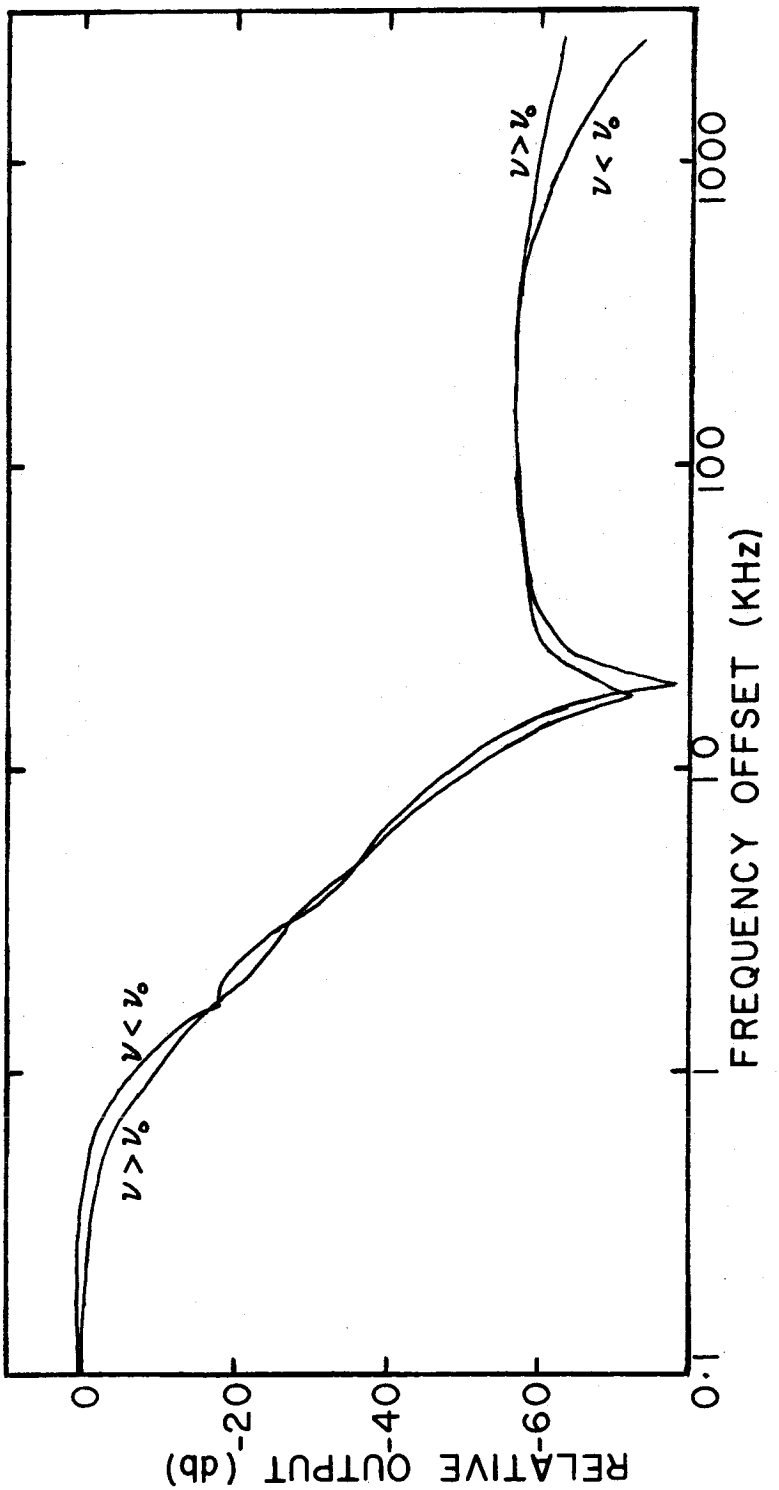

Figure 3b. Response of 10.001 MHz (south) filter as a function of frequency, logarithmic scales.

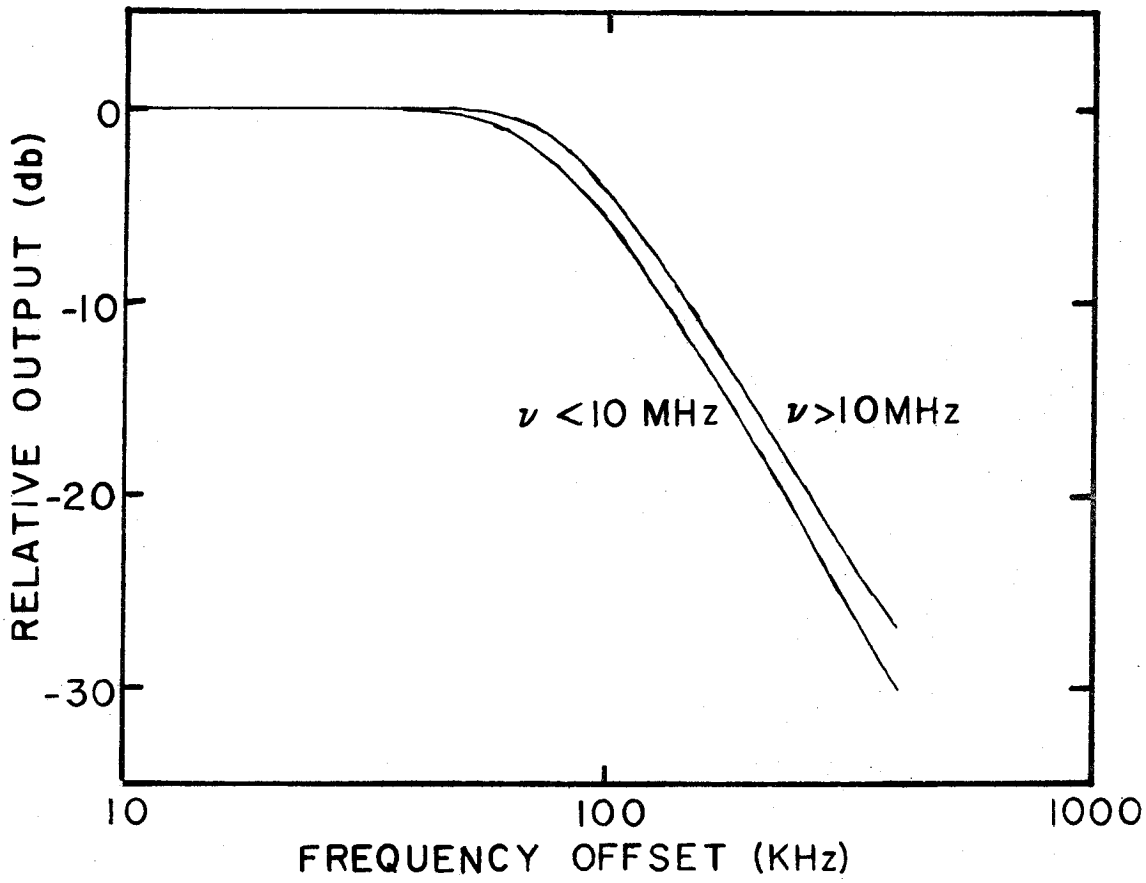

Figure 3c. Response of IF prefilters as function of frequency, logarithmic scales.

The filter profiles were obtained with a frequency synthesizer and a square-law detector calibrated with precision attenuators. Figure 3b reveals that the wings of the narrow filters could provide some difficulties. The full flux of the source over the 5-MHz IF bandwidth can produce an apparent response from the 1-KHz filter down by only 19 db. In other words, an infinite optical depth would be measured as an optical depth about 4.4. An incorrect measurement will also result if the image sideband is not completely rejected. However, the sideband rejection was measured to be greater than 30 db. In addition, since the image sideband enters with a fringe frequency different from that of the signal sideband (see Appendix A), the reduction programs further surpress any response from the image sideband.

Several problems were solved by adding in the base of the telescopes the 160-KHz IF prefilters whose frequency response is plotted in Figure 3c. First, they remove all problems with the wings of the narrow filters. Second, they remove from the broadband channel (and hence from the absolute and relative calibrations) the effects of gain changes at frequencies not relevant to the narrow channels. Third, they reduce the signal levels entering the IF

amplifiers in the base of the telescopes and thereby reduce any problems of overloading these amplifiers. Fourth, they provide the accurate knowledge of the intermediate frequency necessary for the proper measurement of fringe phase. Observations without the prefilters have shown that the effective intermediate frequency varies with time and can reach values seriously different from the formal value of 10 MHz. The loss in signal-to-noise ratio due to these filters is not particularly important for the strong sources in this program. However, the narrow broadband makes it necessary to observe the calibrators at frequencies well removed from any absorption features. This means that careful corrections have to be made for frequency dependent gain and phase effects. The manner by which these corrections are determined and applied is discussed in the next chapter.

CHAPTER 2

THE OBSERVING AND REDUCTION PROCEDURES

This chapter provides brief descriptions of the observing sessions and procedures, of the general principles of the reduction and calibration programs, and of the observed noise diode behavior.

The dates of the observations and the relevant baseline parameters are given in Table III while Table IV gives the list of calibration sources together with their positions and fluxes. The fluxes of those sources used only as phase calibrators are given in parentheses and the range of frequency shifts which were not used because of absorption lines is indicated. The comments column states which calibrators were not used at the longest spacings and which calibrators were assumed to vary in flux. The latter were calibrated at each baseline using rapid comparative observations with sources like 3C295 and 3C147.

The pointing corrections for each antenna were determined using the standard three-point method. The corrections were measured over the full range of hour angle at four declinations between 0° and 60°. The pointing calibration sources were 3C461, 3C405, and 3C144 using single-dish

TABLE III: BASELINE DATA

FORMAL BASELINE (FEET)		DATES OF OBSERVATIONS START	END	SPACING (FEET)	HOUR ANGLE	DECLINATION	PFCOR (FR/MHz)	NOISE DIODE PFCOR (FR/MHz)	BANDPASS SLOPE (%/MHz)
200	EW	3/2/70	3/9/70	199.9460	06 00 05.21	+00 02 16.4	0.273	+0.306	-13.1
400	EW	7/15/70	7/20/70	399.8741	06 00 01.26	+00 01 27.5	0.530	+0.028	0.
800	EW	7/21/70	7/29/70	799.9921	06 00 00.70	+00 00 40.3	1.002	-0.020	0.
400	NS	11/20/70	11/26/70	400.0635	00 00 03.55	-52 46 32.6	0.572	-0.524	+ 6.4
800	NS	12/1/70	12/10/70	800.1852	00 00 02.55	-52 46 41.2	1.099	-0.806	+ 4.3
1200	EW	1/16/71	1/27/71	1199.9843	06 00 00.54	+00 00 42.8	1.559	-0.028	+ 8.8
1200	NS	3/14/71	3/24/71	1200.0411	00 00 00.49	-52 46 30.5	1.683	-1.430	+12.9

TABLE IV: CALIBRATION SOURCES

SOURCE	RIGHT ASCENSION (1950.0)	DECLINATION (1950.0)	ℓ^{II}	b^{II}	FLUX*	FREQUENCY SHIFT RANGE NOT USED	COMMENTS
3C48	01 34 49.82	+32 54 20.4	134.0	-28.7	15.6	-175 +225	
3C123	04 33 55.30	+29 24 13.4	170.6	-11.7	47.0	-175 +220	not 1200'
3C147	05 38 43.49	+49 49 42.4	161.7	+10.3	22.3	-150 +200	
3C161	06 24 43.01	-05 51 15.0	215.4	- 8.1	19.0	-300 +120	not 1200'
3C196	08 09 59.39	+48 22 08.0	171.2	+33.2	14.25	-225 +180	
2C216	09 06 17.26	+43 05 59.0	178.3	+42.8	(4.0)	—	
3C237	10 05 22.07	+07 44 59.0	232.1	+46.6	(6.5)	—	not 1200'

* ( ) means not used a a flux calibrator

Table IV (Continued)

CALIBRATION SOURCES

SOURCE	RIGHT ASCENSION (1950.0)	DECLINATION (1950.0)	ℓ^{II}	b^{II}	FLUX*	FREQUENCY SHIFT RANGE NOT USED	COMMENTS
P1127-14	11 27 35.70	-14 32 54.8	275.3	+43.6	(6.0)	——	
P1151-34	11 51 49.80	-34 48 40.4	289.9	+26.3	(6.4)	——	
3C273	12 26 32.90	+02 19 38.0	290.0	+64.4	(~43)	——	not 1200'
3C286	13 28 49.66	+30 45 58.3	56.5	+80.7	(15.3)	——	
3C295	14 09 33.44	+52 26 13.6	97.5	+60.8	22.7	none	
3C309.1	14 58 56.50	+71 52 10.8	110.0	+42.1	(8.5)	——	
3C380	18 28 13.38	+48 42 39.3	77.2	+23.5	15.6	-225 +400	variable
3C454.3	22 51 29.52	+15 52 53.7	86.1	-38.2	~13.5	-130 +175	variable

* ( ) means not used as a flux calibrator

observations, and 3C273 using interferometer observations. All pointing corrections were determined at frequencies well separated from the Galactic hydrogen emission. A sample of the pointing curves is given in Figure 4. Such complete pointing curves are not required for the simple measurement of fluxes and phases. However, pointing errors can introduce significant errors in the observations of extended sources (Berge and Greisen 1969). The pointing curves are believed to be accurate to better than $\pm$ 1 minute of arc, although systematic errors of this magnitude could also be introduced by winds in excess of 20 miles per hour and by long-term sags in the telescope mounts.

The sources being studied for HI absorption were observed over the full hour angle range (except for 3C353). Five ten-minute observations each with a different frequency shift were taken on the source. Then a ten-minute record on a calibration source was taken, followed by a five-to-ten-minute record on the noise diode. With this scheme, after several days of observation, sufficient integration time and coverage of the (u, v) plane were obtained for each frequency shift. The local oscillator settings were chosen to correct for the motions of the

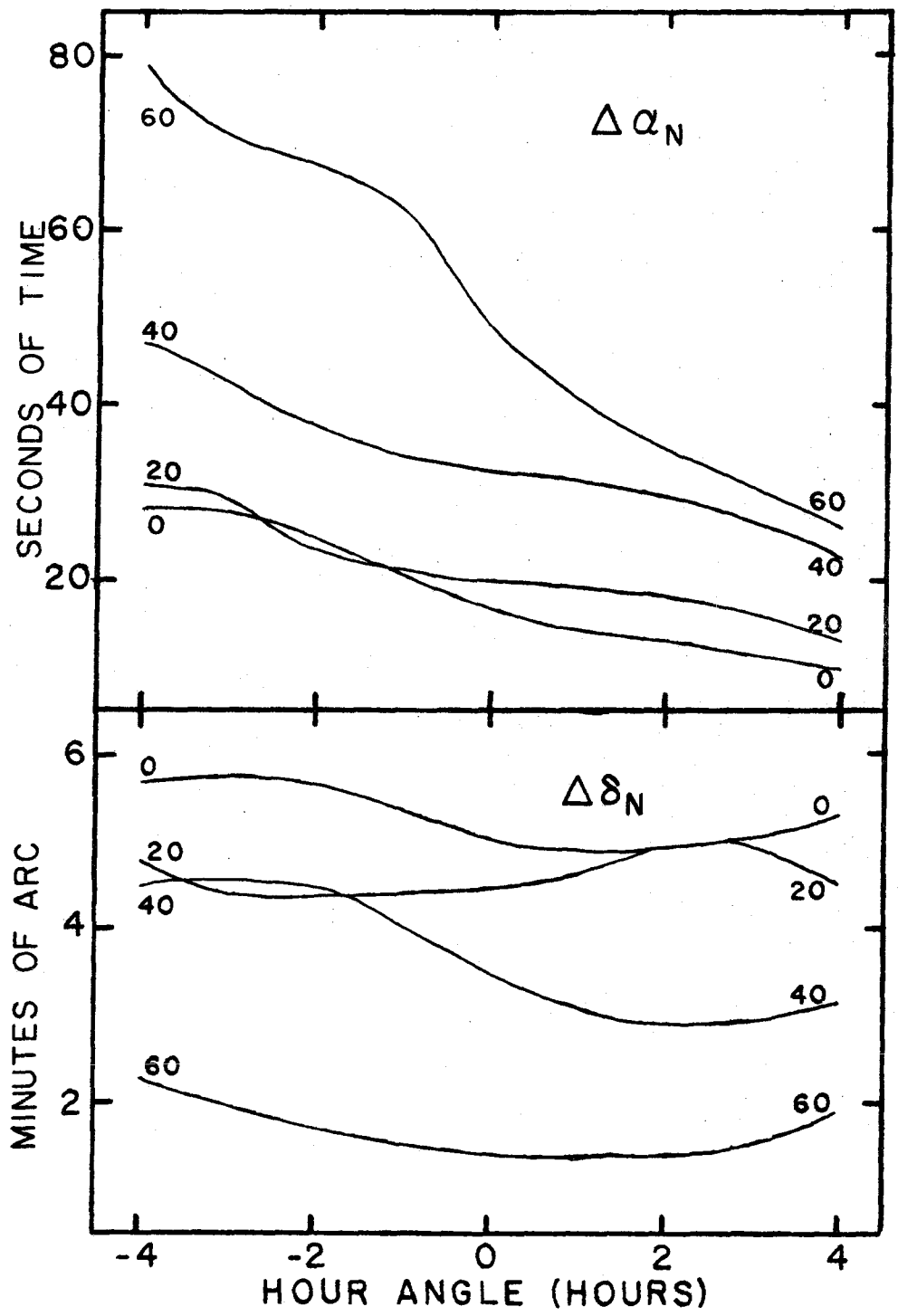

Figure 4a. Sample of pointing curves - corrections for north antenna at 1200 feet north-south.

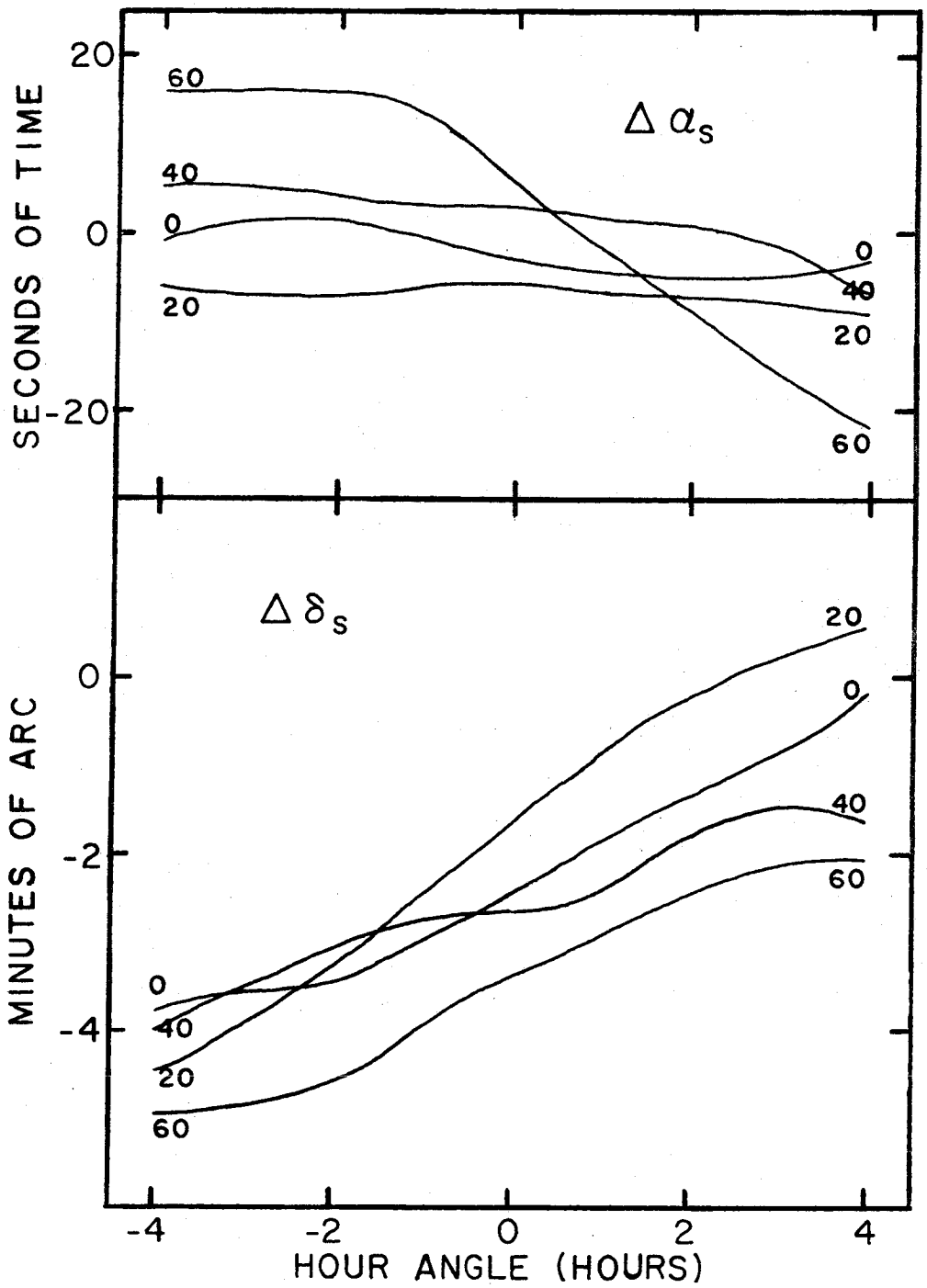

Figure 4b. Sample of pointing curves — corrections for south antenna at 1200 feet north-south.

earth as a function of time and for the standard solar motion. As a result, for a given frequency shift, each channel represents a fixed frequency with respect to the Local Standard of Rest. The duration of each record and other inaccuracies cause an uncertainty in the frequency on the order of 0.1 KHz which is negligible. Because the IF passband is narrow, it was not necessary to track delay. At the 1200-foot spacings, the delay was set to an average value for each record, but at the shorter spacings the delay was held at a fixed value for all observations.

In each day of observation, there was a period of several hours during which none of the principal sources could be observed. This period was used to obtain measurements of the baseline and of the frequency-dependent corrections. The corrections to the formal baseline are found by observing in rapid succession at one frequency a number of point sources of known position well-distributed in hour angle and declination. The frequency-dependent corrections are found by observing alternately 3C295 and the noise diode at many frequencies, with a central frequency used for calibration. In general, it was found that the amplitude correction was essentially a linear function of frequency with only moderate slope.

As is derived in Appendix A, the measured fringe phase will be a linear function of local oscillator frequency whenever the electrical lengths of the local oscillator chains to the two telescopes are different. Also, if the difference in electrical lengths of the cables connecting the noise diode to the two telescopes is not the difference which would obtain for a source at the north celestial pole, then the measured phase of the noise diode will have an additional linear dependence on frequency. Since observations of the noise diode are to be used to calibrate observations of sources and observations at one frequency are to be used to calibrate observations at other frequencies, both these phase-frequency ("PFCOR") corrections must be accurately measured.

The first stage of the computer processing, called INSPECT, locates permanent read errors on the data tapes and provides some checks of the log sheets. A program called ANALYZ is then used to reduce the records to uncalibrated fringe amplitudes and phases. At each data point, the program computes the phase of the natural fringe. The difference between this phase and that of the lobe rotator is then the expected phase, $\theta(t)$, of the

one-minute fringe. The program fits the data to a function of the form

$$x_1 \cos(\theta(t)) + x_2 \sin(\theta(t)) + x_3$$

using a least-squares method and provides estimates of how well the data did fit this function.

The next program in the sequence is used to determine the corrections to the formal baseline. Using only the data specially recorded for the purpose, it iterates between a least-squares determination of the corrections to the baseline length and pole coordinates and an attempt to fit a smooth instrumental phase-time function through the data. The instrumental phase-frequency correction may be determined simultaneously. This procedure was found to converge very rapidly — usually after only two iterations. The noise diode PFCOR and the instrumental bandpass shape are determined by hand from the output of ANALYZ. Finally, the CALIBRATE program applies the baseline and frequency-dependent corrections to the data. It determines smooth functions of time for the instrumental gain and phase and applies these corrections to the data. The data are divided into groups within each of which it is assumed that the gains and phases of the narrowband

channels remain constant with respect to the broadband. The program uses observations of "channel difference" calibrators (principally the noise diode and the continuum frequency shifts of the principal sources) to produce weighted averages of the relative phases and gains within each group. These averages are then applied to all data within the group. In practice, it was found that the assumption of constant relative calibration was not particularly good, despite the use of the IF prefilter. As a consequence, it was necessary to check all data carefully and to divide it into many short (two to four hour) groups.

The noise diode turned out to be an excellent channel difference calibrator. Relative calibrations determined from the sources alone agreed, within the uncertainties, with calibrations determined solely with the noise diode. However, there was a slight systematic difference when the sources were significantly different in flux from the noise diode. Fortunately, the apparent flux of the noise diode decreased with increasing baseline (due to the increase in cable lengths) and remained comparable in strength with Cassiopeia A at all baselines. It was originally hoped that the noise diode would provide a secondary calibration

for the full instrumental function. However, as may be seen in Figures 5, such was not the case. The large lengths of cable involved were simply too sensitive to temperature and other effects.

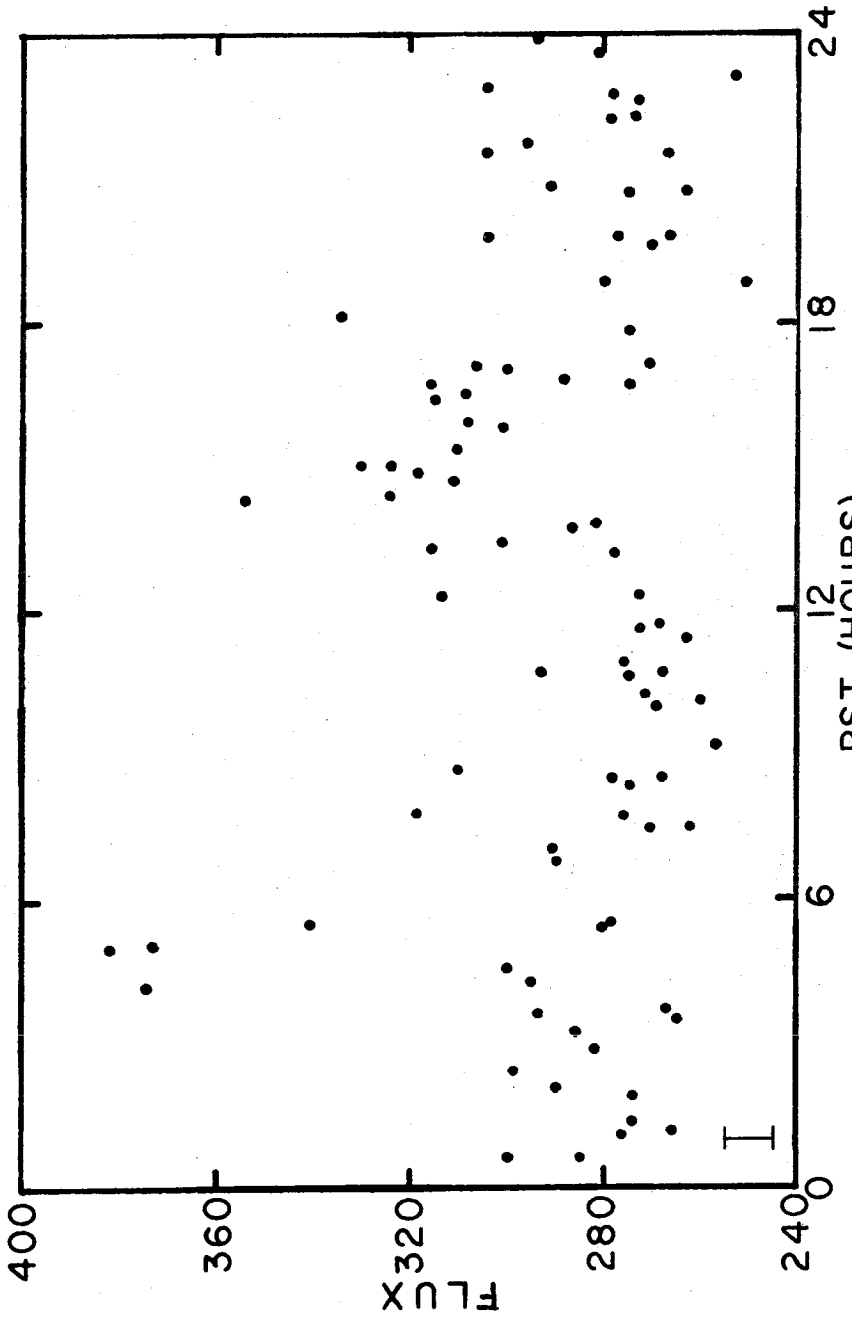

Figure 5a. Noise diode flux as a function of standard time at 800 feet east-west.

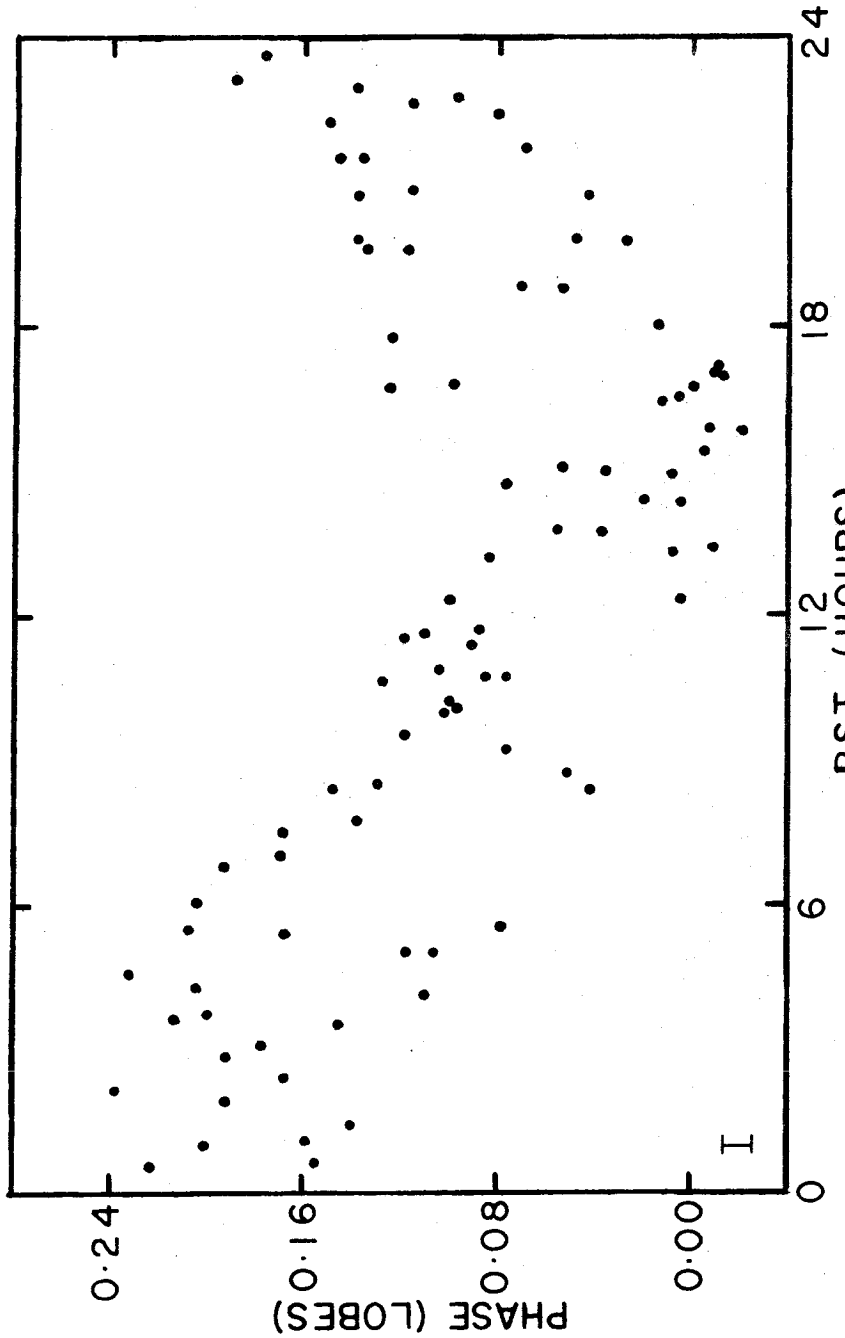

Figure 5b. Noise diode phase as a function of standard time at 800 feet east-west.

CHAPTER 3

POST-CALIBRATION ANALYSIS

This chapter discusses the theory and practice of three aspects of the post-calibration analysis: the Fourier inversion procedure, the noise, and the gaussian fitting of observed spectra.

A. The Fourier Inversion Procedure

It is shown in Appendix A that the interferometer responds to the complex visibility function, $\underset{\sim}{V}(u, v)$, where

$$\underset{\sim}{V}(u, v) = \frac{1}{\kappa} \int_{-\infty}^{\infty}\int T_B(x, y) e^{+i\, 2\Pi(ux + vy)}\, dx\, dy$$

where κ is a constant carrying control of the units and $T_B(x, y)$ is the brightness distribution of the source. We may restore $T_B(x, y)$ using the usual Fourier transform properties as

$$T_B(x, y) = \kappa \int_{-\infty}^{\infty}\int \underset{\sim}{V}(u, v) e^{-i\, 2\Pi(ux + vy)}\, du\, dv \ .$$

Unfortunately, we cannot measure $\underset{\sim}{V}$ except at discrete points in the (u, v) plane and then only for values of (u, v) less than some (u_{max}, v_{max}). In other words, we are restricted to measuring

$$\underset{\sim}{V}_1(u, v) = \underset{\sim}{V}(u, v)\, S(u, v)$$

where the sampling function S is given by

$$S(u, v) = \sum_{i=1}^{N} \omega_i\, {}^2\delta(u - u_i, v - v_i)$$

with the ω_i being the set of weights assigned to the N measurements. The Hermitian property of the visibility function allows us to extend the sampling function to

$$S(u, v) = \sum_{i=1}^{N} \omega_i \left[{}^2\delta(u - v_i, v - v_i) + {}^2\delta(u + u_i, v + v_i) \right].$$

In fact the sampling function should be written to account for the finite size of the antennas and the finite lengths of the observations. However, it may be shown that the effect of the finite dish size is equivalent to expressing

$$T_B(x, y) = T_S(x, y)\, B_{SD}(x, y)$$

where $T_S(x, y)$ is the true source brightness distribution and $B_{SD}(x, y)$ is the beam pattern of the antennas. The other effect may be ignored so long as each observation is of sufficiently short duration.

I have chosen for my observations to perform the Fourier transform directly upon the sampled V_1. This method was suggested to me by D. H. Rogstad (1971, private

communication) from work he had performed with Hogbom, Weiler, and others. The Fourier transform methods used by some other observers are discussed in Appendix D. The exact choice of weights in the sampling function is not of critical importance to the transform procedure described here, but it is clear that some sets are to be preferred over others. To avoid overemphasis of one part of the (u, v) plane to the detriment of others, the weights are first taken to be inversely proportional to the local density of observations in the (u, v) plane. To reduce the effects of the absence of data beyond the maximum spacing, the weights are then tapered with a gaussian having a value 0.3 at the maximum spacing.

When the direct Fourier transform is performed, we obtain a map, called the "dirty" map, which may be expressed as

$$T_D(x, y) \equiv \underset{\sim}{\bar{V}}_1 = \underset{\sim}{\bar{V}} * \bar{S}$$

where the bar indicates a Fourier transform and the asterisk indicates a convolution. Noting that $\underset{\sim}{\bar{V}} = T_B$ and calling $\bar{S}$ the "dirty" beam, $B_D(x, y)$, we see that the dirty map is the convolution of the source brightness (modified by the single-dish beam pattern) with the dirty

beam. Such a result is quite unfortunate for my program. For each frequency shift we obtain a different set of (u_i, v_i) and hence different dirty beams. To obtain optical depth maps it is necessary to take the logarithm of the ratio of maps determined using the frequency shifts in the continuum to maps determined using the frequency shifts in the absorption feature. In so doing, the effects of the different dirty beams would be mixed together and the results would contain large and unknown errors.

Thus, for this program in particular, it is necessary to remove the effects of the dirty beam patterns. Since the dirty beam pattern is simply the dirty map which would be found for a point source, we assume that the source actually consists of a set of such point sources. The deconvolution program, "CLEAN", finds the highest point on the dirty map and removes an appropriately scaled dirty beam pattern centered on that point. It then searches the map which is left for the highest remaining point (in absolute value) and removes another appropriately scaled beam pattern centered on that point. This process continues until the highest remaining point is less than some level defined to be the noise. It is then necessary to add back to what remains of the map the point sources

which have been found. Since the point-source model is obviously incorrect for most sources, the restoration is done with appropriately scaled simple gaussians all having the same width as the central peak of the dirty beam. Until the restoration step the Fourier transform relationship between the data and the map is strictly maintained. However, the restoration process effectively tapers the original data.

In practice, this "cleaning" procedure works very well, expecially for sources for which the point source model is not too far from the truth. Convergence is rapid to noise levels around one percent of the peak brightness of the original dirty map. In order to speed convergence, it has been found that it is best to remove a beam pattern scaled to only one-half the brightness of the peak found by the program. As a test of the cleaning procedure, it is possible to vary the set of weights in the sampling function. This causes significant variations in the dirty beam, the dirty map, and the set of point sources found. However, the clean map is not found to vary by any significant amount. Thus, although the set of point sources found is not a unique set, the restoration process does allow a unique "principal solution" to be obtained.

One of the tests I have performed on this method is to create maps of my sources 18 minutes of arc on a side. This is a serious violation of the sampling theorem which, in its simple form, assumes that the data are sampled on a regular rectangular grid. The use of a direct Fourier transform on data sampled irregularly along elliptical arcs forces the sampling theorem to be modified. The results of the modification are that the map will repeat in the radial direction but the power will be smeared out over the full elliptical ring resulting in a considerably lower intensity in the ring than at the center of the map. The results of this test are presented in the appropriate sections of the following chapters. It is found that side lobe responses which can exceed 50 percent are reduced by the deconvolution process to random noise almost always less than five percent and usually less than one percent.

It is interesting to compare maps obtained using very narrow clean beams with maps obtained by other investigators who actually obtained that good a resolution. One of my maps obtained this way is shown in Figure 6 and should be compared with the map obtained by Ryle, Elsmore, and Neville (1965). Real components of the source, which are unresolved with a proper choice of clean beam, are

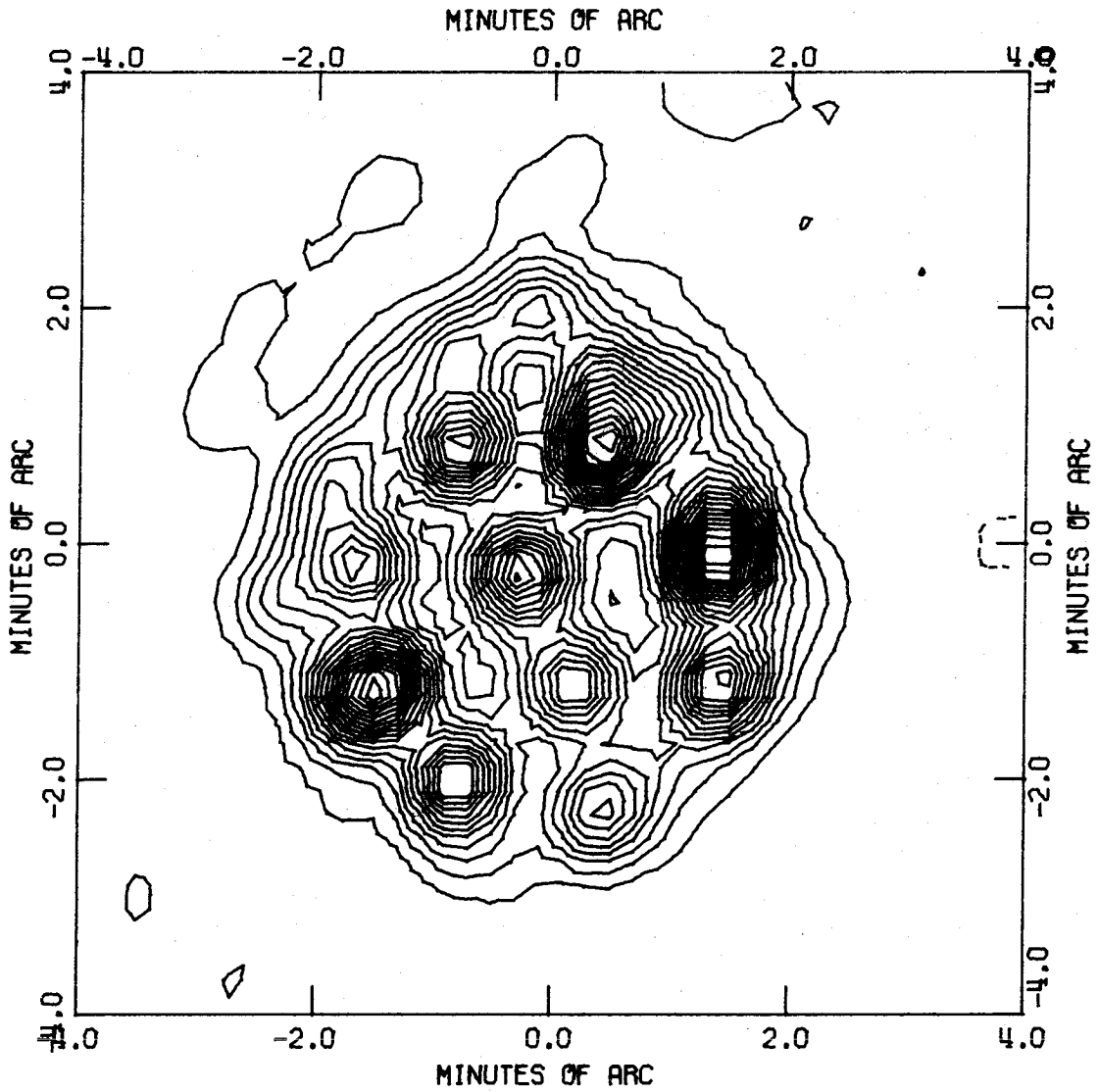

Figure 6. 3C461: continuum map produced with clean beam 0.67 minutes of arc between half maxima. 5% contour interval, zero contour suppressed.

found to be present on the map of Figure 6. However, the intensities of the various components are significantly distorted. Thus the deconvolution procedure can be used to reveal source structure which is smaller than the beam size. Since this is equivalent to an extrapolation of the data to longer spacings than are obtained, the reliability of the source structure revealed depends heavily on the noise at the longest spacings.

There is a difficulty with the deconvolution procedure which should be discussed. The total flux on the dirty map is given by

$$F = \frac{1}{\kappa} \int_{-\infty}^{\infty}\int T_B(x, y)dx\, dy = V_1(0, 0) .$$

Therefore, if the data do not include "zero-spacing" observations, the total fluxes on the dirty maps and dirty beams are zero. However, the cleaned maps and clean beams do not have a zero integral. As a result there are problems with the zero-level and the scaling of the maps. Since my sources are smaller than the map areas the zero-level problem will not seriously affect the brightness distributions. In fact, the lack of zero-level determination is deliberately used in this program to remove most of the effects of the general hydrogen emission. The uncertainty

in the scale factor may be ignored since the desired optical depth maps will only depend on relative values of the brightness.

We may summarize the foregoing discussion as follows. The data are Fourier transformed by a brute force method after which the effects of the beam pattern are mostly removed. For data with good signal-to-noise ratio, this deconvolution procedure is a reliable and systematic way to interpolate between the data points in the (u, v) plane. To an extent limited principally by experimental error, the deconvolution procedure may also be used to extrapolate the data to larger spacings than were actually obtained.

B. Noise

Throughout the preceeding discussion it was implicitly assumed that the observations were made without experimental error or noise. Such an ideal situation cannot, of course, exist. For a correlation interferometer the uncertainty in antenna temperature may be written as

$$\Delta T_S = (T_S + T_a + T_R)/\sqrt{2\tau\Delta\nu}$$

where τ is the integration time, $\Delta\nu$ the bandwidth, T_S the antenna temperature due to the source, T_a the antenna

temperature due to other sources of radiation within the beam, and T_R is the receiver temperature (90 to 150° K). We may substitute the approximate relation

$$T_S = 0.1\ f$$

where f is the source flux in flux units to obtain

$$\Delta f = (0.009)(0.1f + T_a + T_R) \ .$$

Thus, Δf ranged from 0.8 to 1.4 flux units when f and T_a were nearly zero and from 3.2 to 3.8 flux units when $f \sim 2200$ and $T_a \sim 50$ (the case of 3C461 in the wings of the line). The associated phase uncertainty may be visualized in the complex plane as the result of a small vector of magnitude Δf assuming a random angle with respect to the visibility vector (see Figure 7). The rms value of the phase error is given by the approximate empirical formula

$$\Delta\varphi = \frac{x}{1 + x^2} + \frac{x^2}{2 + x^2/\pi}$$

where $x \equiv \Delta f/f$ (Shostak 1972). The uncertainties in the measurements of strong sources are governed more by the uncertainties in calibration than the random noise uncertainties discussed above. The calibration program estimates such uncertainties from the deviations of the data on calibration sources from the smooth instrumental

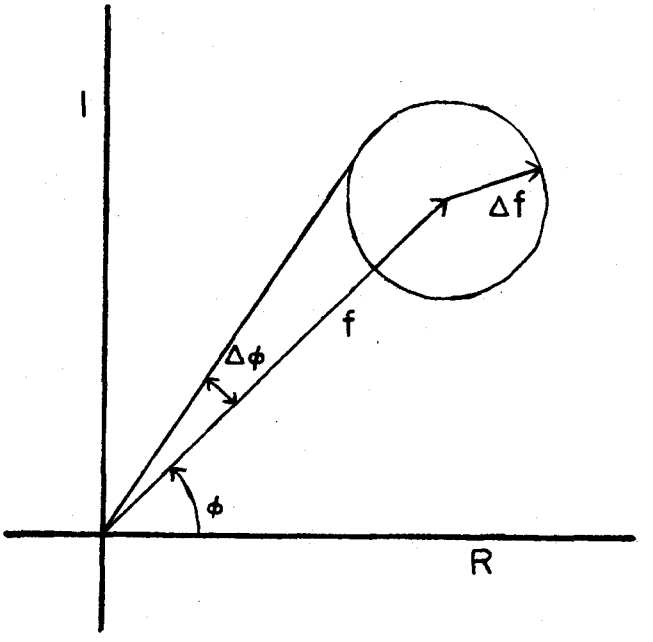

Figure 7. Illustration of phase error in complex plane.

function fit to that data. In practice, the gain uncertainty was at least one percent and the phase uncertainty at least one to two millilobes (where one lobe is a 2π radians change in phase).

We must now determine how the uncertainties of the individual measurements affect the final maps. These maps are produced using the formula

$$T_B(x, y) = \kappa \sum_{i=1}^{N} \omega_i \hat{F}_i \cos\left(\hat{\varphi}_i + 2\pi(u_i x + v_i y)\right).$$

We employ the Hermitian property of the visibility function and define

$$\omega_0 = 0$$

$$\omega_{-m} = \omega_m$$

$$V_{-m} = V_m^*$$

$$u_{-m} = -u_m$$

$$v_{-m} = -v_m$$

to obtain

$$T_B(x, y) = \frac{\kappa}{2} \sum_{i=-N}^{N} \omega_i \underset{\sim}{V}_i e^{-2\pi i(u_i x + v_i y)}.$$

The usual formula for the propagation of errors is

$$\sigma^2(T) = \left\langle \left| \sum_{i=1}^{N} \frac{\partial T}{\partial V_j} \Delta V_j \right|^2 \right\rangle .$$

Using

$$\frac{\partial T}{\partial V_j} = \frac{\kappa}{2}\,\omega_j\, e^{-2\pi i(u_j x + v_j y)}$$

we obtain

$$\sigma^2\left(T_B(x, y)\right) = \sum_{j=-N}^{N}\sum_{k=-N}^{N} \left(\frac{\kappa}{2}\right)^2 \omega_j\omega_k e^{-2\pi i\left[(u_j-u_k)x+(v_j-v_k)y\right]}\langle \Delta V_j\ \Delta V_k^*\rangle \cdot$$

We assume that the individual measurements are independent and thus that all terms of the form

$$\langle \Delta V_j\ \Delta V_k^*\rangle \qquad (j \neq \pm k)$$

in this double sum vanish. Where gain uncertainties are important, this assumption is only valid if each measurement at a given frequency shift is not followed by another at the same frequency shift within the correlation time of the gain instabilities. For my program this condition was nearly always satisfied although for most other programs such a situation does not obtain. With this assumption, the uncertainty becomes

$$\sigma^2\left(T_B(x,y)\right) = \sum_{-N}^{N} (\kappa\omega_j/2)^2 \left\langle |\Delta V_j|^2 + \Delta V_j \Delta V_j e^{-4\pi i(u_j x + v_j y)}\right\rangle$$

or

$$\sigma^2\left(T_B(x,\ y)\right) = \sum_{j=1}^{N} 0.5\kappa^2\omega_j^2 \langle |\Delta V_j|^2 + \mathrm{Re}\left[\Delta V_j \Delta V_j e^{-4\pi i(u_j x + v_j y)}\right]\rangle .$$

If we express the visibility as the sum of a real and an imaginary part as

$$V = R + i\ I$$

and assume the uncertainties in the real and imaginary parts are uncorrelated[1] we obtain

$$\sigma^2\left(T_B(x,\ y)\right) = 0.5\,\kappa^2 \sum_{1}^{N} \omega_j^2 \left[\left(\langle \Delta R_j^2\rangle + \langle \Delta I_j^2\rangle\right) + \left(\langle \Delta R_j^2\rangle - \langle \Delta I_j^2\rangle\right)\cos\ 4\pi(u_j x + v_j y)\right] . \tag{3B-1}$$

The first term yields an uncertainty which does not depend on position. The second term yields a position-dependent uncertainty which is expected to be quite small and, hence, is usually ignored. The uncertainties associated with the observations may be used to compute the values of $\sigma^2\left(T_B(x,\ y)\right)$. The results of such computations are presented in the appropriate sections of the following chapters. For ease in presentation, the value of the

---

1 This assumption is not easily justified when the calibration is the dominant source of the uncertainty.

second term was computed only as an upper limit of the form

$$0.5\,\kappa^2 \sum_{j=1}^{N} \omega_j^2 \left| \langle \Delta R_j^2 \rangle - \langle \Delta I_j^2 \rangle \right| .$$

This procedure is justified by the finding that the upper limit was always small compared to the first term.

The noise on the final maps was also determined in a Monte Carlo fashion. The data prior to inversion were altered by adding the associated visibility errors in a random fashion and with a gaussian distribution.[2] The full inversion procedure was then followed for a number of sets of the altered data and the point-by-point variances of the dirty and cleaned maps were computed. The results of this test are presented in Table V. The first two columns give the source name and the particular frequency used for the Monte Carlo test. The middle columns give the averages of the point-by-point variances of the maps before and after cleaning. The variances of the averages of the variances are also given. The last two columns give, for comparison, the constant and maximum variable parts of the noise

2 All error computations are done with the errors in the real and imaginary parts of the visibility function. These errors may be assumed to have a gaussian distribution while the errors in flux and phase will have much more complicated distributions.

TABLE V: COMPARISON OF MONTE CARLO TESTS TO THEORY

SOURCE	FREQUENCY (KHz)	MONTE CARLO TESTS NOISE ON DIRTY MAPS	MONTE CARLO TESTS NOISE ON CLEAN MAPS	THEORY CONSTANT	THEORY VARIABLE (max)
3C461	199	70.4 ± 16.3 °K	112.7 ± 47.4 °K	72.5 °K	1.84 °K
3C461	229	22.6 ± 4.7	22.0 ± 5.8	23.4*	0.17
3C405	362	248.8 ± 74.0	252.3 ± 104.1	287.3	2.26
3C405	400	189.8 ± 41.6	169.0 ± 41.0	243.0	2.14
3C144	- 94	143.9 ± 17.8	206.9 ± 71.2	197.9	3.24
3C144	- 50	55.3 ± 11.0	58.4 ± 18.9	56.1	2.47
3C353	- 4	19.9 ± 4.7	21.1 ± 7.4	22.9	0.32
3C353	+ 38	19.8 ± 4.6	23.7 ± 10.2	24.9	1.53

* At this frequency, the Monte Carlo test was done with only one of the two overlapping frequency shifts. Hence, the theory result has been increased by a factor of $\sqrt{2}$. This factor was not applied to the variable part of the theory result.

evaluated with the theoretical formula derived above. The table reveals a very pleasing agreement between the two methods of estimating the noise. The Monte Carlo tests indicate that the noise is not constant across the map area and that the deconvolution process adds noise to the maps and greatly increases the variation of the noise across the maps. This disagreement with the theory was not completely unexpected and may be due in part to the use of only twelve or thirteen trials in the Monte Carlo tests.

There are a number of other sources of noise which should be considered. If the baseline parameters used in the reduction are in error, a systematic phase error equivalent to an offset in the apparent position of the source will be introduced. Since these errors are presumably not correlated from spacing to spacing, the net effect of baseline errors will be a slight loss of resolution. This uncertainty in the determination of the baseline parameters will appear as an uncertainty in the determination of the instrumental phase function and hence is already included within the uncertainty in the calibrated phases. The fluxes used for the gain-calibration sources which are variable are another cause of error. However, these fluxes were measured repeatedly throughout

the program and carefully chosen averages were used in the calibration. Such errors would add to the dirty maps distortions which do not have the expected beam patterns. Since the deconvolution process converged rapidly to the one percent level it would appear that this source of error was not of great importance. Round-off and truncation in the computer processing will add some noise to the maps, but this contribution should be small compared to the other errors present.

The preceeding discussion has considered only those sources of error which affect all frequency shifts equally. However, the data are found to show systematic disagreements between the various frequency shifts. Errors in the determination of the frequency-dependent phase and amplitude corrections could produce such an effect. Since these corrections are essentially linear functions of frequency, any error caused by them should be most pronounced in the comparison of the two widely-separated continuum frequency shifts. Since this is not the case, we must blame the "systematic" errors on the random calibration errors of the broadband channel. Such errors are discussed above and will affect all channels of a

frequency shift in a similar manner which will not be directly correlated with frequency.

C. Least-Squares Gaussian Analysis

The fitting of experimental data to some a priori functional form by the method of least squares has come into common use in astronomy since the development of high-speed computers. Below is a brief, computer-oriented development of this method which was used in this program to find fringe amplitudes and phases, to determine the baseline corrections, to do preliminary model fitting, and to parameterize the final spectra.

Let us assume that the measured quantity (a function of ν observations) is also expected to be a function of N parameters p_n, i.e.

$$q(\nu) = f(\underset{\sim}{p}, \nu) \ .$$

We may linearize this equation about an initial guess $\underset{\sim}{p}_0$ for the unknown parameters $\underset{\sim}{p}$ as

$$q_\nu = q_{0\nu} + F_\nu^{\ k} \Delta p_k$$

where we use the summation convention, express the dependence on ν with a subscript and let

$$F_\nu^{\ k} \equiv \left(\frac{\partial f}{\partial p_k}\right)_{\underset{\sim}{p}_0}$$

and

$$q_{0\nu} \equiv f(\underset{\sim}{p}_0, \nu) \ .$$

We wish to minimize the sum of the squares of the residuals S where S is defined by

$$S = \sum_{\nu} (\hat{q}_\nu - q_\nu)^2 = (\hat{q}_\nu - q_\nu)(\hat{q}^\nu - q^\nu) \ .$$

To do this all partial derivatives are set to zero as

$$\frac{\partial S}{\partial p_n} = 0 = -F_\nu{}^k (\hat{q}^\nu - q_0{}^\nu - \Delta p^i F_i{}^\nu) - (\hat{q}_\nu - q_{0\nu} - F_\nu{}^j \Delta p_j) F_k{}^\nu$$

resulting in

$$F_k{}^\nu F_\nu{}^i \Delta p_i = F_k{}^\nu (\hat{q}_\nu - q_{0\nu}) \ .$$

In the computer we sum over the M observations the two-dimensional symmetric matrix

$$A_k{}^i \equiv \sum_{\nu=1}^{M} \left(\frac{\partial f}{\partial p_k}\right)_{\underset{\sim}{p}_0} \left(\frac{\partial f}{\partial p_i}\right)_{\underset{\sim}{p}_0}$$

and the one-dimensional matrix

$$C_k \equiv \sum_{\nu=1}^{M} \left(\frac{\partial f}{\partial p_k}\right)_{\underset{\sim}{p}_0} \left[\hat{q}_\nu - f(\underset{\sim}{p}_0, \nu)\right] \ .$$

The matrix equation is readily solved as

$$\Delta p_j = B_j{}^k C_k$$

where B is the inverse matrix of A. If f is linear in

all the parameters p_n we have now completed the computation. Otherwise, we adopt as a new initial guess

$$\underset{\sim}{p}_0^{(1)} = \underset{\sim}{p}_0 + \beta \underset{\sim}{\Delta p} \qquad (3C\text{-}1)$$

where the factor $\beta\,(0<\beta\leq 1)$ is introduced for later convenience and repeat the operation as many times as seems reasonable. The variance of the final solution may be derived as follows:

$$\sigma^2 = \frac{1}{M-N} \sum_{\nu=1}^{M} (\hat{q} - q)^2$$

$$= \frac{1}{M-N}\left[\hat{q}_\nu - q_{0\nu} - F_\nu{}^k \Delta p_k\right]\left[\hat{q}^\nu - q_0{}^\nu - \Delta p^j F_j{}^\nu\right]$$

$$= \frac{1}{M-N}\left[(\hat{q}_\nu - q_{0\nu})(\hat{q}^\nu - q_0{}^\nu) + \Delta p^j\left[\Delta p_k F_\nu{}^k F_j{}^\nu - 2F_j{}^\nu(\hat{q}_\nu - q_{0\nu})\right]\right]$$

$$= \frac{1}{M-N}\left[(\hat{q}_\nu - q_{0\nu})(\hat{q}^\nu - q_0{}^\nu) + \Delta p^j(\Delta p_k A^k{}_j - 2C_j)\right]$$

where we use the symmetry of the matrix A. The uncertainty of an individual parameter is given by the usual formula

$$\sigma^2(p_i) = \sum_{\nu=1}^{N} \left(\frac{\partial p_i}{\partial q_\nu}\right)^2 \sigma^2$$

which may be converted as follows:

$$\sigma^2(p_i) = \sigma^2 \sum_{\nu} \left[\frac{\partial (B_i{}^k C_k)}{\partial q_\nu} \right]^2$$

$$\sigma^2(p_i) = \sigma^2 \sum_{\nu} \left[\frac{\partial\ B_i{}^k F_k{}^{\nu'} (q_{\nu'} - q_{0\nu'})}{\partial q_\nu} \right]^2$$

$$\sigma^2(p_i) = \sigma^2 \sum_{\nu} (B_i{}^k F_k{}^\nu)^2$$

$$\sigma^2(p_i) = \left[B_i{}^k F_k{}^\nu F_\nu{}^m B_m{}^i \right] \sigma^2$$

$$\sigma^2(p_i) = \left[B_i{}^k A_k{}^m B_m{}^i \right] \sigma^2$$

$$\sigma^2(p_i) = B_i{}^i \sigma^2 \quad .$$

Therefore,

$$\sigma^2(p_i) = \frac{B_i{}^i}{M-N} \left[\sum_{\nu=1}^{M} (q_\nu - q_{0\nu})^2 + \sum_{j=1}^{N} \Delta p_j \left(\sum_k \Delta p_k A^k{}_j - 2C_j \right) \right] .$$

A reasonable point at which to stop the iteration procedure is when

$$|\underset{\sim}{\Delta p}| < \eta\ \underset{\sim}{\sigma}$$

where a reasonable choice for η would be 0.1.

An interesting application of least-squares analysis is the problem of fitting an observed spectrum with sums of gaussians of unknown heights, widths, and central frequencies. This technique has been used by many authors including Shuter and Verschuur (1964), Clark (1965), Takakubo and Van Woerden (1966), and Radhakrishnan, et al (1972d). The gaussian is chosen as the functional form because a cloud in thermodynamic equilibrium will have an optical depth spectrum which is gaussian. Small scale random turbulence should only increase the width of the gaussians. One should not expect all spectra to resemble gaussians, however. A cloud which is only partially resolved and which contains large scale systematic motions such as streaming, rotation, or expansion will not have a gaussian spectrum. Also it may not always be possible to separate the effects of several clouds along the line of sight having approximately the same velocities. In this program one may hope that gaussian analysis will be useful even if little physical significance can be attributed to the results. If the 385 maps of optical depth produced by this program can be reduced to 100 or fewer maps of gaussian parameters, then the fitting procedure will have performed a considerable service.

In principle, any function $\tau(\nu)$ may be exactly fit by a sum of gaussians of the form

$$\tau(\nu) = \sum_{i=1}^{N} \tau_i \, e^{-(\nu-\nu_i)^2/\alpha\sigma_i^2}$$

(Kaper, et al 1966).[3] Unfortunately this theorem requires that $\tau(\nu)$ be known exactly and continuously for all ν, while all experiments are plagued with noise and can only determine $\tau(\nu)$ at some set of discrete values of ν. It is clear that, in this program, we could obtain a perfect fit to the observed spectra by taking a 1-KHz gaussian component for each observed frequency. Such a solution is a valid solution, but it ignores experimental error and whatever physical meaning one might wish to attribute to the solution. For such reasons, one generally seeks an approximate solution having only a few components each of which is significantly wider than the bandwidth of the experiment. Since the least-squares method requires the linearization of the non-linear functional form, the method can only find local minima in the sum of the squares of the residuals (S). Therefore, the set of components found is not unique.

---

3 Normally $\alpha = 2$ for a gaussian. However, in this program $\alpha = (\ell n\ 16)^{-1}$ so that σ becomes the full width at half maximum.

In practice, the gaussian fitting procedure is not easy to perform. Considerable trial and error was necessary to determine initial guesses which would converge for those spectra having the highest signal-to-noise ratio. Some of these initial guesses failed to converge for some (or all) of the other spectra on the source despite the features of the computer program designed to force convergence. It may be shown that

$$\left(\frac{\partial S}{\partial \beta}\right)_{\beta=0} < 0$$

where $S(\beta)$ is the sum of the squares of the residuals and β is defined in equation (3C-1). However $S(1)$ may exceed $S(0)$ by a large amount. If the program found that at some iteration $S(1)-S(0)$ exceeded some predetermined parameter then the iteration was repeated at $\beta=0.5$. This test was repeated until a value of β was found for that iteration step for which $S(\beta)-S(0)$ was less than the test amount. Also, the program was capable of reducing the number of components, restoring a component to its initial guess, and solving only for a given subset of the gaussian parameters holding all others fixed. The results of the attempts to fit gaussians will be discussed in the

appropriate sections of the following chapters. Results illustrating the non-gaussian nature of some spectra, the non-physical nature of at least some of the gaussian components and the non-uniqueness of the solutions will be presented.

CHAPTER 4

CYGNUS A (3C405)

A. Results — Beam Pattern and Continuum Map

Cygnus A is at a favorable declination for aperture synthesis. The distribution of data points in the (u, v) plane obtained for one of the continuum frequency shifts is illustrated in Figure 8. This figure shows both the actual data points and those obtained with the hermitian property of the visibility function. The plane is well sampled despite the small gap between the data obtained with north-south baselines and those obtained with east-west baselines. As discussed in Chapter 3A, the Fourier inversion method was tested by producing maps 18 minutes of arc on a side. The results of this test for Cygnus A are illustrated in Figures 9. The dirty beam obtained from the distribution of data points of Figure 8 is shown in Figure 9a. In this figure, the contour interval is 10 percent with the zero contour shown as a heavy line and negative contours as dashed lines. The central beam is slightly elliptical with full width at half maximum about 1.3 arc minutes. Because of the discrete sampling, the roughly circular pattern of the sidelobes is highly

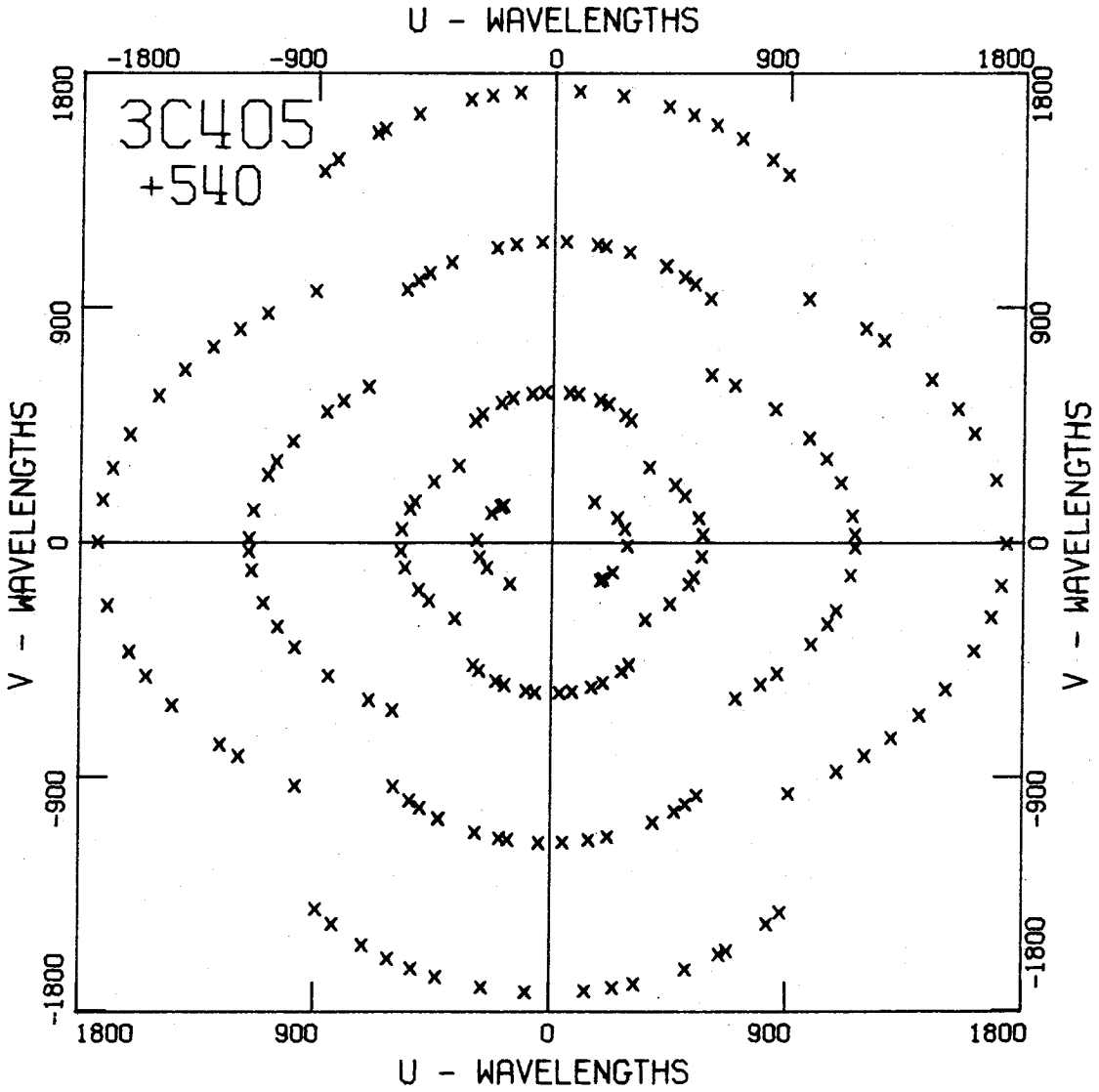

Figure 8. 3C405, continuum frequency shift: distribution of data points.

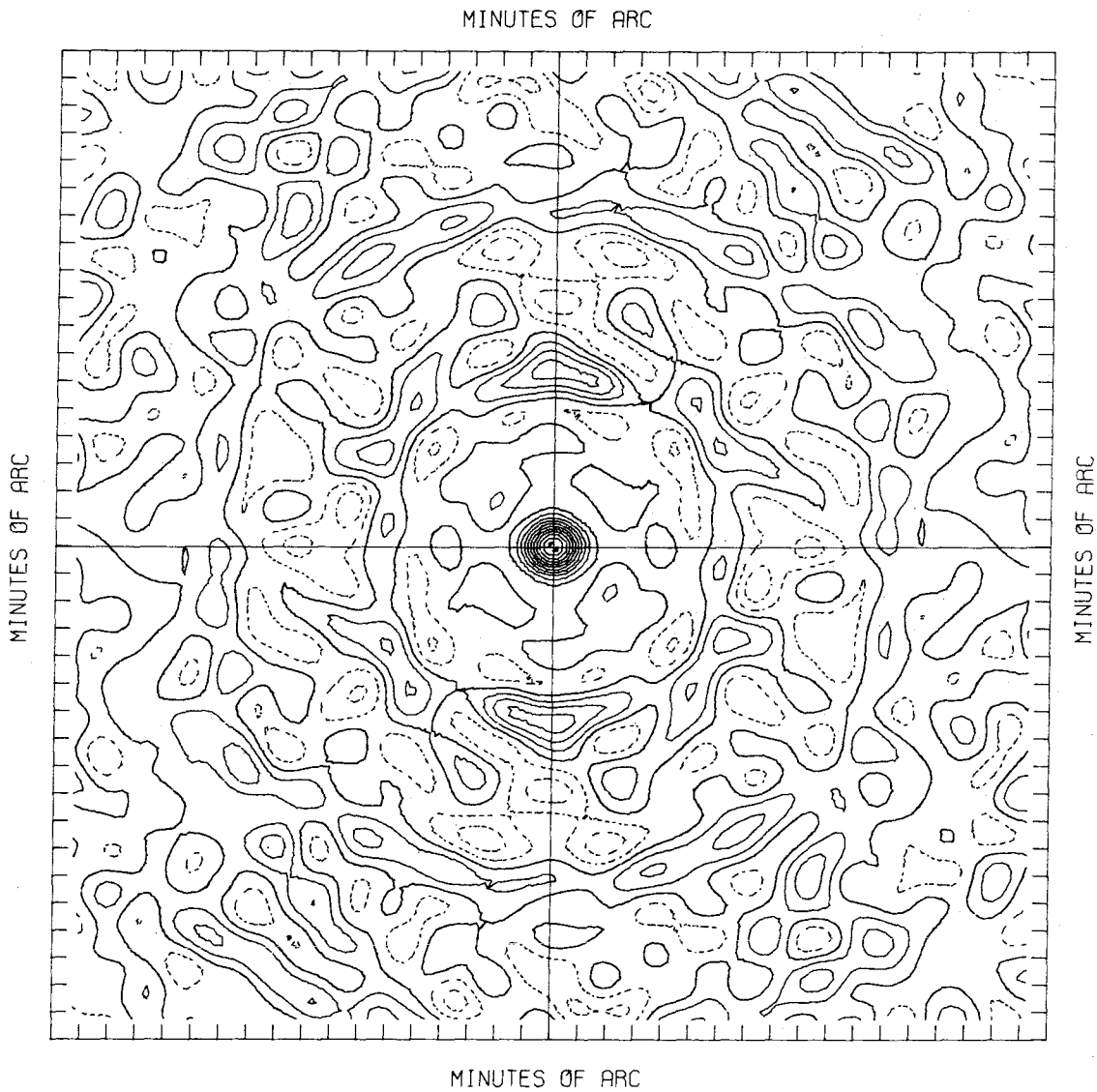

Figure 9a. 3C405, continuum frequency shift: dirty beam contour interval = 10%, large area.

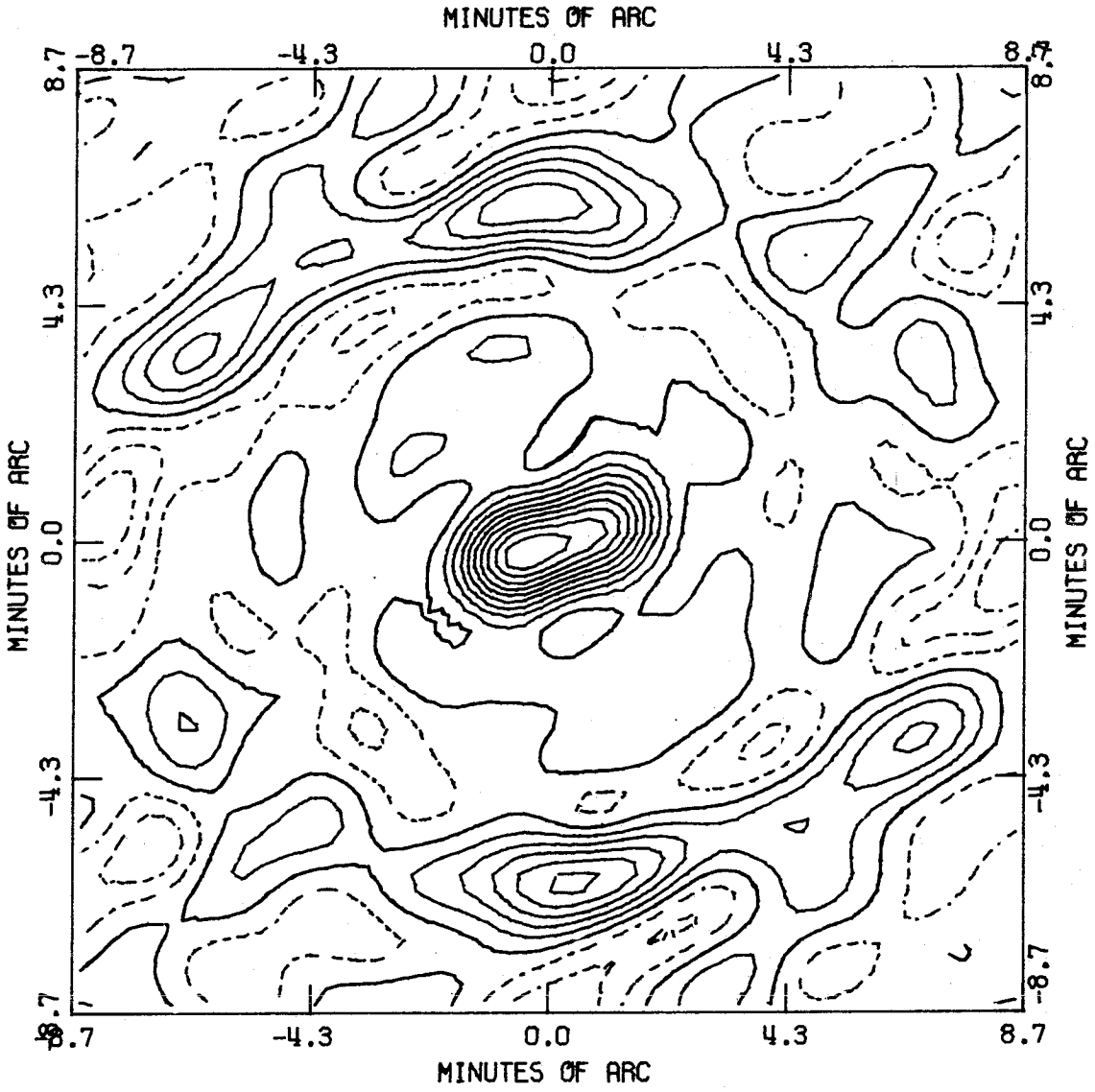

Figure 9b. 3C405, continuum frequency shift: dirty map contour interval = 10%, large area.

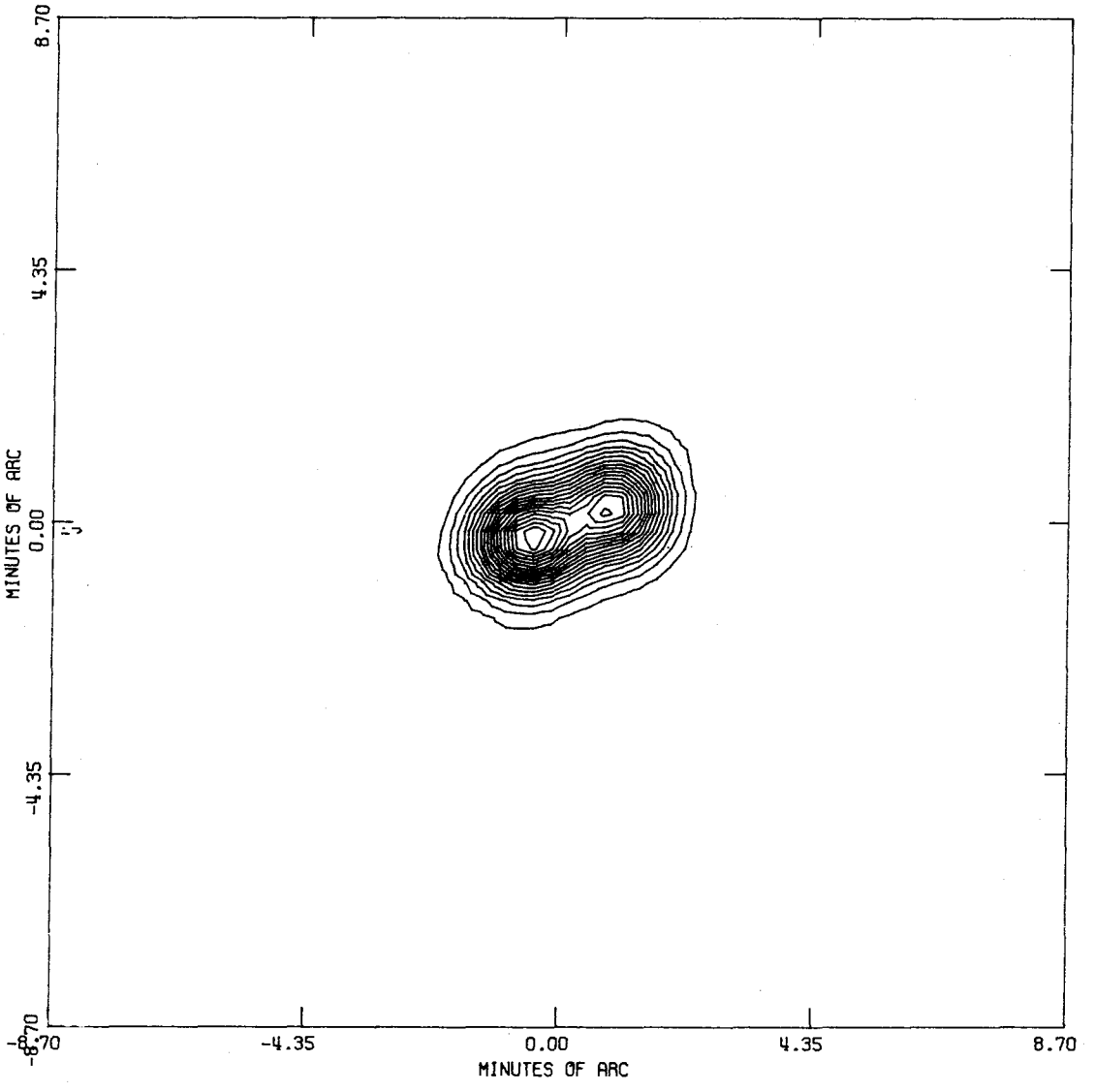

Figure 9c. 3C405, continuum frequency shift: clean map contour interval = 5%, zero contour suppressed, large area.

irregular. Within three minutes of the center no sidelobes significantly exceed ten percent, but at larger distances there are sidelobes exceeding 30 percent

The dirty map obtained with this beam pattern is shown in Figure 9b. To obtain this map (and all other continuum maps) the data from all channels of the continuum frequency shift were averaged vectorially before inversion. The contour interval is ten percent and the zero contour is shown. Although apparently spurious responses exceeding 50 percent occur on the map, such responses are limited to less than five percent near the source. This "clean" area results from the small size of the source in comparison with the 6' by 6' area allowed by the basic sampling theorem. The result of the deconvolution process is shown in Figure 9c. The contour interval is five percent and the zero contour is not shown. The brightness off the source is generally less than one percent although a few bumps at the two-to-three percent level occur. We see from the map that, while reducing the spurious responses to a reasonable noise level, the deconvolution process also improves the resolution on the source despite the use of a restoring beam having the same width as the central part of the dirty beam.

For reasons of economy, most maps of this source were made over a more limited area. The continuum map used to compute optical depths is given in Figure 10. Lines of constant galactic coordinates are drawn through the center of this map. The level of spurious responses is higher near the source in Figure 10 than in Figure 9c. Since only 40 iterations are required to reach the one percent iteration limit over the small area of Figure 10 while 97 iterations are required over the large area of Figure 9c, we may presume that the increased noise level is due to edge affects in limiting the deconvolution to a small area.

B. Results — Observed Spectra

The spectrum of Cygnus A contains two major absorption features. This chapter is devoted to the feature arising from hydrogen in the Perseus arm of the Galaxy. The other feature, due to more local hydrogen, will be discussed briefly in Chapter 8. The short-spacing spectrum of the Perseus arm feature is shown in Figure 11a. The points represent the average of about 75 minutes of data at the 200 foot east-west baseline. At the top of the figure is plotted the relative flux and at the bottom the relative

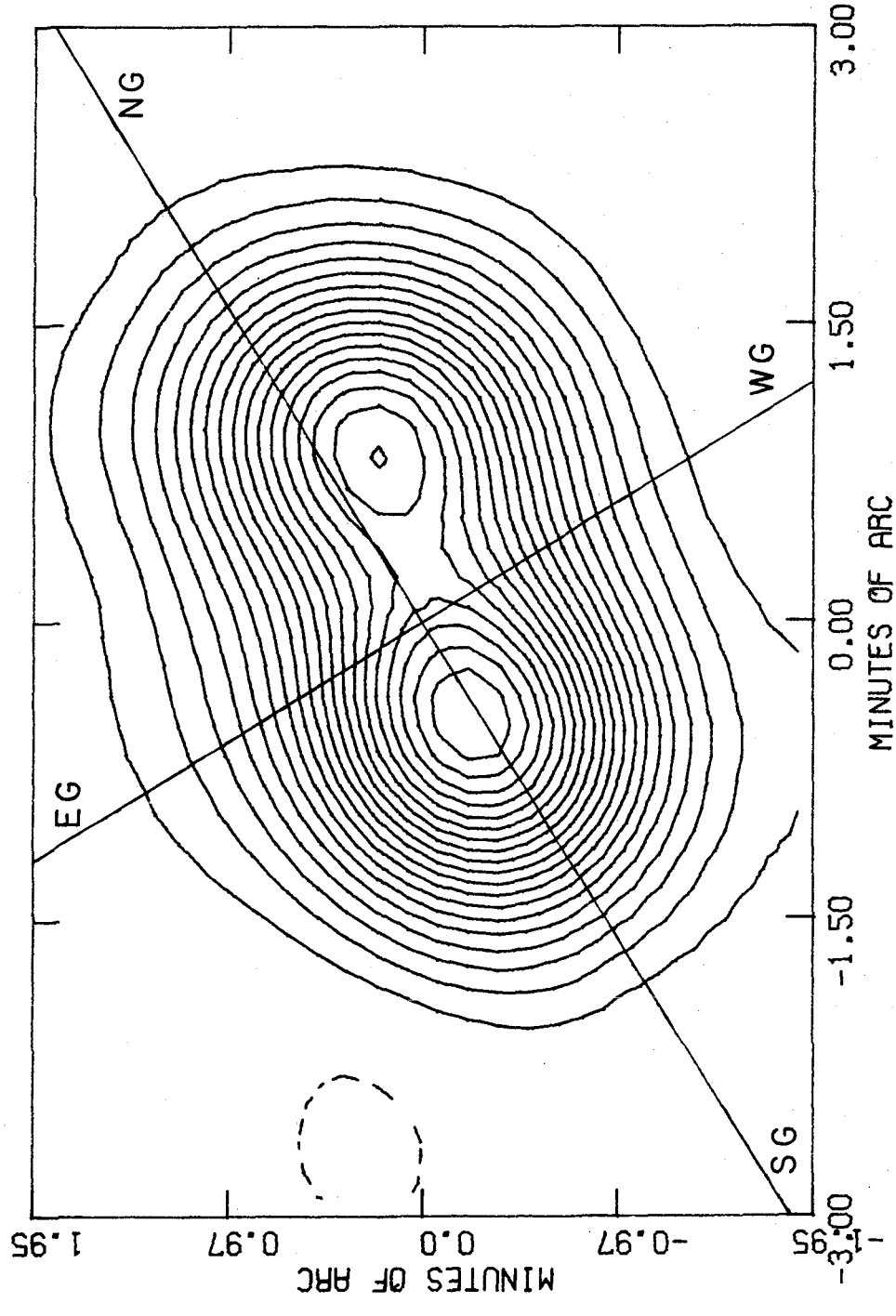

Figure 10. 3C405: continuum map — contour interval = 5%, zero contour suppressed. Lines of constant galactic coordinates drawn with NG being galactic north and EG galactic east (i.e. increasing longitude at constant latitude).

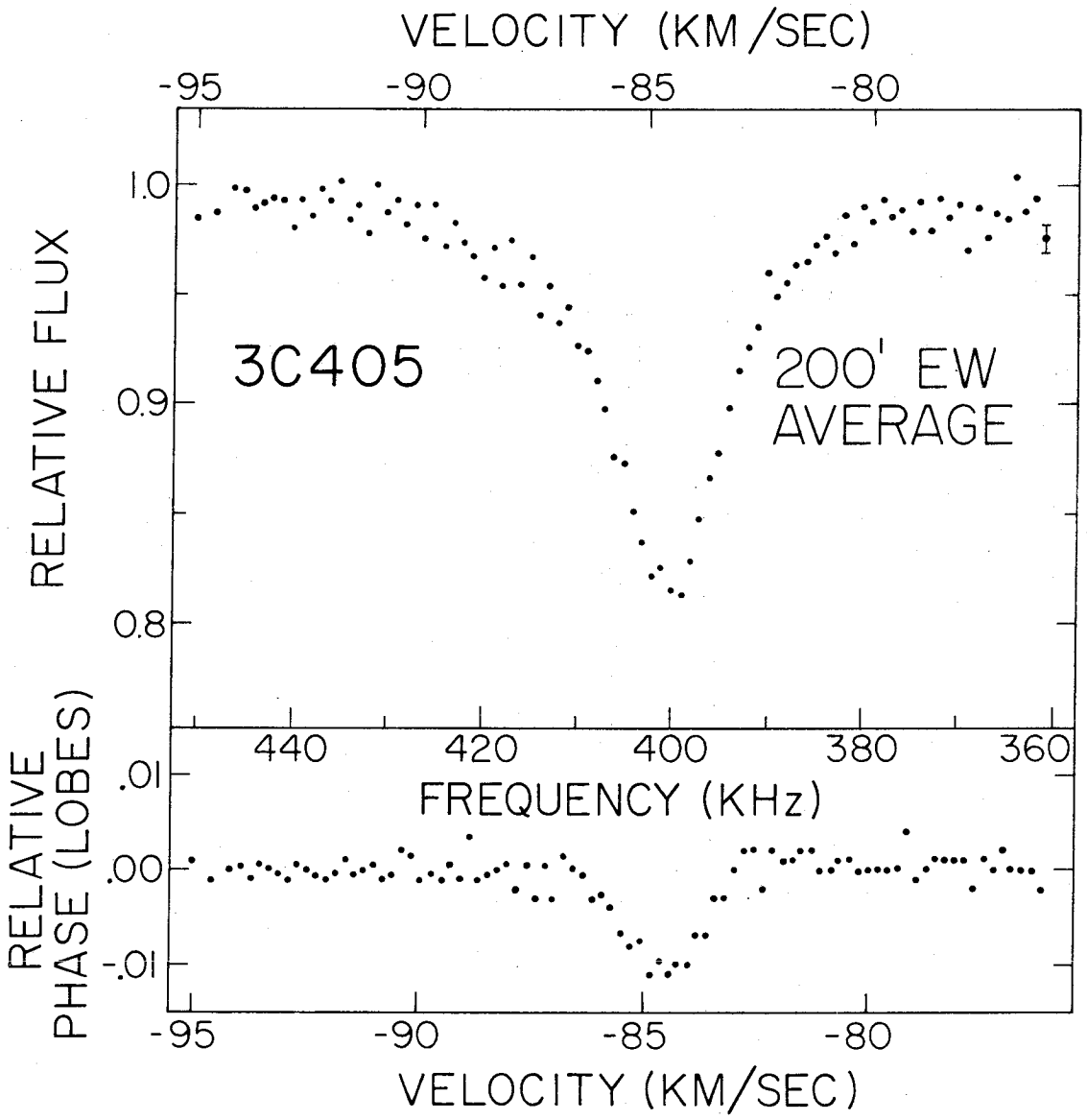

Figure 11a. 3C405: relative flux and phase spectra at 200 feet east-west. Average of 75 minutes of observation.

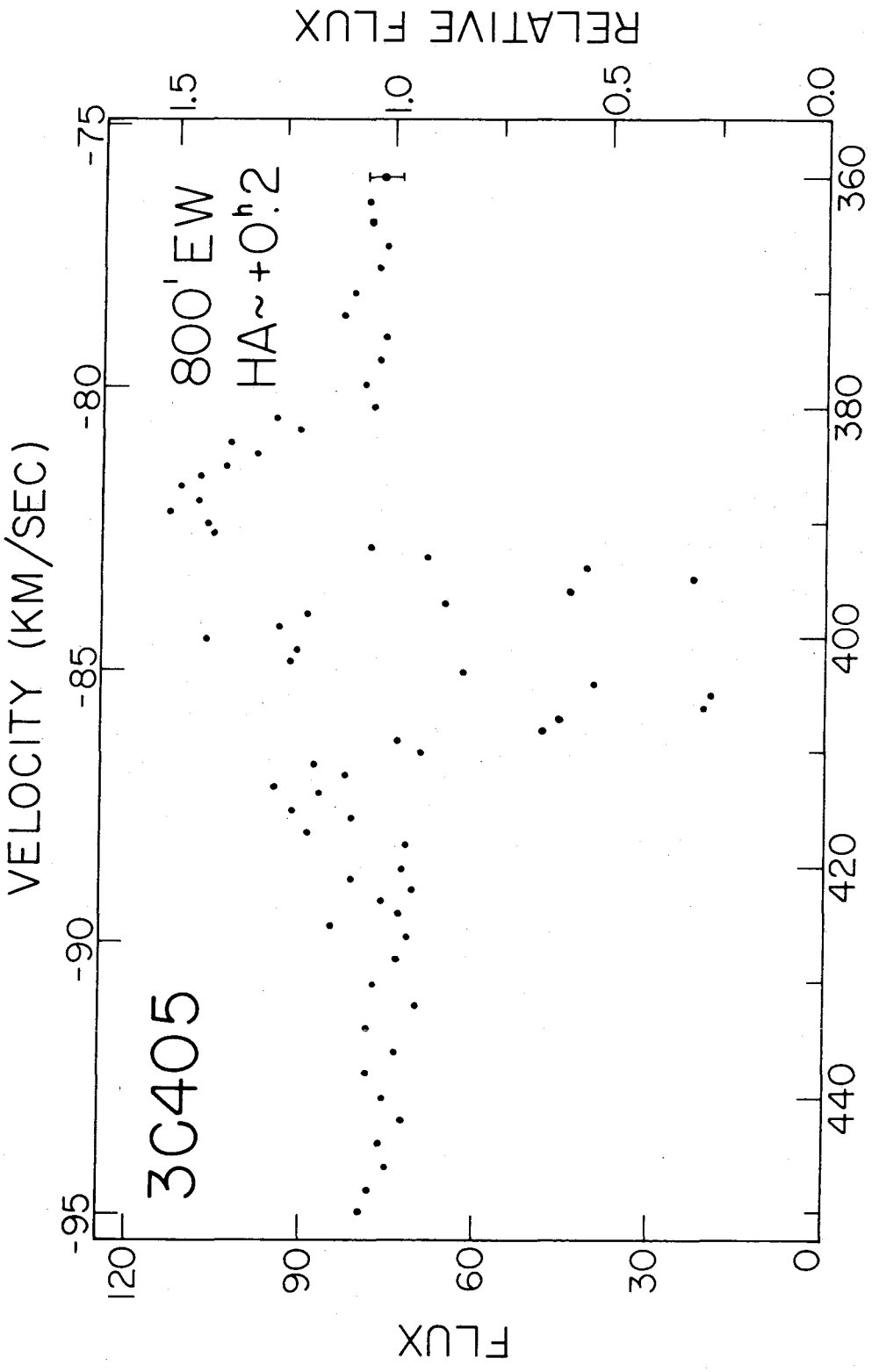

Figure 11b. 3C405: flux spectrum at 800 feet east-west hour angle about 0.2.

phase both as functions of frequency or velocity.[1] The absorption line has a simple, approximately gaussian shape with somewhat assymetrically broadened wings. The maximum optical depth is only 0.195 while the width of the line implies an apparent temperature of 140° K. The phase data reveal a change in the apparent centroid of the source due to the absorption line. At the center of the line this shift is about ten seconds of arc to the west. Figure 11b gives the spectrum at the first minimum in the visibility function. Apparent flux is plotted as a function of frequency or velocity with each point representing a single ten-minute observation at an hour angle near 0.2 hours with the 800-foot east-west baseline. Since the source is essentially just two point sources (see Figure 10), this spectrum represents the absolute value of the difference of the (absorbed) fluxes of the two components. As such it shows that the hydrogen in the wings of the absorption line causes a decrease in the relative strength of the weaker western component while

---

1 All frequencies and velocities are expressed with respect to the Local Standard of Rest and all phases are expressed in lobes where a lobe is defined as a change in phase of 2π radians.

the hydrogen in the center of the line causes the western component to appear the stronger of the two components.

C. Results — Optical Depth Maps

Optical depth maps are produced from the cleaned maps using the formula

$$\tau_\nu(x, y) = - \ell n \left(\frac{T_{B\nu}(x, y)}{T_{BC}(x, y)} \right)$$

where T_{BC} is the brightness temperature in the continuum and $T_{B\nu}$ is the brightness temperature in the line at frequency ν. The computation is carried out only at those points where $T_{BC}(x, y)$ is greater than 15 percent of its peak value and $T_{B\nu}(x, y)$ is greater than 0.1 percent of its peak value. A representative, but by no means complete, sample of the optical depth maps for Cygnus A is given in Figures 12. In these maps, the heavy line surrounding the source indicates the boundary of the source given by the above criteria. The heavy lines on source are zero contours and the broken lines are negative contours. The values of some of the contour lines are labelled and the the contour intervals are given in the captions. Local minima are indicated by tick marks. For all maps, north is at the top, east is at the left, and the axes are in

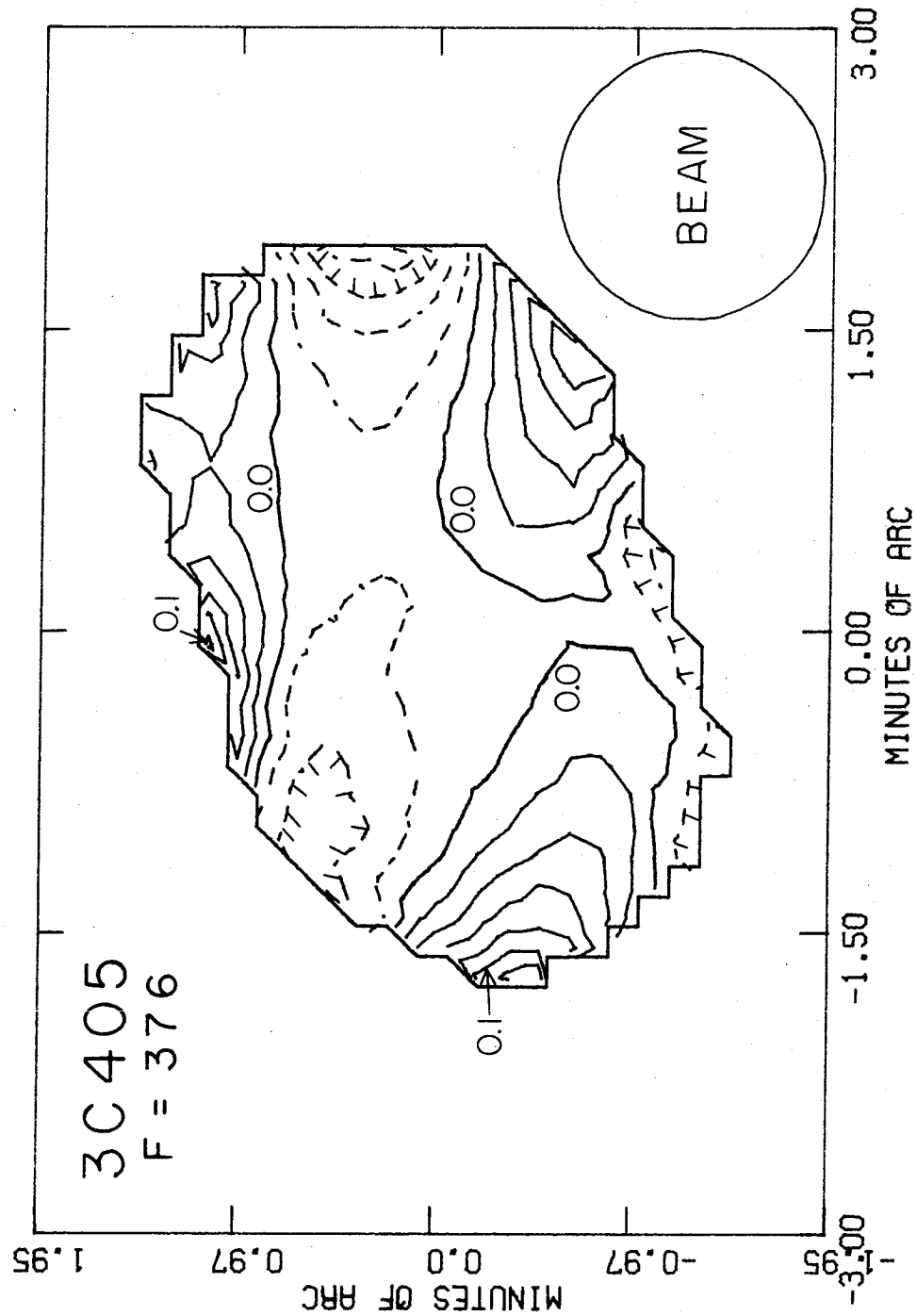

Figure 12a. 3C405: optical depth map at -79.5 km/sec, contour interval = 0.02. Illustrates beam size (full width at half maximum) and DC offsets.

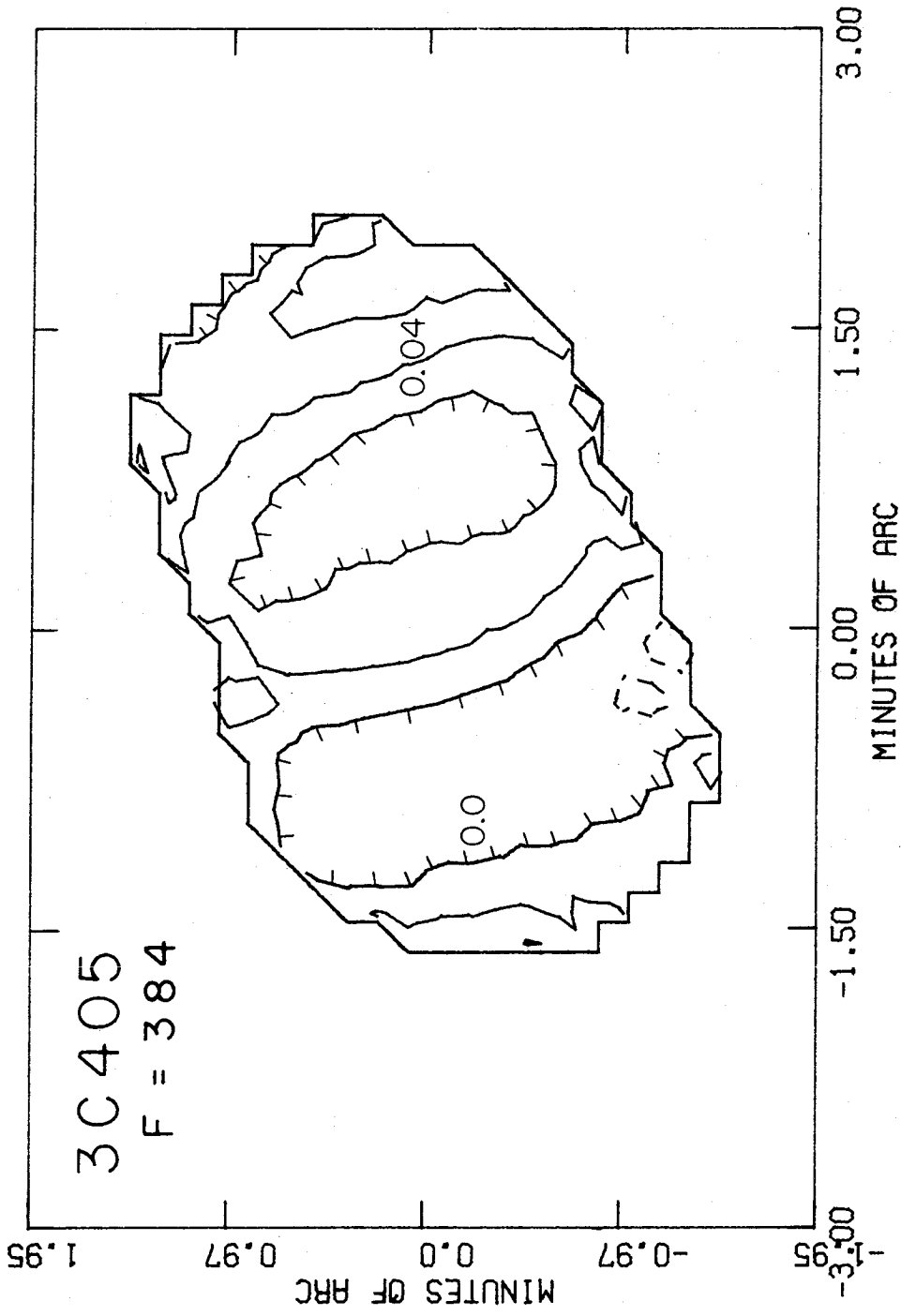

Figure 12b. 3C405: optical depth map at -81.3 km/sec, contour interval = 0.02.

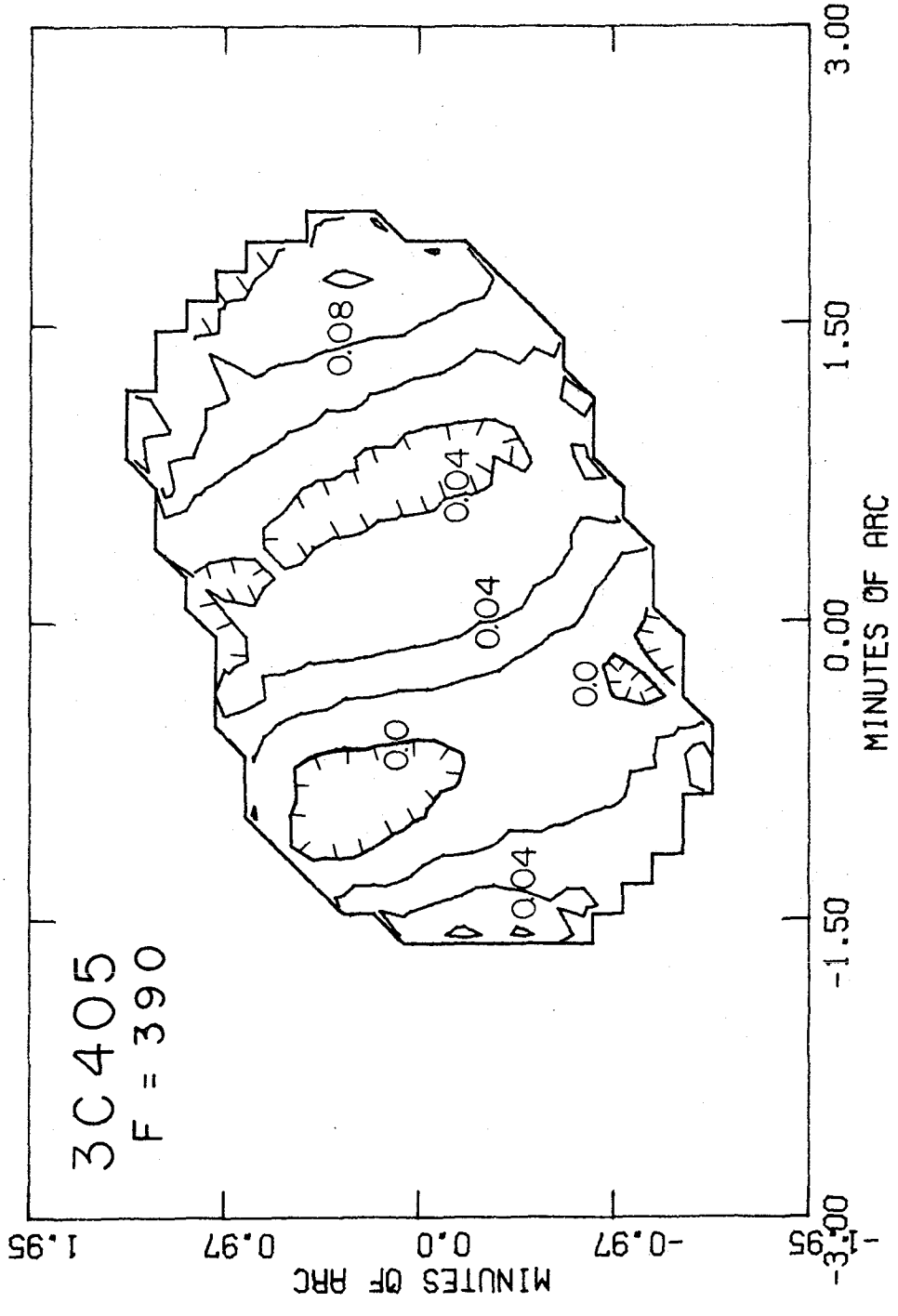

Figure 12c. 3C405: optical depth map at -82.5 km/sec, contour interval = 0.02.

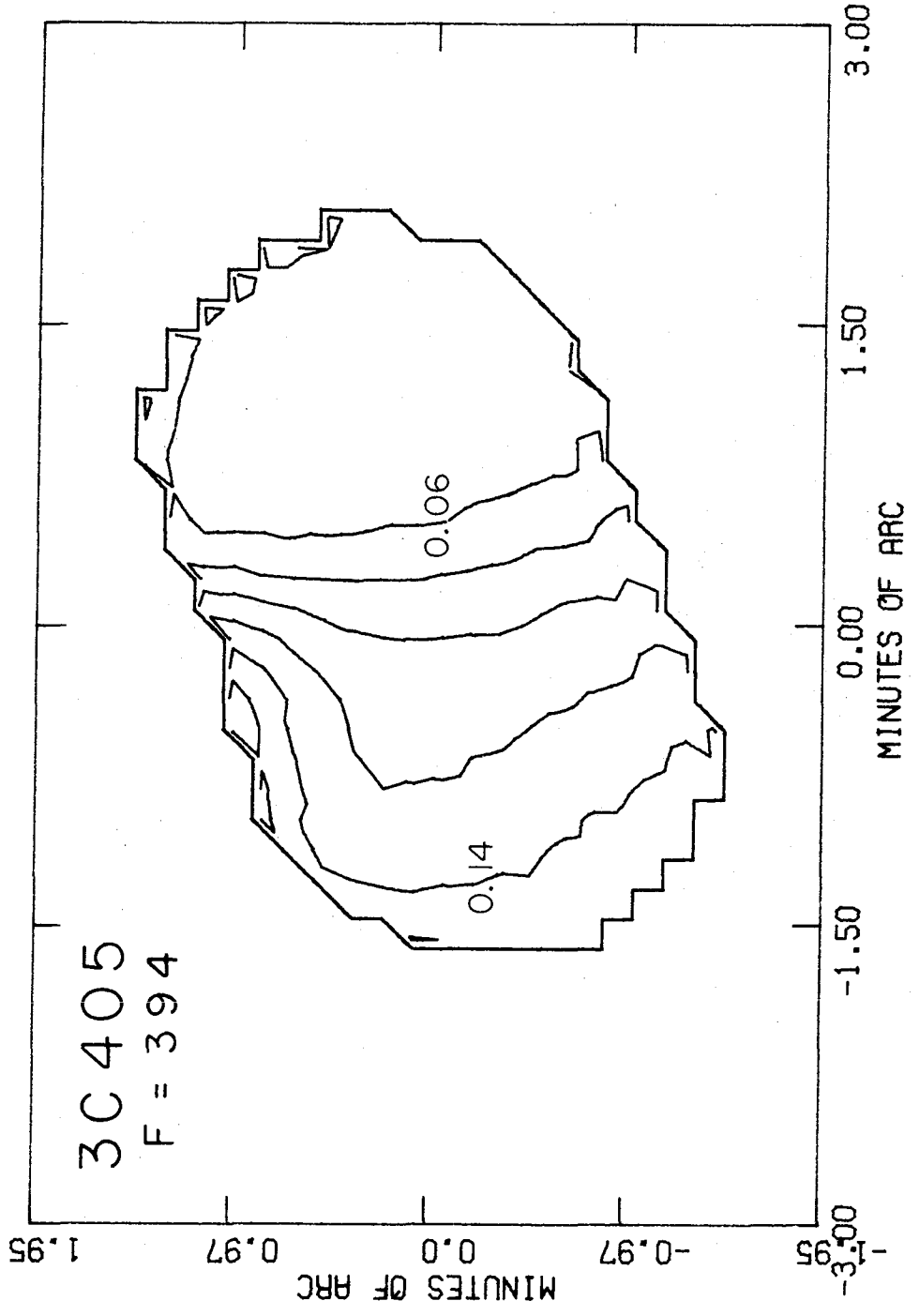

Figure 12d. 3C405: optical depth map at -83.4 km/sec, contour interval = 0.02.

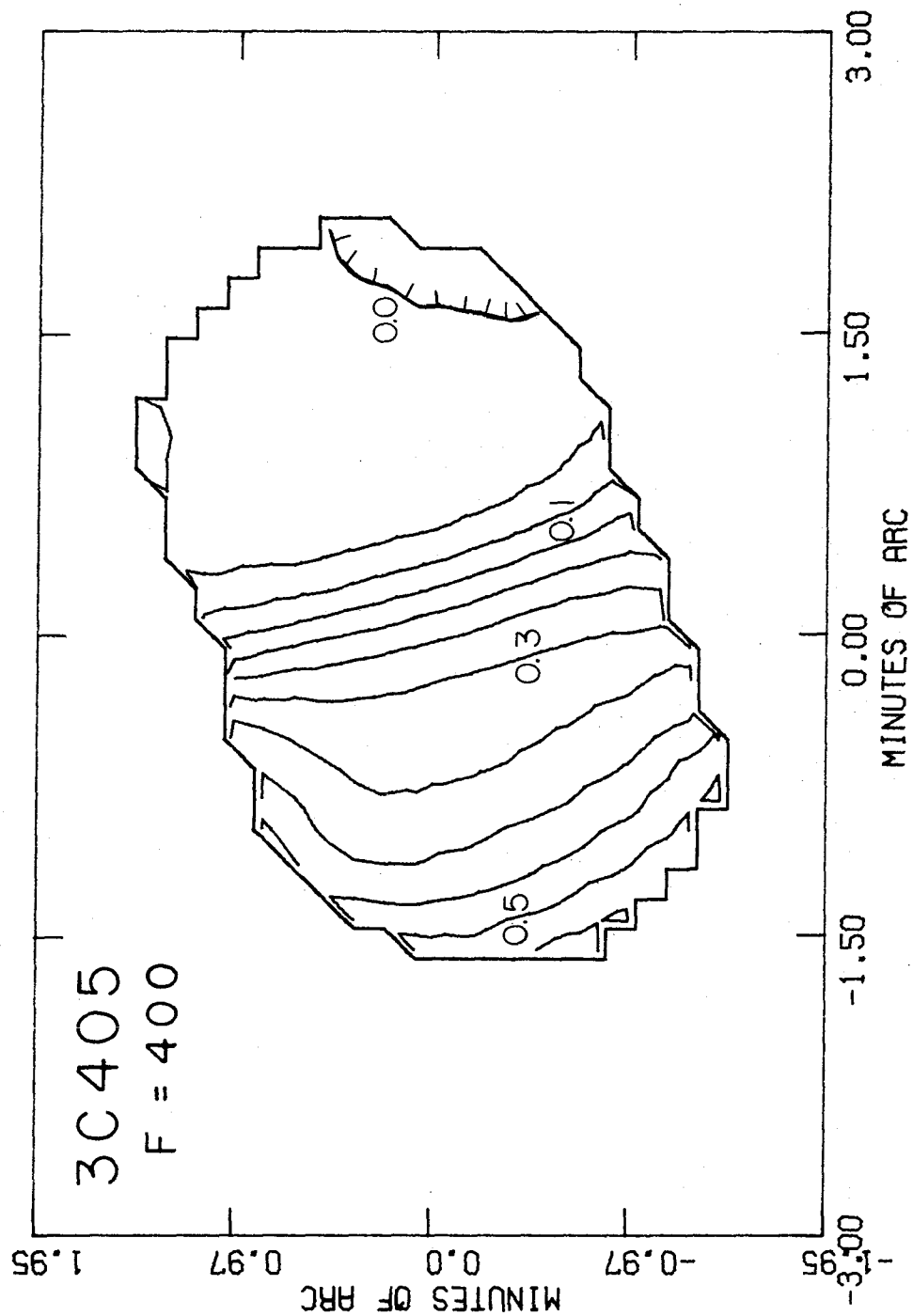

Figure 12e. 3C405: optical depth map at -84.7 km/sec, contour interval = 0.05.

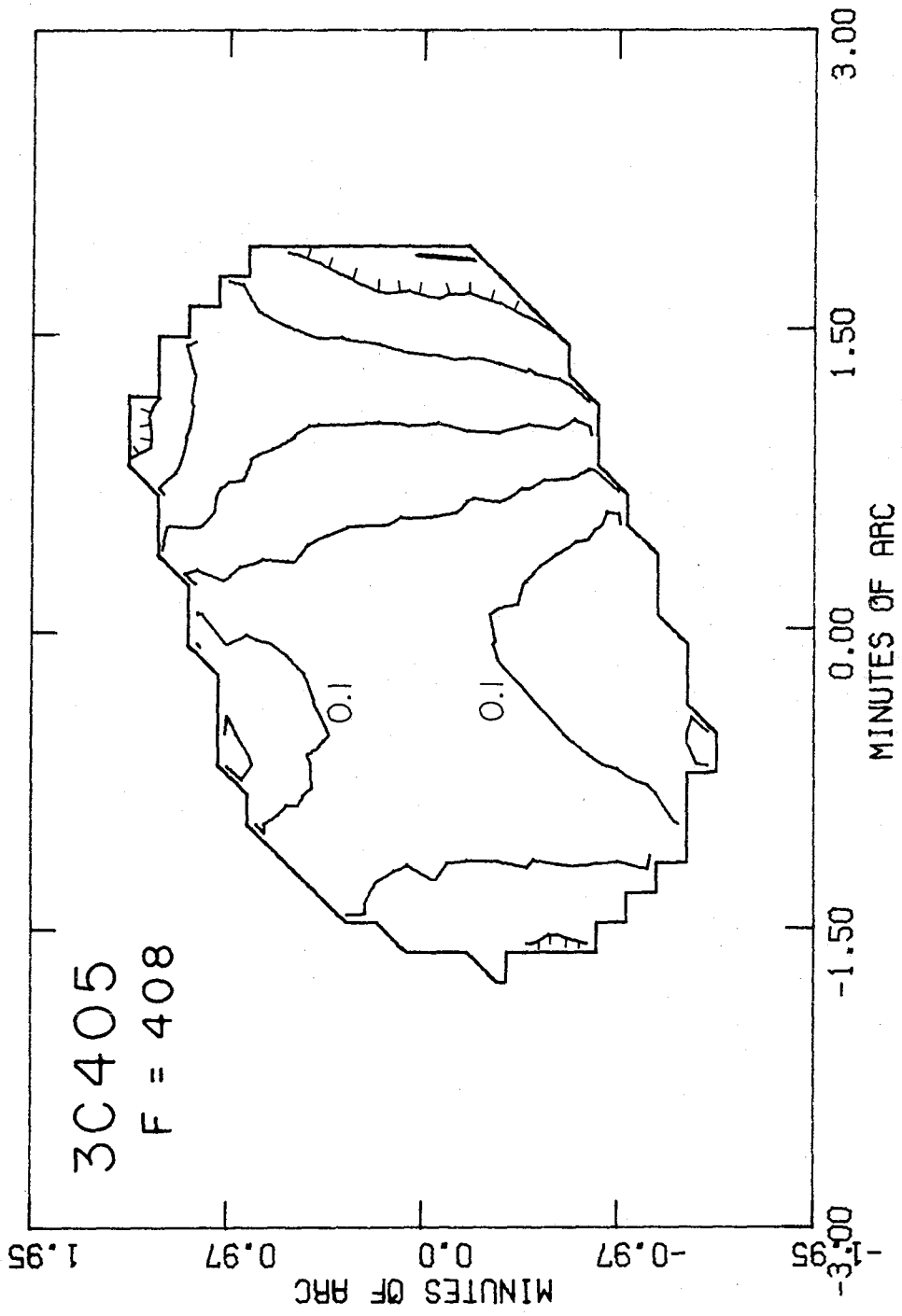

Figure 12f. 3C405: optical depth map at -86.3 km/sec, contour interval = 0.02.

minutes of arc. The source name and the observing frequency (in KHz) are given in the north-east corner of each map. The sharp bends in the contour lines as they strike the edge of the source are an artifact of the plotting program and should be ignored. The diameter of the clean beam is indicated in Figure 12a.

The first of these maps, Figure 12a, is typical of maps at frequencies outside the absorption line. The apparent optical depths vary across the source from about 0.13 to -0.10, but remain nearly constant with frequency. (Maps at the adjacent frequencies are not shown.) Such "DC offsets" are almost certainly due to the uncertainties in the instrumental calibration which affect all channels of a frequency shift equally. It is possible to remove such DC offsets but only for those frequency shifts having some channels outside the absorption line. This has been done for the rest of the optical depth maps of Figures 12.

As the spectra to be discussed shortly will reveal, there are several features in the hydrogen distribution. In Figure 12b at a frequency of 384 KHz we see the first of these developing as a ridge along the western edge of the source. An attribute of almost all maps is a local minimum in optical depth just east of the peak of the

western component of the source. By 390 KHz, this feature is fully developed with a ridge near 0.1 along the western edge of the source and a weaker ridge through the center of the source. At 394 KHz, the first feature has become weaker and the principal feature has begun to dominate the map. This second feature is characterized by considerable optical depth concentrated over the eastern half of the source with a slight trough separating peaks to the southeast and north. This principal feature reaches a peak optical depth greater than 0.5 at 400 KHz. From the shape of the contours, it is reasonable to presume that even higher optical depths occur off the source. At frequencies greater than 400 KHz a third feature becomes visible although it is strongly blended with the principal feature over the eastern half of the source. This feature attains a peak optical depth around 0.1 along the minor axis of the source at about 405 KHz and a somewhat weaker peak along the western edge of the source around 410 KHz. A wide, barely significant feature peaks around 418 KHz but shows little structure across the source.

D. Results — Spectra and Gaussian Fitting

Several map points may be averaged at each frequency and at intervals of about one-half beamwidth to produce a

map of semi-independent optical depth spectra. As indicated in Chapter 3C we may attempt to express these spectra as sums of gaussians. The results of such an attempt are indicated in Figures 13. Figure 13a shows how well the spectra were fit (the "RMS"), Figures 13b show the DC offsets for each frequency shift, and Figures 13c show the gaussian parameters for each of the four features. Along the top and left side of the figures are, respectively, the x coordinate which increases to the west and the y coordinate which increases to the north. Both coordinates are in minutes of arc at the source and the central frequency and full width (at half maximum) are in KHz. A number in parentheses is the uncertainty in the fit of the number immediately above the parentheses. An uncertainty of 0.0 indicates that the computer program removed the particular component from the fit while a blank uncertainty indicates that I did not attempt to fit the particular component to the spectrum at that point on the map.

The problems encountered in fitting gaussians to the spectra of Cygnus A were somewhat different from those encountered with the other sources. More than one initial guess was required since the spectra completely change shape across the source. At the eastern and western edges

3C405 - RMS

	-1.425	-0.975	-0.525	-0.075	0.375	0.825	1.275	1.725
1.125			0.0184	0.0192	0.0101	0.0084	0.0109	0.0137
0.675		0.0117	0.0087	0.0076	0.0088	0.0052	0.0063	0.0109
0.225	0.0136	0.0069	0.0048	0.0093	0.0042	0.0063	0.0050	0.0113
-0.225	0.0138	0.0057	0.0049	0.0079	0.0063	0.0061	0.0063	0.0101
-0.675	0.0162	0.0051	0.0068	0.0050	0.0103	0.0099	0.0110	
-1.125	0.0178	0.0108	0.0069	0.0101	0.0187			

Figure 13a. 3C405: Results of gaussian analysis — the RMS deviations of the data from the sums of the gaussians measured in optical depth.

3C405 - DC OFFSET : +382 FREQUENCY SHIFT

	-1.425	-0.975	-0.525	-0.075	0.375	0.825	1.275	1.725
1.125			0.054 (0.004)	0.043 (0.021)	0.019 (0.004)	0.014 (0.003)	0.031 (0.003)	0.042 (0.003)
0.675		-0.056 (0.004)	-0.032 (0.002)	-0.008 (0.003)	-0.019 (0.004)	-0.020 (0.002)	-0.012 (0.002)	-0.032 (0.004)
0.225	0.002 (0.002)	-0.042 (0.002)	-0.032 (0.002)	-0.006 (0.003)	-0.019 (0.001)	-0.029 (0.002)	-0.026 (0.001)	-0.055 (0.003)
-0.225	0.067 (0.003)	0.003 (0.002)	-0.016 (0.002)	0.002 (0.003)	0.008 (0.002)	0.001 (0.002)	0.008 (0.002)	0.002 (0.003)
-0.675	0.078 (0.004)	0.033 (0.002)	0.005 (0.002)	0.002 (0.002)	0.012 (0.003)	0.021 (0.005)	0.062 (0.003)	
-1.125	0.019 (0.005)	0.007 (0.003)	0.002 (0.002)	-0.020 (0.003)	-0.038 (0.004)			

Figures 13b. 3C405: Results of gaussian analysis — DC offsets in optical depth, by frequency shift.

3C405 - DC OFFSET : +403 FREQUENCY SHIFT

	-1.425	-0.975	-0.525	-0.075	0.375	0.825	1.275	1.725
1.125			-0.000 (0.002)	-0.005 (0.005)	-0.014 (0.001)	0.005 (0.001)	0.038 (0.001)	0.076 (0.002)
0.675		-0.055 (0.005)	-0.037 (0.001)	-0.015 (0.001)	-0.035 (0.008)	-0.016 (0.001)	0.012 (0.006)	0.032 (0.008)
0.225	-0.042 (0.002)	-0.055 (0.005)	-0.019 (0.002)	0.009 (0.001)	-0.007 (0.001)	-0.012 (0.007)	0.007 (0.001)	0.024 (0.001)
-0.225	0.003 (0.002)	-0.022 (0.003)	-0.017 (0.002)	0.025 (0.006)	0.030 (0.001)	0.030 (0.006)	0.050 (0.001)	0.075 (0.001)
-0.675	0.029 (0.002)	0.006 (0.003)	-0.007 (0.003)	0.026 (0.002)	0.063 (0.008)	0.081 (0.001)	0.135 (0.001)	
-1.125	0.023 (0.002)	0.025 (0.006)	0.010 (0.003)	0.015 (0.005)	0.047 (0.002)			

Figure 13b. (continued)

3C405 - DC OFFSET : +428 FREQUENCY SHIFT

	-1.425	-0.975	-0.525	-0.075	0.375	0.825	1.275	1.725
1.125			0.034 (0.007)	0.012 (0.020)	-0.010 (0.004)	-0.000 (0.003)	0.010 (0.004)	0.026 (0.004)
0.675		-0.009 (0.006)	0.004 (0.003)	0.000 (0.003)	-0.010 (0.009)	-0.012 (0.002)	-0.012 (0.006)	-0.007 (0.008)
0.225	-0.003 (0.003)	-0.006 (0.003)	0.008 (0.002)	0.007 (0.003)	-0.002 (0.001)	-0.004 (0.007)	-0.009 (0.002)	-0.019 (0.004)
-0.225	0.026 (0.004)	0.004 (0.003)	-0.000 (0.002)	0.003 (0.005)	0.006 (0.002)	0.014 (0.007)	0.016 (0.002)	0.008 (0.003)
-0.675	0.042 (0.006)	0.011 (0.003)	-0.002 (0.003)	-0.005 (0.002)	0.001 (0.008)	0.017 (0.006)	0.036 (0.004)	
-1.125	0.033 (0.007)	0.005 (0.006)	-0.012 (0.003)	-0.013 (0.005)	-0.010 (0.005)			

Figure 13b. (continued)

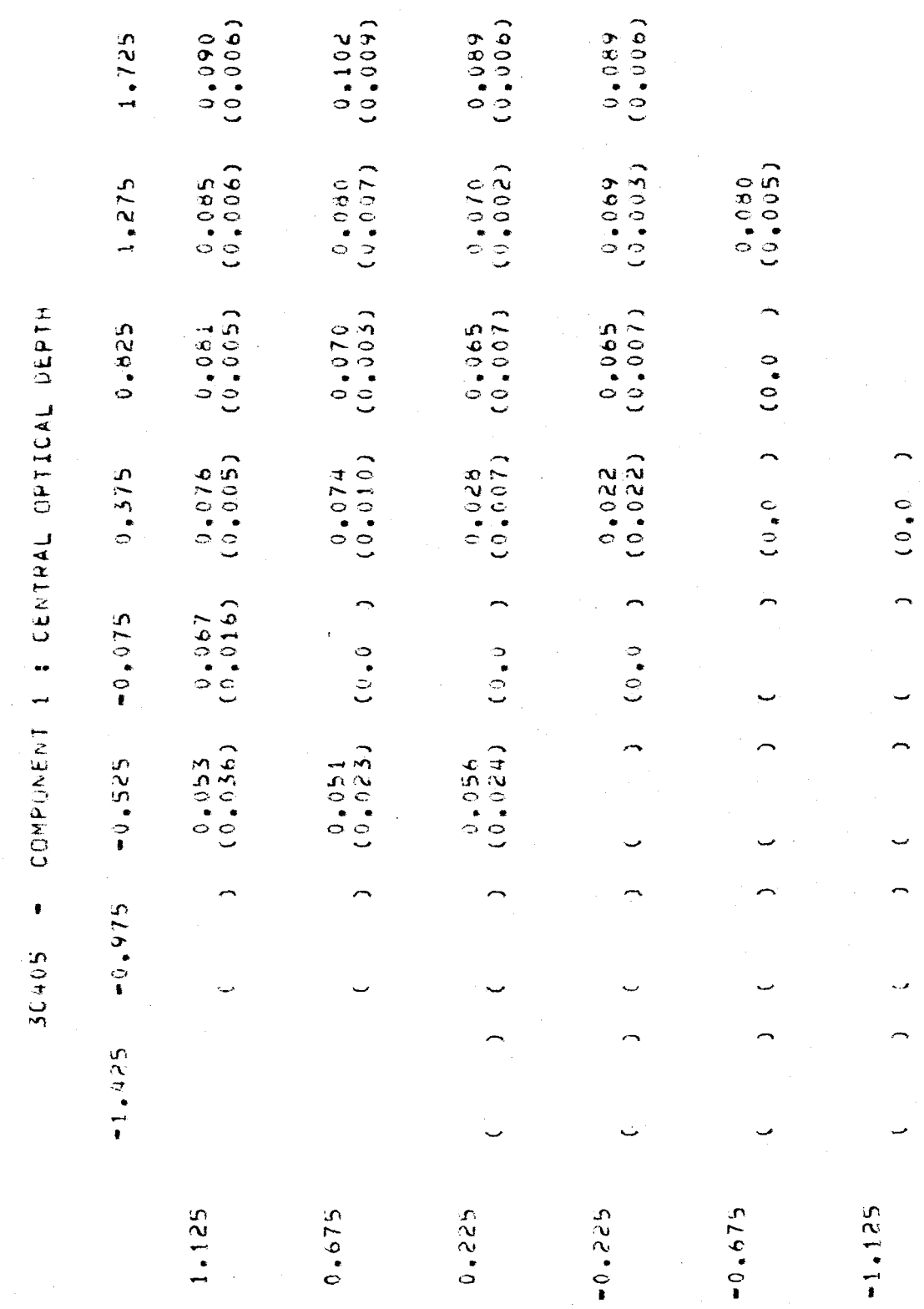

Figures 13c. 3C405: Results of gaussian analysis — central optical depths, central frequencies (KHz), and full widths at half maximum (KHz) of gaussian components, by component.

3C405 - COMPONENT 1 : CENTRAL FREQUENCY

	-1.425	-0.975	-0.525	-0.075	0.375	0.825	1.275	1.725
1.125			397.82 (0.86)	394.50 (5.70)	391.80 (0.88)	389.25 (0.42)	389.03 (0.36)	390.17 (0.45)
0.675		( )	397.46 (0.49)	(0.0)	393.80 (0.99)	389.82 (0.33)	388.95 (0.19)	388.87 (0.26)
0.225	( )	( )	397.74 (0.35)	(0.0)	389.52 (1.10)	390.85 (0.28)	389.23 (0.19)	388.38 (0.33)
-0.225	( )	( )	( )	(0.0)	387.23 (1.61)	391.32 (0.30)	389.76 (0.28)	388.35 (0.31)
-0.675	( )	( )	( )	( )	(0.0)	(0.0)	389.21 (0.55)	
-1.125	( )	( )	( )	( )	(0.0)			

Figure 13c. (continued)

3C405 - COMPONENT 1 : FULL WIDTH

	-1.425	-0.975	-0.525	-0.075	0.375	0.825	1.275	1.725
1.125			4.79 (2.80)	43.95 (10.4)	18.30 (2.23)	12.83 (1.15)	11.95 (1.01)	10.85 (1.16)
0.675		( )	5.15 (1.63)	(0.0)	19.06 (2.46)	12.06 (0.87)	11.84 (0.78)	11.78 (1.01)
0.225	( )	( )	5.90 (1.19)	(0.0)	13.34 (1.99)	13.10 (1.21)	11.62 (0.55)	10.54 (0.91)
-0.225	( )	( )	( )	(0.0)	8.99 (3.52)	13.37 (1.20)	12.25 (0.77)	10.99 (0.87)
-0.675	( )	( )	( )	( )	(0.0)	(0.0)	13.46 (1.42)	
-1.125	( )	( )	( )	( )	(0.0)			

Figure 13c. (continued)

3C405 - COMPONENT 2 : CENTRAL OPTICAL DEPTH

	-1.425	-0.975	-0.525	-0.075	0.375	0.825	1.275	1.725
1.125			0.343 (0.033)	0.138 (0.022)	( )	(0.0)	( )	( )
0.675		0.413 (0.010)	0.319 (0.018)	0.126 (0.011)	( )	( )	( )	( )
0.225	0.458 (0.008)	0.378 (0.013)	0.295 (0.020)	0.140 (0.013)	(0.0)	( )	( )	( )
-0.225	0.443 (0.017)	0.379 (0.053)	0.316 (0.076)	0.207 (0.012)	0.038 (0.074)	( )	( )	( )
-0.675	0.478 (0.026)	0.393 (0.018)	0.370 (0.006)	0.295 (0.009)	0.075 (0.014)	0.087 (0.005)	( )	
-1.125	0.503 (0.031)	0.444 (0.023)	0.411 (0.006)	0.348 (0.007)	0.143 (0.025)			

Figure 13c. (continued)

3C405 - COMPONENT 2 : CENTRAL FREQUENCY

	-1.425	-0.975	-0.525	-0.075	0.375	0.825	1.275	1.725
1.125			400.55 (0.41)	400.20 (0.47)	( )	(0.0)	( )	( )
0.675		399.32 (0.26)	400.50 (0.35)	400.13 (0.21)	( )	( )	( )	( )
0.225	400.06 (0.07)	399.62 (0.30)	400.62 (0.30)	399.60 (0.24)	(0.0)	( )	( )	( )
-0.225	400.02 (0.09)	399.78 (0.66)	399.45 (0.99)	400.02 (0.14)	398.88 (1.04)	( )	( )	( )
-0.675	400.01 (0.12)	399.96 (0.07)	400.03 (0.19)	399.90 (0.30)	399.94 (0.48)	399.72 (1.13)	( )	
-1.125	400.03 (0.14)	399.97 (0.10)	399.98 (0.14)	399.85 (0.26)	399.92 (0.40)			

Figure 13c. (continued)

3C405 - COMPONENT 2 : FULL WIDTH

	-1.425	-0.975	-0.525	-0.075	0.375	0.825	1.275	1.725
1.125			12.10 (0.65)	13.07 (1.45)	( )	(0.0)	( )	( )
0.675		8.84 (0.46)	11.13 (0.41)	10.30 (0.78)	( )	( )	( )	( )
0.225	9.27 (0.16)	9.23 (0.42)	10.69 (0.28)	8.42 (0.74)	(0.0)	( )	( )	( )
-0.225	8.64 (0.29)	9.28 (0.58)	9.23 (0.76)	9.53 (0.45)	10.30 (6.36)	( )	( )	( )
-0.675	8.39 (0.39)	9.08 (0.22)	9.76 (0.33)	9.78 (0.42)	8.49 (1.30)	31.62 (2.30)	( )	
-1.125	8.43 (0.46)	8.70 (0.31)	9.45 (0.26)	9.73 (0.47)	10.20 (1.33)			

Figure 13c. (continued)

3C405 - COMPONENT 3 : CENTRAL OPTICAL DEPTH

	-1.425	-0.975	-0.525	-0.075	0.375	0.825	1.275	1.725
1.125					0.061	0.069	0.070	0.052
			( )	( )	(0.025)	(0.005)	(0.005)	(0.006)
0.675		0.086		0.084	0.052	0.058	0.055	0.052
		(0.027)	( )	(0.011)	(0.025)	(0.003)	(0.004)	(0.005)
0.225		0.061		0.111	0.089	0.061	0.051	0.066
	(0.0)	(0.027)	( )	(0.012)	(0.002)	(0.008)	(0.002)	(0.007)
-0.225	0.043	0.049	0.082	0.066	0.099	0.053	0.042	0.042
	(0.016)	(0.057)	(0.083)	(0.011)	(0.038)	(0.029)	(0.003)	(0.007)
-0.675	0.061	0.049	0.040	0.047	0.107		0.041	
	(0.025)	(0.015)	(0.016)	(0.026)	(0.014)	(0.0)	(0.005)	
-1.125	0.073	0.059	0.039	0.055	0.102			
	(0.026)	(0.015)	(0.016)	(0.024)	(0.022)			

Figure 13c. (continued)

3C405 - COMPONENT 3 : CENTRAL FREQUENCY

	-1.425	-0.975	-0.525	-0.075	0.375	0.825	1.275	1.725
1.125					405.67	408.28	409.30	405.73
			( )	( )	(0.44)	(0.52)	(0.46)	(0.82)
0.675		405.67		403.00	406.39	407.78	409.35	409.61
		(0.56)	( )	(0.82)	(0.71)	(0.44)	(0.70)	(0.58)
0.225		406.02		404.82	404.56	406.77	409.13	410.92
	(0.0)	(0.93)	( )	(0.86)	(0.76)	(0.62)	(0.28)	(0.37)
-0.225	404.68	406.20	405.32	406.00	405.49	406.40	407.98	410.51
	(2.64)	(4.37)	(3.18)	(1.87)	(5.53)	(0.63)	(0.46)	(0.51)
-0.675	405.01	405.15	407.09	406.55	403.00		407.17	
	(2.85)	(2.21)	(0.80)	(0.84)	(0.96)	(0.0)	(1.03)	
-1.125	405.78	405.98	406.85	406.68	405.57			
	(3.08)	(3.02)	(0.68)	(0.66)	(1.79)			

Figure 13c. (continued)

3C405 - COMPONENT 3 : FULL WIDTH

	-1.425	-0.975	-0.525	-0.075	0.375	0.825	1.275	1.725
1.125			( )	( )	5.92 (1.74)	13.20 (1.27)	12.11 (1.13)	11.09 (2.20)
0.675		5.41 (1.18)	( )	26.94 (2.09)	7.58 (2.15)	13.27 (1.06)	10.71 (2.06)	9.81 (1.56)
0.225	(0.0)	6.60 (1.48)	( )	20.44 (1.14)	21.13 (1.24)	7.57 (1.14)	12.31 (0.70)	7.16 (0.91)
-0.225	19.97 (3.53)	8.76 (4.42)	8.72 (2.92)	21.09 (2.20)	20.35 (5.40)	7.50 (1.79)	11.34 (1.12)	6.45 (1.26)
-0.675	19.20 (3.48)	15.95 (2.30)	6.10 (1.78)	6.84 (1.84)	21.32 (1.83)	(0.0)	12.72 (2.43)	
-1.125	19.29 (3.51)	16.20 (3.76)	5.60 (1.68)	5.53 (1.75)	21.20 (1.92)			

Figure 13c. (continued)

3C405 - COMPONENT 4 : CENTRAL OPTICAL DEPTH

	-1.425	-0.975	-0.525	-0.075	0.375	0.825	1.275	1.725
1.125			0.035 (0.009)	( )	0.034 (0.009)	( )	( )	0.019 (0.008)
0.675		0.015 (0.006)	0.032 (0.004)	( )	0.041 (0.008)	( )	0.005 (0.005)	(0.0)
0.225	0.014 (0.004)	0.023 (0.004)	0.029 (0.002)	( )	( )	0.027 (0.004)	(0.0)	( )
-0.225	(0.0)	0.023 (0.003)	0.027 (0.003)	( )	( )	0.033 (0.011)	( )	(0.0)
-0.675	(0.0)	0.021 (0.004)	0.029 (0.003)	0.026 (0.003)	( )	( )	(0.0)	
-1.125	(0.0)	0.019 (0.006)	0.031 (0.003)	0.027 (0.005)	( )			

Figure 13c. (continued)

3C405 - COMPONENT 4 : CENTRAL FREQUENCY

	-1.425	-0.975	-0.525	-0.075	0.375	0.825	1.275	1.725
1.125			421.03 (2.21)	( )	412.90 (4.80)	( )	( )	419.54 (1.26)
0.675		418.64 (2.66)	415.72 (2.61)	( )	415.11 (3.67)	( )	421.07 (7.38)	(0.0)
0.225	414.04 (4.33)	418.96 (0.92)	415.52 (1.52)	( )	( )	415.56 (1.94)	(0.0)	( )
-0.225	(0.0)	419.69 (0.67)	418.46 (0.92)	( )	( )	415.58 (4.61)	( )	(0.0)
-0.675	(0.0)	421.70 (0.62)	418.40 (0.89)	415.34 (2.34)	( )	( )	(0.0)	
-1.125	(0.0)	422.51 (1.12)	416.40 (1.98)	416.27 (2.32)	( )			

Figure 13c. (continued)

SC405 - COMPONENT 4 : FULL WIDTH

	-1.425	-0.975	-0.525	-0.075	0.375	0.825	1.275	1.725
1.125			16.04 (6.44)	( )	14.22 (7.59)	( )	( )	5.80 (5.13)
0.675		14.97 (9.06)	17.35 (5.34)	( )	15.45 (6.20)	( )	9.79 (15.1)	(0.0)
0.225	17.47 (10.6)	12.10 (2.96)	16.66 (3.40)	( )	( )	9.94 (3.49)	(0.0)	( )
-0.225	(0.0)	10.00 (2.47)	11.68 (2.36)	( )	( )	13.29 (6.17)	( )	(0.0)
-0.675	(0.0)	7.03 (1.67)	12.41 (2.75)	14.21 (4.34)	( )	( )	(0.0)	
-1.125	(0.0)	5.85 (3.16)	17.97 (5.01)	14.28 (5.99)	( )			

Figure 13c. (continued)

of the source the spectra are fairly simple, but in the center of the source the spectra are so blended as to make the separation into components nearly impossible. Because of the low optical depths, the DC offsets were very important and hence had to be determined separately for each frequency shift. Such DC offsets are presumably partly DC offsets in brightness temperature, but for low optical depths, they are equivalent to DC offsets in optical depth. This linear approximation does not apply to the other sources where high optical depths are found, but, fortunately, the DC offsets are also less important for the other sources. In the attempt to determine the three DC offsets the program would often increase the separation of the spectra of the frequency shifts. The sum of the gaussians would then be close to the data of one frequency shift at one frequency and close to the data of another frequency shift at another frequency. In the end it was necessary, for about half the spectra, to do the gaussian fitting without the data of the odd (+403) frequency shift. For these cases, the DC offset of the odd frequency shift and the total RMS were evaluated by holding

the other gaussian parameters (determined without the odd frequency shift) fixed.

Figures 14 illustrate the gaussian fits for a sample of the spectra. The data are plotted as points (with the DC offsets removed) while the individual gaussian components and their sum are plotted as smooth lines. The source name, the coordinates of the spectrum, and the RMS of the fit are given in the upper left corner. I suspect that all four hydrogen features are present in the spectra of Figures 14a and 14b. However, where the principal feature is strong, the program was unable to separate from it both of features one and three. For these two spectra, which are separated by less than a beamwidth, the program determined qualitatively different solutions.[2] The residual effects of the DC offsets may be seen around 420 KHz in these two spectra. In Figure 14c, feature 4 is clearly present, but, with the noise present, the

---

2 It should be noted that, although both the continuum and line maps of brightness temperature may be represented as convolutions of the true brightness maps with the restoring beam, the optical depth maps cannot be represented in such a simple fashion. Thus, the beam will affect the optical depth maps in a manner which is not intuitively obvious.

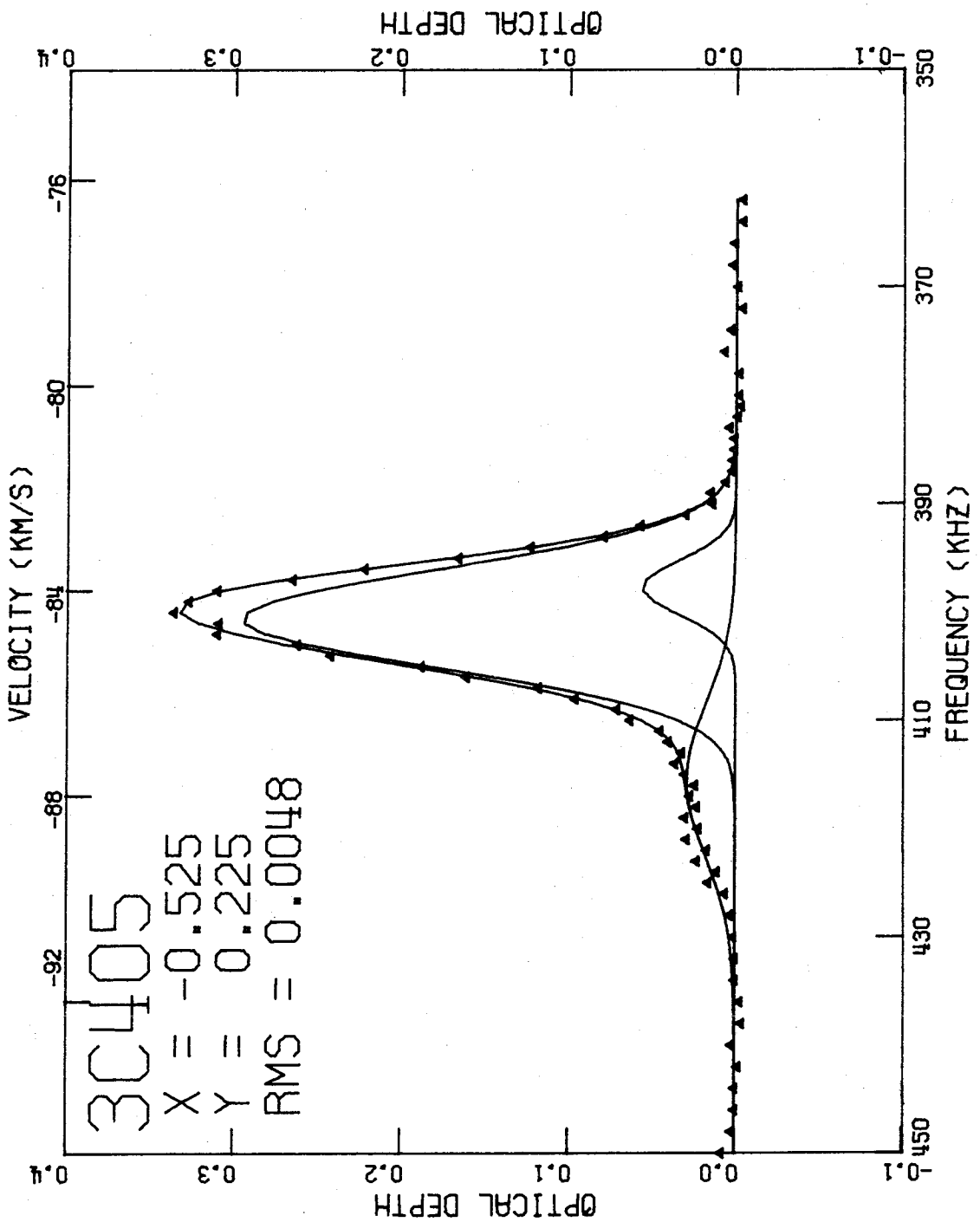

Figure 14a. 3C405: Gaussian fit spectrum at (-0.525, 0.225).

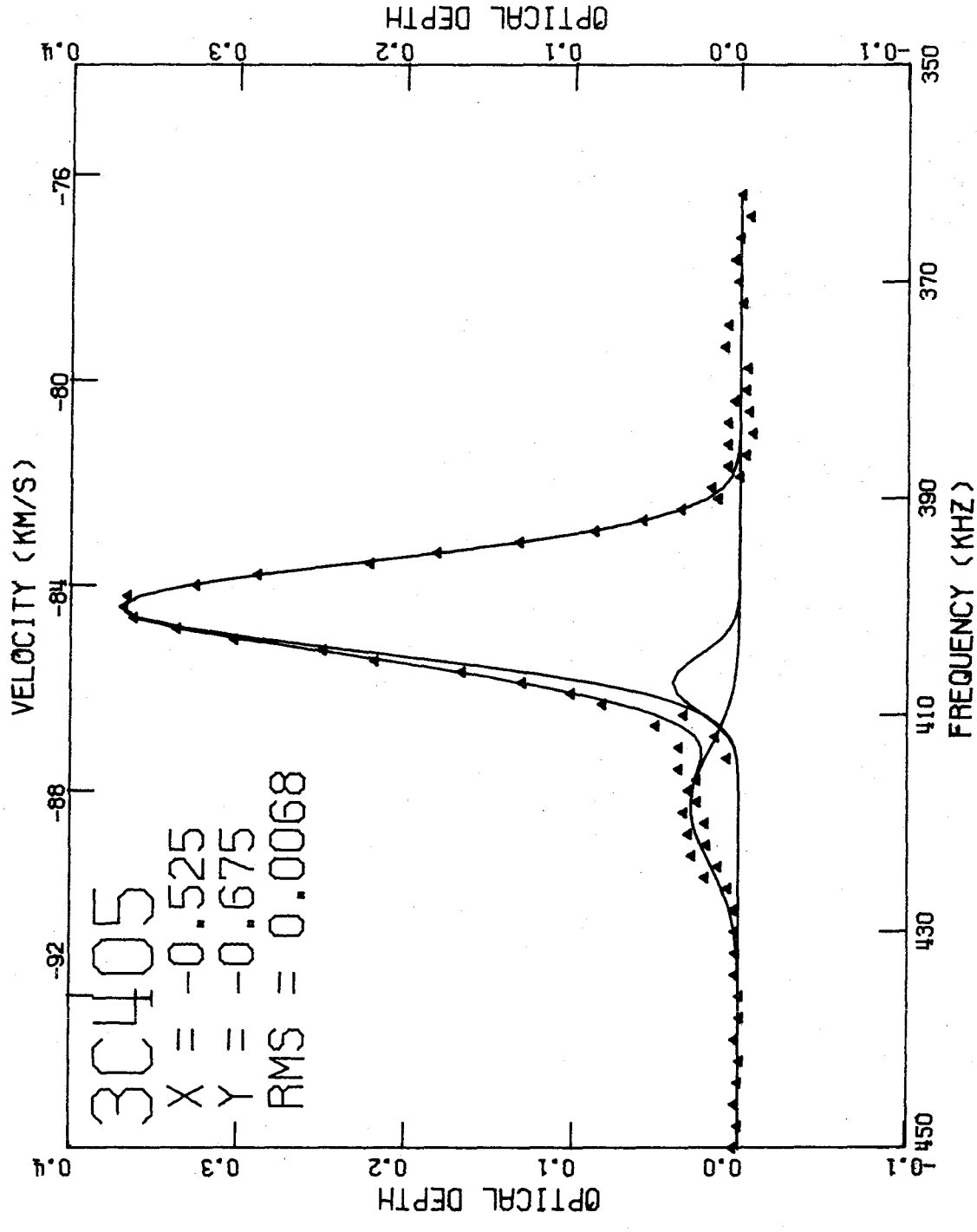

Figure 14b. 3C405: Gaussian fit spectrum at (-0.525, -0.675).

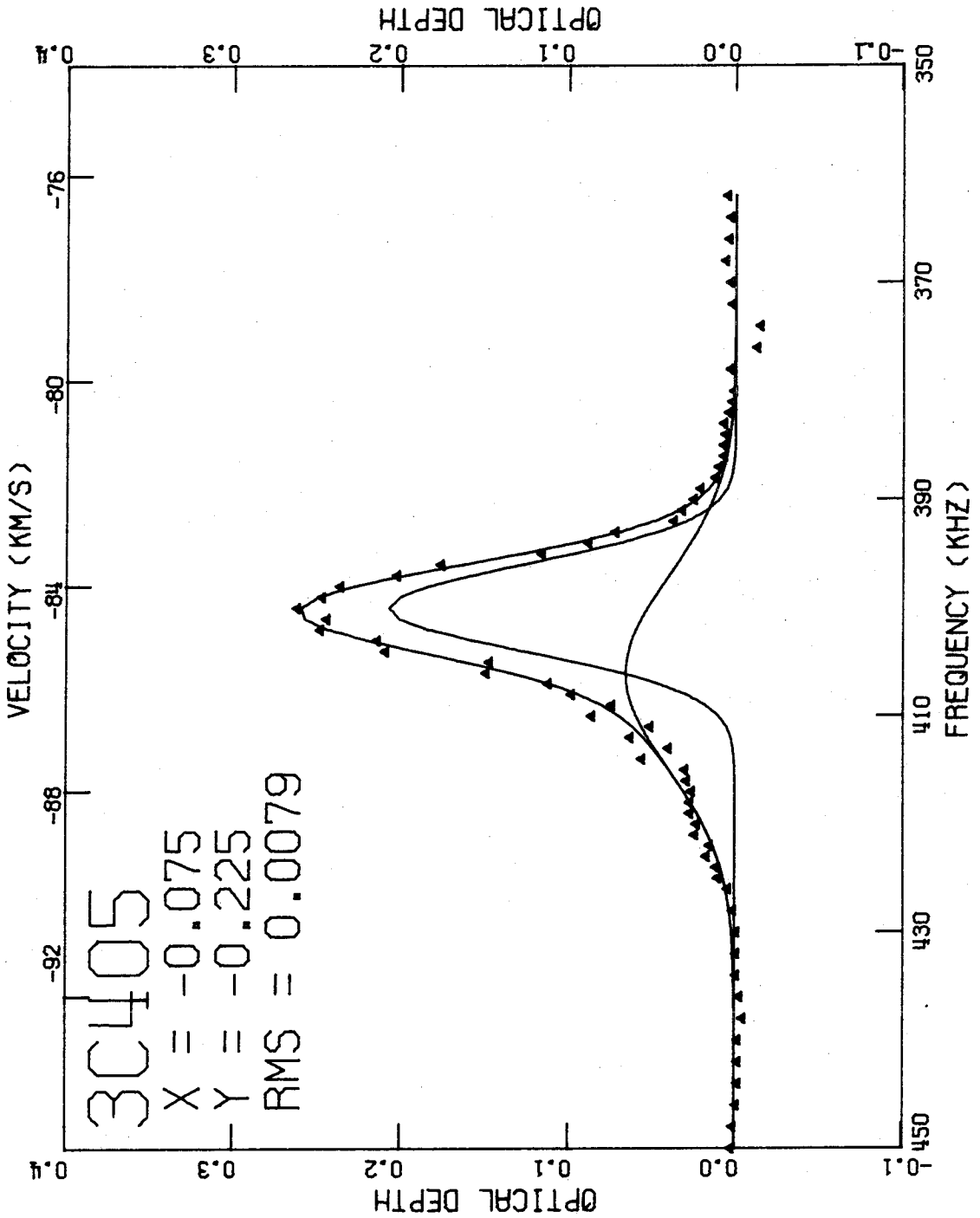

Figure 14c. 3C405: Gaussian fit spectrum at (-0.075, -0.225).

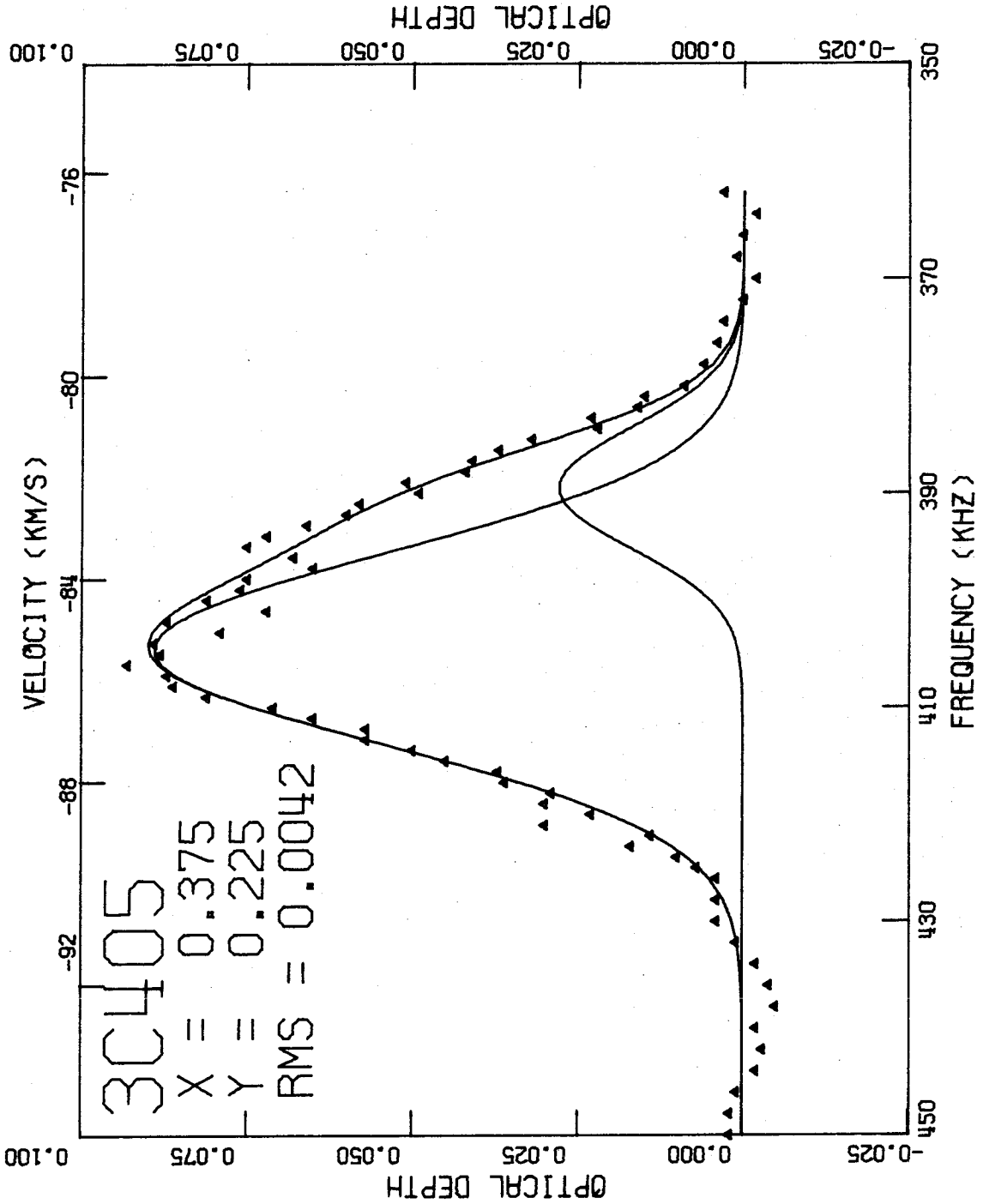

Figure 14d. 3C405: Gaussian fit spectrum at (0.375, 0.225).

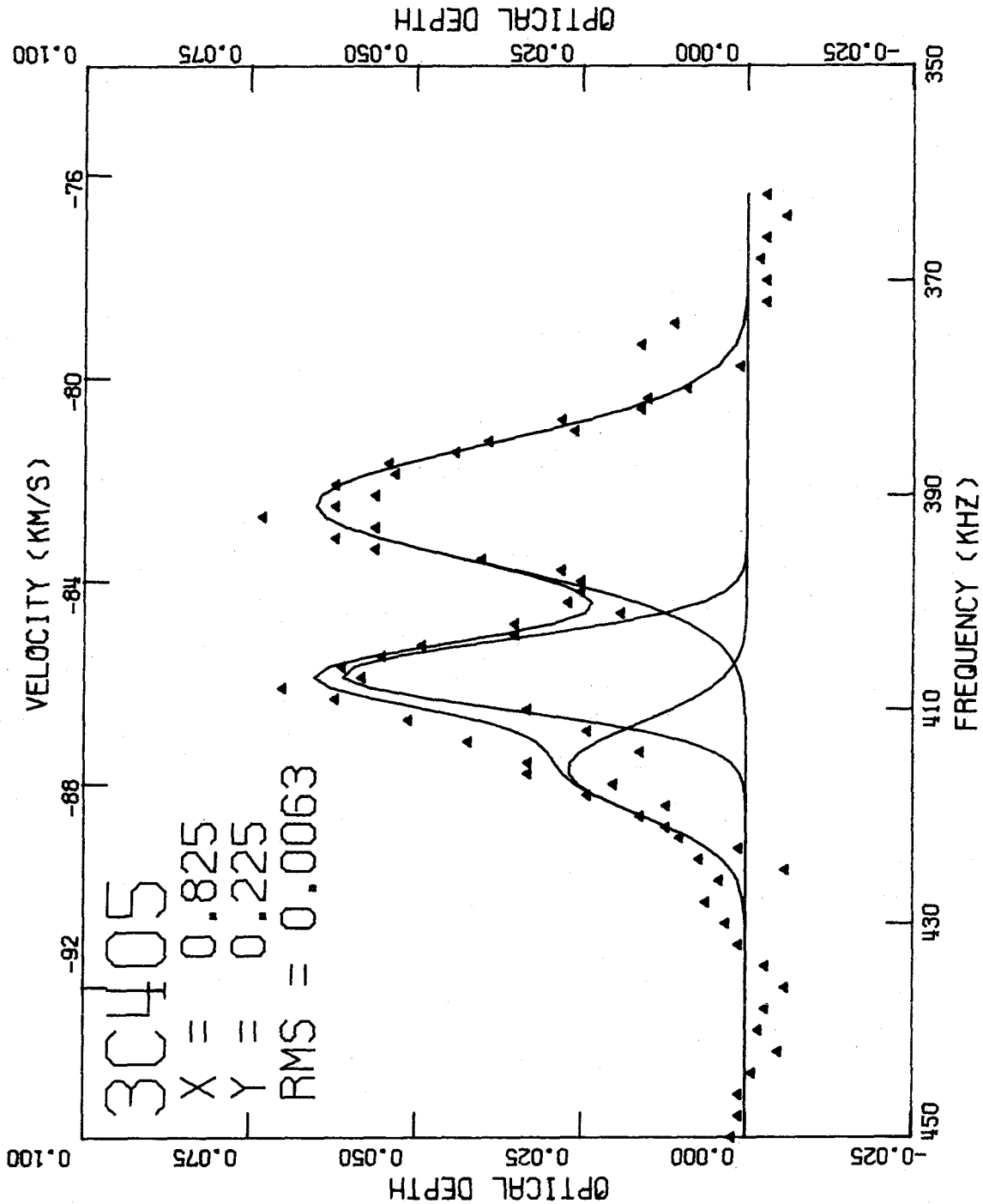

Figure 14e. 3C405: Gaussian fit spectrum at (0.825, 0.225).

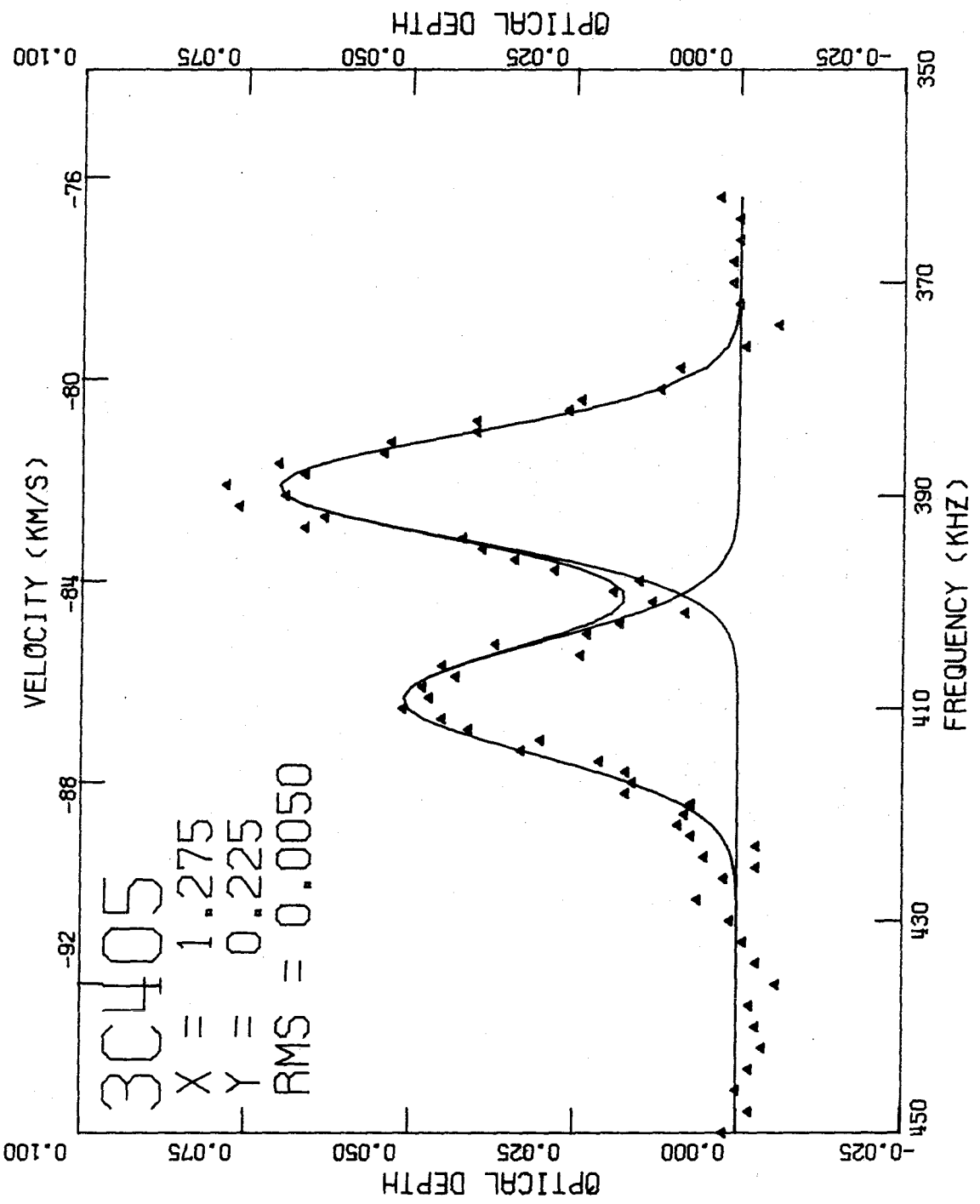

Figure 14f. 3C405: Gaussian fit spectrum at (1.275, 0.225).

program was not able to separate features 3 and 4. The remaining spectra show, with a change in the optical depth scale, the absence of the principal feature over the western half of the source.

E. Results — Noise

In Chapter 3B it was shown that the noise on the synthesized maps consists of two parts; a large term which is independent of x and y and a smaller term which will vary across the map. The uncertainties assigned to the data by CALIBRATE may be substituted in equation (3B-1) to obtain estimates of the noise on the maps. Figures 15 display the results of that substitution for Cygnus A. Figure 15a shows the constant term in both °K and relative to the peak continuum brightness as a function of frequency. The lines join the points of each frequency shift separately. We see that the noise decreases within the absorption line. This behavior which arises from the importance of the gain uncertainties is common to all the noise computations and will be discussed in more detail in the next chapter. In Figure 15b the upper limit to the variable noise term is plotted as a function of frequency. Again each frequency shift is plotted as a separate line. The weak absorption line for this source does not cause a

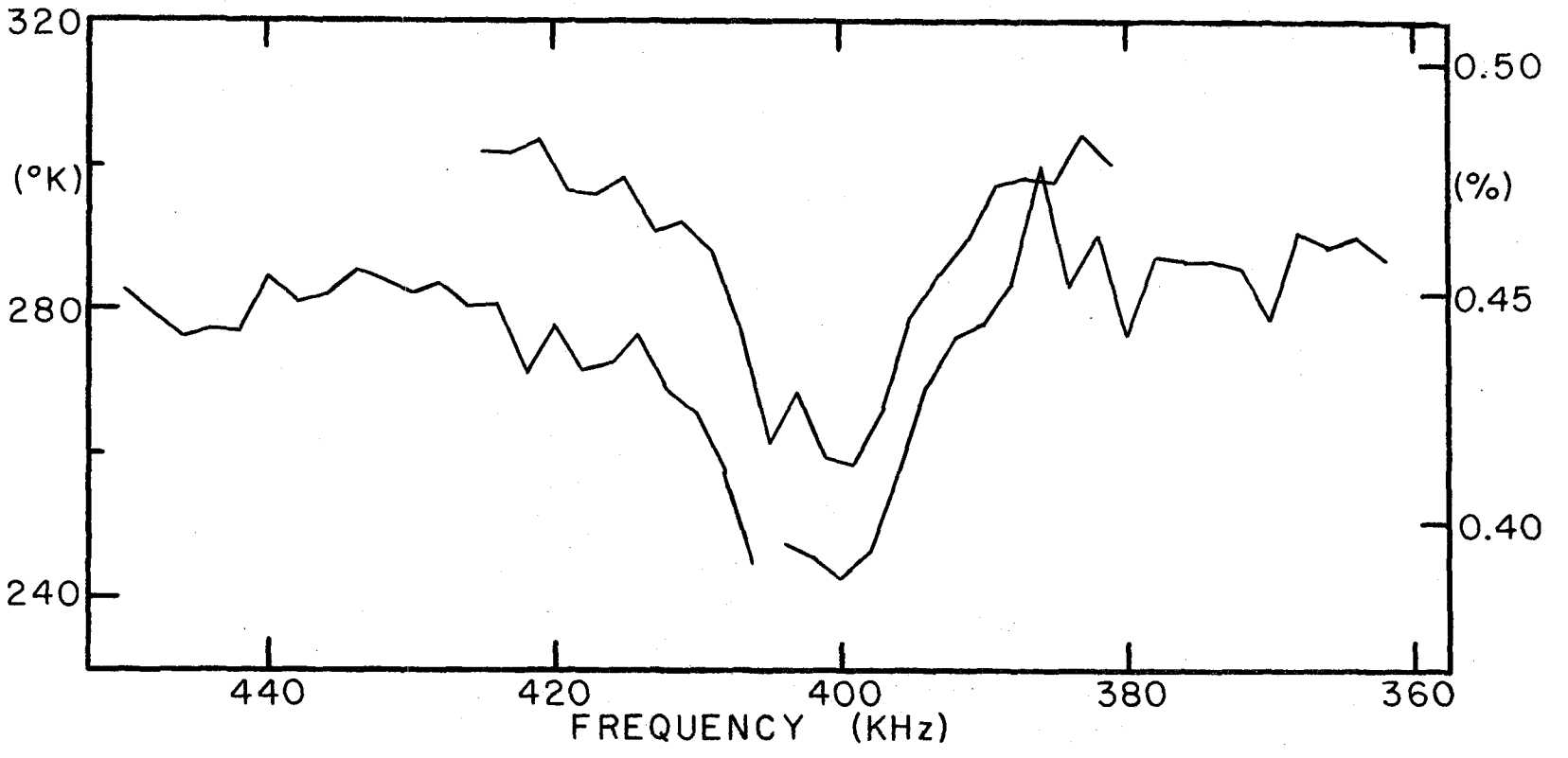

Figure 15a. 3C405: Spatially constant part of the noise as a function of frequency in °K (left hand scale) and in percent of the peak brightness on the continuum map (right hand scale). Each continuous line represents a different frequency shift.

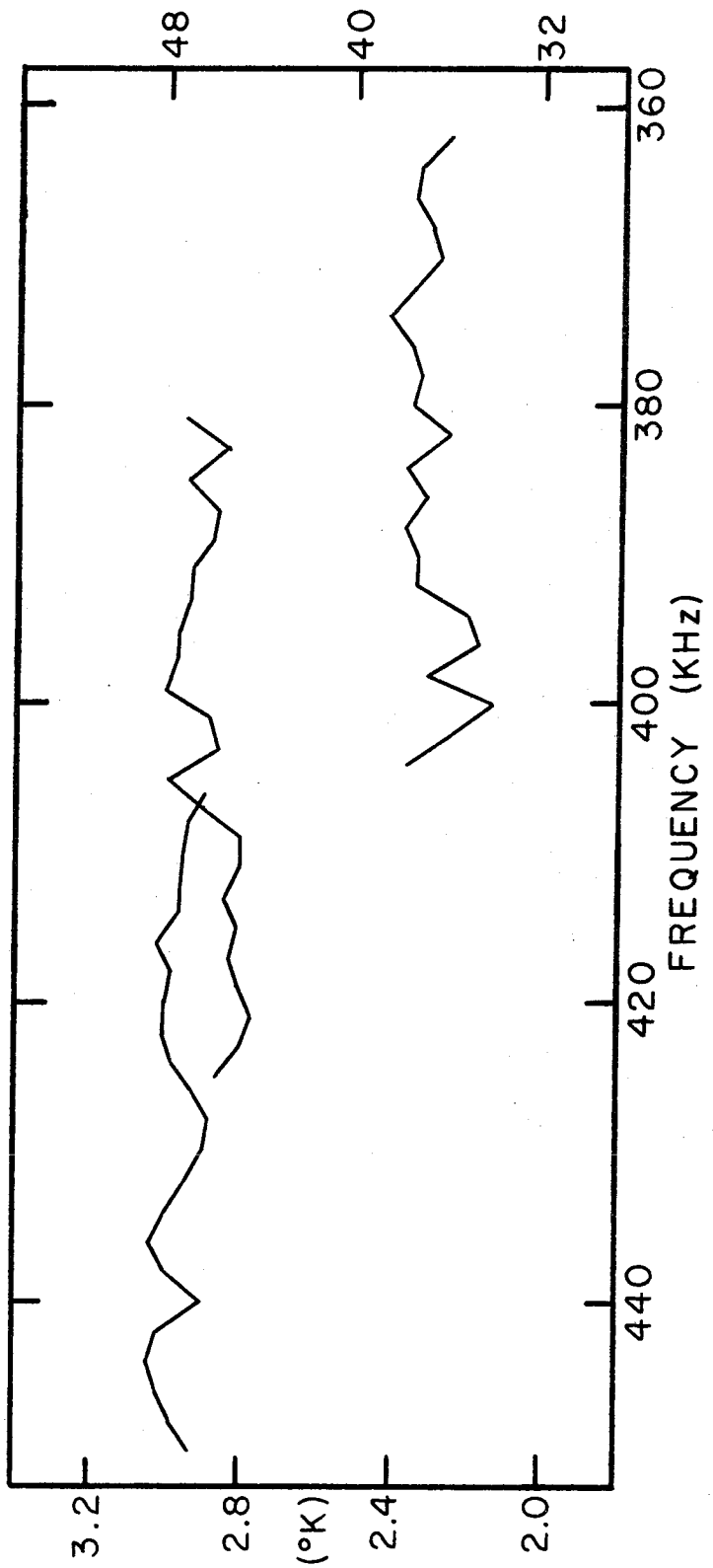

Figure 15b. 3C405: Upper limit to the spatially variable part of the noise as a function of frequency in °K (left hand scale) and relative to the peak brightness on the continuum map (times 10^6) (right hand scale). Each continuous line represents a different frequency shift.

reduction in this part of the noise. The variable term is only about one percent of the constant term and hence may be ignored.

Table V of Chapter 3B shows that the Monte Carlo tests give values for the noise consistent with, but actually lower than, the values derived from the theory. At 362 KHz, the Monte Carlo tests indicate a higher noise on the source than off particularly after the deconvolution. However, at 400 KHz, there is no correlation between the source and the noise maps. The computations place the uncertainties in optical depth due to noise around 0.03 at the edges of the source and less than 0.01 over the main part of the source.

F. Interpretation

The standard Schmidt (1965) model of galactic rotation gives a distance to the hydrogen observed at 400 $\pm$ 10 KHz of 12.3 $\pm$ 0.2 Kpc. If the hydrogen has a peculiar motion of 10 Km/sec along the line of sight, then this distance estimate would be changed by about one Kpc. It is interesting to note that, at this distance, the hydrogen is about 1.25 Kpc above the plane of the Galaxy and about 0.75 Kpc above the peak emission regions of the

Perseus arm at this longitude (Kepner 1970). The separation of the grid points in Figures 13, 0.45 minutes of arc, corresponds to 1.6 parsecs at the distance of the hydrogen.

Although the gaussian fitting procedure does not work well for this source, it does introduce a useful characterization of the data. The column density is given by

$$\frac{N_H}{T_s} = 3.88 \times 10^{17} \int \tau \, d\nu = 4.13 \times 10^{17} \, \tau_0 \sigma \left(\frac{1}{cm^2 \, ^\circ K} \right)$$

or

$$\frac{N_H}{T_s} = 0.134 \, \tau_0 \sigma \left(\frac{pc}{cm^3 \, ^\circ K} \right) \qquad (4\text{-}1)$$

and the apparent temperature is given by

$$T_a = 0.975 \, \sigma^2 \quad (^\circ K) \qquad (4\text{-}2)$$

where σ is the full width at half maximum in KHz. The reader is reminded of the discussion in Chapter 3C which indicated that the apparent temperature is at best an unreliable upper limit to the actual physical temperature.

It may be seen from Figures 11a and 14a that, as the resolution is improved, the observed width of the principal hydrogen feature decreases. The moderate improvement in spatial resolution between these two figures causes the

apparent temperature to decrease from 140° K to 115° K. The gaussian analysis assigns an apparent temperature of 83 ± 13 °K to the principal feature in Figure 14a while farther to the east where this feature is less confused with other features apparent temperatures as low as 68 ± 6 °K are found. The gaussian analysis assigns apparent temperatures around 100 to 200 °K to the other features, at least where the blending of the features is not too serious a problem. For the following discussion, we will assume that all the hydrogen observed is at 70° K since this is the lowest reliably determined apparent temperature.

Using equation (4-1) we find that the column densities of the individual components range from zero to about 0.57 $pc/cm^3/°K$. Summing this parameter over all components we find it to vary from 0.18 $pc/cm^3/°K$ at the western edge of the source to 0.75 $pc/cm^3/°K$ at the eastern edge of the source. If we assume the 12.3 Kpc distance and 70° K temperature we may convert the column densities into masses within the 0!45 by 0!45 cell surrounding each grid point. Substituting we find a range of 0.8 to 3.4 solar masses

per cell and a total mass observed around 78.5 solar masses.[3]

Since the spatial distribution of optical depth varies radically over a beamwidth (4.8 pc), we may adopt this length as a conservative estimate of the size of the hydrogen clouds along the line of sight. Doing this, we find from the column densities that the space densities range up to 8.3 cm^{-3} for the individual gaussian components and from 2.8 to 11 cm^{-3} for the total of all features. Since the choice of depth scale was quite conservative, it would not be surprising if the true densities were larger by factors of two or more.

It is not unreasonable to assume that all the observed hydrogen is physically associated for this particular absorption feature. It is well separated in velocity from the only other significant absorption feature in the spectrum of 3C405 (see Chapter 8C). Its dispersion is much less than the 5 to 10 km/sec dispersions in cloud

---

3 This number should be regarded with considerable caution because of the possible effects of resolution. For example, if the background source is a point source then the total hydrogen actually observed is very small. However, the beam size will cause the hydrogen to appear to have the same column density over the full beam area and hence to have a significant total mass.

velocities reported by numerous observers (see Spitzer 1968). Furthermore, the hydrogen is well above the main parts of the Perseus arm in which one would expect clouds of hydrogen to overlap along the line of sight.

A model, with which the data appear to be consistent, is a shell of hydrogen. The shell is expanding (or collapsing - the two are indistinguishable) at about 2 km/sec from a point along the line of sight toward the western edge of the source (see Figure 14f). The line of sight toward the eastern edge of the source is tangential to the inner surface of the shell (see Figures 12e and 14b). The details of this model are computed in Appendix E. Assuming a uniform, spherical shell we find an outer radius of 9.7 $\pm$ 0.7 parsecs and a shell thickness $12\ ^{+6}_{-12}$ percent of the outer radius. Assuming a temperature of 70° K, the density is found to be $6.0^{+\infty}_{-2.5}$ cm^{-3} and the total mass to be 175 $\pm$ 15 solar masses. It is interesting to note that these parameters are not unlike those of a "standard cloud" (Spitzer 1968). Of course, the standard cloud does not have a shell structure.

The data are consistent with the model, but only a small portion of the shell is observed because of the small angular size of the background source. The densities

within the shell are not completely uniform, but appear more uniform than in other well-known shells such as the supernova remnant of Cassiopeia A. The velocity dispersion in the direction of expansion is, quite reasonably, somewhat greater than in the transverse direction. The velocity of expansion, if it is expansion, is about four times larger than the escape velocity from the surface of the shell. As a result, in the absence of strong external pressures, this shell is not gravitationally bound and will eventually dissipate. The cause of the expansion is not clear. The velocity is an order of magnitude too low for a shell surrounding an HII region (Thompson, et al 1969). Stone (1970) has found that cloud-cloud collisions will produce velocities of a few km/sec during the re-expansion stage. Unfortunately, none of his models would have a shell-like appearance.

CHAPTER 5

CASSIOPEIA A (3C461)

A. Results — Beam Patterns and Brightness Maps

Cassiopeia A, the well-known radio source thought to be a supernova remnant, lies at a declination which is ideal for aperture synthesis. The loci of projected baseline vectors ("tracks") of the east-west and north-south spacings are nearly circular and actually overlap slightly. This is illustrated in Figure 16 which shows the location in the (u, v) plane of the data points obtained for the continuum frequency shift including those obtained with the hermitian property of the visibility function. The continuum frequency shift of 3C461 was used to produce maps covering a large area as part of the test discussed in Chapter 3A. The dirty beam obtained (Figure 17a) is dominated by nearly circular features with irregularities resulting from the uneven distribution of data points along the tracks in the (u, v) plane. Sidelobes are less than 7 percent near the main beam but sidelobes as great as 30 percent occur at distances from the center exceeding six minutes of arc. The main beam has a full width at half maximum about 1.3 arc minutes.

The dirty map of the continuum (Figure 17b) shows the effects of the circular sidelobe pattern, but is more

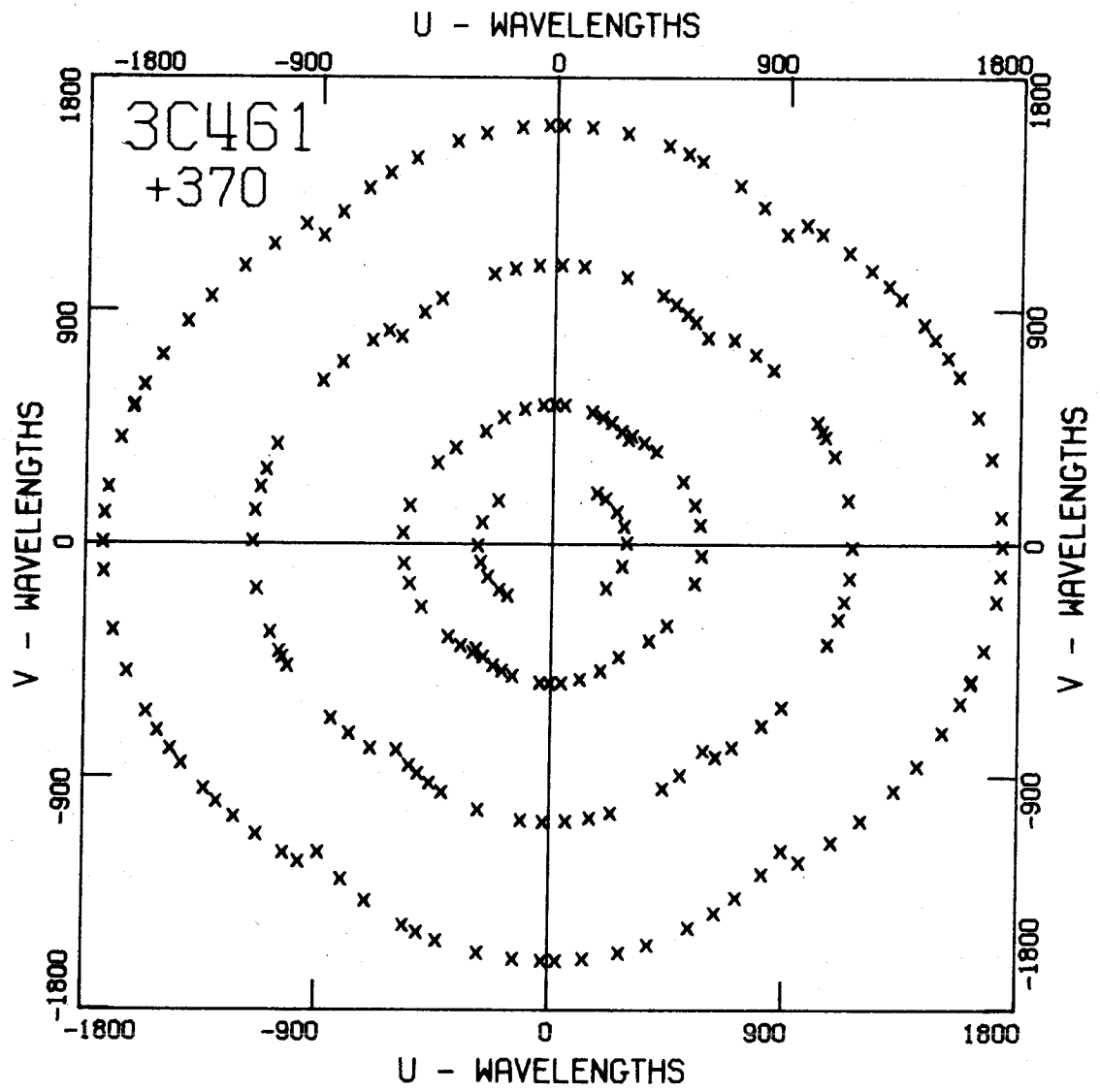

Figure 16. 3C461, continuum frequency shift: distribution of data points.

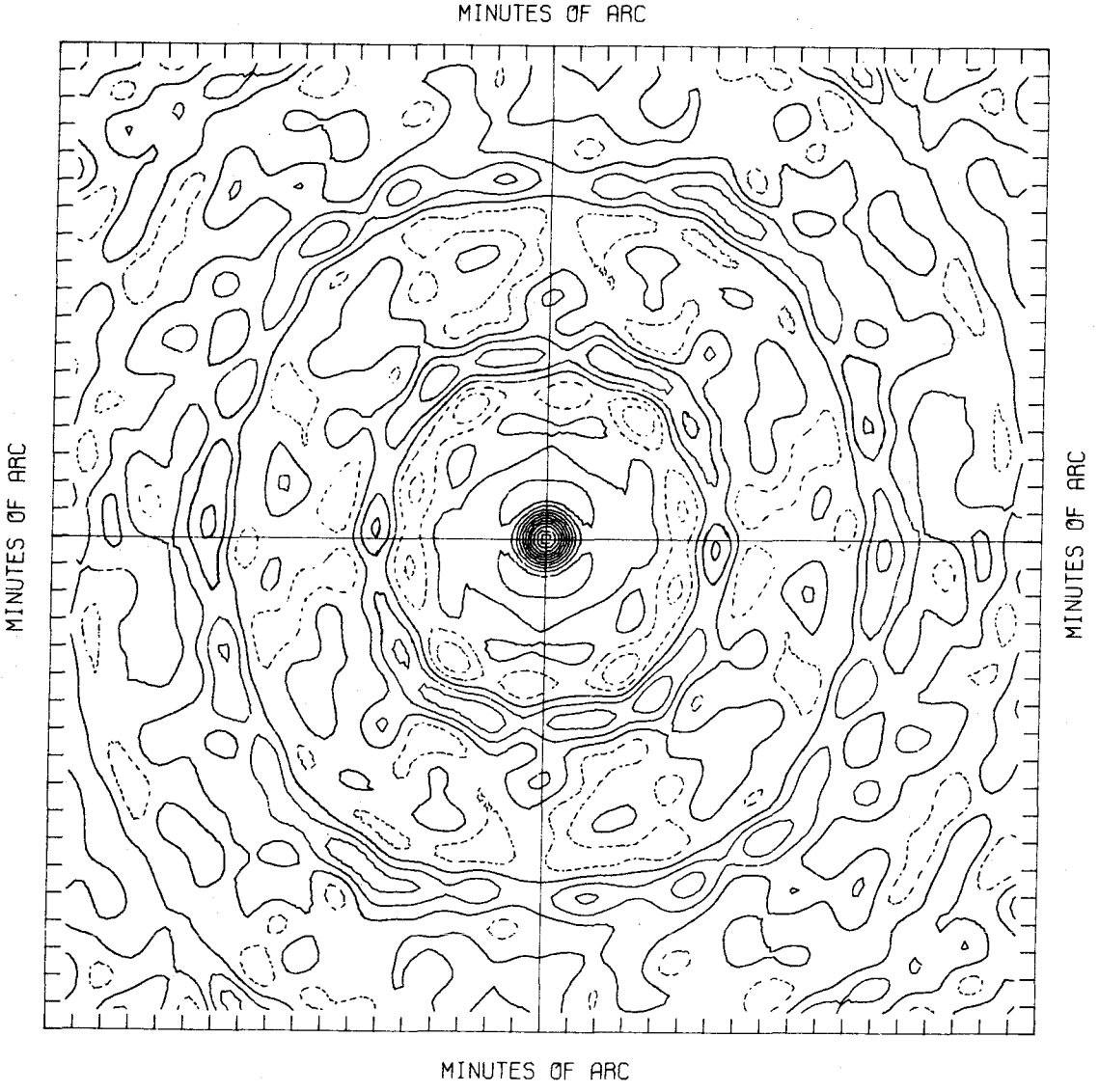

Figure 17a. 3C461, continuum frequency shift: dirty beam pattern, contour interval = 10%, large area.

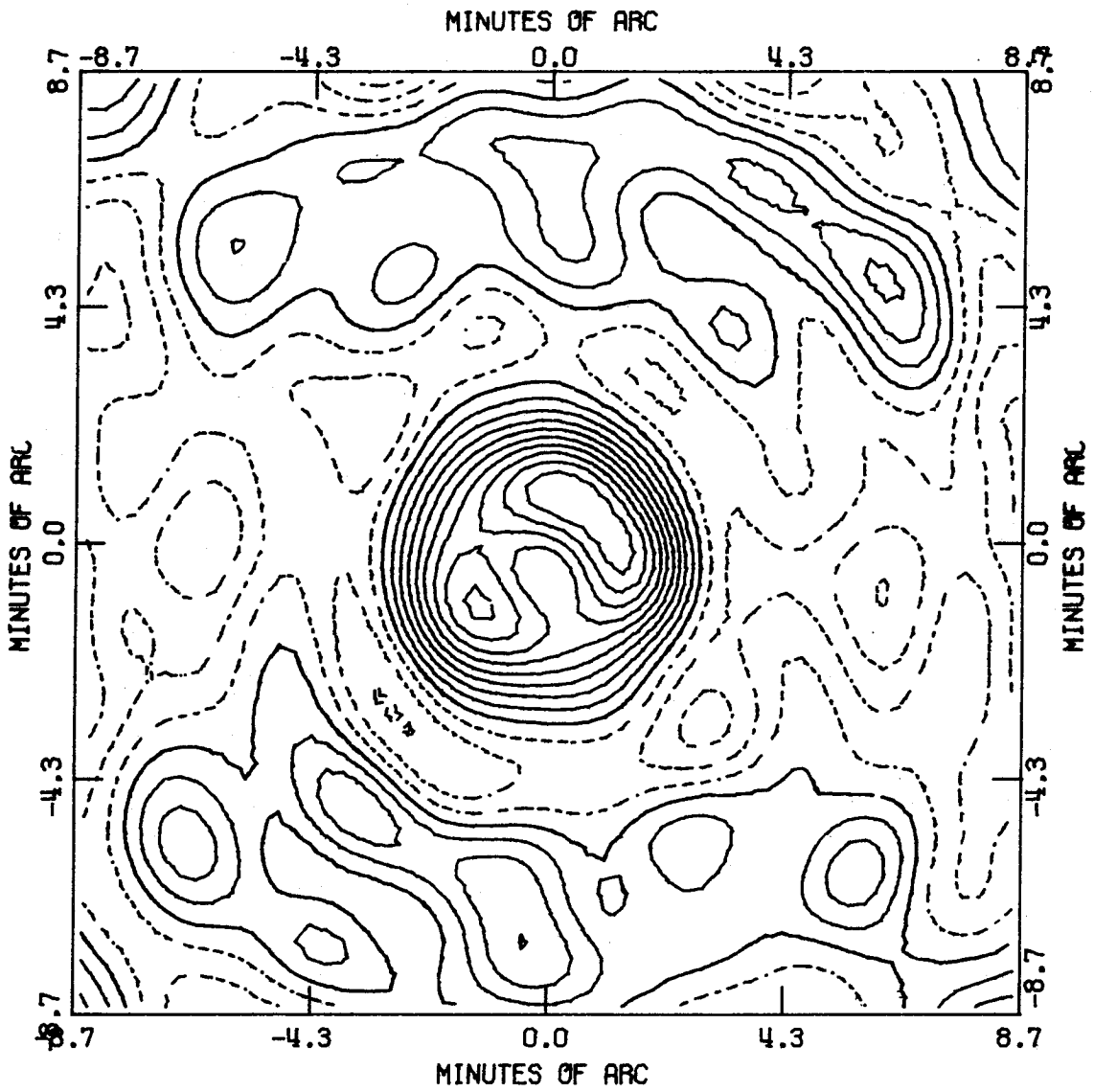

Figure 17b. 3C461, continuum frequency shift: dirty map, contour interval = 10%, large area.

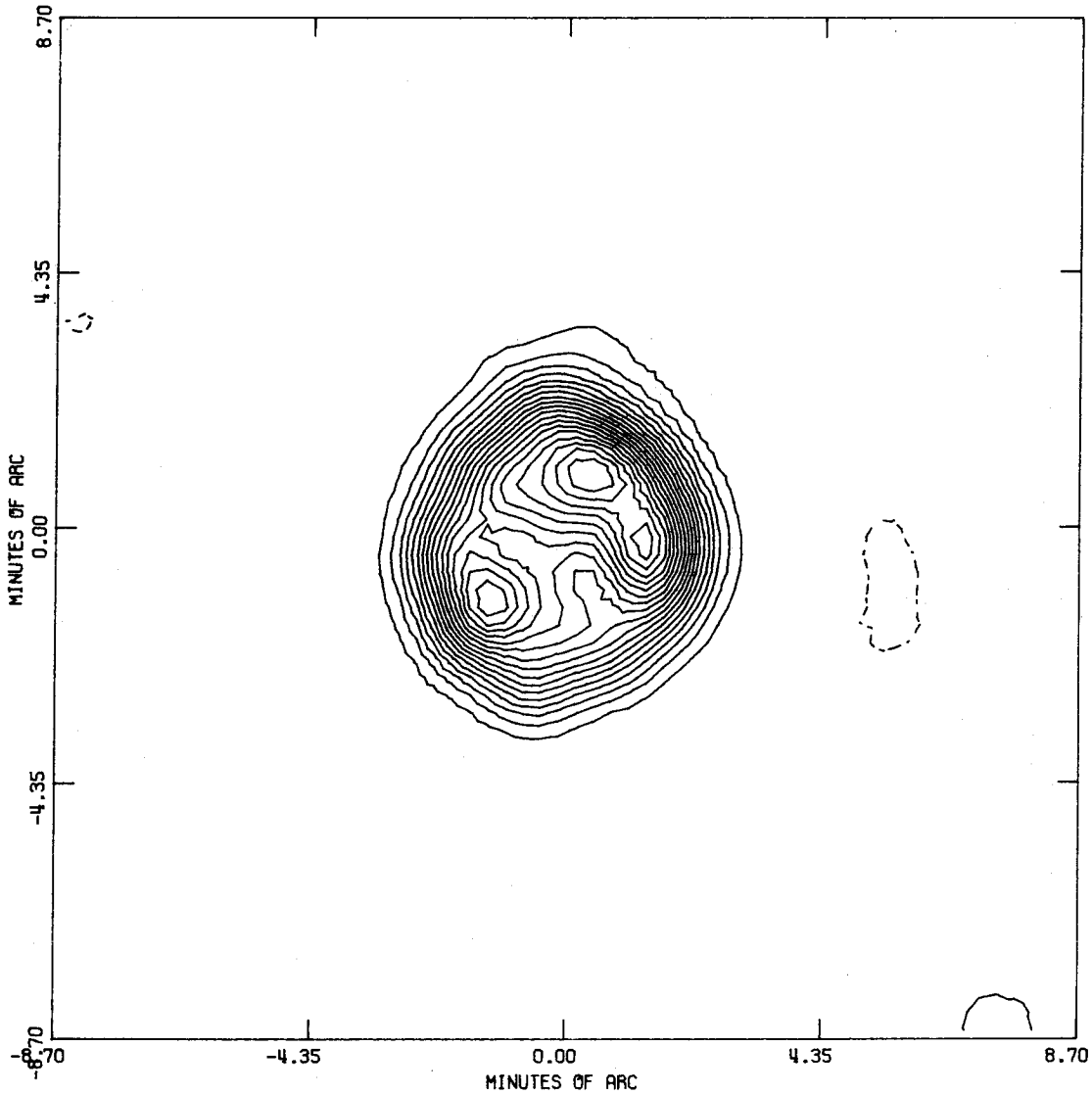

Figure 17c. 3C461, continuum frequency shift: clean map, contour interval = 5%, zero contour suppressed, large area.

irregular due to the irregularities in the source itself. Spurious responses as high as 40 percent are seen on the map. Again we find that the deconvolution procedure both improves the resolution on the source and removes the major portion of the spurious responses off the source. The clean map of the continuum (Figure 17c) shows only five presumably spurious responses exceeding 4 percent of the peak brightness while most of the area surrounding the source has brightness less than one percent of the peak. There is a slight increase again in the spurious responses surrounding the source when the deconvolution is done over a more restricted area. This is illustrated in Figure 18 which shows the continuum map used to produce optical depth maps. The lines of constant galactic coordinates are drawn through the center of this map.

To demonstrate the importance of good coverage in the (u, v) plane and of good signal-to-noise ratio the large area test was also conducted at a frequency near the bottom of the deep absorption line. Two frequency shifts overlapped at this frequency doubling the number of data points obtained (Figure 19a). With this increase in the density of data along the tracks in the (u, v) plane, the importance of the discrete nature of the data sampling is reduced.

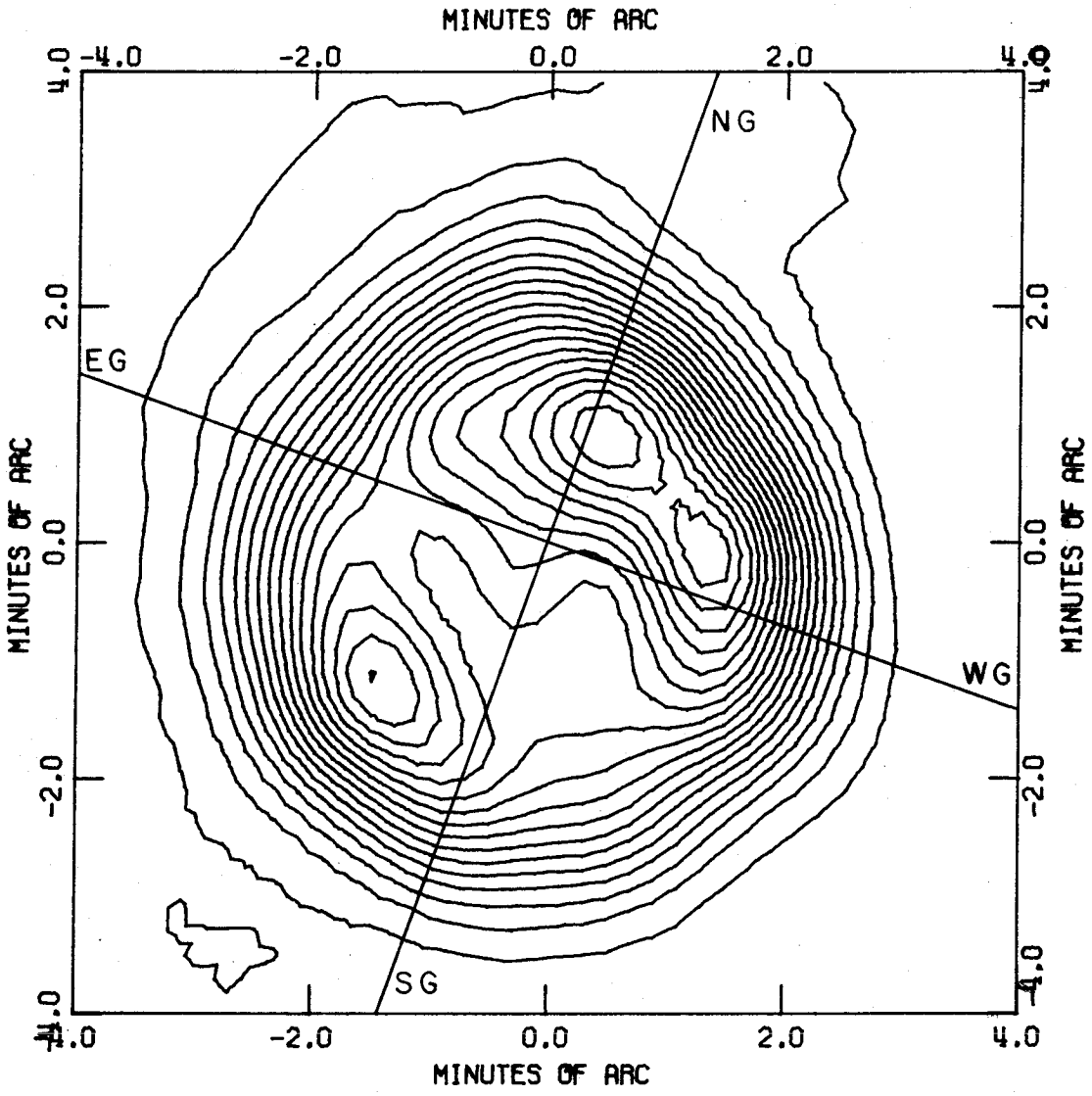

Figure 18. 3C461: continuum map, contour interval = 5% , zero contour suppressed. Lines of constant galactic coordinates drawn with NG being galactic north and EG galactic east (i.e. increasing longitude at constant latitude).

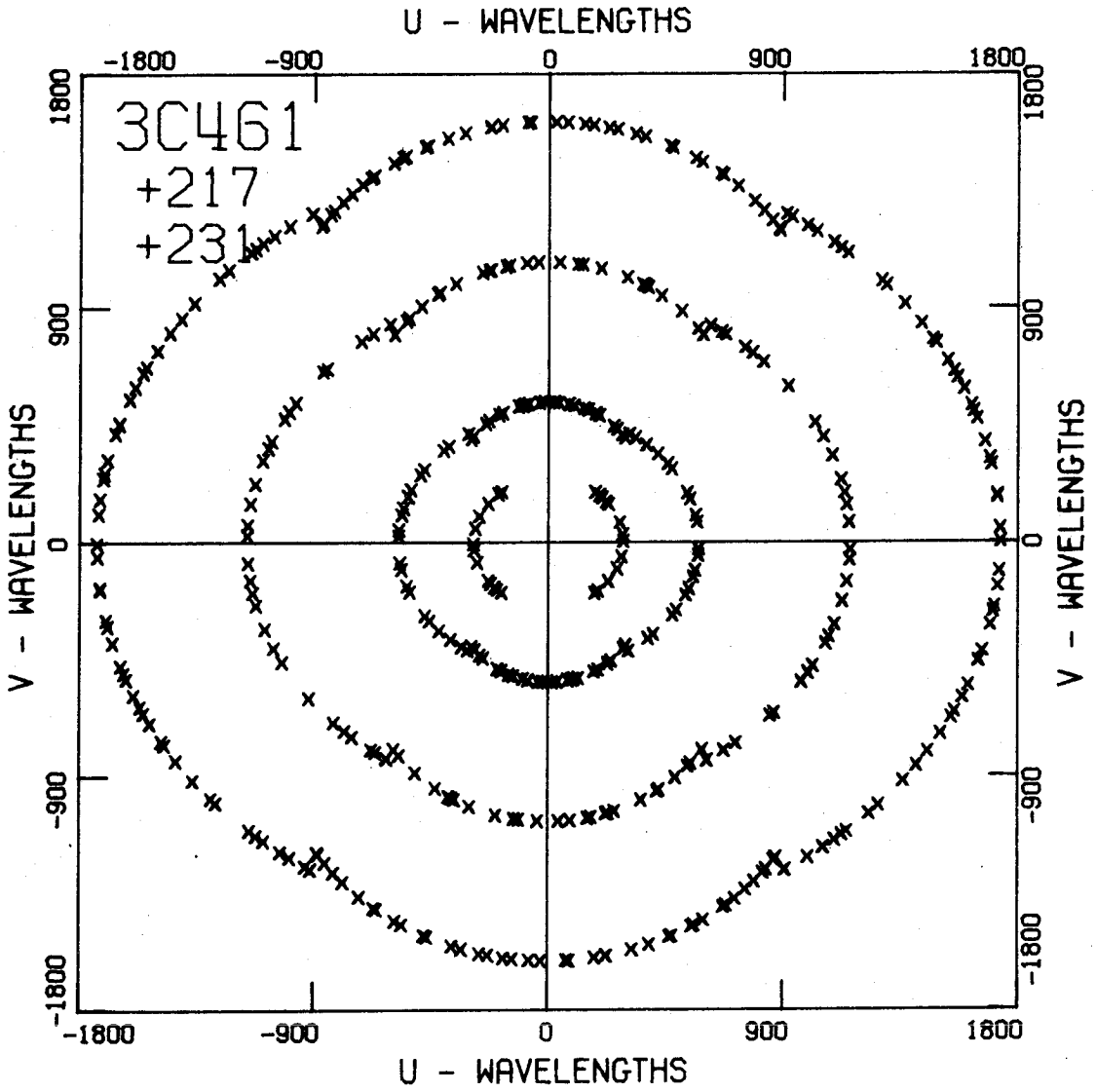

Figure 19a. 3C461, overlapped frequency shifts (+217 and +231): distribution of data points.

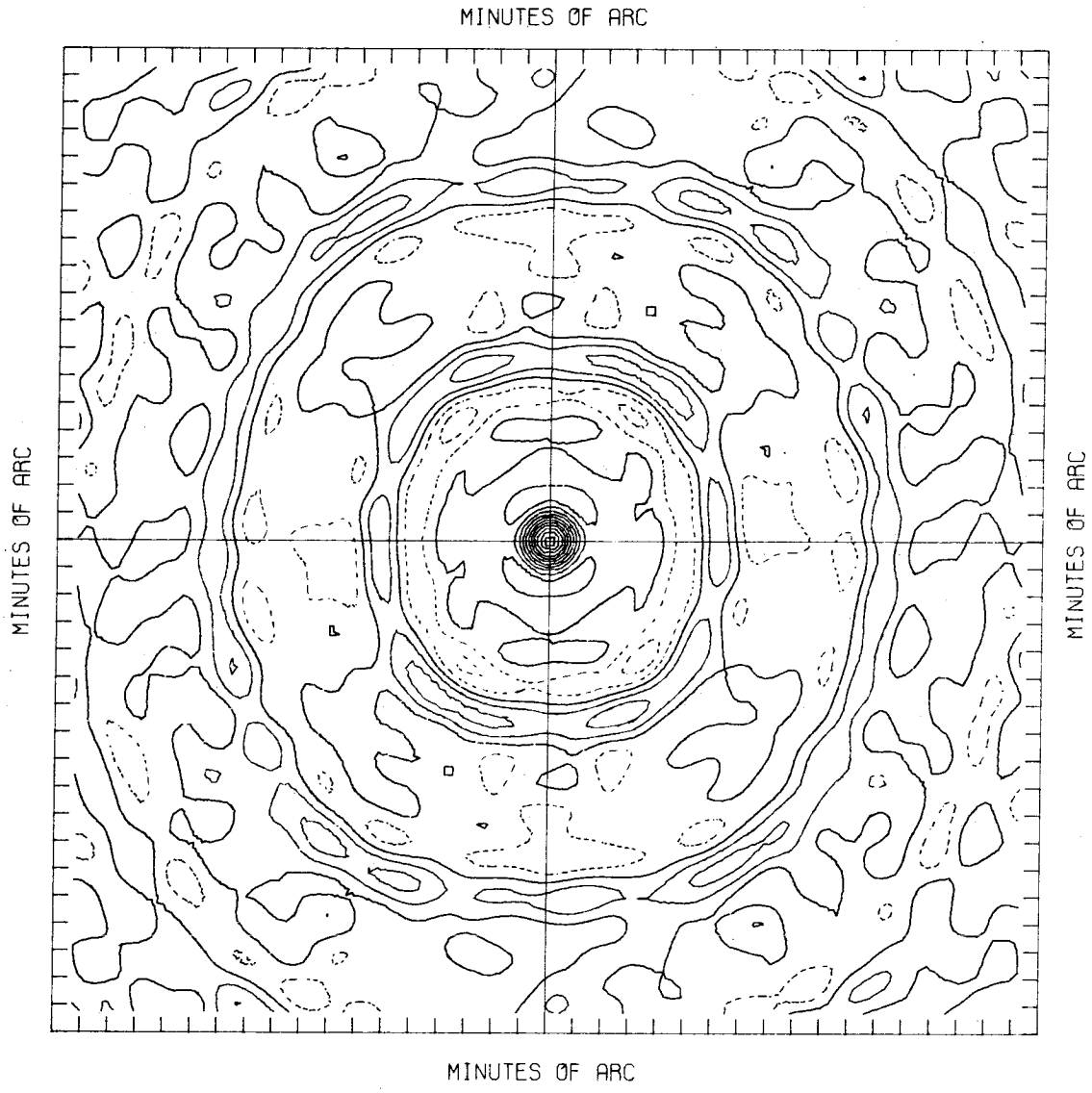

Figure 19b. 3C461, overlapped frequency shifts (+217 and +231): dirty beam pattern, contour interval = 10%, large area.

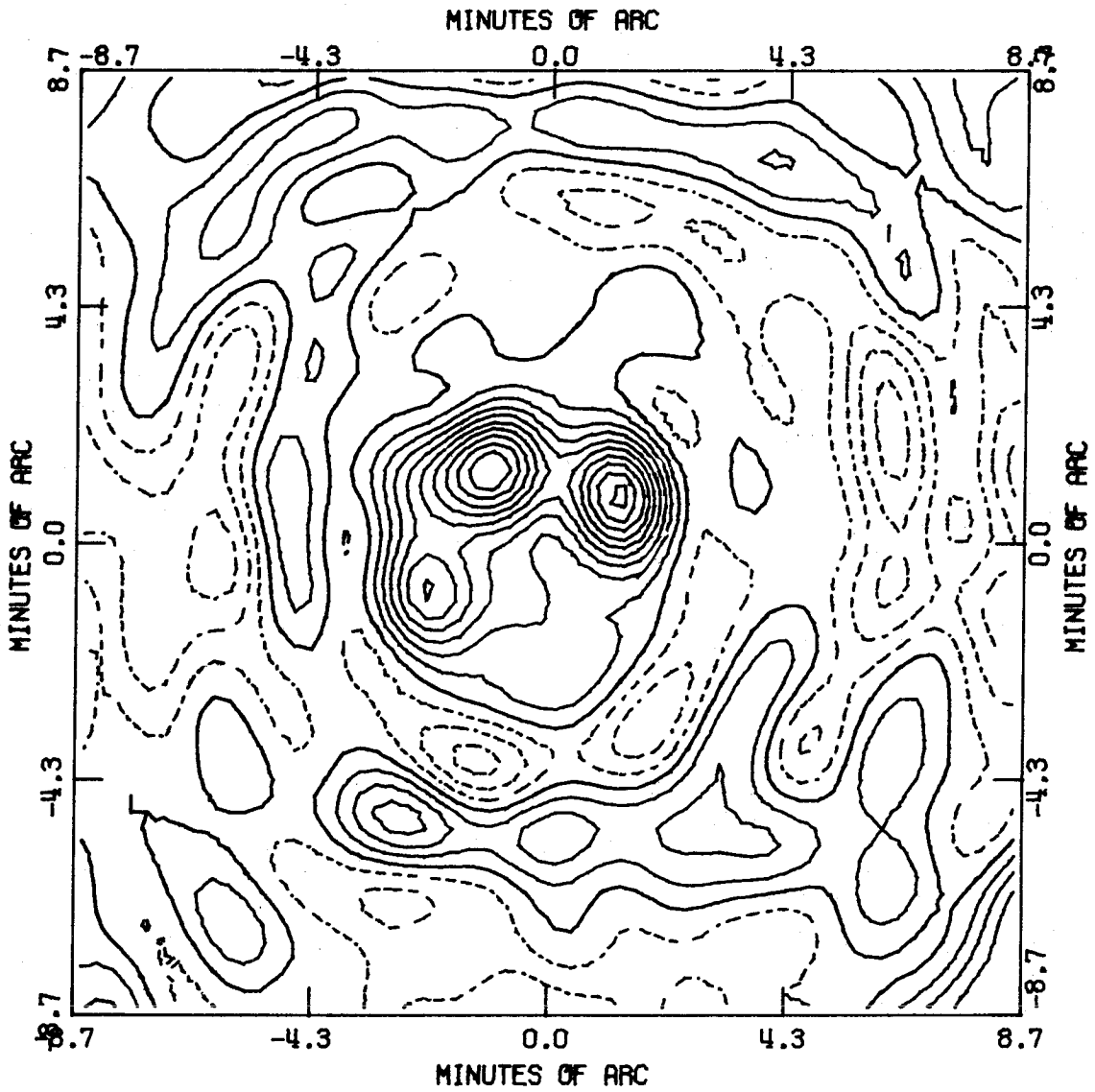

Figure 19c. 3C461, overlapped frequency shifts (+217 and +231): dirty map at 227 KHz, contour interval = 10%, large area.

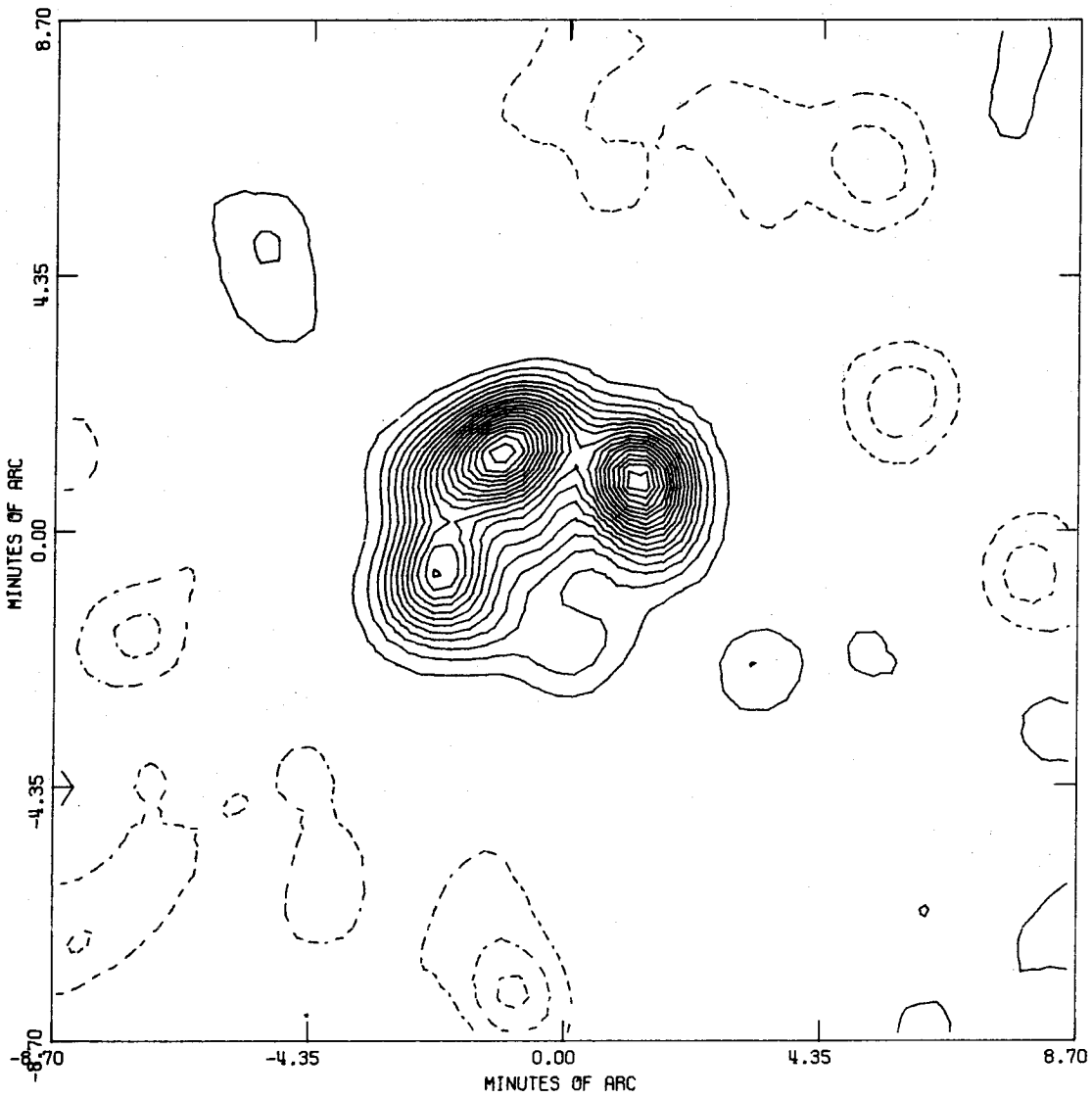

Figure 19d. 3C461, overlapped frequency shifts (+217 and +231): clean map at 227 KHz, contour interval = 5%, zero contour suppressed, large area.

As a result, the dirty beam pattern (Figure 19b) contains fewer bumps and irregularities than the beam of Figure 17a and the peak sidelobes are reduced to around 25 percent. Since the flux at the bottom of the absorption line is only 18 $\pm$ 1 flux units (at 200 feet east-west), the signal-to-noise ratio is much poorer for these frequencies than for the continuum. As a result, despite the improved beam pattern, the dirty map shown in Figure 19c contains spurious responses of nearly 50 percent. After the deconvolution procedure, responses of 10 and 15 percent remain (Figure 19d). The rough symmetry with respect to the source of these responses suggests that they are indeed noise rather than local variations in the general hydrogen emission.

B. Results — Observed Spectra

The spectrum of Cassiopeia A contains two major absorption features, one associated with the local arm and one with the Perseus arm of the Galaxy. Only the latter was observed in this program. In Figure 20 are plotted the averages of the data obtained at the 200-foot east-west spacing. The relative flux and phase are plotted as functions of frequency or velocity. The right hand scales show the relative flux in terms of optical depth

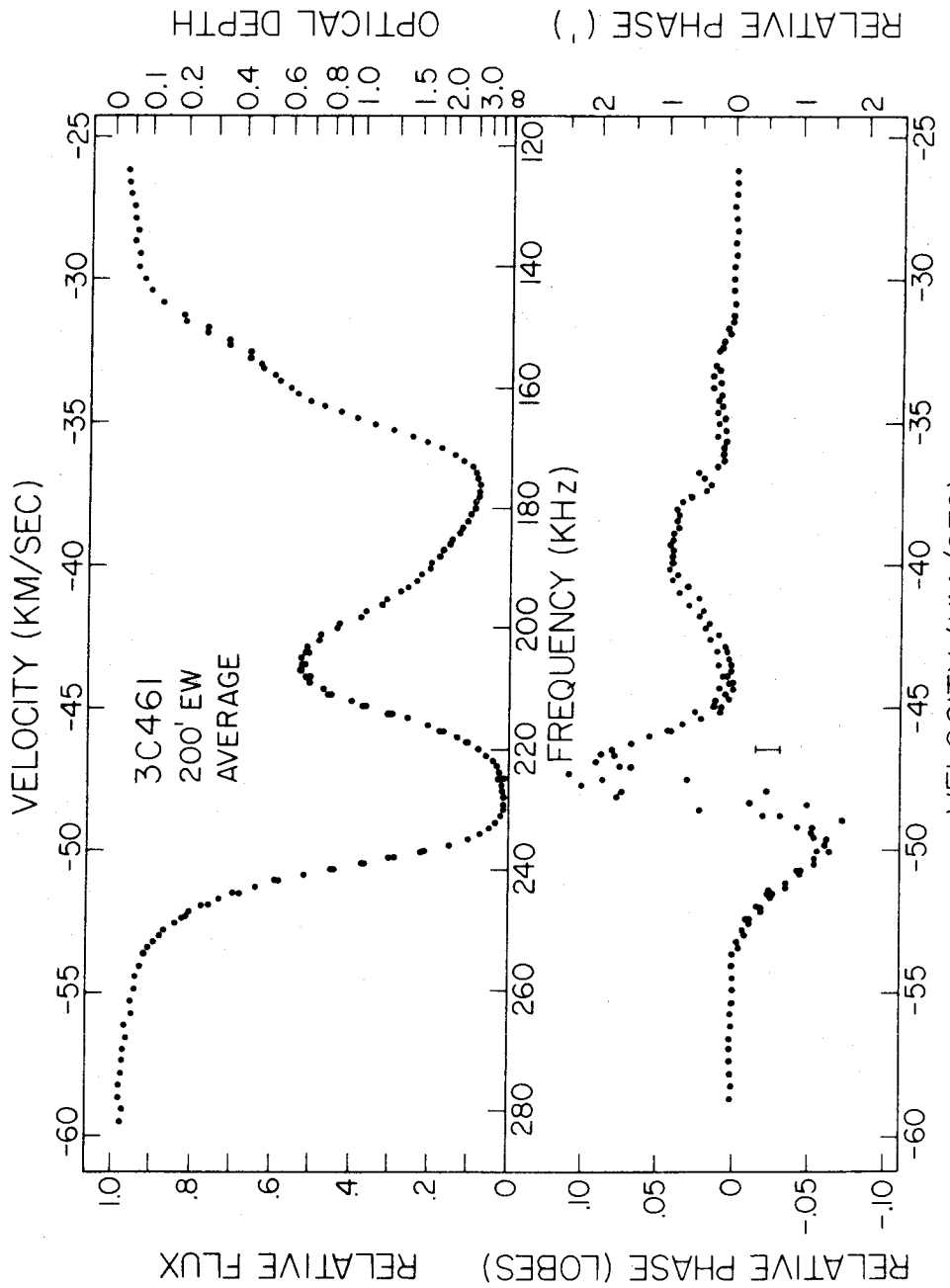

Figure 20. 3C461: relative flux and phase spectra at 200 feet east-west. Average of 60 minutes of observation.

and the relative phase as a displacement of the centroid of the source. Each point represents an integration time of about 60 minutes. The dispersion in the data is mostly due to different resolution effects for the different frequency shifts. The uncertainties in the data are generally smaller than the dots except for the phase errors around 225KHz.

Since this source is at lower galactic latitude, its absorption feature is deeper, wider, and considerably more complex than the Perseus arm feature discussed in the previous chapter. Throughout the absorption line, the relative phases measured indicate that the absorbing medium is not uniformly distributed across the source. In particular, at frequencies around 235 KHz the residual emission comes almost completely from one side of the source while at frequencies around 223 KHz the residual emission comes completely from the other side of the source (see Figure 19d).

The flux and phase spectra shown in Figures 21 were obtained with the projected baseline having nearly constant length but position angle varying by 42°. Each point on the spectra represents a single ten-minute observation. Again some of the dispersion in the data is due to the

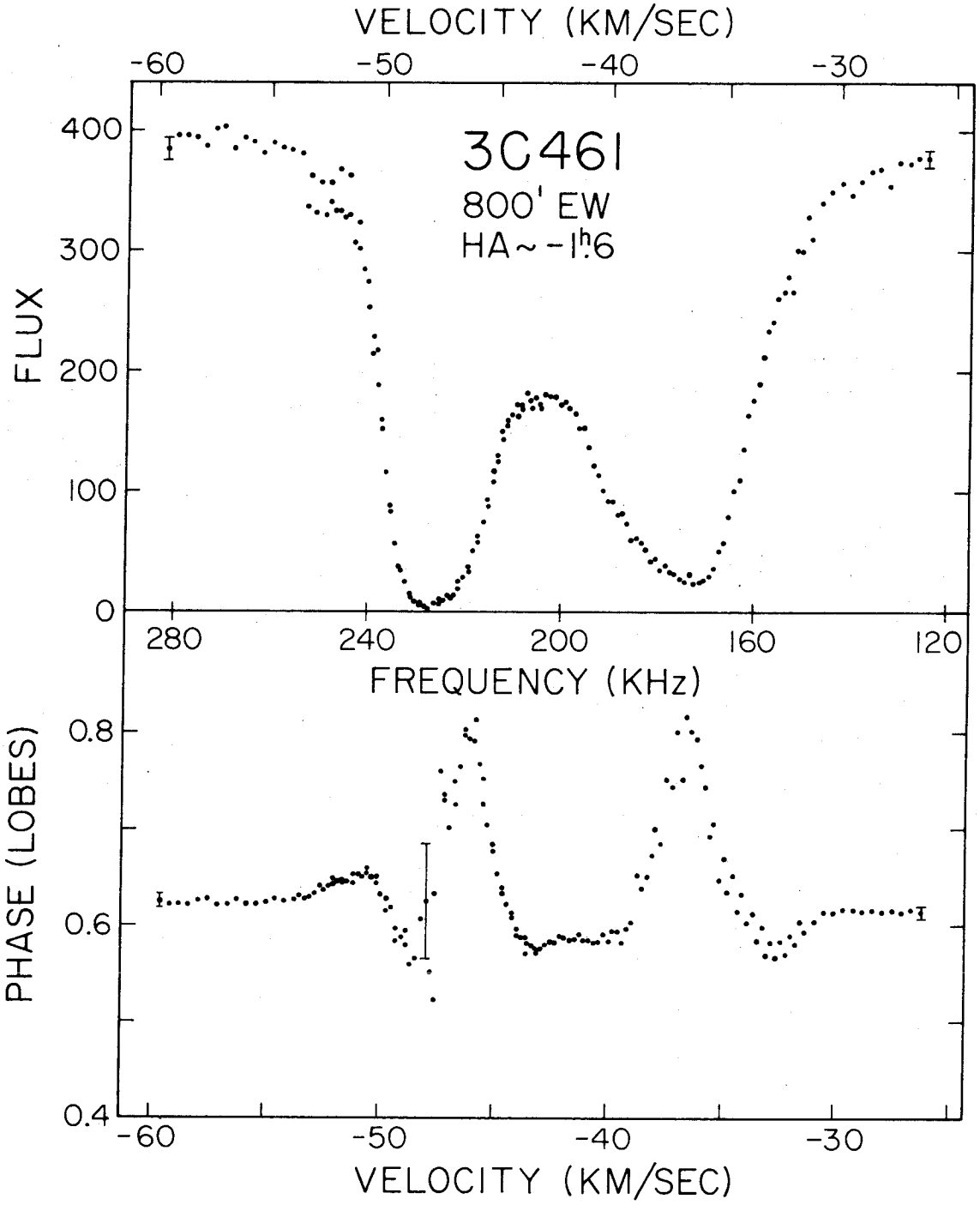

Figure 21a. 3C461: flux and phase spectra at 800 feet east-west at hour angle about -1.6 hours. Single 10-minute observations.

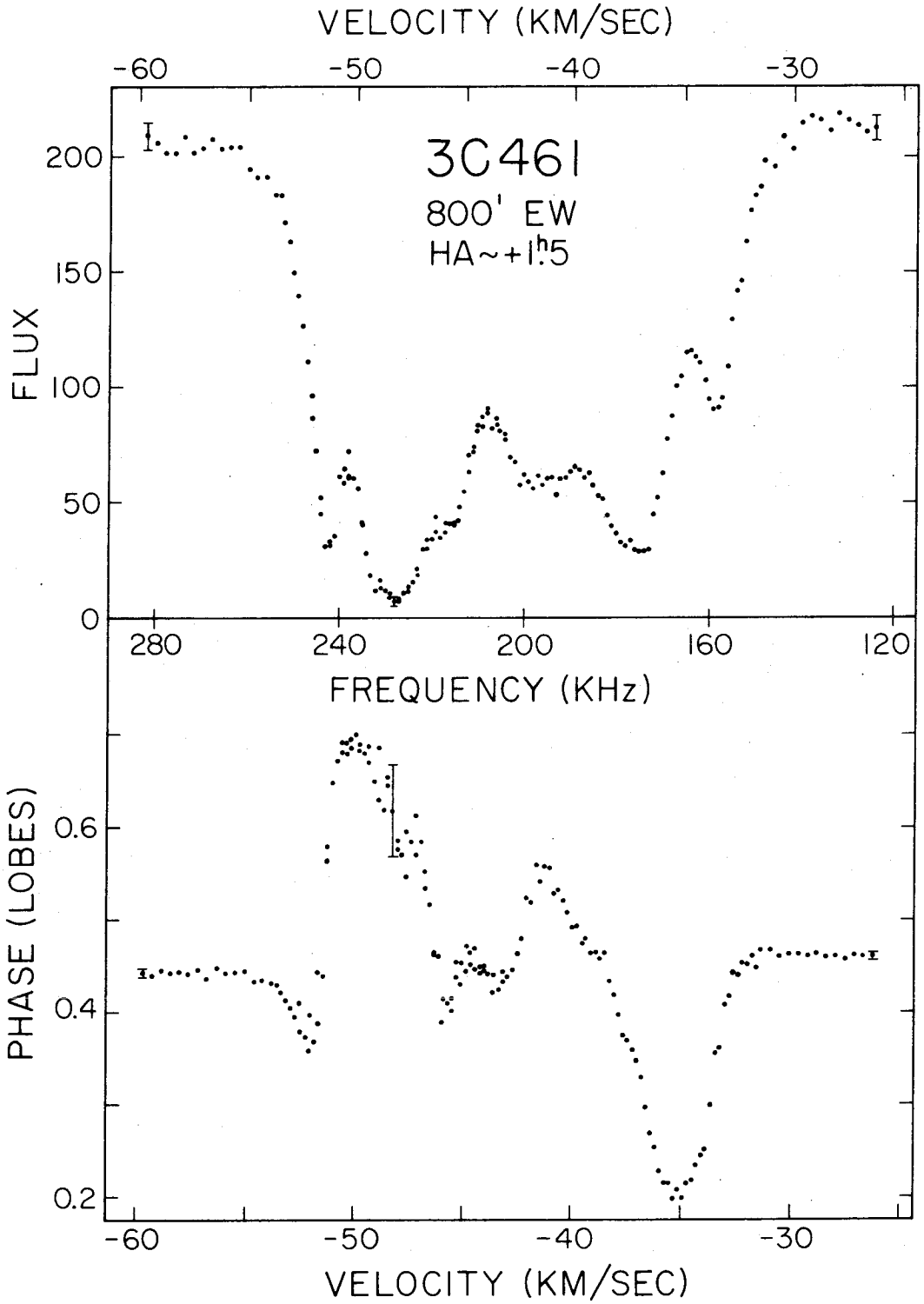

Figure 21b. 3C461: flux and phase spectra at 800 feet east-west at hour angle about +1.5 hours. Single 10-minute observations.

fact that the observations were not all made at quite the same hour angles. The baseline rotation causes a factor of two decrease in the visibility amplitude accompanied by a two-fold increase in the phase effects. This rotation changes an almost featureless double absorption line into a complex line containing at least six spectral features. Such violent behavior in the visibility spectra clearly establishes the presence of complicated spatial and frequency structure in the absorbing medium.

C. Results — Optical Depth Maps

Representative samples of the optical depth maps for 3C461 are given in Figures 22 and 23, which, together with a detailed description, are deferred to Appendix F. These maps reveal qualitatively different types of spatial structure in the two main absorption features. At frequencies less than about 212 KHz, the maps show a bewildering variety of peaks, ridges, and minima which vary, in general, fairly rapidly with frequency. There are three main spectral components in this range with peak optical depths around 155, 172, and 184 KHz. At frequencies greater than 212 KHz, the maps are dominated by one or two peaks of extremely high optical depth (τ) with very steep

gradients in τ across the source. In both frequency ranges many of the maxima appear unresolved.

In the low frequency range, the maximum τ is nearly always along the western edge. This predominance begins with a long wing at lower frequencies rising gradually to a peak $\tau \approx 4$ around 174 KHz. At higher frequencies, τ remains around 3 along the western edge while dropping elsewhere. Finally about 200 KHz, τ decreases along the western edge as well. A major peak at the eastern edge of the source is much narrower than that already mentioned. It rises rapidly to a maximum τ around 3 at 172 KHz and then abruptly appears to move northward while decreasing in strength. The spectral component about 155 KHz is found mostly north of the coordinate origin and is strongest off the source to the north. In addition to these major features, there are numerous other peaks, ridges, and minima.

The western edge is also a maximum in τ through part of the high frequency range. From a minimum near 1 at 212 KHz, τ along this edge increases to a peak of more than 7 at 222 KHz. After apparently moving southward this feature reaches another peak of τ greater than 8 at 227 KHz. At higher frequencies, τ drops rapidly along the

western edge, but a new feature appears. This feature, at an optical depth of around 6, moves steadily from the center of the source off the northeastern edge of the source as the frequency increases from 229 to 239 KHz. The only other major peak in the higher frequency range is seen over the southern parts of the source at frequencies less than 225 KHz.

D. Results — Spectra and Gaussian Fitting

The spectra for a number of interesting map points are given in Figures 24. Optical depth is plotted against frequency or velocity with the coordinates of the map points given in the upper left corners. (X and Y are in minutes of arc to the west and north, respectively.) The optical depths which are plotted as precisely 8.0 were not computable under the criteria outlined in the previous section. Since the noise is some constant brightness temperature across a map, the uncertainties in the highest optical depths are quite large. The effects of the DC offsets are easily seen in these figures (particularly Figure 24k).

Despite the wealth of small detail seen on the optical depth maps, the spectra are qualitatively very similar across the source. The optical depths rise from near 0.0

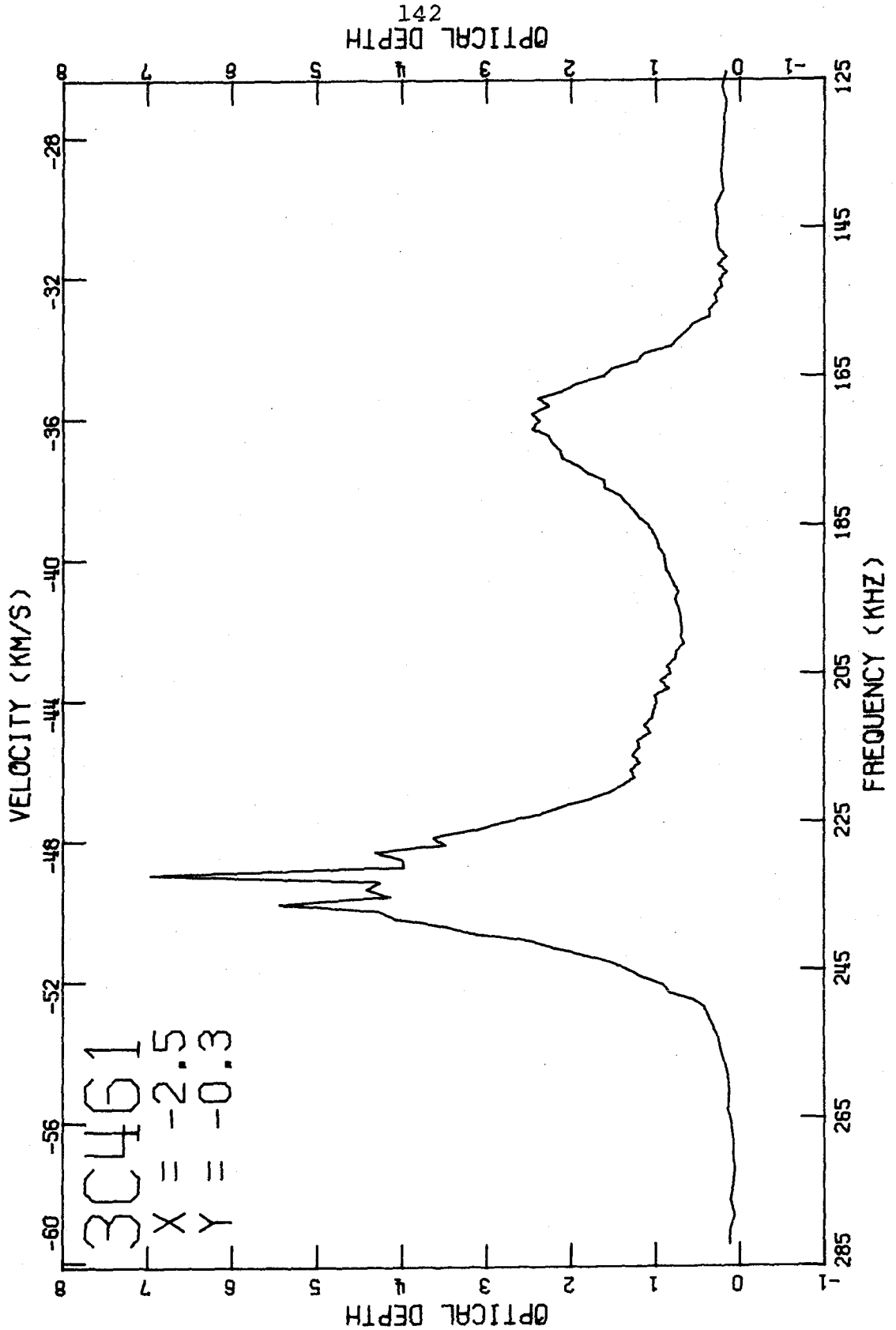

Figure 24a. 3C461: Spectrum at (-2.5, -0.3)

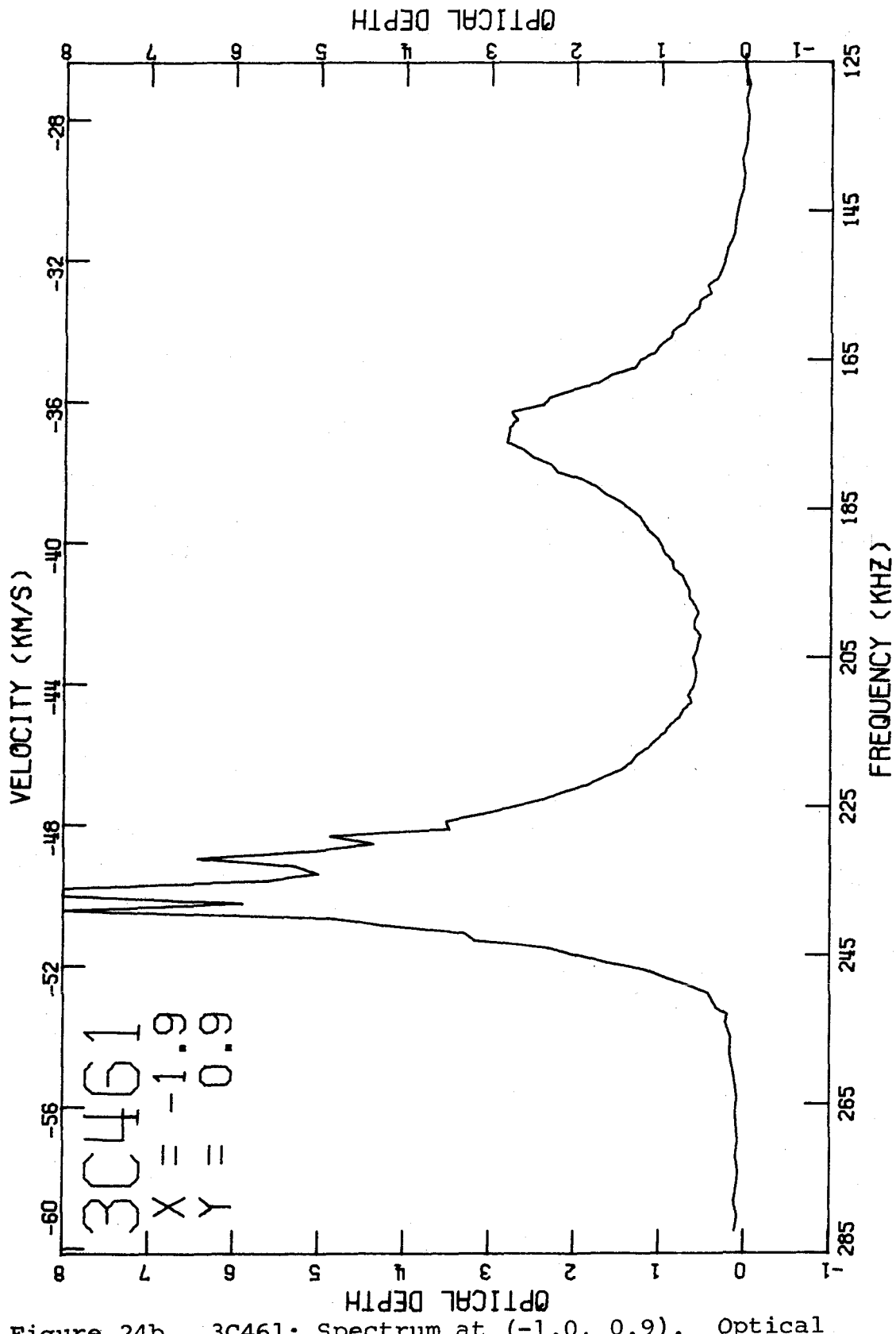

Figure 24b. 3C461: Spectrum at (-1.0, 0.9). Optical depths which are uncomputable are defined as 8.0.

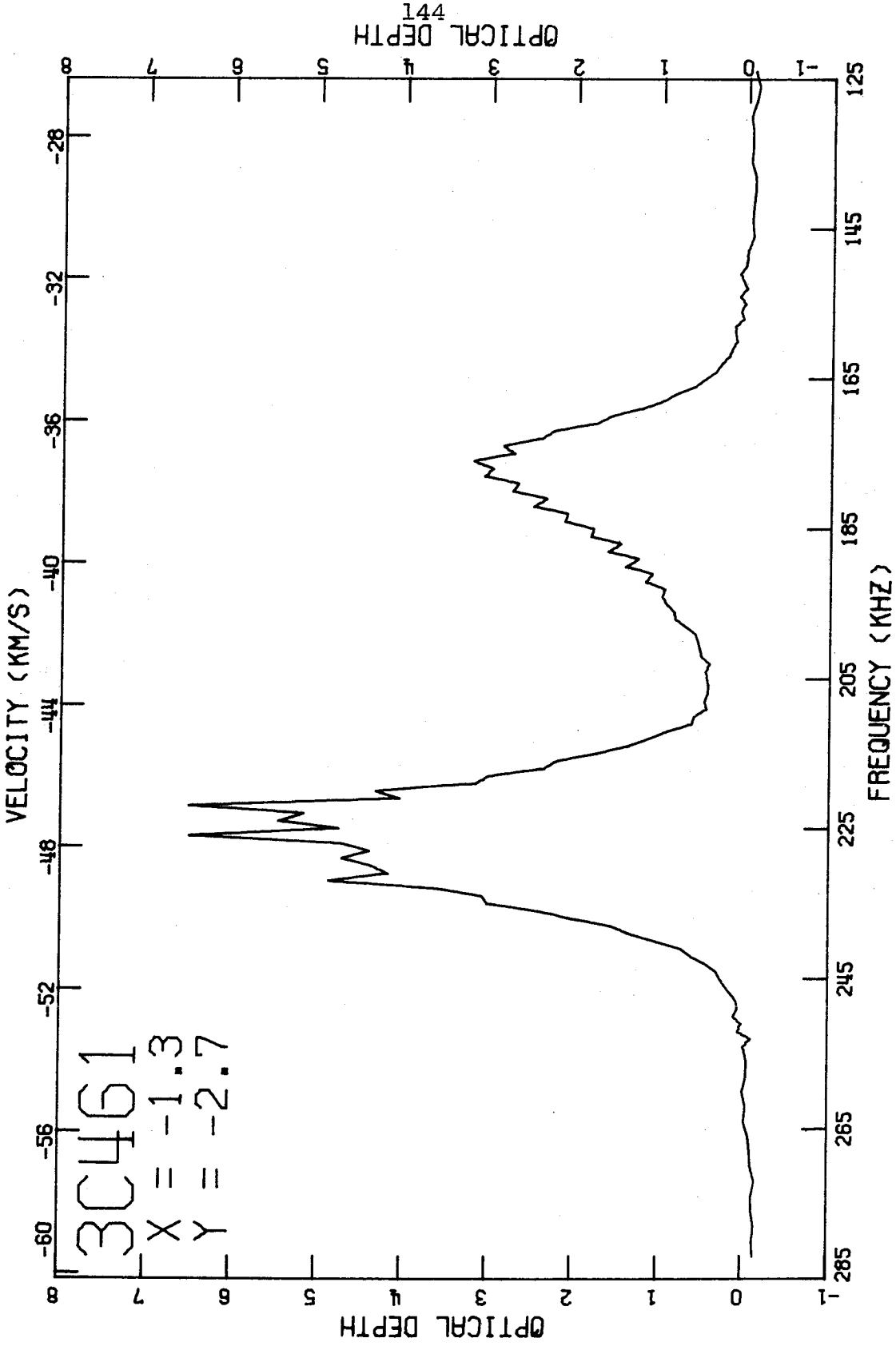

Figure 24c. 3C461: Spectrum at (-1.3, 2.7).

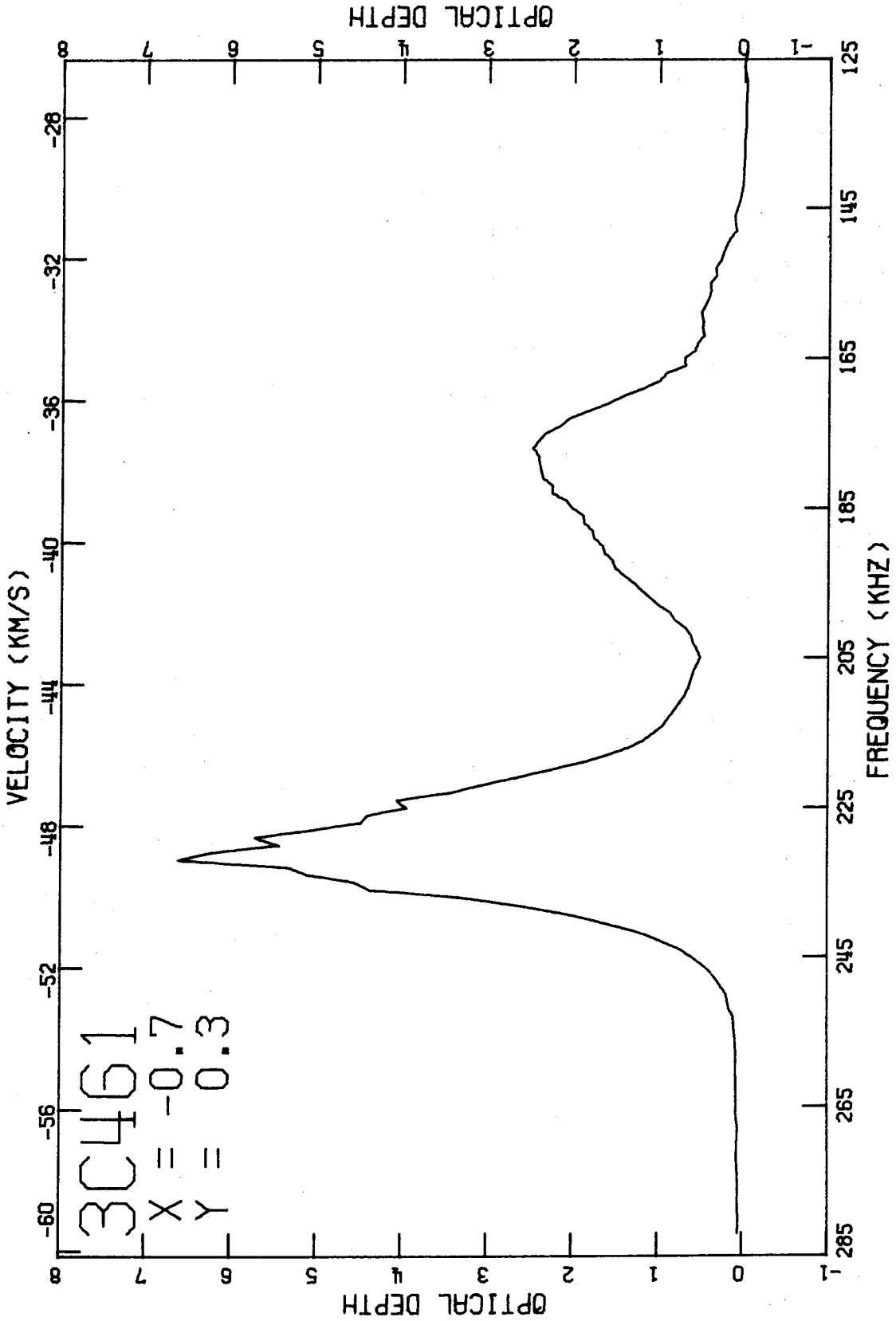

Figure 24d. 3C461: Spectrum at (-0.7, 0.3).

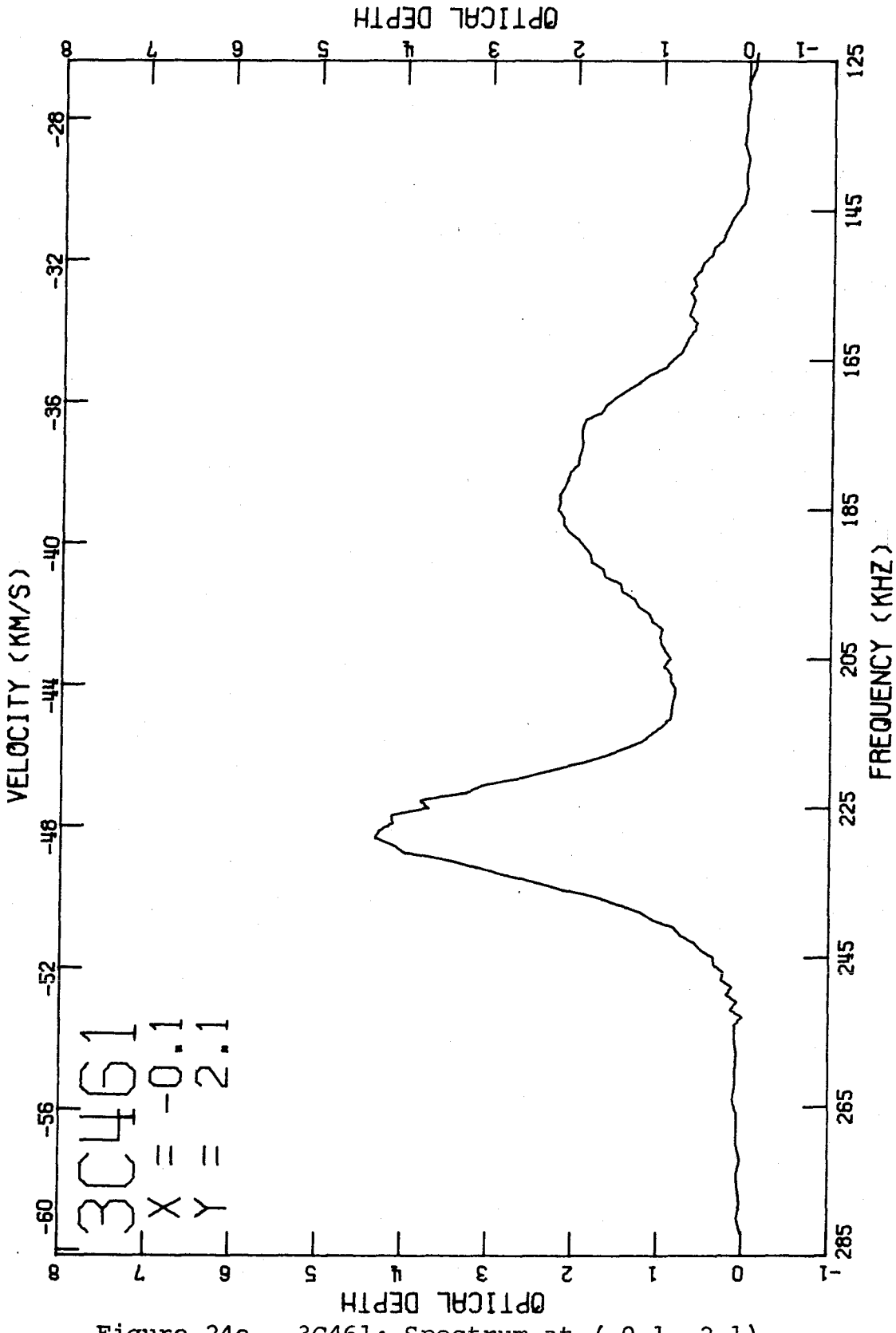

Figure 24e. 3C461: Spectrum at (-0.1, 2.1).

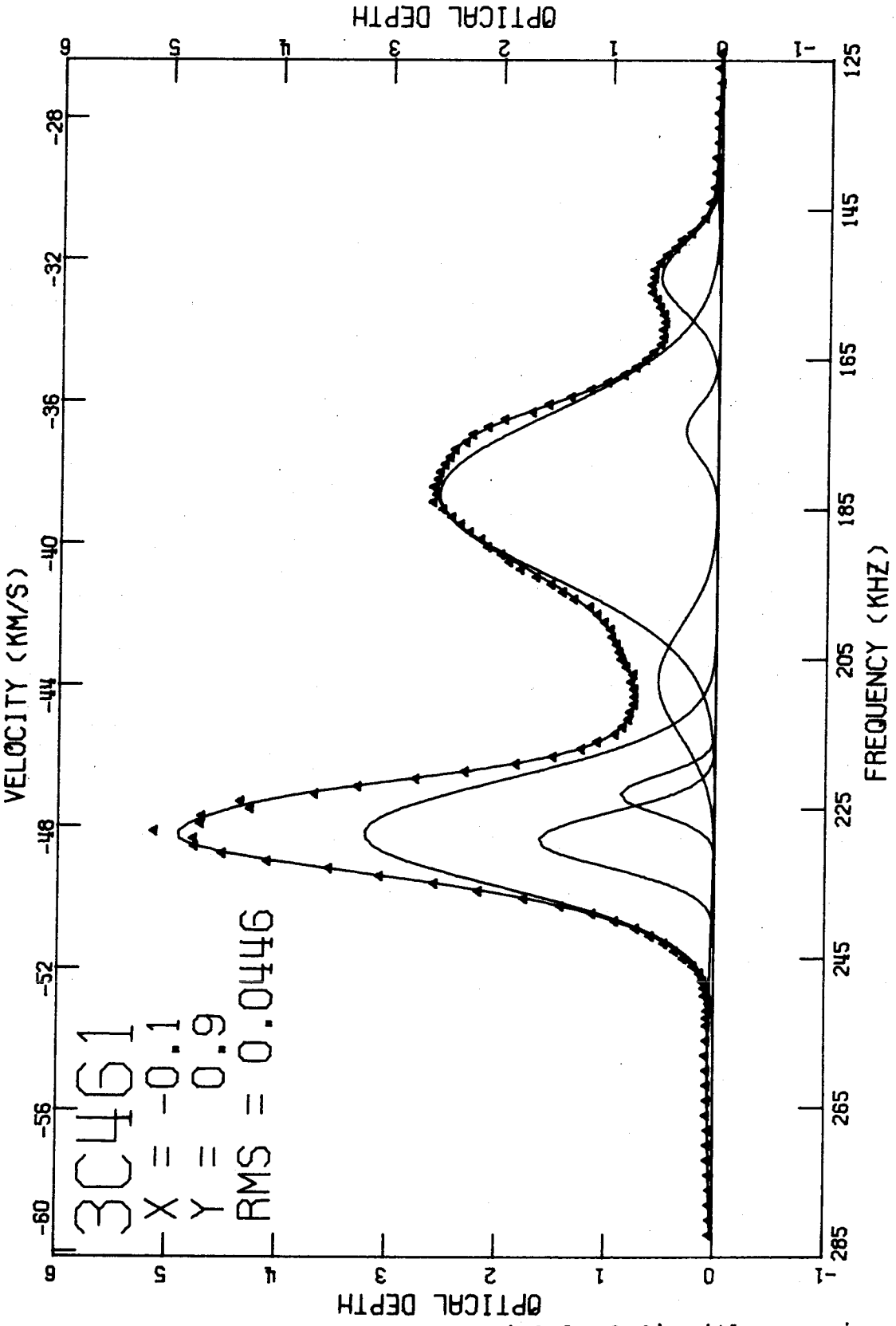

Figure 24f. 3C461: Spectrum at (-0.1, 0.9) with gaussian fit. Note systematic disagreement between data (points) and fit (line) around 200 KHz.

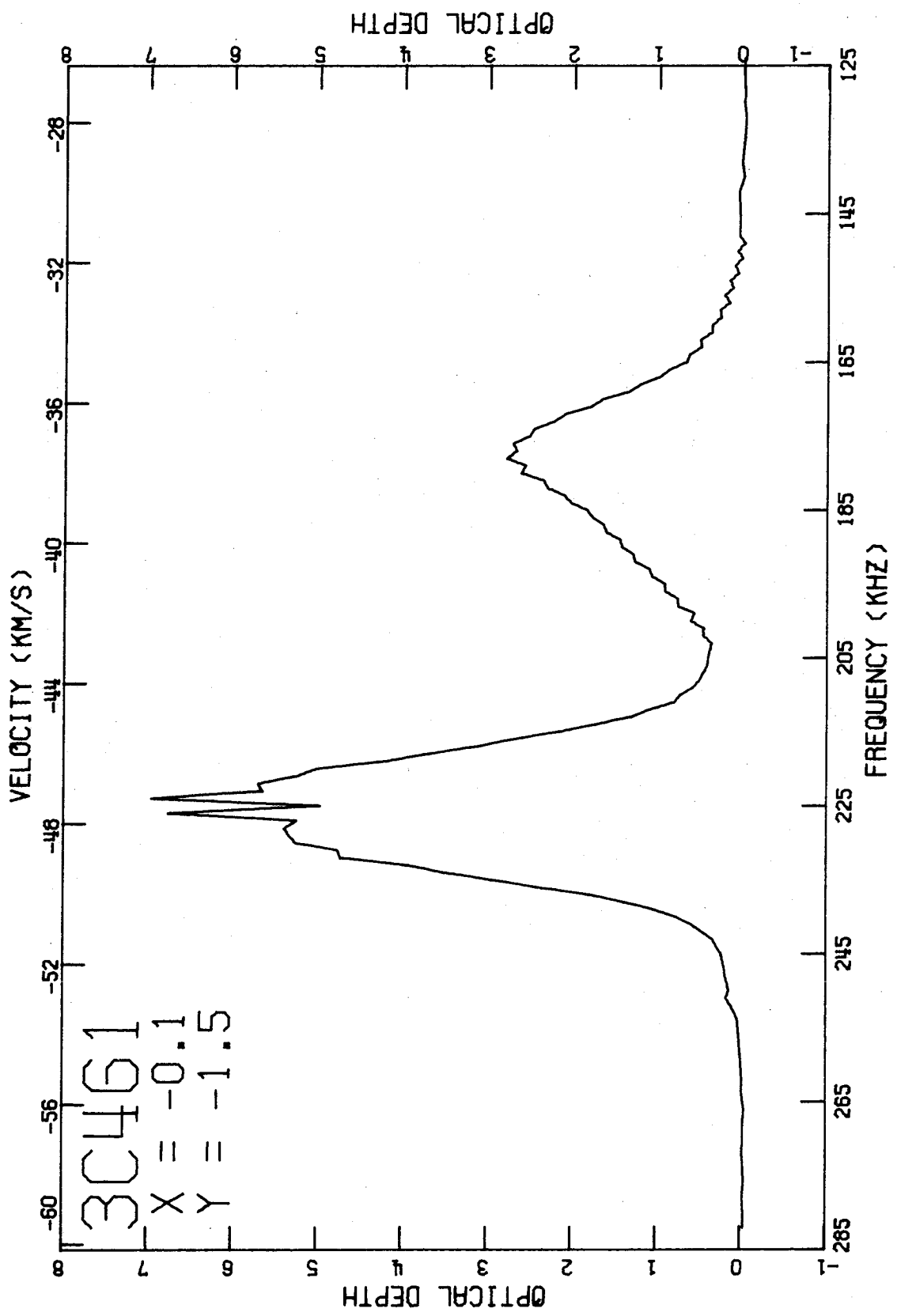

Figure 24g. 3C461: Spectrum at (-0.1, -1.5).

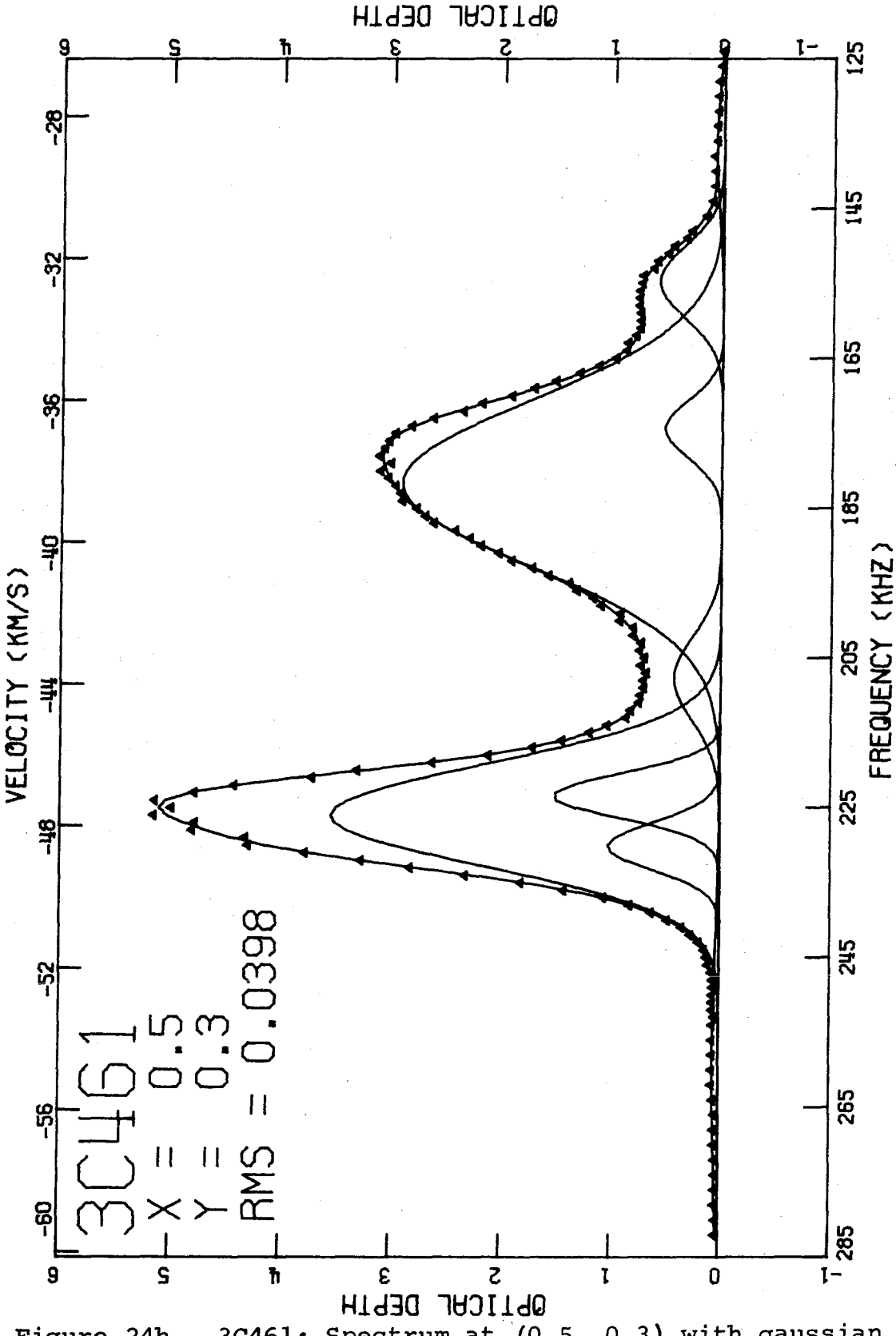

Figure 24h. 3C461: Spectrum at (0.5, 0.3) with gaussian fit.

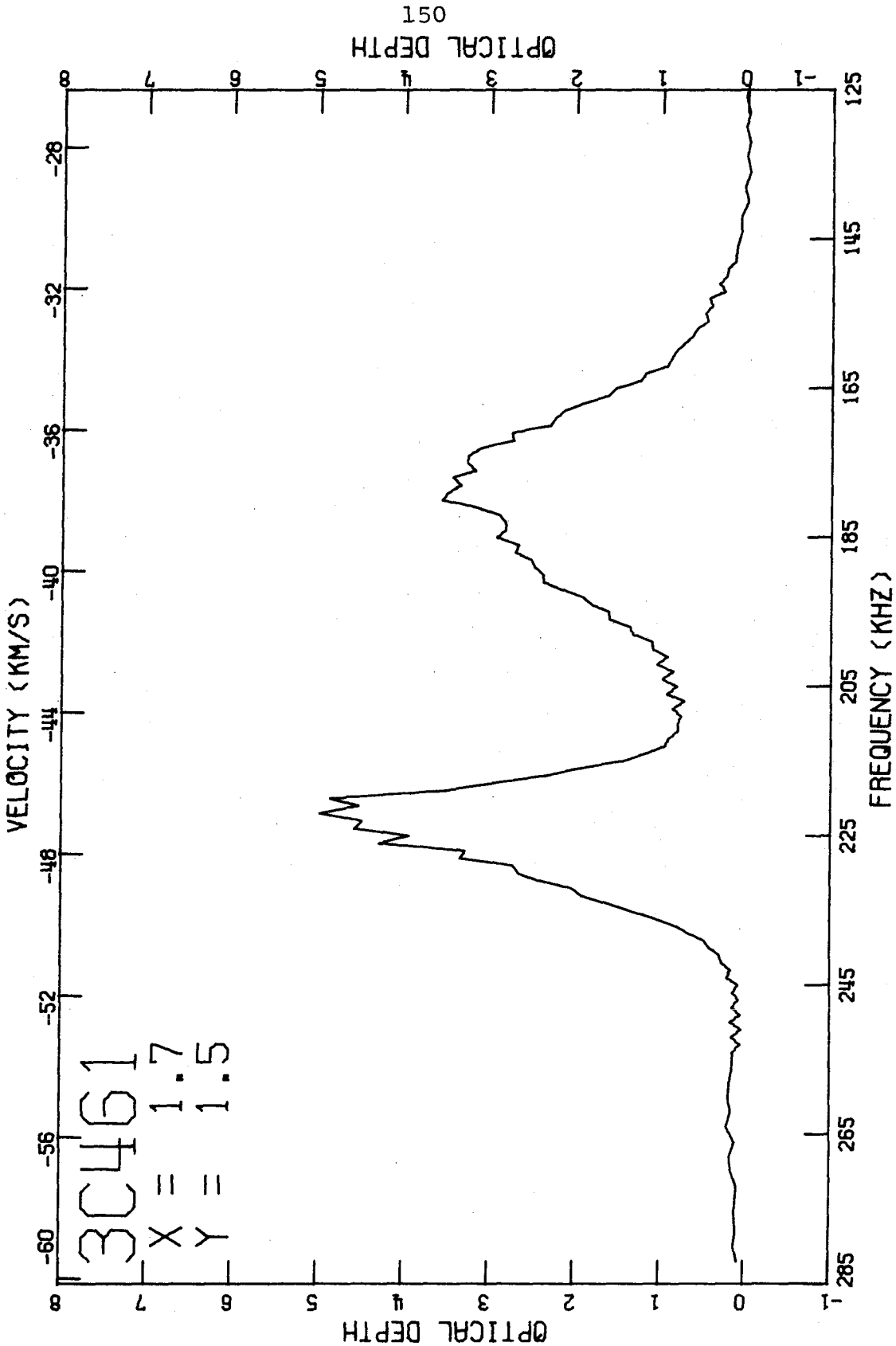

Figure 24i. 3C461: Spectrum at (1.7, 1.5).

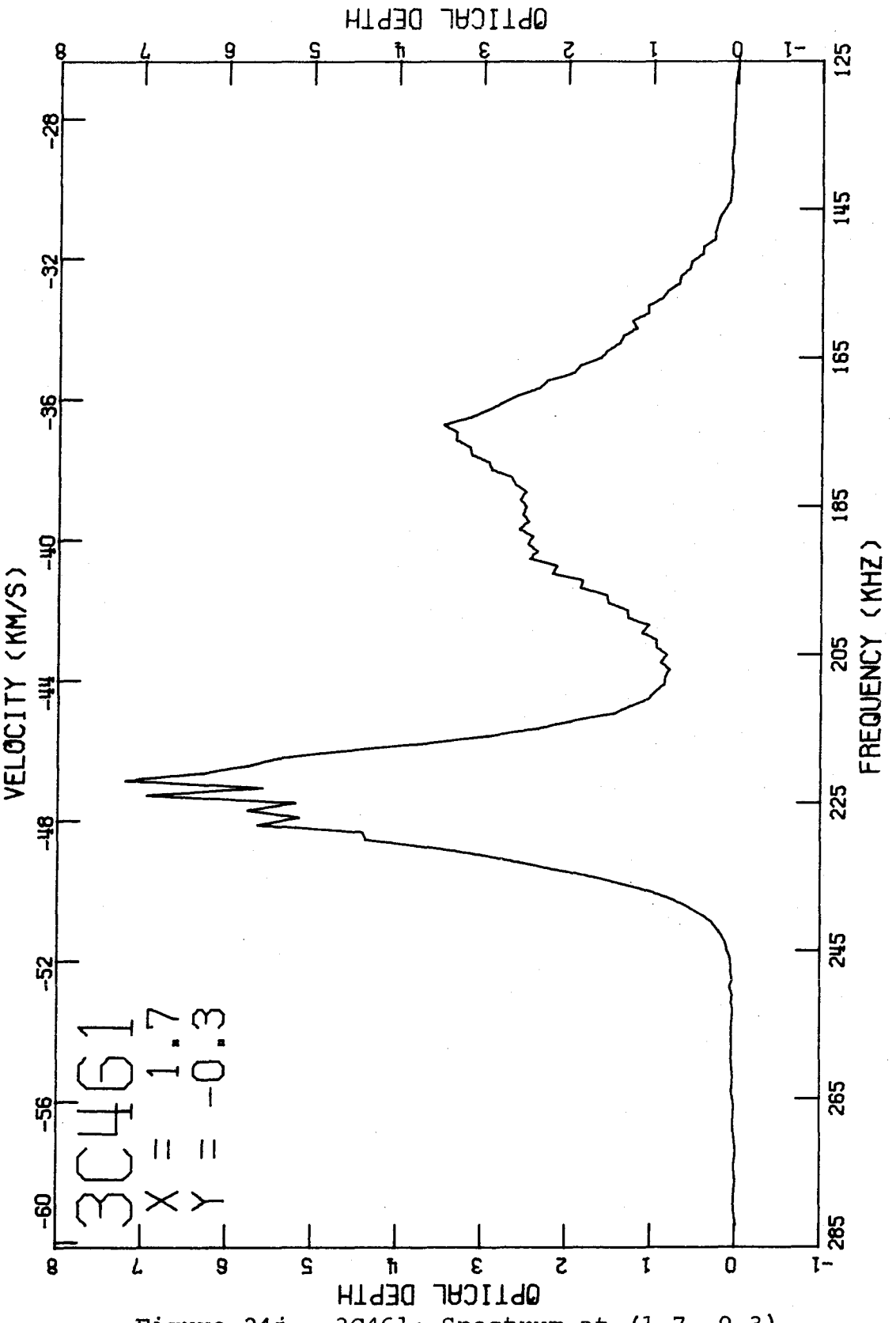

Figure 24j. 3C461: Spectrum at (1.7, 0.3).

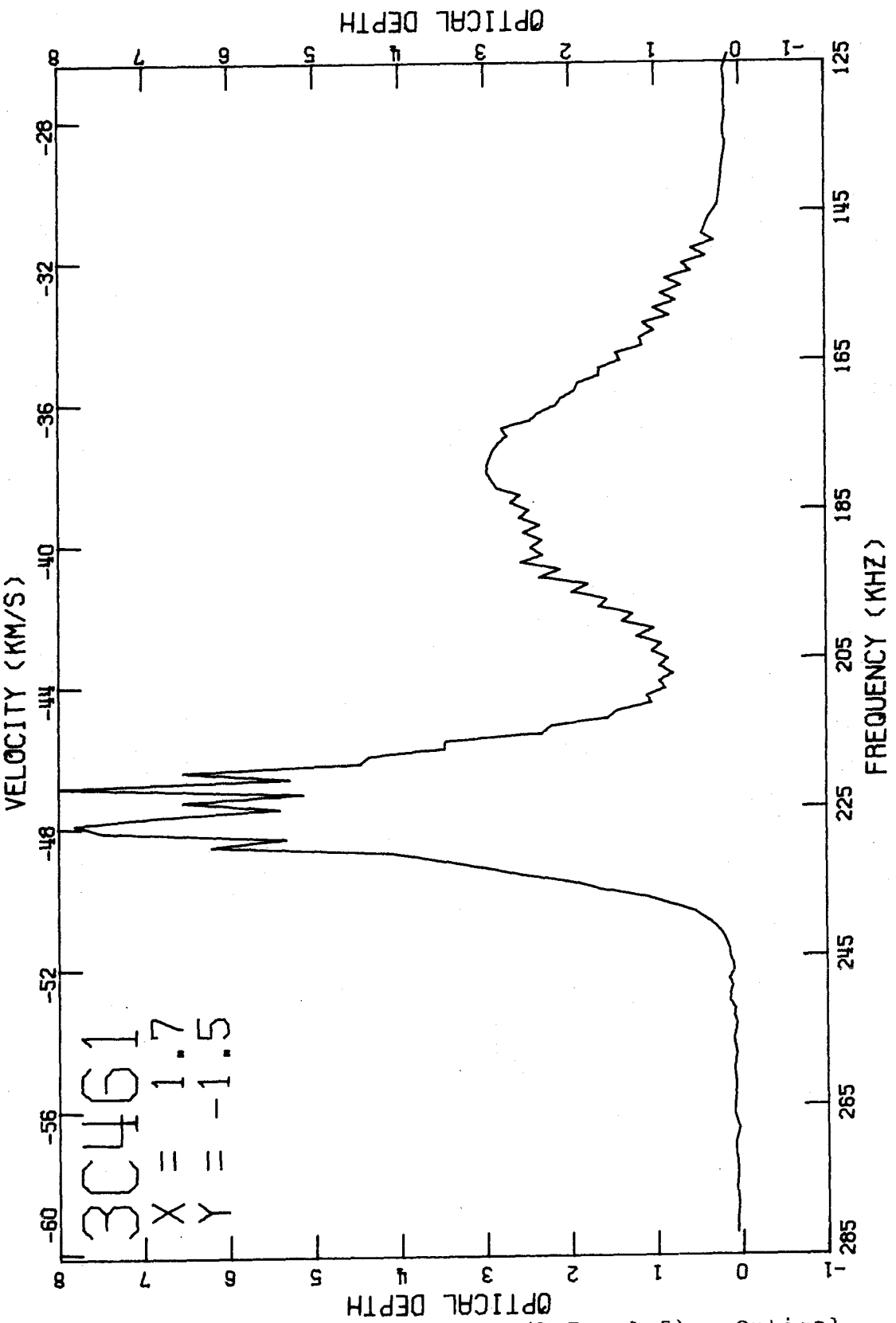

Figure 24k. 3C461: Spectrum at (1.7, -1.5). Optical depths which are uncomputable are defined as 8.0.

at 140 KHz to peaks between 2 and 4 at frequencies between 170 and 185 KHz. The optical depths drop to minima of 0.5 to 1.0 at 200 to 210 KHz and then rise steeply to peaks greater than 4 or 5 between 225 and 235 KHz. All optical depths are again near zero by 255 KHz. This similarity is principally the result of the laws governing galactic structure and, thus, does not imply that the hydrogen seen over one side of the source is physically related to the hydrogen seen over the other side of the source. In addition, these laws will be seen to imply that the hydrogen seen along any specific line of sight (at least in the lower frequency peak) is probably not all physcially associated. This situation is in sharp contrast with the isolated hydrogen cloud described in the previous chapter.

Two of the spectra (Figures 24f and h) are shown with gaussian fits. For the other sources, the gaussian fitting was done to the optical depth spectrum in the form

$$\tau(\nu) = \sum_i \tau_i e^{-(\nu-\nu_i)^2/\alpha\sigma_i^2} + c + s(\nu-\nu_0)$$

where the τ_i are the central optical depths, ν_i the central frequencies, and σ_i the full widths of the components and c and s are a constant and a slope (in MHz^{-1}), respectively. For Cassiopeia A, however, it is necessary to use the function

$$T(\nu) \equiv e^{-\tau(\nu)} = \exp\left[- c - s(\nu - \nu_0) - \sum_i \tau_i e^{-(\nu-\nu_i)^2/\alpha\sigma_i^2}\right]$$

in order to reduce the effects of the large uncertainties in τ present at high optical depths. Table VI lists four of the nine fits obtained for 3C461 with this functional form. Despite repeated and varied attempts, no convergent and reasonable solutions could be obtained outside a small region centered on (0.5, 0.3). The first two columns of Table VI give the component number and the type of the parameter determined. The remaining four pairs of columns are headed by the (X, Y) coordinates of the map points and list the values of the parameters determined and the uncertainties assigned to them. The RMS is given both in units of T and of τ. In order to fit the wings of the spectra, it was necessary to hold the poorly determined widths and central frequencies of components 1 and 9 fixed. It may be seen from the table that the fit to the high frequency peak is quite uncertain and that qualitatively different solutions are obtained at locations only about a half beamwidth apart. For most of the convergent solutions there is a systematic discrepancy between the data and the solution at frequencies about 192 KHz (see Figure 24f). However, almost all attempts to obtain a convergent

TABLE VI: 3C461 GAUSSIAN FIT RESULTS

COMPONENT	PARAMETER	p	σ(p)	p	σ(p)	p	σ(p)	p	σ(p)
	x	-0.1		-0.1		-0.5		+0.5	
	y	+0.9		+0.3		+0.3		-0.3	
	RMS(T)	0.0079		0.0070		0.0072		0.0129	
	RMS(τ)	0.0494		0.0530		0.0422		0.0797	
	CONST	-0.013	0.008	-0.035	0.007	-0.018	0.007	-0.003	0.013
	SLOPE	0.159	0.067	0.219	0.058	0.108	0.060	-0.232	0.105
1	τ	0.033	0.010	0.033	0.009	0.072	0.009	0.018	0.016
	f	137.0	—	137.0	—	137.0	—	137.0	—
	d	20.0	—	20.0	—	20.0	—	20.0	—
2	τ	0.544	0.009	0.531	0.011	0.588	0.012	0.458	0.022
	f	153.9	0.1	154.9	0.2	154.8	0.1	154.5	0.3
	d	11.1	0.2	12.3	0.3	11.4	0.3	12.1	0.6
3	τ	0.320	0.055	0.718	0.076	0.555	0.073	0.851	0.136
	f	174.6	0.6	175.4	0.4	174.4	0.5	175.6	0.6
	d	7.9	1.2	10.7	1.0	9.1	1.2	9.5	1.4
4	τ	2.549	0.047	2.532	0.063	2.889	0.062	2.607	0.109
	f	183.2	0.3	183.5	0.3	181.7	0.2	181.9	0.3
	d	25.6	0.5	25.6	0.4	26.0	0.4	27.4	0.8
5	τ	0.532	0.036	0.437	0.075	0.428	0.029	0.204	0.087
	f	208.0	0.5	210.6	1.5	207.8	0.5	206.3	1.9
	d	16.3	2.1	14.5	2.6	12.7	1.3	10.9	4.0
6	τ	1.256	0.481	1.310	0.934	1.661	0.451	1.594	1.631
	f	224.3	1.7	223.3	2.0	224.2	1.3	223.6	4.0
	d	6.8	2.0	6.5	2.1	7.5	1.7	7.2	4.0

Table VI (Continued)

3C461 GAUSSIAN FIT RESULTS

COMPONENT	PARAMETER	p	σ(p)	p	σ(p)	p	σ(p)	p	σ(p)
7	τ	3.439	0.171	3.504	0.290	3.645	0.253	3.749	1.261
	f	228.4	0.3	228.1	0.5	226.1	0.2	224.8	0.8
	d	16.6	0.3	17.0	0.4	16.0	0.3	16.5	1.4
8	τ	1.187	0.548	1.763	0.782	0.782	0.420	1.545	1.543
	f	230.7	1.8	229.8	2.1	231.3	1.6	230.3	3.4
	d	6.3	1.9	8.0	2.1	6.0	1.7	8.3	3.6
9	τ	0.054	0.009	0.060	0.008	0.057	0.008	0.068	0.014
	f	260.0	—	260.0	—	260.0	—	260.0	—
	d	40.0	—	40.0	—	40.0	—	40.0	—

solution with an extra component in this frequency range failed. I am forced to conclude that, with the present signal to noise and spatial resolution, these spectra cannot be expressed as the sum of a reasonable number of gaussians. I suspect that this is due to the blending of a considerable number of gaussians, although large-scale motions may also be important.

E. Results — Noise

Figures 25 display the results of substituting the uncertainties assigned to the data on Cassiopeia A into the equations derived in Chapter 3B. Figure 25a, which displays the constant term of the noise as a function of frequency, shows that the noise decreases sharply within the absorption line. The separate lines in the figure join the results for those frequencies affected by the same dirty beam. We note that for frequencies at which frequency shifts overlapped (doubling the number of data points), the noise is a factor of roughly $\sqrt{2}$ less than for adjacent frequencies of those frequency shifts for which there was no overlap. This is, of course, the expected behavior for noise. The same results are expressed in Figure 25b as a function of the flux observed at 200 feet east-west (Figure 20). For plotting in this

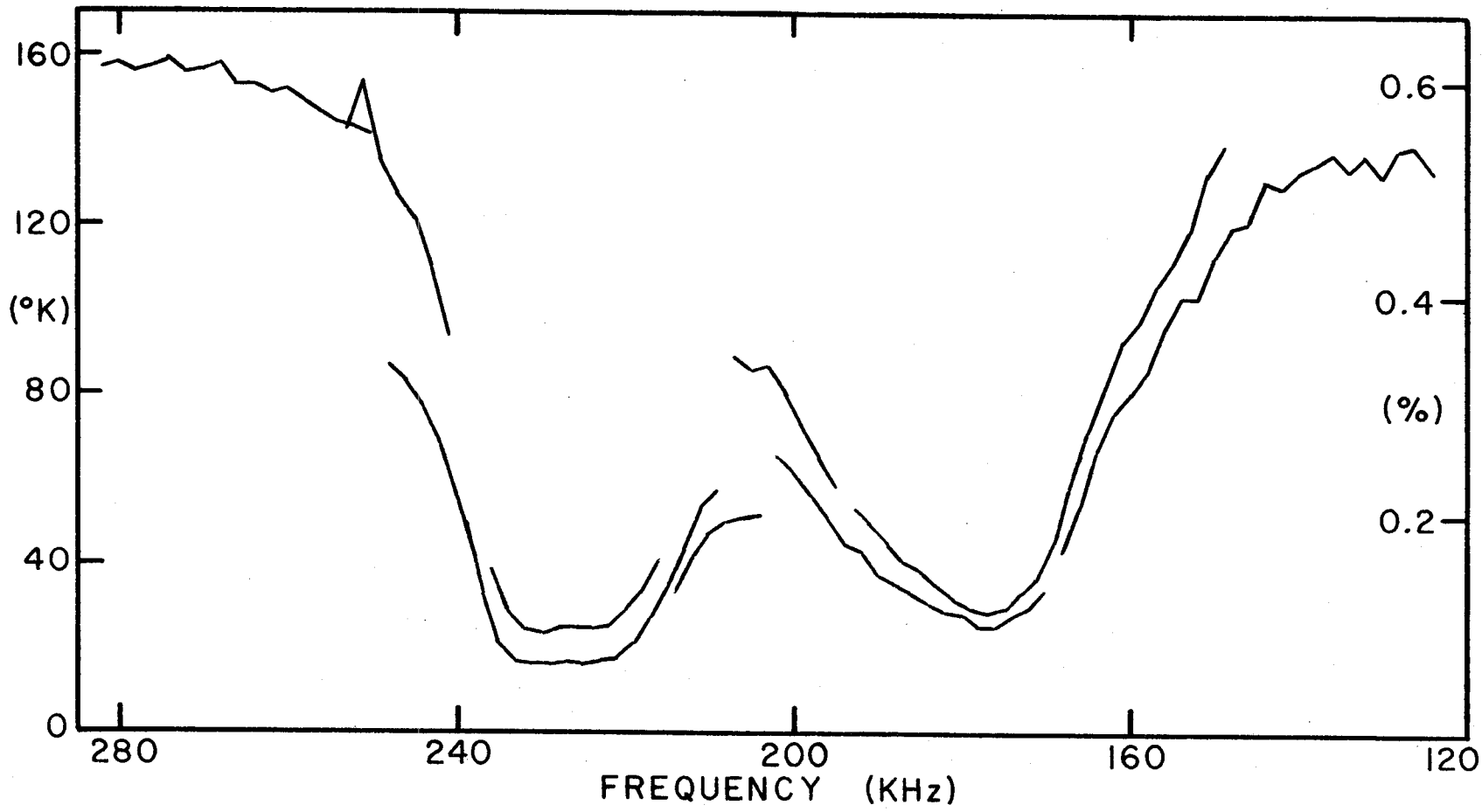

Figure 25a. 3C461: Spatially constant part of the noise as a function of frequency in °K (left hand scale) and in percent of the peak brightness on the continuum map (right hand scale). Each continuous line represents a different frequency shift or combination of frequency shifts.

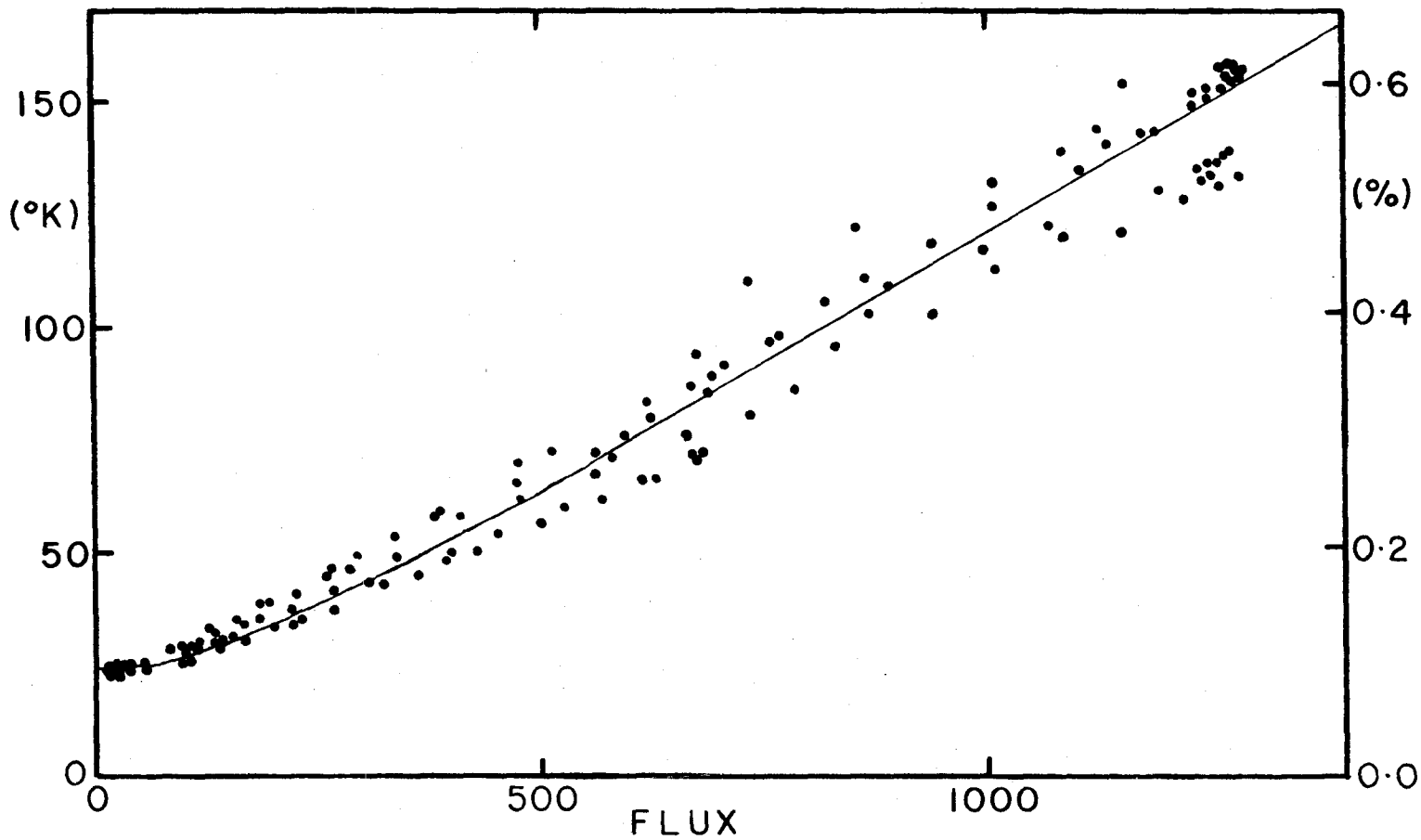

Figure 25b. 3C461: Spatially constant part of the noise as a function of flux at 200 feet east-west in °K (left hand scale) and in percent of the peak brightness on the continuum map (right hand scale). The noise plotted here for frequencies at which frequency shifts overlapped has been increased by a factor of $\sqrt{2}$.

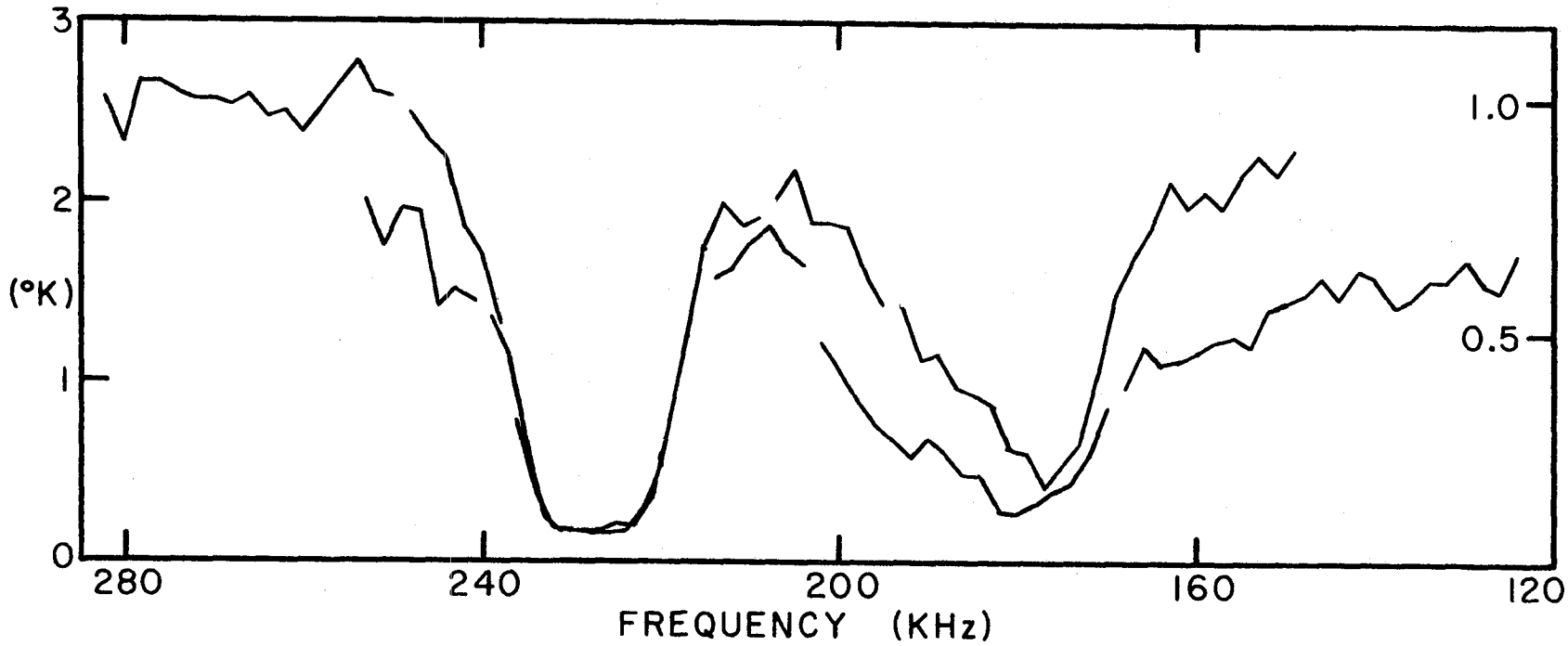

Figure 25c. 3C461: Upper limit to the spatially variable part of the noise as a function of frequency in °K (left hand scale) and relative to the peak brightness of the continuum map (times 10^4) (right hand scale). Each continuous line represents a different frequency shift or combination of frequency shifts.

figure, the noise at those frequencies at which frequency shifts overlapped has been increased by a factor of $\sqrt{2}$. It may be seen that the noise has the form

$$T_N = \sqrt{(T_0)^2 + (gF)^2}$$

with

$$T_0 \sim 24\ ^\circ K$$

$$g \sim 0.12\ ^\circ K/f.u.$$

This function is sketched in the figure. Such a result is not surprising since the flux error is known to follow a similar functional form. Figure 25c shows the computed upper limit to that part of the noise which may vary across the map. This upper limit decreases within the absorption line, but does not decrease for an increase in the number of observations. Thus, this variable part of the noise does not show the typical noise behavior. Fortunately, this part of the noise is again a very small fraction of the total noise and, hence, may be ignored.

The Monte Carlo tests give noise levels in good agreement with those presented here (see Table V, Chapter 3B). At 229 KHz the deconvolution process does not significantly alter the noise levels. For both dirty and clean maps the

noise levels show some correlation with source brightness, although there are also peaks in the noise off the source. At 199 KHz, the deconvolution process causes a sharp increase in the noise and the variability in the noise across the map. On the dirty maps there is no correlation between the noise and the source brightness, but on the clean maps there is a moderately good correlation. This change is not surprising since the errors in the deconvolution process should be larger where the source brightness is larger.

F. Interpretation

We need to determine the distance to the hydrogen observed using some model of the Galaxy to provide the distance-velocity relation. The most successful such model is the two-arm spiral shock ("TASS") model developed by Roberts (1969) as a non-linear extension of the density wave model of Lin and Shu (1964, 1966). The density wave model views the spiral pattern of the Galaxy as a quasi-stationary wave phenomenon superposed on the equilibrium disk given by Schmidt (1965). The spiral wave pattern in the gravitational potential and in the density is assumed to rotate about the center of the Galaxy at a constant angular speed while the stars and gas move in essentially

circular orbits through the wave pattern. Roberts (1969) points out that when the gas encounters the spiral pattern a shock front may develop. This shock front causes the gas to be compressed and to change the direction and magnitude of its velocity. Roberts (1972) has applied this model to the Perseus arm of the Galaxy over the longitude range 100° to 200°. Figure 26 shows his results for the direction of Cassiopeia A. As functions of distance from the Sun, the upper part of the figure gives the predicted average gas densities and the lower part gives the predicted line of sight velocities. The shock is seen to occur at a distance of 2.5 Kpc causing an enormous increase in density and an abrupt change in the line of sight velocity from -27 to - 53 km/sec (120 to 250 KHz). The gas, although heated by the shock, will cool very rapidly at these high densities. As a result, the hydrogen is expected to show considerable optical depth in a narrow region immediately following the shock. In other words, we should expect to see only a few hydrogen clouds at velocities around - 53 km/sec and a bit more, but these clouds should have very high optical depths. As the gas moves into the main arm region, the density drops considerably and the velocity becomes about - 42 km/sec (198 KHz). This velocity is

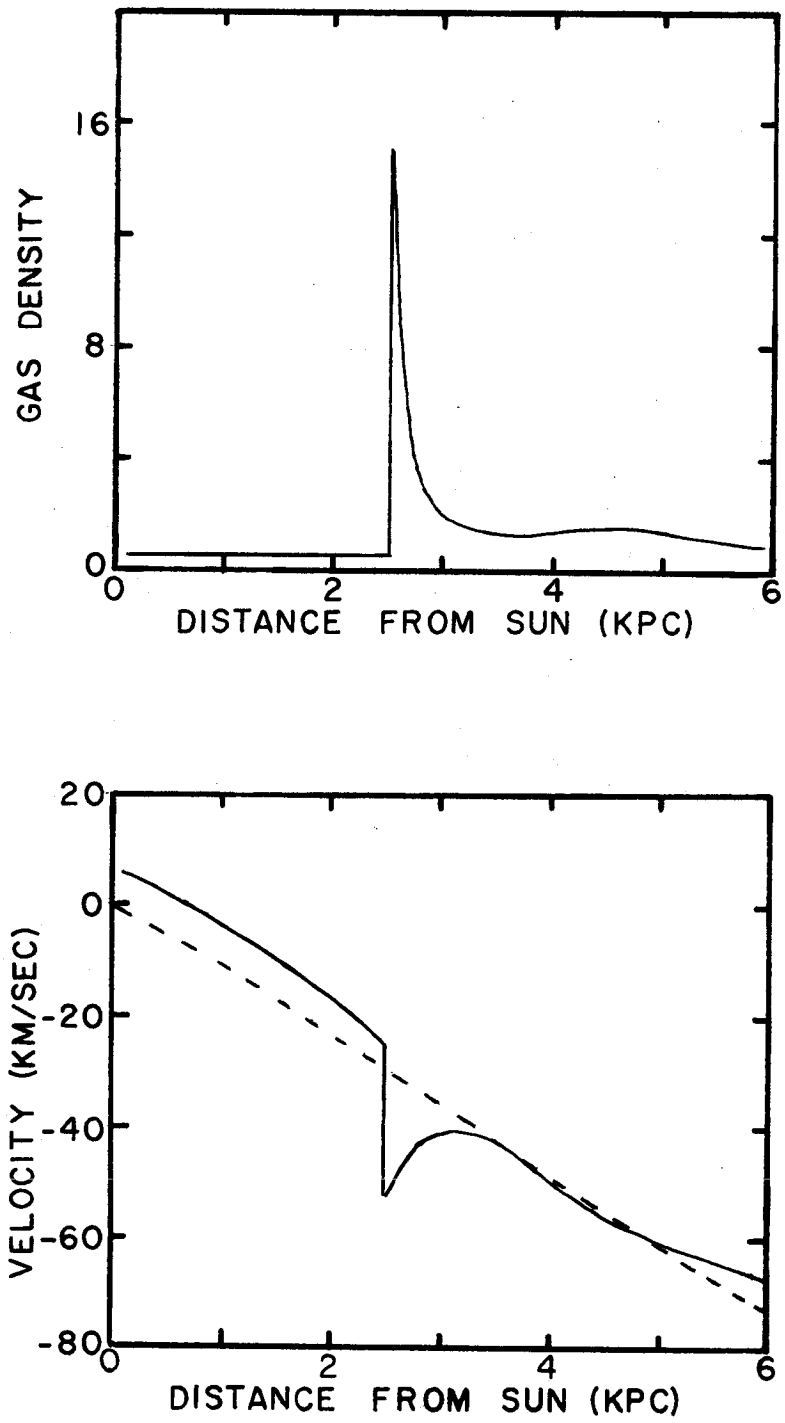

Figure 26. Predicted average gas density and line of sight velocity as functions of distance from the Sun in the TASS model for galactic longitudes 110°-115°. From Roberts (1972). Broken line from equilibrium model of Schmidt (1965).

essentially constant over a distance of 2/3 Kpc centered about 3.25 Kpc from the Sun. Because of the large distance range we should expect to see a large number of hydrogen clouds at velocities around - 42 km/sec and a bit lower. Each of these clouds should have a fairly low optical depth, but the total optical depth should be considerable.

The TASS model has been proposed only recently and is plagued with a number of serious dynamical difficulties as are all other spiral structure models. We must then examine the data themselves to see if the use of this model is justified. The qualitative predictions given above for this model do provide a good description of the optical depth maps. At frequencies above 212 KHz (- 45 km/sec) we find the optical depth maps (Figures 23, Appendix F) to be dominated by one or two peaks having extremely high optical depths. These maps often show contrasts in optical depth across the source exceeding factors of 6 or more. In contrast, at frequencies less than 212 KHz, the maps of Figures 22 reveal a wealth of detail including numerous peaks and ridges which vary fairly rapidly with frequency. However, the contrast in optical depth across these maps seldom exceeds a factor of two. The quantitative predictions of Roberts' model

do not fare quite so well. The predicted line frequencies are both 20 KHz higher than observed (Figure 20). Since the distance to the arm is to some extent a free parameter, we may alter the predicted line frequencies by altering the distance. Since small changes in the predicted velocity-distance relationship may be found using the equilibrium relationship (broken line in Figure 26), we find a correction of - 0.23 Kpc to be indicated. In the following discussion then we shall adopt distances of 2.25 Kpc to the high frequency feature and 3.0 $\pm$ 0.3 Kpc to the low frequency feature. This distance correction has the effect of removing the 155 KHz spectral feature from the "forbidden" velocity region of Roberts' model and suggests a small increase in the angle of inclination of the spiral arms in the model.[1]

The failure of the gaussian fitting procedure makes the deduction of temperatures rather difficult. The few spectra which were fit by sums of gaussians do not provide

---

1 Roberts (1972) used as parameters for his model an inclination of 12° and a spiral perturbation of the gravitational field of 7.5 percent of the axisymmetric field. He also computed a model using parameters of 8° and 5 percent, respectively. Such a model predicts spectral features at 226 and 190 KHz and, as a result, cannot be made to fit the observations through a simple alteration of the distance.

much assistance. If the apparent temperatures of the components found in the fitting are taken as physical temperatures, then we would obtain brightness temperatures in the hydrogen emission considerably in excess of the 50 °K observed (Clark 1965). The few components found to have reasonably narrow widths seem to be quite uncertain even as to their very existence. All we can say with certainty about the line widths is that as the resolution is improved the lines observed become narrower. This is, of course, just the natural consequence of observing with improved resolution a number of distinct features each having somewhat different location and central frequency.

We may look at some of the integral properties of the spectra, however. A map of the integral of the optical depths over frequencies less than 212 KHz is given in Figure 27a while a similar map over frequencies greater than 211 KHz is given in Figure 27b. In the construction of these maps, all uncomputable optical depths were assumed equal to 8.0. The x and y coordinates are given along the tops and left hand sides, respectively, of these maps. It may be seen that the total optical depths range from 57.6 to 130.2 KHz for the low frequency feature and from 73.3 to 125.0 KHz for the high frequency feature.

3C461 LOW FREQUENCY SIDE

	-2.5	-1.9	-1.3	-0.7	-0.1	0.5	1.1	1.7	2.3
2.7				82.3	92.3	93.9			
2.1			73.2	77.4	82.1	86.2	95.8		
1.5		70.6	74.2	76.7	77.5	86.9	94.5	107.5	
0.9	82.3	72.7	75.0	80.5	85.4	94.7	96.7	107.4	122.5
0.3	83.3	78.0	71.3	73.3	86.7	98.1	103.8	115.2	122.9
-0.3	75.4	73.4	69.4	68.0	82.3	93.3	102.9	113.5	121.5
-0.9	59.5	61.3	63.8	63.8	80.8	91.8	97.8	111.5	124.5
-1.5	57.6	60.4	61.6	60.3	68.3	80.0	91.4	112.5	130.2
-2.1		57.9	62.0	66.9	66.5	77.1	85.6	101.6	
-2.7			64.7	71.0	70.0	82.6	89.1		

Figure 27a. 3C461: Integral of optical depth over frequency for 124 KHz $\leq \nu <$ 212 KHz.

3C461 HIGH FREQUENCY SIDE

	-2.5	-1.9	-1.3	-0.7	-0.1	0.5	1.1	1.7	2.3
2.7				83.8	87.0	83.1			
2.1			93.6	83.6	78.6	76.6	76.4		
1.5		114.2	99.7	84.4	75.6	76.6	75.7	76.8	
0.9	120.4	125.0	111.9	94.3	83.5	78.6	73.3	77.7	89.0
0.3	119.0	123.0	120.9	104.7	92.0	82.5	82.2	92.8	104.9
-0.3	101.7	106.2	113.4	108.7	100.5	91.0	93.4	104.6	115.9
-0.9	82.7	90.9	102.7	109.3	112.4	105.3	103.1	113.5	123.8
-1.5	74.9	84.8	96.1	106.4	111.0	105.4	105.8	117.2	122.6
-2.1		80.7	92.0	106.9	108.8	101.7	96.7	103.0	
-2.7			97.3	111.0	107.8	102.1	93.7		

Figure 27b. 3C461: Integral of optical depth over frequency for 211 KHz $< \nu \leq$ 282 KHz. Optical depths which are not computable are defined as 8.0.

Table VII gives a sample of the types of numbers which may be computed from the total optical depths. The first two columns give the parameter computed and the units. The remaining six columns give the values of the parameters for the minimum, average, and maximum total optical depths on each of the maps in Figures 27. For this table a "cell" is defined as the 0!6 x 0!6 area surrounding the map point at which the total optical depth is computed. For the low frequency feature we assume a temperature of 70 °K as for Cygnus A. In the post-shock region a lower temperature is to be expected (Shu, et al 1972), so we assume a temperature of 50 °K. The densities given in Table VII as n(Galactic) are computed on the assumption that the hydrogen is uniformly distributed over the full distance which the galactic rotation model would suggest. This distance is about 650 pc for the low frequency feature and 200 pc for the high frequency feature. However, the optical depth maps rule out any assumption that the density is uniform over galactic scale sizes. Instead, these maps suggest that the scale sizes of individual clouds are more like a beamwidth i.e. 0.9 pc for the high frequency feature and 1.2 pc for the low frequency feature. The densities n(Beam) in Table VII are computed on this assumption. In

TABLE VII: 3C461 SAMPLE DENSITY AND MASS COMPUTATION

PARAMETER	UNITS	ν < 212 KHz			ν > 212 KHz		
		MIN	AV	MAX	MIN	AV	MAX
Total optical depth	KHz	57.6	84.6	130.2	73.3	97.9	125.0
Column density	$pc/cm^3/^\circ K$	7.45	10.7	16.4	9.23	12.3	15.7
Mass per cell	$M_\odot/^\circ K$	.049	.072	.111	.035	.047	.060
Column density	pc/cm^3	520	750	1150	460	620	780
Mass per cell	$M_\odot$	3.4	5.0	7.8	1.8	2.4	3.0
density n(Galaxy)	cm^{-3}	0.8	1.2	1.8	2.3	3.2	3.9
density n(Beam)	cm^{-3}	450	650	990	530	710	900
total mass*	$M_\odot$		360			170	

* As explained in Chapter 4, this "total mass" observed may be severely affected by the beam pattern.

fact, since the total optical depths are integrals over a number of distinct features, we should divide n(Beam) by the number of clouds along the line of sight to obtain an average density. This number is probably fairly large, say 10 or 20, for the low frequency feature, but is probably only 2 or 3 for the high frequency feature. Thus, clouds within the arm would seem to have densities between 10 and 100 cm^{-3}, but clouds in the post-shock region can have densities more like 200 to 500 cm^{-3}.

It would be impossible to make a detailed model to describe the complex spatial and spectral structure found in the data. Indeed, there is no reason to suppose that the many features observed are even physically associated. However, there is one feature for which a model can be discussed. This feature is seen to move steadily with frequency from (- 0.7, - 0.3) at 229 KHz to (- 1.3, 0.5) at 235 KHz and beyond. (See Figures 23e-h in Appendix F.) At the assumed distance (2.25 Kpc) this motion is 0.5 pc/km/sec along a position angle of 217°. A rotating and perhaps flattened cloud of hydrogen is certainly suggested. Before we allow ourselves to put too much weight on this model we should note that the cloud is suspiciously aligned along a minimum in the brightness temperature of the background

source and that the total measurable motion of the peak is somewhat less than a beamwidth. However, it is clear from the maps that the motion does continue over longer distances.

If we adopt this model, we note immediately that the maximum rotation period of the cloud is about 3 million years which is roughly a tenth the time the cloud will spend in the region just behind the density wave shock (Roberts 1969). If we assume the cloud to have an optical depth of 6.4, a depth of 0.9 pc, and apparent and real temperatures of 50 °K, we find the density to be 350 cm^{-3}. Acceptable ranges of the various parameters suggest that the density is somewhere between 90 and 700 cm^{-3}. To obtain an estimate of the minimum density necessary to maintain such a rotation, we equate the gravitational force with the centrifugal force. Assuming a spherical cloud of uniform density, we find that the minimum density required is equivalent to 9500 hydrogen atoms per cm^3 (independent of radius). With a radius of one parsec, the cloud has a mass of at least 900 solar masses. Since we have ignored the pressure force supporting the cloud and have assumed the rotation axis to be perpendicular to the

line of sight, the density and mass given here must be regarded as lower limits.

There is a considerable difference between the density required for stability (10^4 cm^{-3}) and that deduced from the observations (350 cm^{-3}). Since there is a large amount of reddening in the direction of Cassiopeia A (Van den Bergh 1971), we may surmise that this "missing mass" is accounted for by dust and molecular hydrogen. However, such a large dust cloud would certainly obscure the filament of the supernova remnant seen on the 200" plates at the north-eastern part of the source (Van den Bergh and Dodd 1970). The most probable conclusion we may draw is that the cloud, having only recently condensed after passing through the density wave shock, is simply rotationally unstable. Two other possibilities are that the missing mass is more concentrated than the hydrogen toward the center of the cloud or that the model is in error due either to noise or lack of resolution.

CHAPTER 6

THE CRAB NEBULA (3C144)

A. Results — Beam Patterns and Continuum Maps

The distribution of data points obtained for one of the continuum frequency shifts of the Crab Nebula is indicated in Figure 28. The relatively low declination of this source causes large gaps between the tracks from the east-west and the north-south baselines. Diagonal baselines would have greatly improved the sampling of the (u, v) plane for this source. But, since such baselines were of little use for 3C461, they were not used for any source. On the days that 3C461 was observed, the Crab Nebula could only be observed for about five hours resulting in a fairly low density of data along parts of the tracks. Since the source did not become a principal source until the 800-foot east-west spacing, there are only a few data points at the 200 and 400-foot east-west spacings and the calibration of those data points is not as good as the rest.

The results of the test of the inversion procedure over a large map area are presented in Figures 29. The dirty beam (Figure 29a) is quite complicated with sidelobes exceeding 15 percent within 2 minutes of arc of the main beam. The near-in sidelobes arise from the many

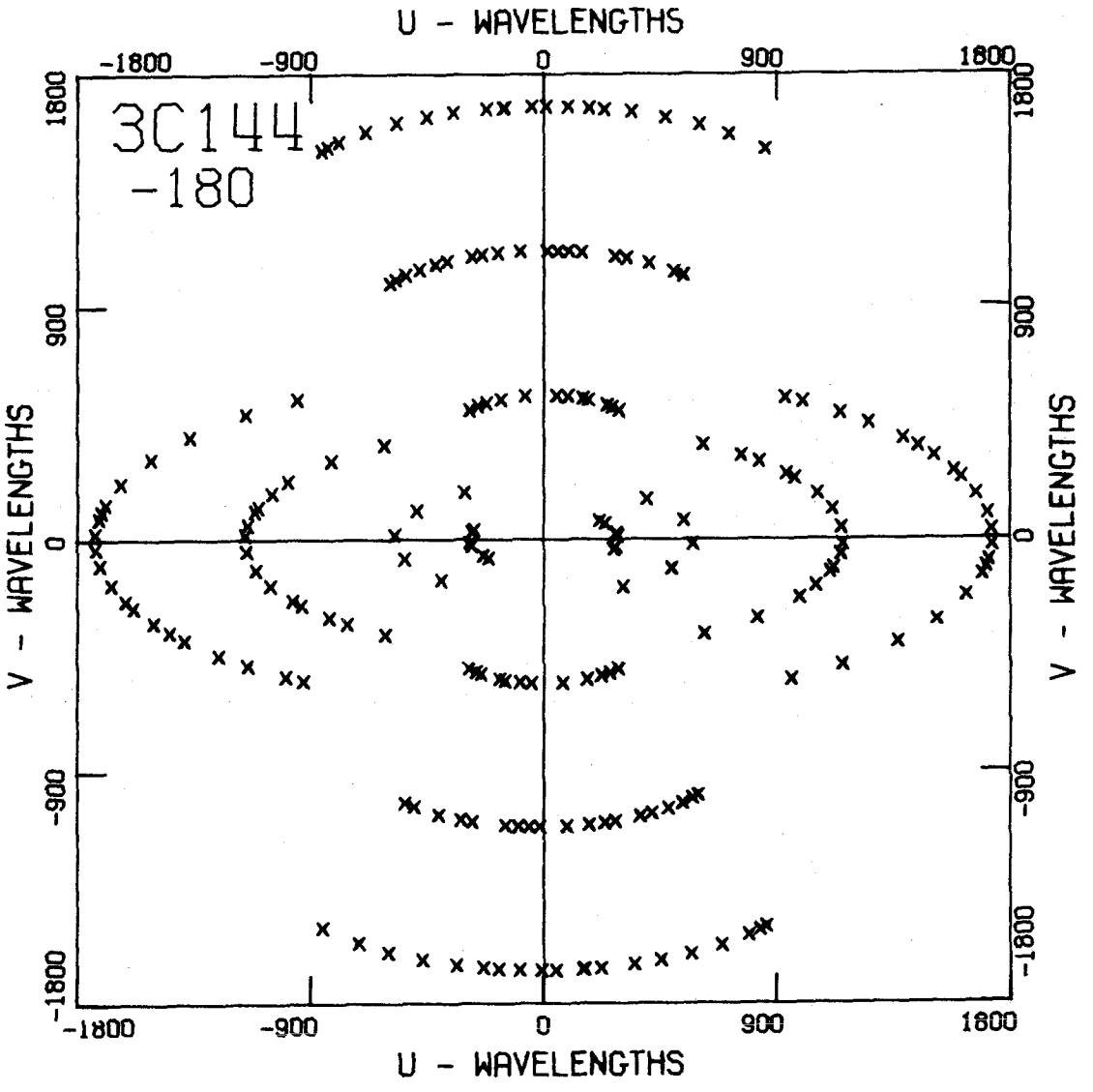

Figure 28. 3C144, continuum frequency shift: distribution of data points.

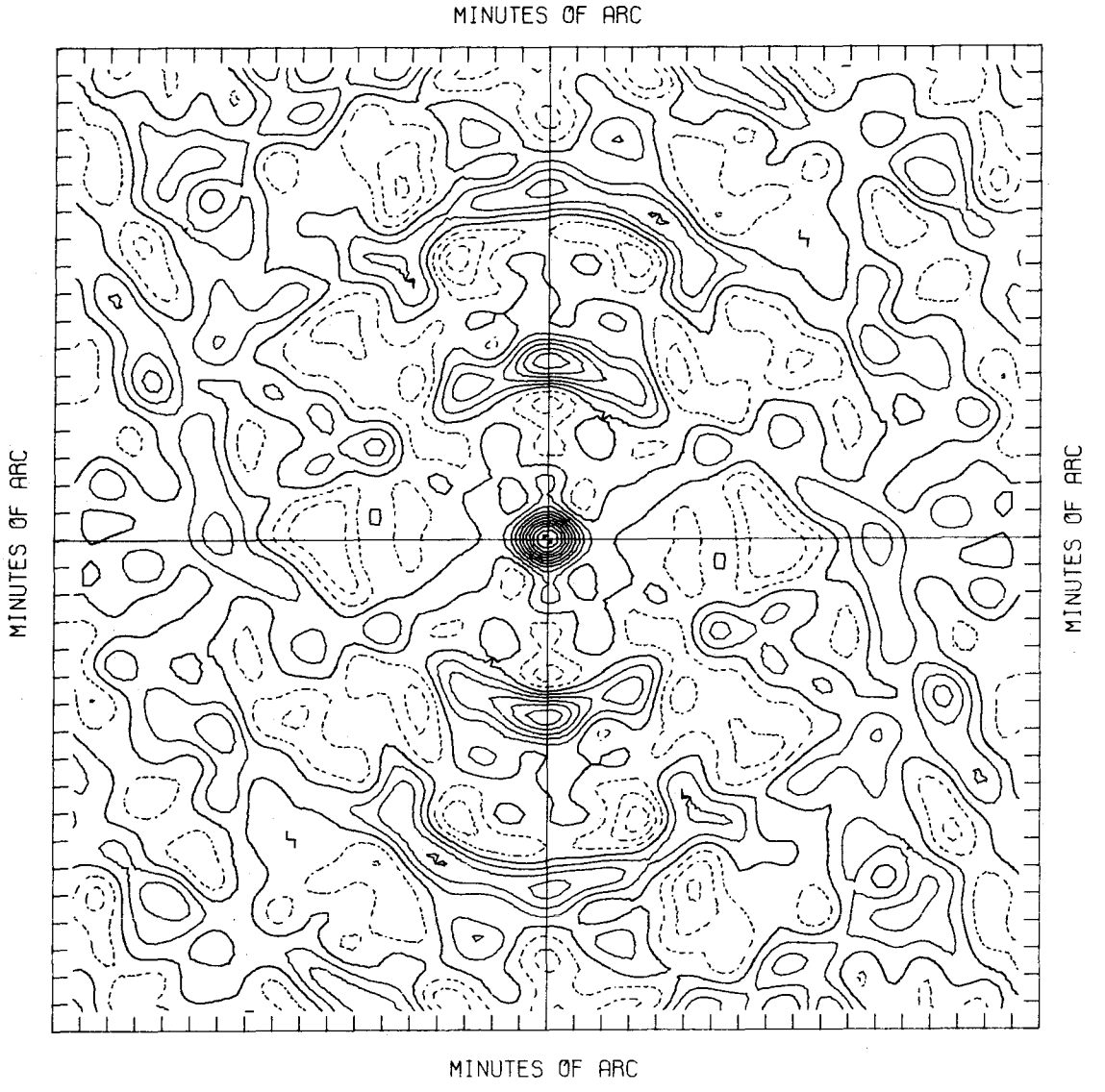

Figure 29a. 3C144, continuum frequency shift: dirty beam pattern, contour interval = 10%, large area.

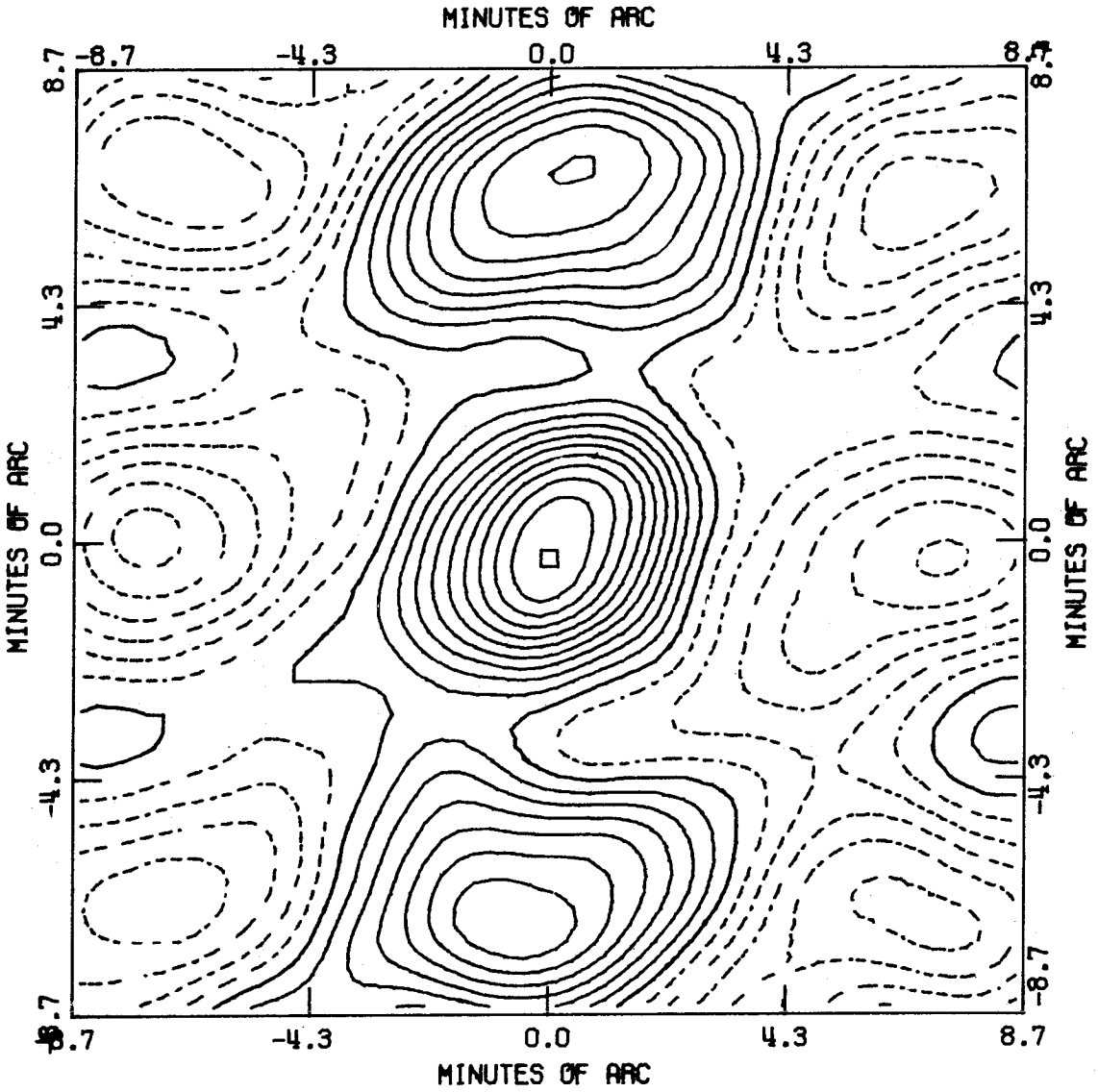

Figure 29b. 3C144, continuum frequency shift: dirty map, contour interval = 10%, large area.

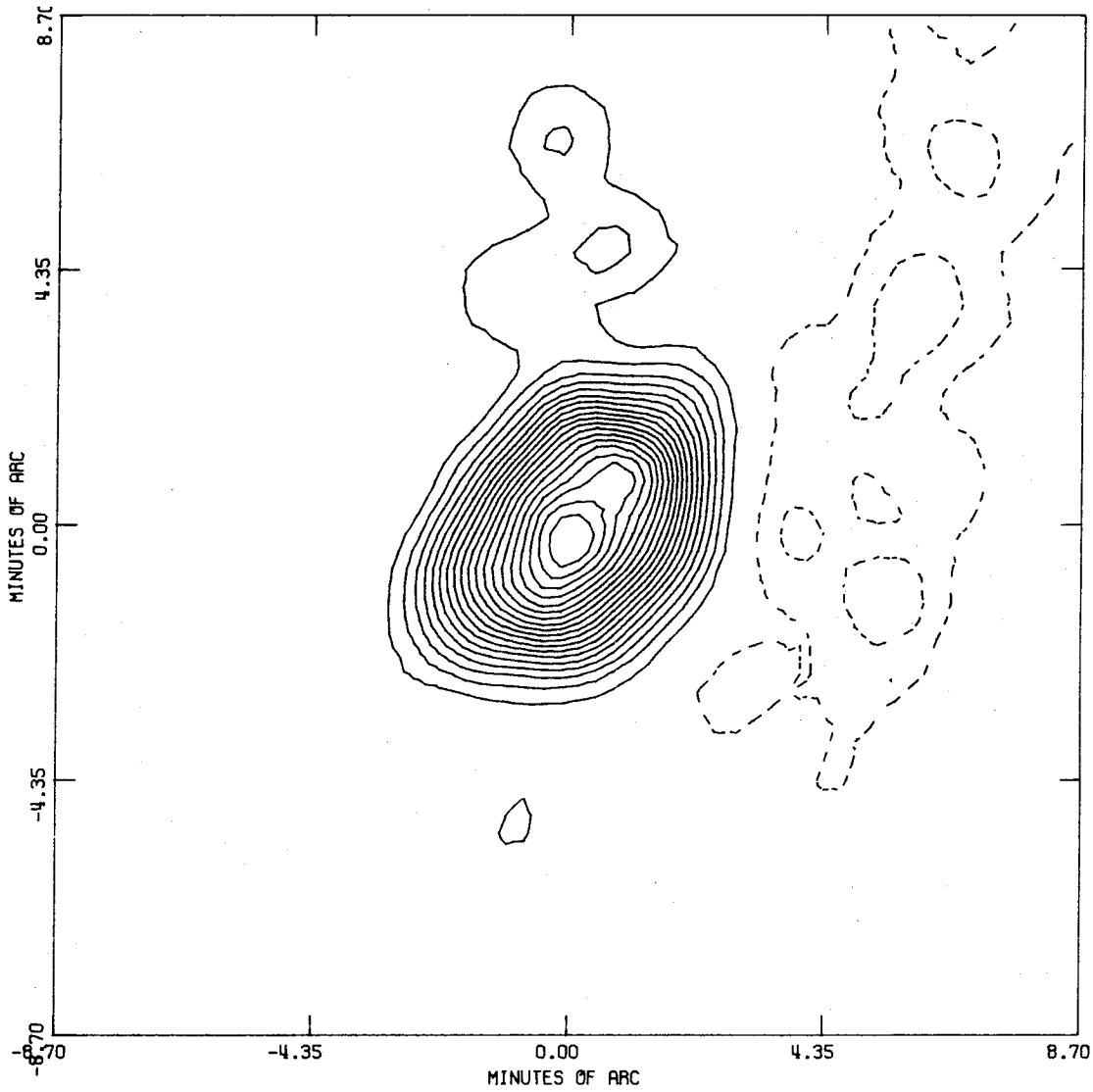

Figure 29c. 3C144, continuum frequency shift: clean map, contour interval = 5%, zero contour suppressed, large area.

serious gaps in the data sampling. Sidelobes exceeding 50 percent occur north and south of the main beam at distances equivalent to the reciprocal of the 400-foot baseline interval. The low degree of curvature of the north-south tracks causes the considerable magnitude of these responses. The dirty map (Figure 29b) reveals eight spurious "sources" each of which is at least half as strong as the source itself. The positive spurious responses arise from the strong positive sidelobes north and south of the main beam. However, the negative spurious responses are surprisingly strong since they arise from moderately weak negative sidelobes. As a result of this excess strength, the map after the deconvolution process (Figure 29c) shows greater spurious responses than for any of the other sources. Although much of the map area has brightness less than one percent, there are large regions with peaks around 10 to 15 percent. A combination of poor calibration at short spacings and the absence of data in large wedges of the (u, v) plane is suggested as the cause of these unwanted responses.

We again find that spurious response levels increase when the deconvolution is carried out over a restricted area. The continuum map used to compute optical depth

maps is shown together with lines of constant galactic coordinates in Figure 30. The clean beam used for this source is circular with a width between half-maxima of 1.5 arc minutes representing the average of the north-south and east-west widths of the main response in the dirty beam pattern. The large negative response at the south-west corner is found on all maps of the source and has a magnitude which is roughly proportional to the peak brightnesses of the maps. There is a tendency for this response to be stronger at the higher frequencies.

B. Results — Observed Spectra

Two of the spectra obtained on the Crab Nebula are plotted in Figures 31 and 32. The first represents the average of about 60 minutes of observation at the 200-foot east-west spacing while the second represents a single ten-minute observation at the 400-foot north-south spacing. Both spectra reveal a narrow feature around -50 KHz and a broad feature with peaks about - 23 and - 14 KHz. In Figure 31, the relative flux exceeds 1.0 at the low frequency end and is less than 1.0 at the high frequency end. This result is believed to be real since the continuum observations which provide the normalization are made at

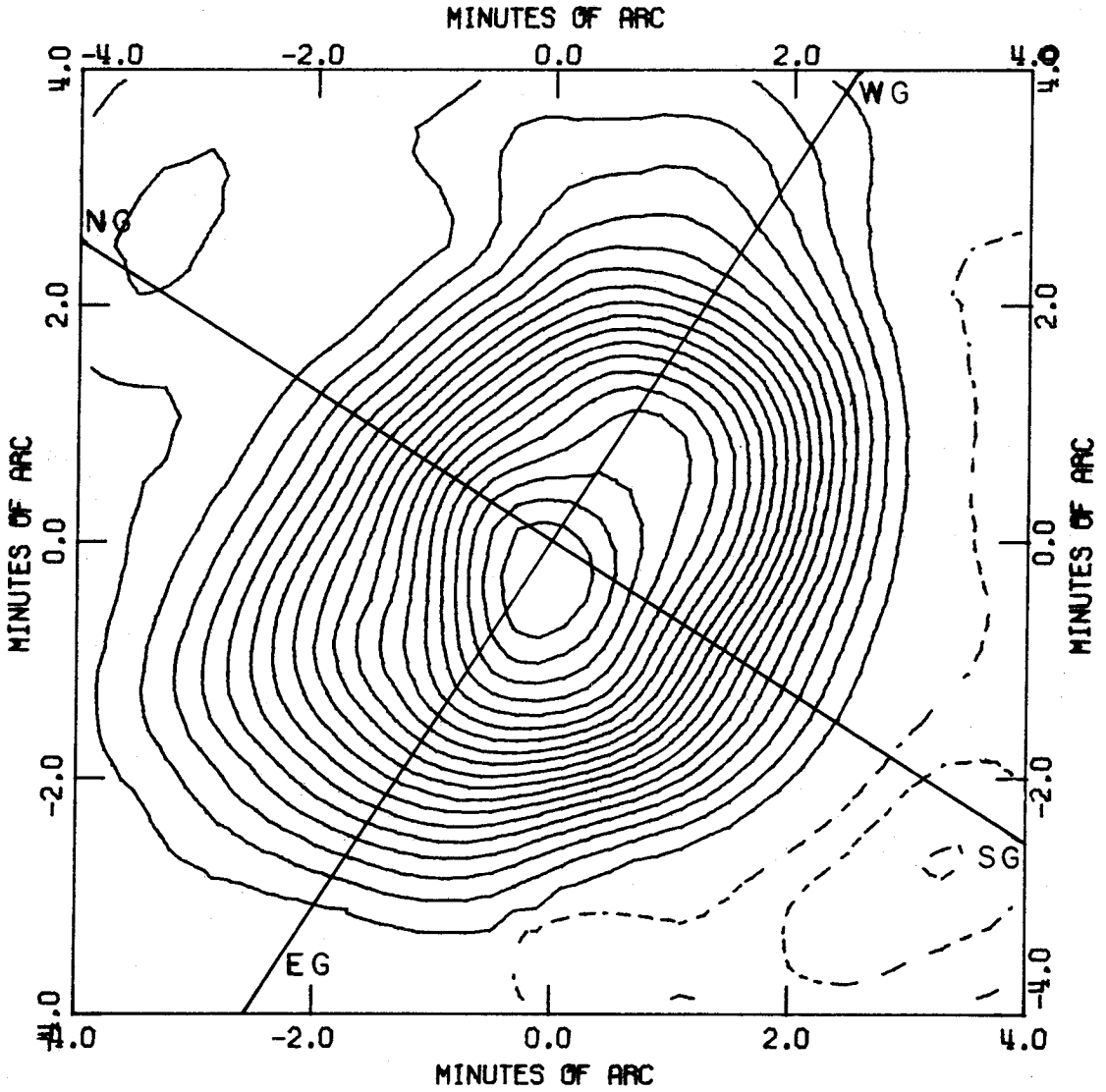

Figure 30. 3C144: continuum map, contour interval = 5%, zero contour suppressed. Lines of constant galactic coordinates drawn with NG being galactic north and EG being galactic east (i.e. increasing longitude at constant latitude).

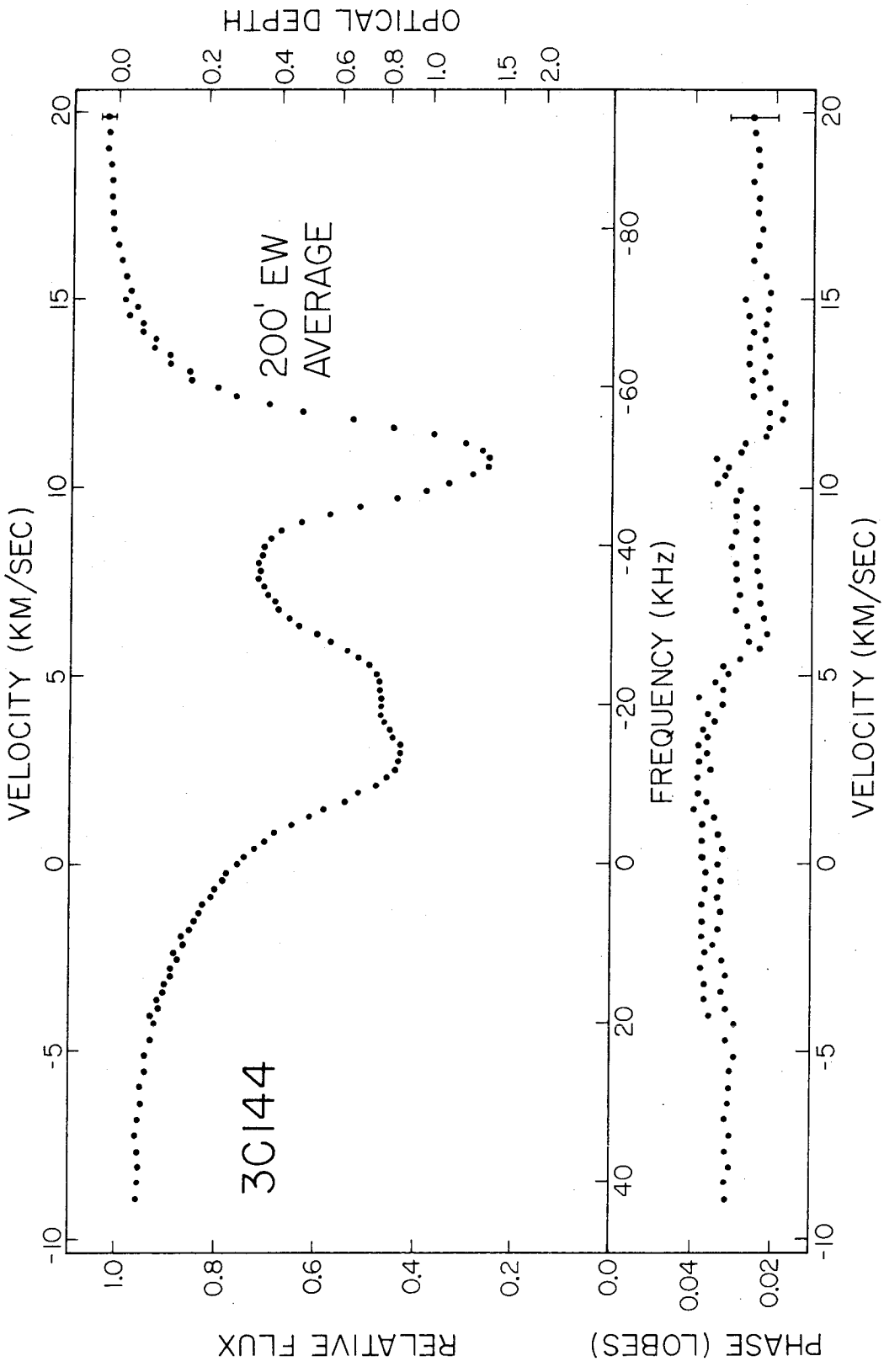

Figure 31. 3C144: relative flux and phase spectra at 200 feet east-west. Average of 60 minutes of observation.

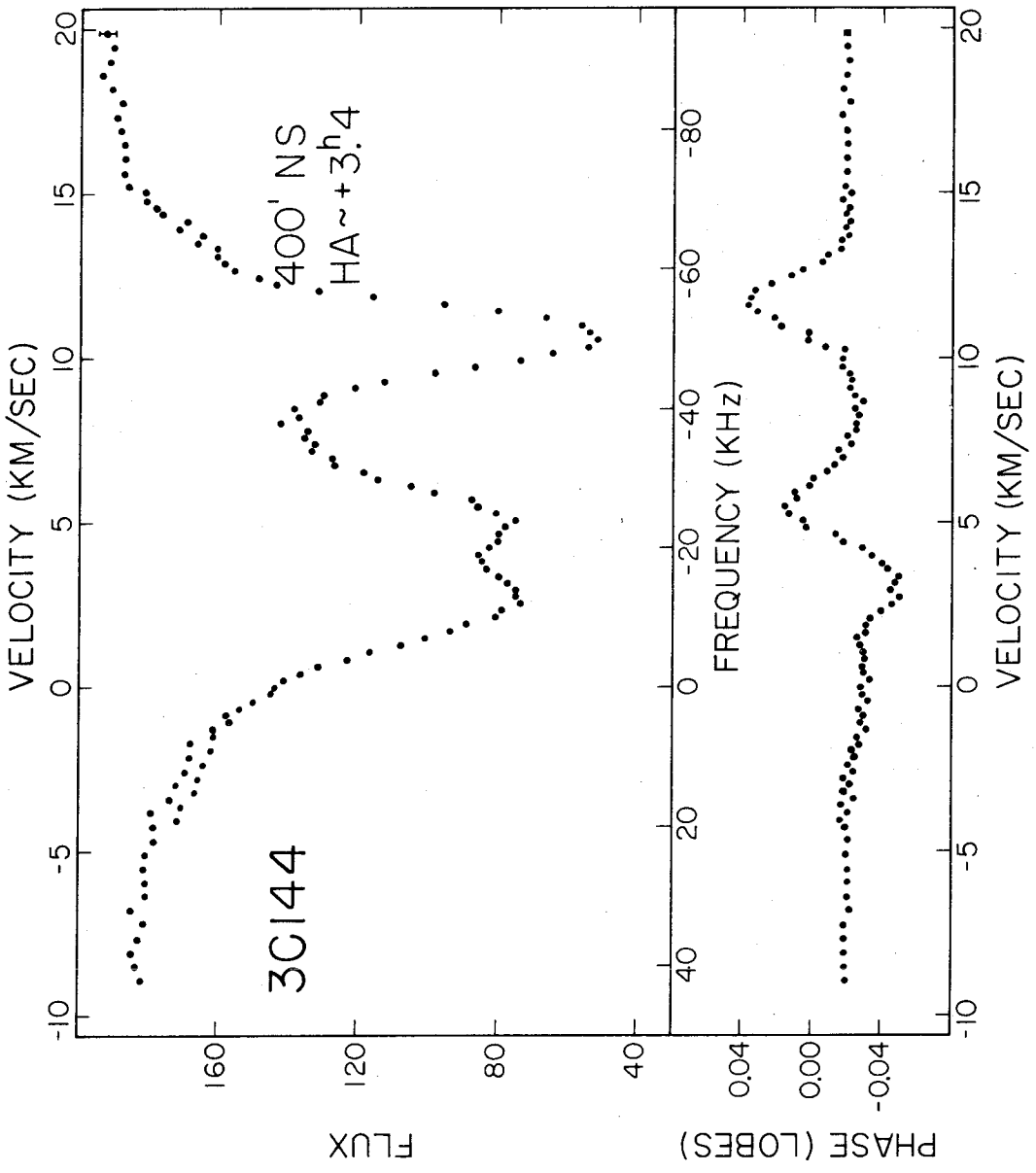

Figure 32. 3C144: flux and phase spectra at 400 feet north-south at hour angle about +3.4 hours. Single ten-minute observations.

both - 180 and + 125 KHz and disagree by less than 0.3 percent. The effects of the inadequate calibration are shown by the phase spectrum in this figure. The error bar given is typical, but represents the absolute uncertainty in phase while relative phases within each frequency shift are expected to be more accurate. Thus, the features in the phase around - 56, - 49, and - 25 KHz suggest that the absorbing material is not uniformly distributed over the source. Figure 32 allows this point to be established unambiguously. In this figure, the features in phase are much larger than the uncertainties and the flux spectrum has a different shape, especially around - 23 KHz.

C. Results — Optical Depth Maps

The optical depth maps are presented in Figures 33 which, along with a detailed description, are deferred to Appendix G. The maps within the narrow absorption feature (- 60 to - 40 KHz) show a bumpy but consistent gradient across the source. The maximum is off the source to the south at the low frequency end and moves steadily around to the northwest as the frequency increases through the absorption feature. At the center of the feature (- 50 KHz) the optical depth reaches 1.65 around most of the southern

and western boundary of the source. This is the largest τ found on any of the maps for the Crab Nebula, but is much lower than the peak values found in front of Cassiopeia A. The fine structure on the maps appears to be real and to be unresolved. At the high frequency end of the feature maxima toward the northeast are also found.

The broad absorption feature runs from about - 30 to 0 KHz with peaks around - 23 and - 12 KHz and a long tail at positive frequencies. Maximum optical depth on all maps is found at the western edge of the source about (2.3, 0.9). Minor peaks occur which are also found on all maps. A ridge in τ goes from the maximum across the source to the eastern edge. This ridge curves through the southern part of the source at lower frequencies, but is found farther to the north at higher frequencies. This difference, as well as differences in the fine-structure on the maps suggests that the spectral components around - 23 and - 12 KHz are independent "clouds". In addition, the many similarities in the distribution of optical depth seen through this broad absorption feature suggest the presence of a third spectral component having a large dispersion.

D. Results — Spectra and Gaussian Fitting

Although there are some serious problems, the gaussian analysis can be said to be more successful for 3C144 than for 3C461 and 3C405. Figures 34 give a sample of the spectra together with gaussian fits obtained. Figures 35 and 36 show alternative fits to these same spectra. The gaussian parameters are mapped in Figures 37 and 38.

Since the long high-frequency wing was not observed over its full range in frequency, it was necessary to fit this wing in all solutions with a broad component having a fixed central frequency and width. The first solution which was attempted contained six components: the fixed one at high frequency, three narrow ones for the three peaks, and two broader ones to account for the wings around - 48 and + 4 KHz. This solution converges for only 30 of the 64 spectra and only after the component at + 4 KHz is changed into a very broad component around - 18 KHz. This solution also produces qualitatively different fits to spectra less than half a beamwidth apart, especially for component 2 (see Figure 38). Another solution, to which some of the six-component attempts converged, is a five-component fit having a single broad component to account

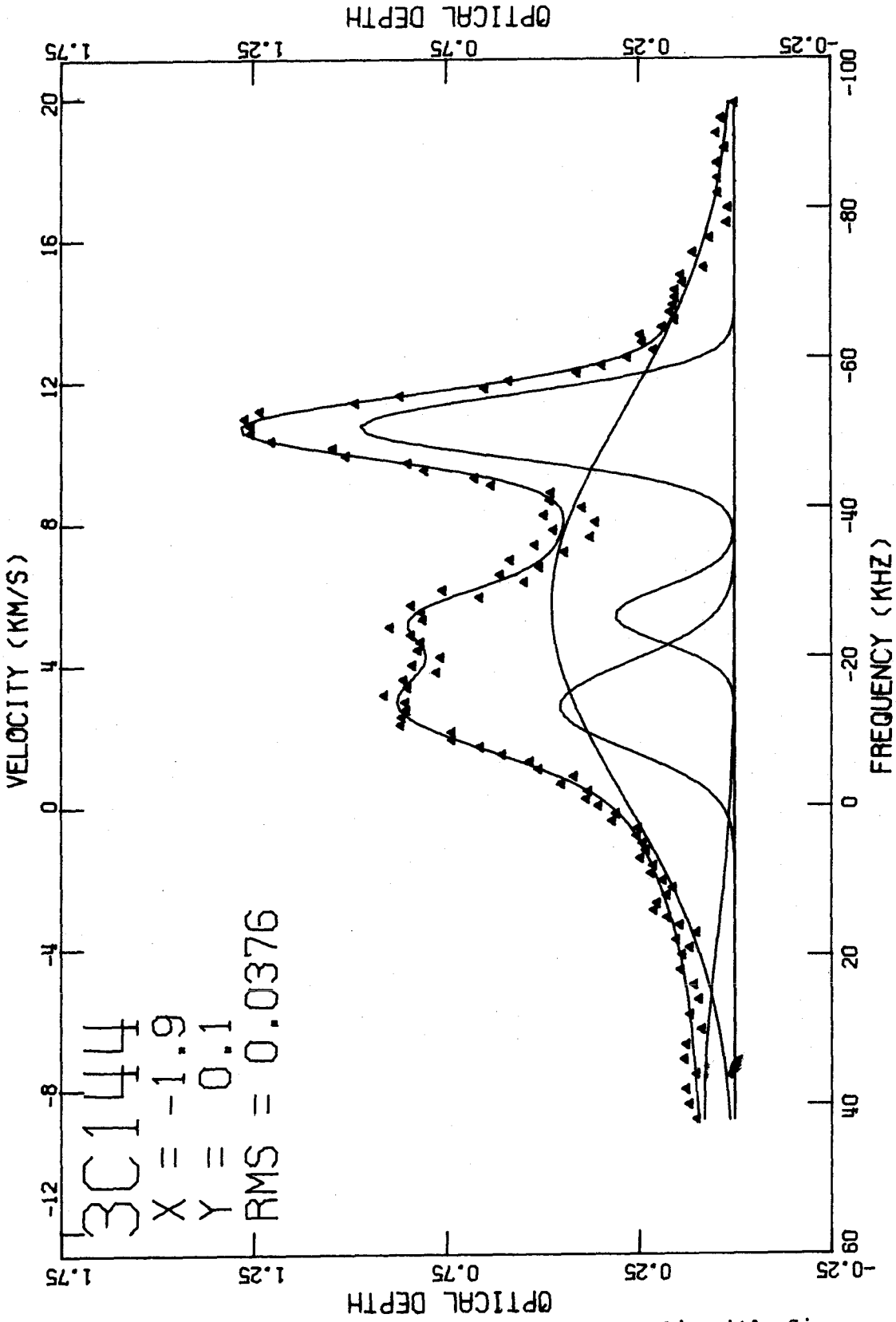

Figure 34a. 3C144: Spectrum at (-1.9,0.1) with five-component gaussian fit.

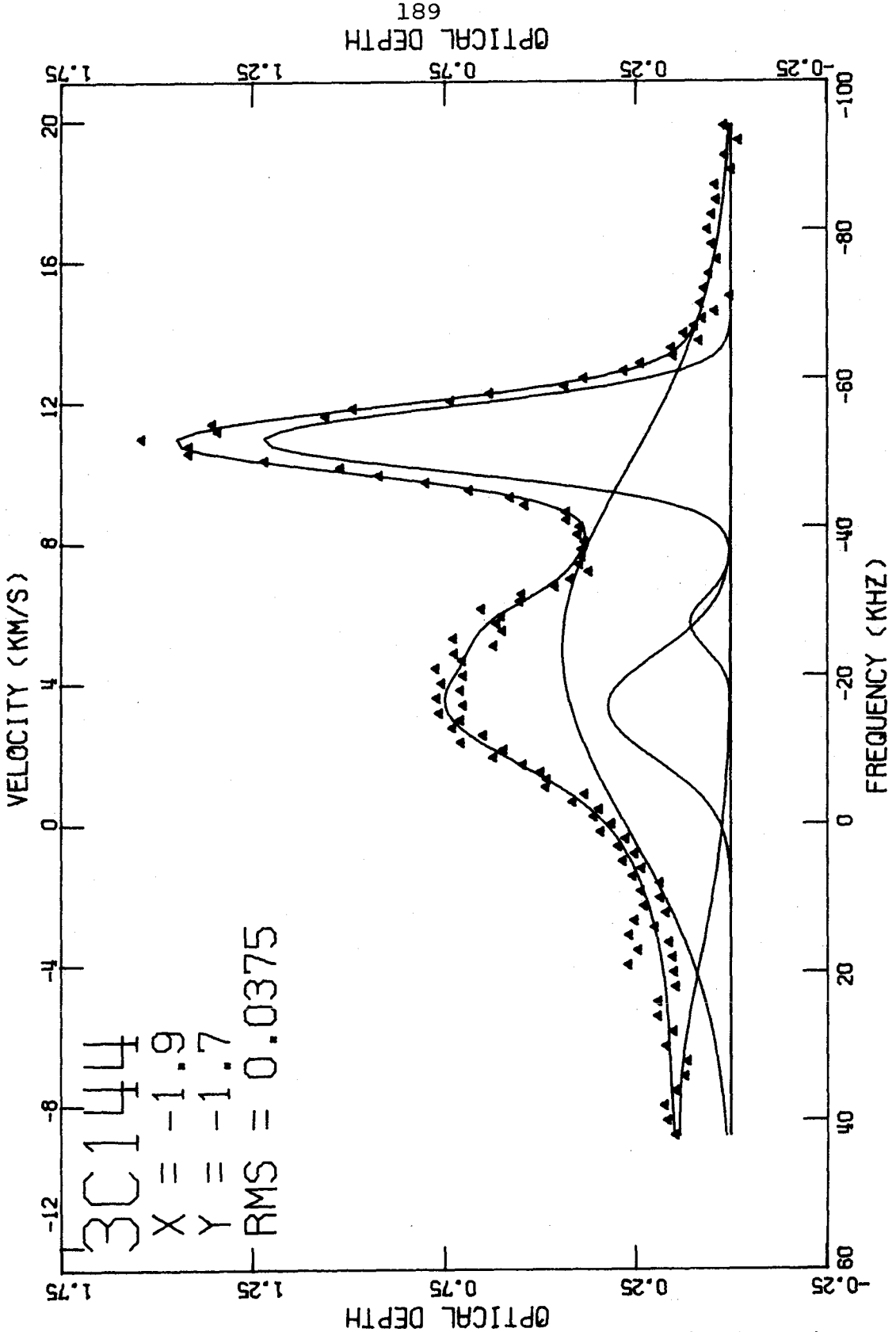

Figure 34b. 3C144: Spectrum at (-1.9, -1.7) with five-component gaussian fit.

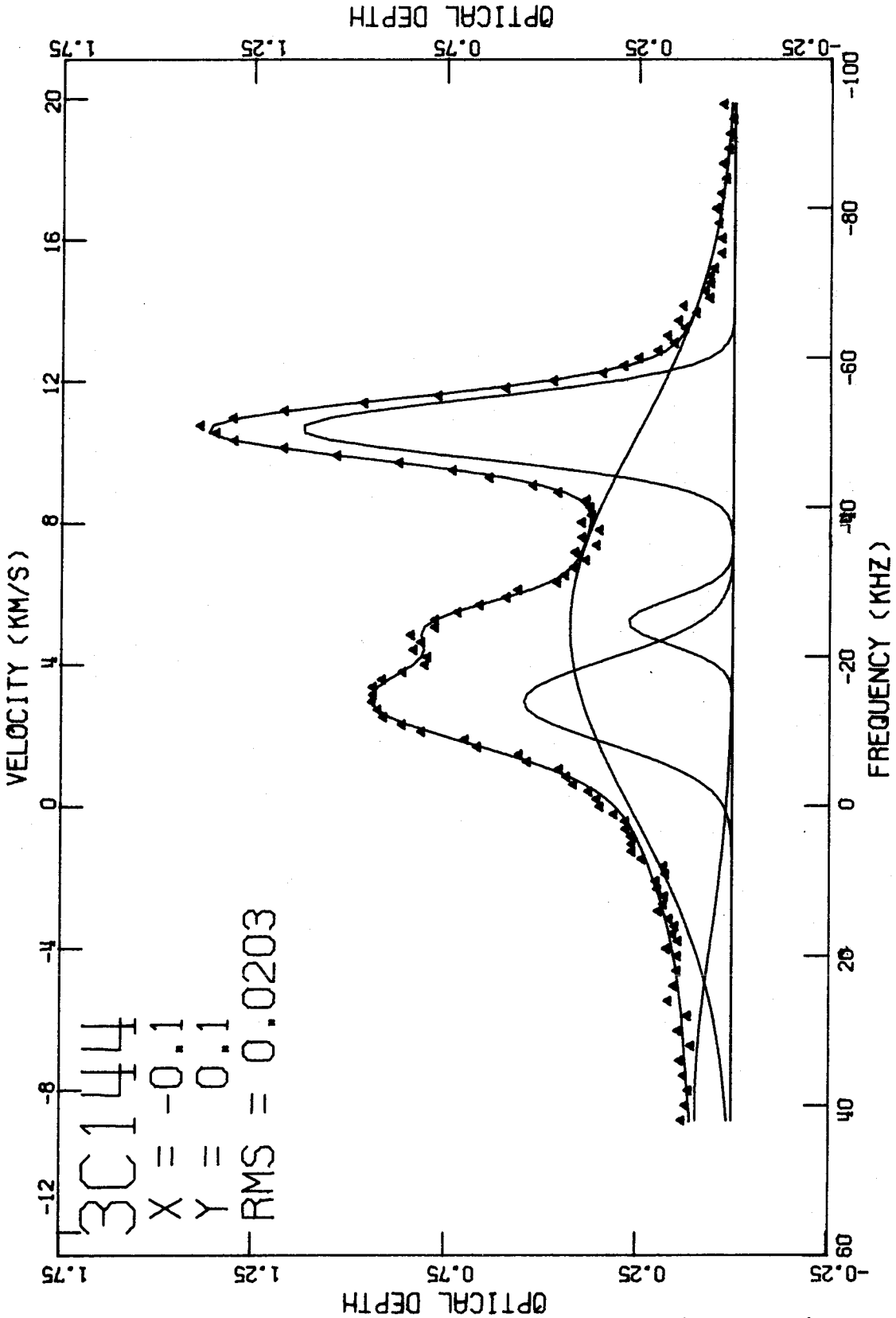

Figure 34c. 3C144: Spectrum at (-0.1, 0.1) with five-component gaussian fit.

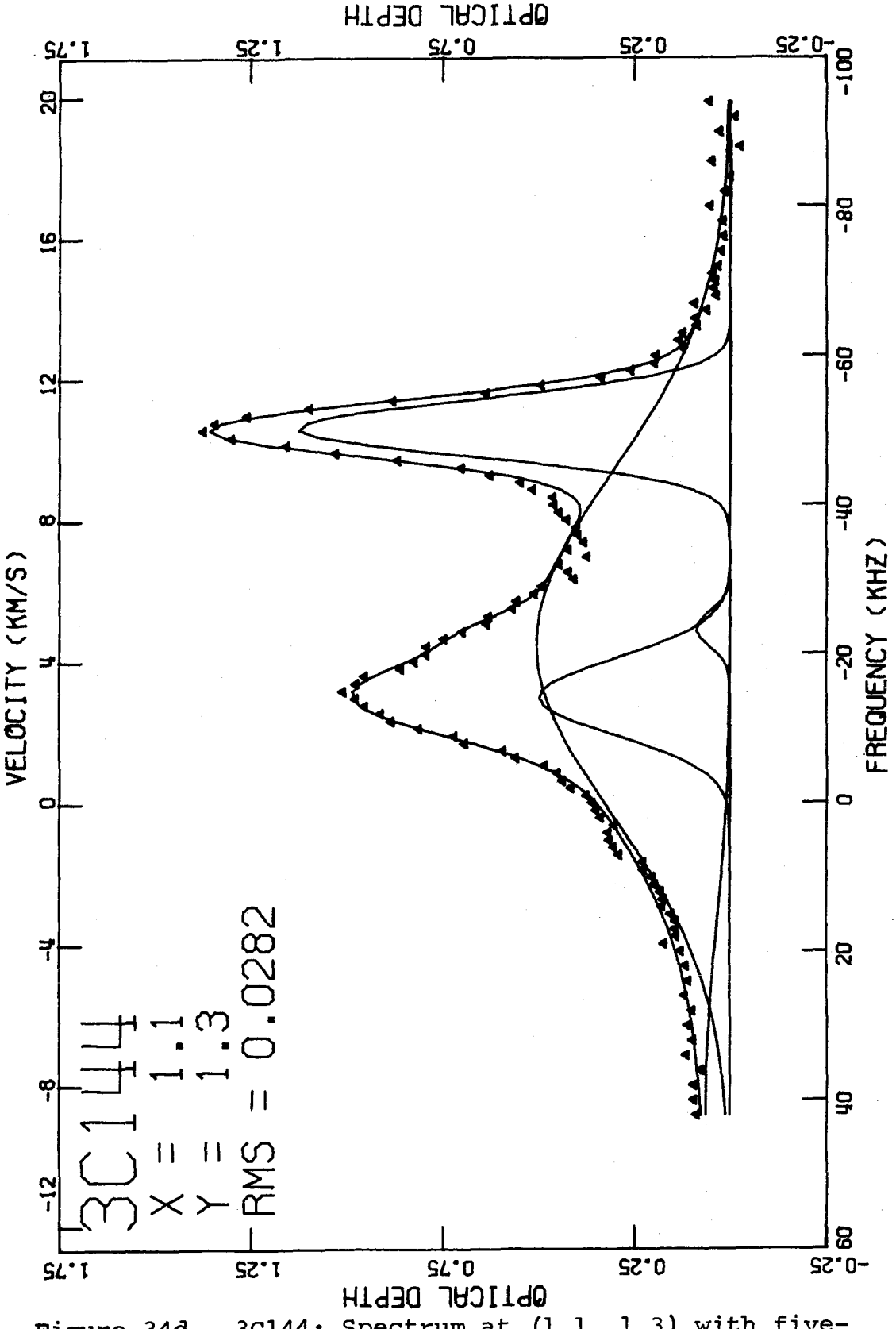

Figure 34d. 3C144: Spectrum at (1.1, 1.3) with five-component gaussian fit.

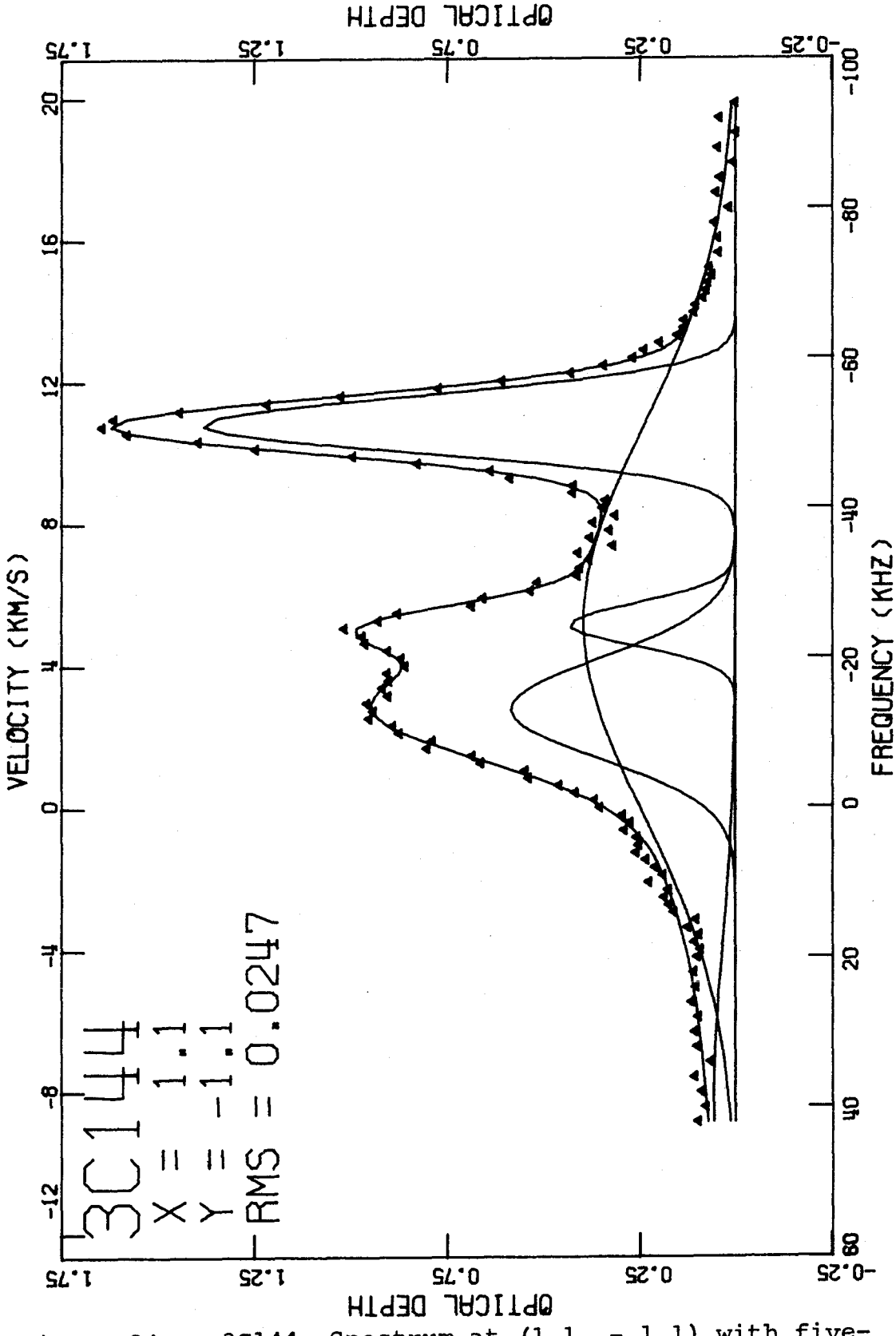

Figure 34e. 3C144: Spectrum at (1.1, - 1.1) with five-component gaussian fit.

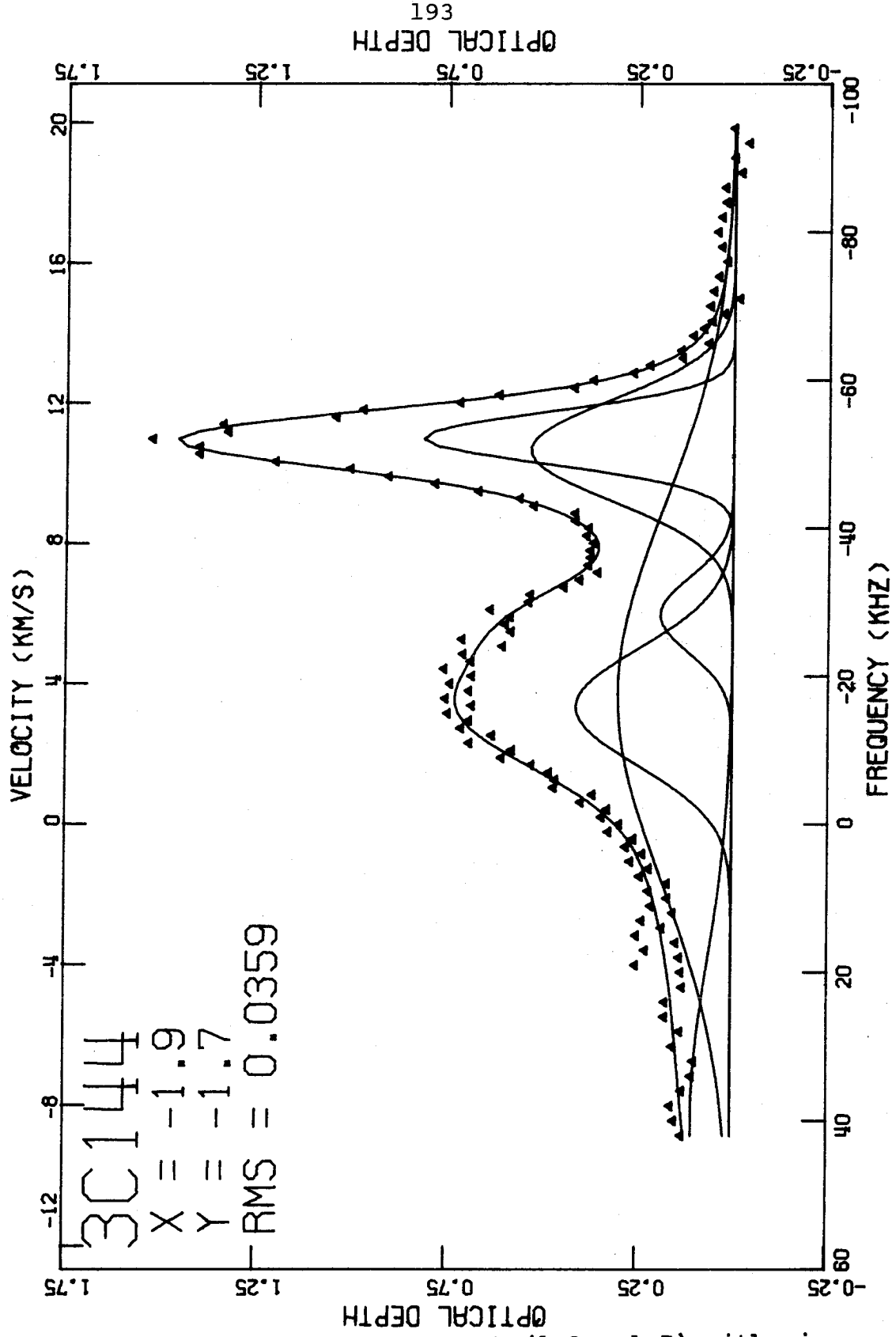

Figure 35a. 3C144: Spectrum at (1.9, -1.7) with six-component gaussian fit.

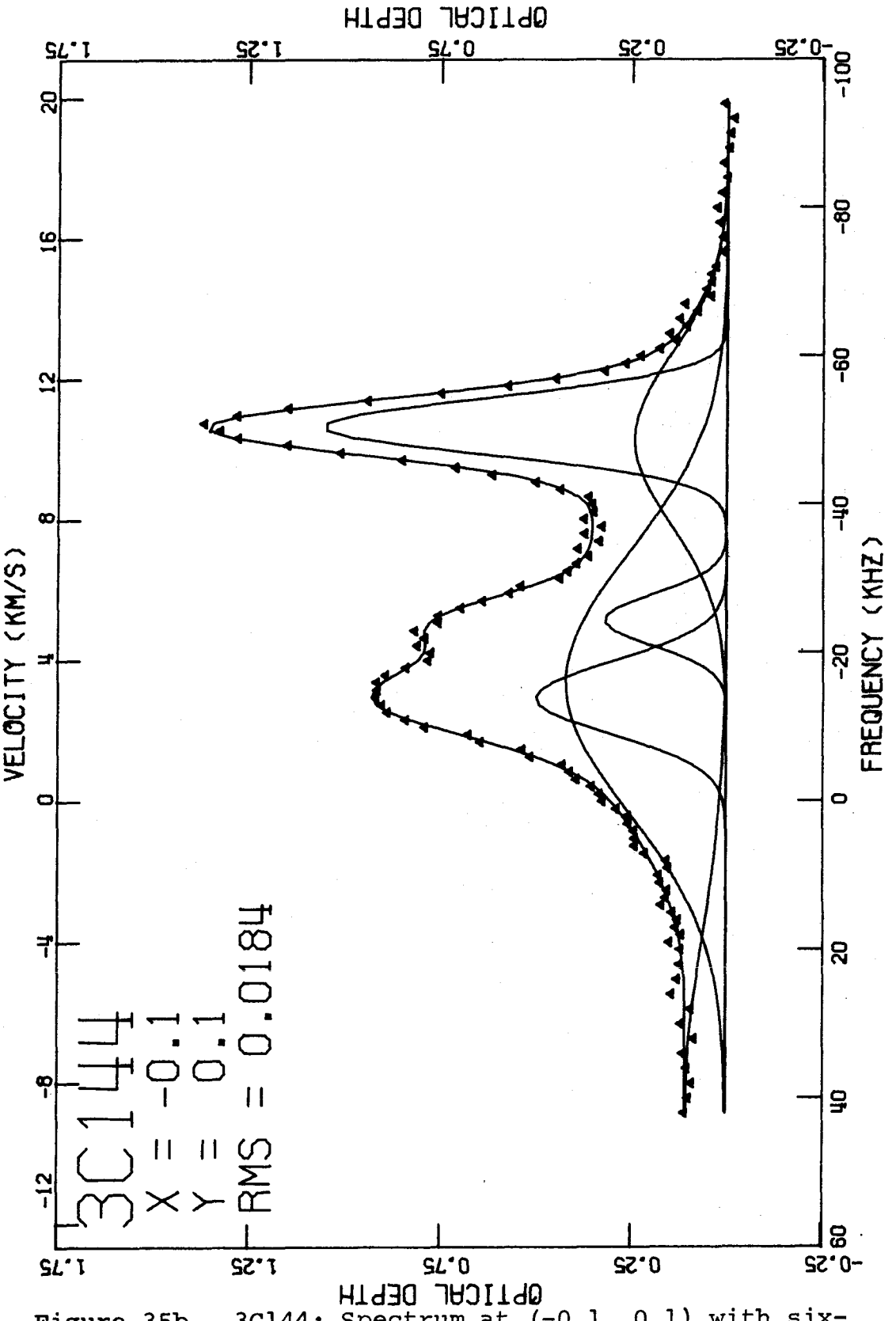

Figure 35b. 3C144: Spectrum at (-0.1, 0.1) with six-component gaussian fit.

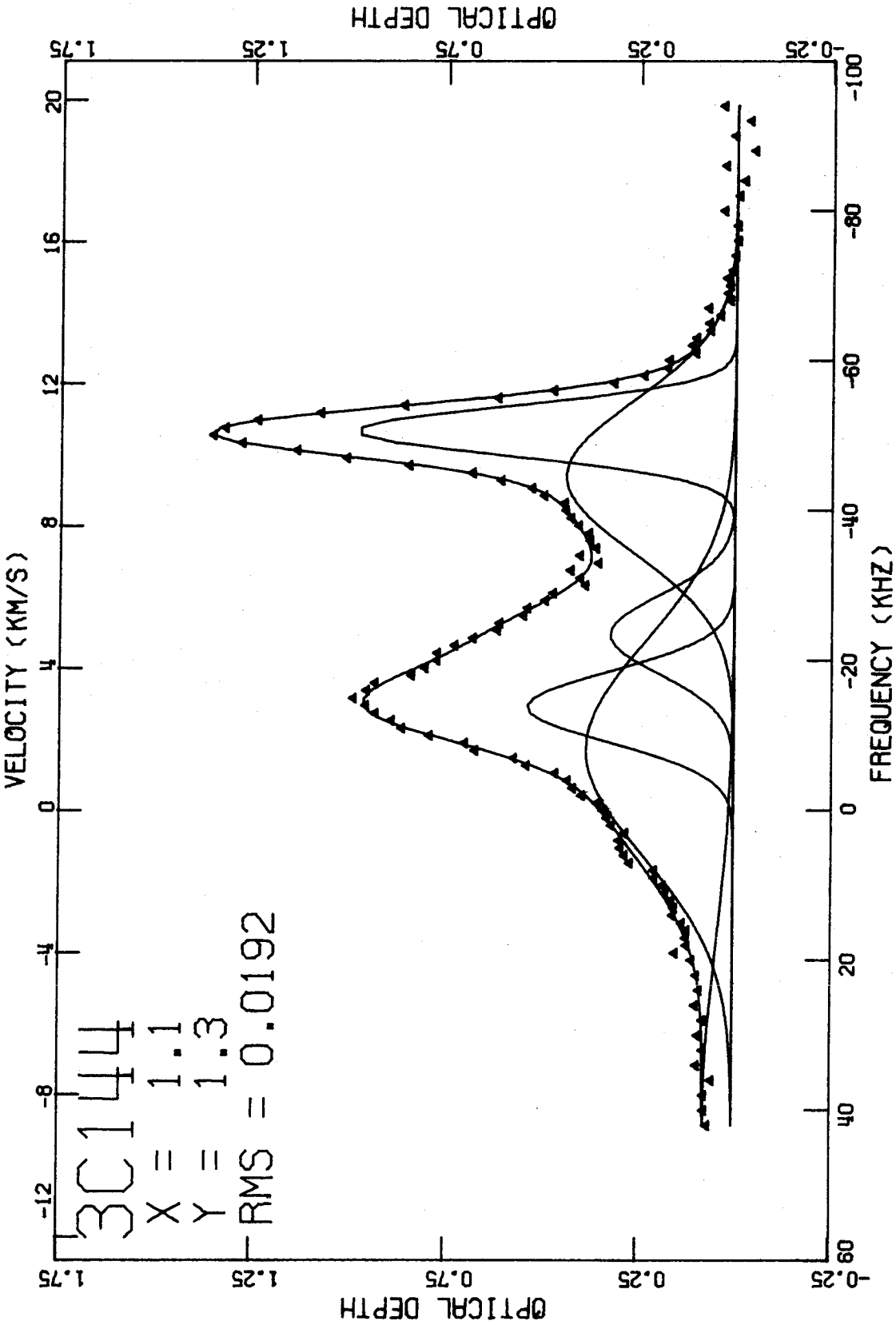

Figure 35c. 3C144: Spectrum at (1.1, 1.3) with six-component gaussian fit.

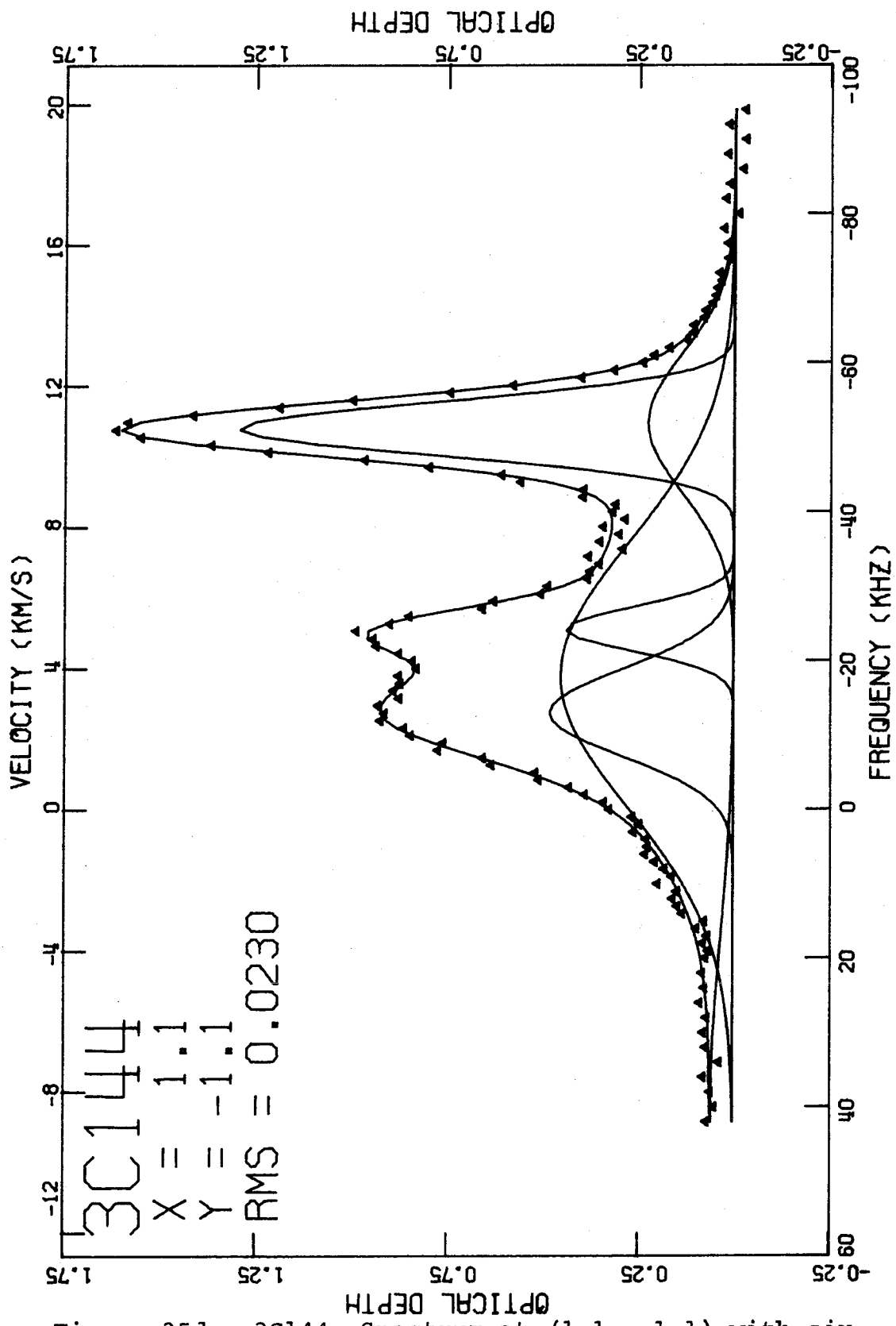

Figure 35d. 3C144: Spectrum at (1.1, -1.1) with six-component gaussian fit.

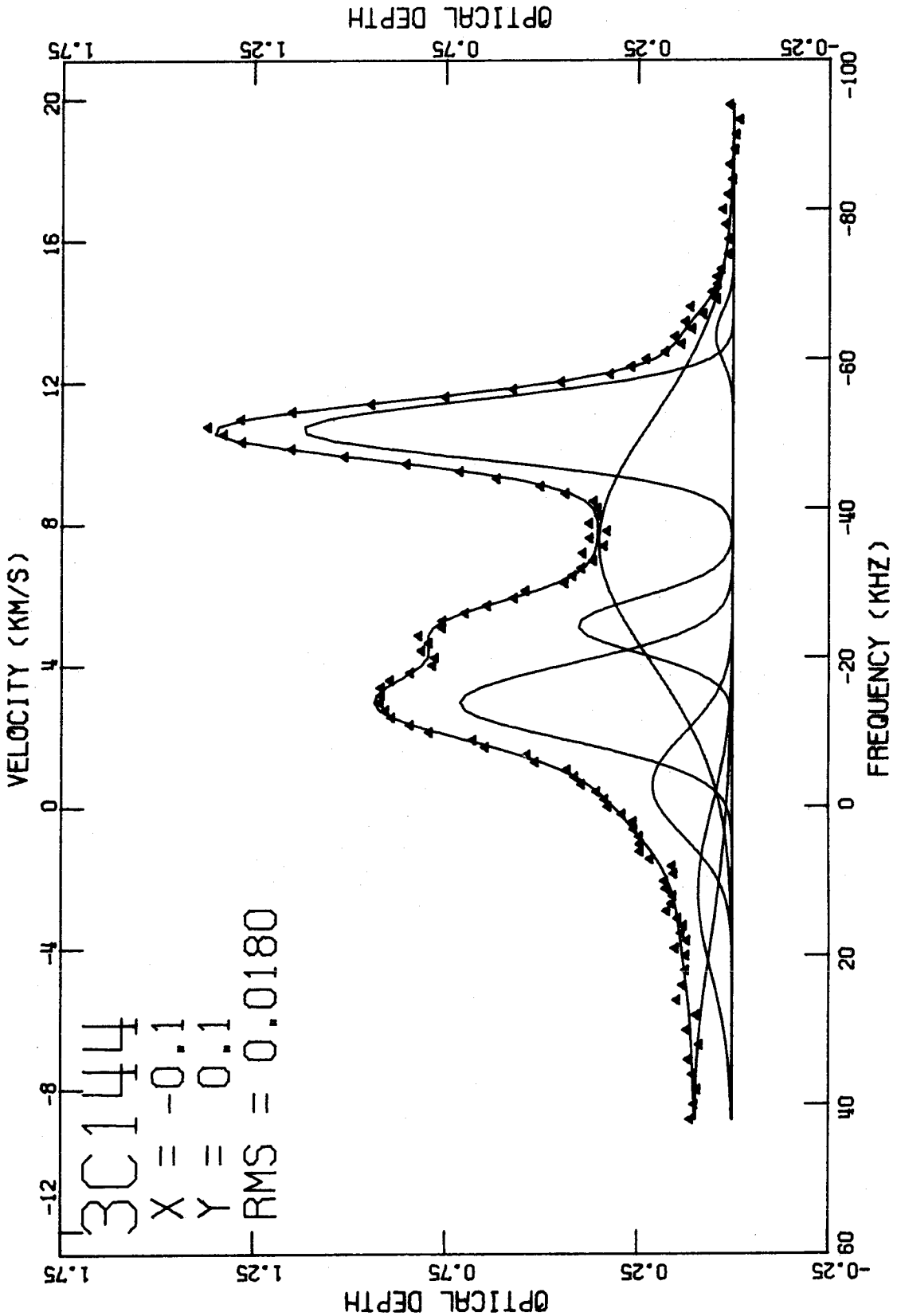

Figure 36. 3C144: Spectrum at (-0.1, 0.1) with eight-component gaussian fit.

3C144 - 5 COMPONENT FIT : RMS

	-2.5	-1.9	-1.3	-0.7	-0.1	0.5	1.1	1.7	2.3
2.5					0.0528	0.0758	0.0954	******	
1.9				0.0370	0.0343	0.0402	0.0470	0.0437	0.0599
1.3			0.0497	0.0280	0.0248	0.0224	0.0282	0.0303	0.0436
0.7		0.0438	0.0310	0.0207	0.0198	0.0194	0.0239	0.0295	0.0432
0.1	0.0584	0.0376	0.0256	0.0209	0.0203	0.0240	0.0251	0.0270	0.0467
-0.5	0.0527	0.0358	0.0241	0.0200	0.0193	0.0238	0.0294	0.0343	0.0485
-1.1	******	0.0329	0.0231	0.0182	0.0201	0.0169	0.0247	0.0397	
-1.7	0.0448	0.0375	0.0308	0.0260	0.0240	0.0251	0.0337	0.0567	
-2.3		******	0.0633	0.0472	0.0523	0.0552			

Figure 37a. 3C144: Results of gaussian analysis — five-component solution — RMS (in optical depth).

3C144 - 5 COMPONENT FIT : DC OFFSET

	-2.5	-1.9	-1.3	-0.7	-0.1	0.5	1.1	1.7	2.3
2.5					-0.041 (0.021)	-0.073 (0.036)	-0.121 (0.062)		
1.9				-0.011 (0.014)	-0.036 (0.013)	-0.025 (0.018)	0.008 (0.018)	0.028 (0.019)	0.078 (0.033)
1.3			-0.051 (0.031)	-0.015 (0.013)	0.007 (0.011)	0.008 (0.010)	0.014 (0.011)	0.080 (0.012)	0.166 (0.021)
0.7		-0.021 (0.027)	-0.036 (0.020)	-0.023 (0.012)	0.011 (0.009)	-0.007 (0.009)	-0.003 (0.010)	0.065 (0.012)	0.131 (0.020)
0.1	-0.111 (0.040)	-0.050 (0.023)	-0.036 (0.015)	-0.036 (0.013)	0.001 (0.011)	0.018 (0.011)	0.030 (0.012)	0.061 (0.012)	0.093 (0.019)
-0.5	-0.066 (0.032)	-0.077 (0.023)	-0.058 (0.016)	-0.047 (0.013)	-0.025 (0.011)	0.007 (0.011)	0.015 (0.015)	0.035 (0.018)	0.053 (0.019)
-1.1		-0.044 (0.019)	-0.062 (0.016)	-0.048 (0.012)	-0.015 (0.010)	0.025 (0.007)	-0.012 (0.014)	0.001 (0.021)	
-1.7	-0.038 (0.019)	-0.063 (0.020)	-0.049 (0.017)	-0.026 (0.013)	-0.052 (0.012)	-0.026 (0.012)	0.015 (0.016)	0.002 (0.042)	
-2.3			-0.049 (0.034)	-0.012 (0.024)	-0.126 (0.034)	-0.156 (0.035)			

Figure 37b. 3C144: Results of gaussian analysis — five-component solution — DC offset (in optical depth).

3C144 - 5 COMPONENT FIT : CENTRAL OPTICAL DEPTH OF COMPONENT 1

	-2.5	-1.9	-1.3	-0.7	-0.1	0.5	1.1	1.7	2.3
2.5					1.082 (0.027)	1.147 (0.039)	1.167 (0.049)		
1.9				1.000 (0.021)	1.020 (0.019)	1.062 (0.022)	1.106 (0.026)	1.251 (0.024)	1.427 (0.032)
1.3			0.949 (0.026)	0.981 (0.015)	0.958 (0.014)	1.010 (0.012)	1.126 (0.016)	1.236 (0.017)	1.312 (0.024)
0.7		0.912 (0.023)	0.945 (0.016)	0.991 (0.011)	0.963 (0.011)	1.028 (0.011)	1.184 (0.013)	1.233 (0.017)	1.234 (0.024)
0.1	0.963 (0.031)	0.973 (0.020)	0.976 (0.014)	1.057 (0.011)	1.127 (0.011)	1.156 (0.013)	1.233 (0.014)	1.287 (0.015)	1.292 (0.026)
-0.5	0.996 (0.030)	1.066 (0.019)	1.061 (0.013)	1.124 (0.011)	1.272 (0.010)	1.312 (0.013)	1.305 (0.016)	1.364 (0.019)	1.386 (0.027)
-1.1		1.118 (0.018)	1.199 (0.012)	1.245 (0.010)	1.318 (0.011)	1.382 (0.010)	1.383 (0.013)	1.413 (0.021)	
-1.7	1.164 (0.027)	1.221 (0.021)	1.350 (0.017)	1.383 (0.015)	1.368 (0.013)	1.426 (0.014)	1.439 (0.018)	1.430 (0.029)	
-2.3			1.455 (0.035)	1.440 (0.026)	1.416 (0.028)	1.474 (0.029)			

Figures 37c. 3C144: Results of gaussian analysis — five-component solution — central optical depths, central frequencies (KHz) and full widths at half maximum (KHz) of gaussian components, by component. For component 5, the central frequency and full width were held fixed at 40.0 and 50.0 KHz, respectively.

3C144 - 5 COMPONENT FIT : CENTRAL FREQUENCY OF COMPONENT 1

	-2.5	-1.9	-1.3	-0.7	-0.1	0.5	1.1	1.7	2.3
2.5					-50.19 (0.11)	-50.32 (0.14)	-50.16 (0.17)		
1.9				-50.07 (0.08)	-50.22 (0.07)	-50.25 (0.08)	-50.10 (0.09)	-50.00 (0.07)	-50.00 (0.08)
1.3			-50.08 (0.12)	-50.11 (0.06)	-50.25 (0.06)	-50.32 (0.05)	-50.25 (0.05)	-50.17 (0.05)	-50.21 (0.07)
0.7		-50.38 (0.11)	-50.21 (0.08)	-50.22 (0.05)	-50.20 (0.04)	-50.36 (0.04)	-50.50 (0.04)	-50.48 (0.05)	-50.48 (0.07)
0.1	-51.16 (0.14)	-50.81 (0.09)	-50.55 (0.06)	-50.51 (0.04)	-50.51 (0.04)	-50.53 (0.04)	-50.61 (0.04)	-50.71 (0.04)	-50.74 (0.08)
-0.5	-51.40 (0.14)	-51.35 (0.08)	-50.94 (0.05)	-50.71 (0.04)	-50.84 (0.04)	-50.91 (0.04)	-50.82 (0.05)	-50.86 (0.05)	-50.92 (0.08)
-1.1		-51.60 (0.08)	-51.40 (0.05)	-51.16 (0.04)	-51.10 (0.04)	-51.17 (0.03)	-51.16 (0.04)	-51.08 (0.06)	
-1.7	-51.76 (0.09)	-51.83 (0.08)	-51.82 (0.06)	-51.70 (0.04)	-51.44 (0.04)	-51.34 (0.04)	-51.34 (0.05)	-51.26 (0.09)	
-2.3			-51.93 (0.11)	-51.90 (0.08)	-51.74 (0.08)	-51.56 (0.08)			

Figure 37c. (continued)

3C144 - 5 COMPONENT FIT : FULL WIDTH OF COMPONENT 1

	-2.5	-1.9	-1.3	-0.7	-0.1	0.5	1.1	1.7	2.3
2.5					9.15 (0.29)	8.68 (0.37)	8.34 (0.44)		
1.9				9.85 (0.26)	9.19 (0.22)	8.77 (0.23)	8.63 (0.25)	8.16 (0.19)	8.03 (0.23)
1.3			9.65 (0.34)	9.55 (0.19)	9.01 (0.16)	8.79 (0.14)	8.89 (0.16)	8.52 (0.15)	8.13 (0.19)
0.7		9.60 (0.32)	9.69 (0.22)	9.49 (0.14)	9.06 (0.13)	8.85 (0.12)	8.91 (0.13)	8.53 (0.15)	8.13 (0.20)
0.1	9.81 (0.41)	9.84 (0.26)	9.56 (0.17)	9.47 (0.13)	9.32 (0.12)	8.87 (0.13)	8.62 (0.12)	8.58 (0.13)	8.37 (0.21)
-0.5	10.28 (0.41)	10.22 (0.24)	9.88 (0.15)	9.65 (0.12)	9.58 (0.10)	9.18 (0.12)	8.61 (0.14)	8.66 (0.15)	8.84 (0.21)
-1.1		10.37 (0.22)	10.38 (0.14)	10.00 (0.10)	9.48 (0.10)	9.19 (0.08)	8.85 (0.11)	8.86 (0.16)	
-1.7	10.01 (0.28)	10.26 (0.22)	10.48 (0.17)	10.22 (0.14)	9.60 (0.12)	9.30 (0.12)	9.24 (0.15)	9.23 (0.24)	
-2.3			10.20 (0.32)	9.89 (0.22)	9.54 (0.24)	9.47 (0.24)			

Figure 37c. (continued)

3C144 - 5 COMPONENT FIT : CENTRAL OPTICAL DEPTH OF COMPONENT 2

	-2.5	-1.9	-1.3	-0.7	-0.1	0.5	1.1	1.7	2.3
2.5					0.244 (0.044)	0.175 (0.061)	0.120 (0.094)		
1.9				0.147 (0.029)	0.154 (0.034)	0.089 (0.039)	0.057 (0.045)	0.181 (0.065)	0.343 (0.120)
1.3			0.309 (0.046)	0.192 (0.023)	0.118 (0.022)	0.106 (0.024)	0.089 (0.030)	0.147 (0.042)	0.181 (0.069)
0.7		0.303 (0.035)	0.382 (0.025)	0.309 (0.019)	0.130 (0.018)	0.130 (0.024)	0.211 (0.027)	0.186 (0.033)	0.179 (0.048)
0.1	0.285 (0.055)	0.311 (0.033)	0.355 (0.022)	0.361 (0.023)	0.274 (0.020)	0.217 (0.023)	0.280 (0.026)	0.275 (0.029)	0.234 (0.048)
-0.5	0.234 (0.083)	0.354 (0.041)	0.363 (0.025)	0.379 (0.023)	0.435 (0.017)	0.415 (0.018)	0.369 (0.028)	0.395 (0.042)	0.360 (0.064)
-1.1		0.302 (0.055)	0.395 (0.027)	0.399 (0.015)	0.401 (0.016)	0.440 (0.013)	0.432 (0.026)	0.460 (0.058)	
-1.7	0.199 (0.066)	0.107 (0.057)	0.302 (0.042)	0.425 (0.019)	0.396 (0.017)	0.408 (0.020)	0.438 (0.036)	0.465 (0.082)	
-2.3			0.284 (0.070)	0.358 (0.032)	0.394 (0.034)	0.431 (0.040)			

Figure 37c. (continued)

3C144 - 5 COMPONENT FIT : CENTRAL FREQUENCY OF COMPONENT 2

	-2,5	-1,9	-1,3	-0,7	-0,1	0,5	1,1	1,7	2,3
2,5					-23,68 (0,66)	-24,53 (0,97)	-24,01 (1,77)		
1,9				-25,00 (0,37)	-23,34 (0,64)	-23,56 (0,97)	-22,53 (1,23)	-21,86 (1,06)	-20,80 (2.59)
1,3			-24,91 (0,62)	-24,92 (0,34)	-24,04 (0,40)	-23,43 (0,53)	-23,20 (0,77)	-22,28 (0,56)	-22,40 (0,49)
0,7		-25,91 (0,51)	-24,22 (0,45)	-24,25 (0,29)	-24,17 (0,32)	-23,45 (0,48)	-23,52 (0,42)	-23,29 (0,34)	-22,86 (0,39)
0,1	-26,30 (0,74)	-25,42 (0,48)	-24,06 (0,44)	-24,08 (0,35)	-24,61 (0,24)	-24,06 (0,36)	-23,39 (0,34)	-23,55 (0,21)	-23,09 (0,32)
-0,5	-26,46 (1,67)	-25,10 (0,66)	-24,54 (0,41)	-24,14 (0,37)	-24,34 (0,21)	-24,28 (0,20)	-23,69 (0,26)	-23,22 (0,26)	-23,10 (0,29)
-1,1		-24,98 (1,19)	-24,89 (0,40)	-24,69 (0,22)	-24,24 (0,23)	-24,32 (0,13)	-24,31 (0,14)	-23,49 (0,24)	
-1,7	-21,28 (3,50)	-26,98 (1,29)	-25,34 (0,66)	-24,76 (0,24)	-24,36 (0,24)	-24,14 (0,24)	-24,30 (0,21)	-23,92 (0,29)	
-2,3			-21,81 (3,30)	-24,29 (0,61)	-24,23 (0,56)	-23,70 (0,66)			

Figure 37c. (continued)

3C144 - 5 COMPONENT FIT : FULL WIDTH OF COMPONENT 2

	-2.5	-1.9	-1.3	-0.7	-0.1	0.5	1.1	1.7	2.3
2.5					6.84 (1.46)	5.86 (2.43)	5.62 (4.68)		
1.9				3.79 (0.96)	6.45 (1.47)	5.53 (2.57)	3.55 (3.44)	6.06 (1.87)	8.93 (3.40)
1.3			8.24 (1.34)	6.07 (0.84)	4.97 (1.06)	5.96 (1.34)	5.58 (1.90)	5.39 (1.35)	4.91 (1.65)
0.7		8.36 (1.17)	9.73 (0.91)	8.39 (0.59)	5.49 (0.86)	6.89 (1.10)	7.32 (0.88)	5.55 (0.98)	4.39 (1.28)
0.1	8.58 (1.74)	8.57 (1.04)	9.63 (0.83)	9.18 (0.62)	7.08 (0.53)	7.05 (0.79)	7.65 (0.71)	5.97 (0.63)	4.64 (1.08)
-0.5	10.99 (3.22)	10.31 (1.25)	9.56 (0.75)	9.61 (0.64)	8.63 (0.41)	7.87 (0.44)	7.46 (0.59)	7.18 (0.67)	6.28 (1.01)
-1.1		11.40 (1.91)	9.93 (0.71)	8.82 (0.43)	8.66 (0.46)	7.86 (0.29)	6.73 (0.39)	7.27 (0.73)	
-1.7	12.69 (5.57)	8.30 (3.31)	9.74 (1.19)	8.55 (0.52)	8.59 (0.51)	8.38 (0.51)	7.02 (0.55)	6.98 (1.03)	
-2.3			14.29 (5.97)	9.50 (1.33)	9.33 (1.23)	9.77 (1.34)			

Figure 37c. (continued)

3C144 - 5 COMPONENT FIT : CENTRAL OPTICAL DEPTH OF COMPONENT 3

	-2.5	-1.9	-1.3	-0.7	-0.1	0.5	1.1	1.7	2.3
2.5					0.475 (0.025)	0.549 (0.040)	0.636 (0.062)		
1.9				0.498 (0.018)	0.503 (0.016)	0.538 (0.018)	0.506 (0.019)	0.469 (0.019)	0.478 (0.030)
1.3			0.476 (0.031)	0.470 (0.014)	0.491 (0.011)	0.524 (0.010)	0.507 (0.013)	0.481 (0.013)	0.504 (0.020)
0.7		0.475 (0.028)	0.476 (0.020)	0.455 (0.012)	0.445 (0.009)	0.469 (0.009)	0.472 (0.011)	0.479 (0.014)	0.503 (0.020)
0.1	0.520 (0.041)	0.476 (0.024)	0.464 (0.016)	0.460 (0.013)	0.426 (0.011)	0.431 (0.012)	0.446 (0.012)	0.454 (0.013)	0.462 (0.024)
-0.5	0.494 (0.042)	0.475 (0.025)	0.438 (0.016)	0.444 (0.013)	0.422 (0.011)	0.415 (0.012)	0.433 (0.015)	0.435 (0.017)	0.429 (0.026)
-1.1		0.453 (0.023)	0.416 (0.016)	0.429 (0.011)	0.427 (0.011)	0.404 (0.009)	0.397 (0.013)	0.402 (0.022)	
-1.7	0.495 (0.030)	0.442 (0.024)	0.402 (0.019)	0.417 (0.014)	0.436 (0.013)	0.424 (0.013)	0.394 (0.017)	0.411 (0.040)	
-2.3			0.488 (0.042)	0.470 (0.025)	0.481 (0.029)	0.465 (0.030)			

Figure 37c. (continued)

3C144 - 5 COMPONENT FIT : CENTRAL FREQUENCY OF COMPONENT 3

	-2.5	-1.9	-1.3	-0.7	-0.1	0.5	1.1	1.7	2.3
2.5					-27.37 (0.97)	-29.79 (1.20)	-33.59 (1.36)		
1.9				-20.89 (0.82)	-20.10 (0.63)	-21.34 (0.83)	-22.16 (0.78)	-24.68 (0.74)	-24.24 (0.99)
1.3			-25.53 (1.34)	-22.30 (0.70)	-21.00 (0.55)	-21.66 (0.48)	-21.39 (0.58)	-20.84 (0.61)	-21.11 (0.89)
0.7		-26.12 (1.19)	-24.88 (0.82)	-24.23 (0.56)	-22.46 (0.51)	-22.34 (0.46)	-22.46 (0.58)	-21.52 (0.69)	-20.20 (0.89)
0.1	-28.85 (1.56)	-27.01 (1.03)	-25.66 (0.67)	-26.26 (0.56)	-24.06 (0.57)	-22.28 (0.62)	-23.41 (0.66)	-23.51 (0.75)	-21.87 (0.95)
-0.5	-28.71 (1.51)	-28.49 (1.02)	-26.07 (0.72)	-25.95 (0.57)	-25.16 (0.56)	-23.45 (0.67)	-23.55 (0.84)	-22.74 (1.02)	-22.80 (1.17)
-1.1		-26.09 (1.00)	-25.04 (0.76)	-24.03 (0.54)	-24.46 (0.57)	-24.24 (0.52)	-24.91 (0.84)	-23.68 (0.94)	
-1.7	-22.49 (1.18)	-23.67 (1.18)	-24.81 (1.06)	-23.56 (0.78)	-22.82 (0.67)	-22.29 (0.71)	-21.59 (0.83)	-23.78 (1.32)	
-2.3			-18.66 (1.89)	-20.34 (1.17)	-18.71 (1.44)	-17.04 (1.66)			

Figure 37c. (continued)

3C144 - 5 COMPONENT FIT : FULL WIDTH OF COMPONENT 3

	-2.5	-1.9	-1.3	-0.7	-0.1	0.5	1.1	1.7	2.3
2.5					60.4 (4.0)	65.5 (5.4)	76.0 (8.0)		
1.9				52.3 (3.0)	55.6 (2.9)	58.0 (3.1)	57.1 (3.4)	61.3 (3.5)	66.8 (6.0)
1.3			62.9 (4.8)	56.7 (2.5)	56.2 (2.1)	57.8 (1.8)	54.4 (2.2)	54.0 (2.4)	60.8 (3.8)
0.7		62.1 (4.3)	64.1 (3.2)	61.2 (2.1)	57.0 (1.8)	57.3 (1.7)	55.1 (2.0)	55.1 (2.5)	59.5 (3.8)
0.1	62.1 (5.3)	60.9 (3.5)	61.6 (2.5)	62.4 (2.1)	59.1 (2.0)	56.5 (2.3)	56.2 (2.2)	55.8 (2.3)	58.2 (4.3)
-0.5	57.9 (4.8)	60.6 (3.5)	64.3 (2.8)	64.9 (2.3)	60.5 (2.0)	56.7 (2.4)	59.6 (2.9)	59.6 (3.4)	56.8 (4.5)
-1.1		58.5 (3.4)	65.2 (3.0)	64.4 (2.2)	58.2 (2.0)	53.0 (1.6)	61.0 (2.7)	65.7 (4.9)	
-1.7	52.1 (4.3)	57.7 (4.2)	58.1 (3.6)	56.7 (2.9)	59.2 (2.6)	56.9 (2.7)	61.4 (4.2)	73.7 (9.1)	
-2.3			64.3 (8.2)	61.2 (5.4)	69.1 (7.4)	69.8 (8.6)			

Figure 37c. (continued)

3C144 - 5 COMPONENT FIT : CENTRAL OPTICAL DEPTH OF COMPONENT 4

	-2.5	-1.9	-1.3	-0.7	-0.1	0.5	1.1	1.7	2.3
2.5					0.590 (0.027)	0.576 (0.036)	0.582 (0.044)		
1.9				0.501 (0.025)	0.512 (0.022)	0.517 (0.023)	0.524 (0.025)	0.554 (0.028)	0.488 (0.160)
1.3			0.555 (0.028)	0.523 (0.017)	0.504 (0.015)	0.507 (0.013)	0.500 (0.017)	0.512 (0.019)	0.554 (0.026)
0.7		0.470 (0.025)	0.556 (0.018)	0.547 (0.012)	0.517 (0.012)	0.502 (0.012)	0.500 (0.015)	0.527 (0.018)	0.592 (0.025)
0.1	0.395 (0.033)	0.455 (0.021)	0.524 (0.016)	0.551 (0.013)	0.546 (0.012)	0.511 (0.015)	0.512 (0.015)	0.553 (0.017)	0.626 (0.029)
-0.5	0.366 (0.040)	0.403 (0.023)	0.479 (0.015)	0.532 (0.014)	0.533 (0.011)	0.525 (0.015)	0.561 (0.017)	0.589 (0.021)	0.627 (0.032)
-1.1		0.321 (0.035)	0.416 (0.016)	0.494 (0.011)	0.505 (0.012)	0.517 (0.011)	0.585 (0.014)	0.631 (0.023)	
-1.7	0.160 (0.094)	0.323 (0.030)	0.374 (0.023)	0.435 (0.017)	0.501 (0.015)	0.533 (0.016)	0.551 (0.020)	0.600 (0.034)	
-2.3			0.273 (0.137)	0.396 (0.030)	0.488 (0.031)	0.547 (0.034)			

Figure 37c. (continued)

3C144 - 5 COMPONENT FIT : CENTRAL FREQUENCY OF COMPONENT 4

	-2.5	-1.9	-1.3	-0.7	-0.1	0.5	1.1	1.7	2.3
2.5					-13.25 (0.44)	-13.80 (0.56)	-14.39 (0.84)		
1.9				-14.24 (0.22)	-13.56 (0.37)	-13.85 (0.38)	-14.56 (0.32)	-14.44 (0.58)	-13.47 (1.52)
1.3			-13.33 (0.56)	-13.95 (0.23)	-14.07 (0.21)	-13.90 (0.25)	-14.18 (0.30)	-14.46 (0.38)	-15.02 (0.60)
0.7		-13.39 (0.50)	-12.58 (0.36)	-13.13 (0.24)	-14.22 (0.18)	-14.00 (0.27)	-13.41 (0.32)	-13.93 (0.33)	-14.52 (0.40)
0.1	-13.55 (0.96)	-13.35 (0.50)	-12.86 (0.35)	-13.20 (0.31)	-14.02 (0.22)	-13.67 (0.26)	-12.77 (0.31)	-13.29 (0.31)	-14.05 (0.46)
-0.5	-13.82 (1.72)	-12.97 (0.80)	-13.30 (0.41)	-13.38 (0.34)	-13.30 (0.23)	-12.92 (0.22)	-12.62 (0.31)	-12.62 (0.44)	-13.29 (0.67)
-1.1		-13.44 (1.40)	-13.52 (0.50)	-13.41 (0.23)	-12.92 (0.23)	-12.69 (0.16)	-13.18 (0.27)	-13.15 (0.60)	
-1.7	-10.78 (3.42)	-15.72 (1.21)	-13.92 (0.81)	-12.96 (0.28)	-12.49 (0.23)	-12.45 (0.25)	-13.37 (0.41)	-13.76 (0.95)	
-2.3			-11.29 (1.99)	-12.50 (0.60)	-12.01 (0.51)	-11.74 (0.59)			

Figure 37c. (continued)

3C144 - 5 COMPONENT FIT : FULL WIDTH OF COMPONENT 4

	-2.5	-1.9	-1.3	-0.7	-0.1	0.5	1.1	1.7	2.3
2.5					12.09 (1.07)	13.26 (1.51)	12.96 (2.08)		
1.9				12.60 (0.72)	12.40 (0.91)	13.10 (1.03)	10.99 (0.91)	9.21 (1.06)	7.92 (1.78)
1.3			13.67 (1.30)	13.40 (0.66)	13.16 (0.60)	12.86 (0.62)	11.99 (0.75)	10.86 (0.84)	11.96 (1.28)
0.7		14.18 (1.27)	11.59 (0.74)	12.66 (0.54)	13.35 (0.50)	12.68 (0.60)	12.75 (0.73)	13.60 (0.86)	13.52 (1.07)
0.1	15.99 (2.42)	13.83 (1.19)	11.45 (0.68)	12.28 (0.60)	13.14 (0.52)	12.53 (0.64)	12.89 (0.72)	15.24 (0.81)	15.90 (1.19)
-0.5	15.73 (3.19)	13.78 (1.56)	12.44 (0.79)	11.85 (0.60)	11.88 (0.49)	12.02 (0.55)	13.63 (0.76)	14.96 (1.03)	16.63 (1.55)
-1.1		13.34 (2.16)	12.74 (0.93)	12.06 (0.50)	11.85 (0.52)	12.65 (0.41)	15.78 (0.70)	16.37 (1.28)	
-1.7	10.71 (4.50)	16.77 (2.65)	13.86 (1.55)	11.68 (0.70)	11.86 (0.57)	12.53 (0.62)	15.11 (0.98)	17.18 (2.02)	
-2.3			9.88 (2.88)	10.78 (1.36)	11.42 (1.22)	11.57 (1.28)			

Figure 37c. (continued)

3C144 - 5 COMPONENT FIT : CENTRAL OPTICAL DEPTH OF COMPONENT 5

	-2.5	-1.9	-1.3	-0.7	-0.1	0.5	1.1	1.7	2.3
2.5					(0.0)	(0.0)	(0.0)		
1.9				0.071 (0.016)	(0.0)	0.017 (0.019)	(0.0)	(0.0)	(0.0)
1.3			0.171 (0.028)	0.088 (0.013)	0.048 (0.012)	0.061 (0.011)	0.064 (0.013)	0.048 (0.013)	0.081 (0.021)
0.7		0.102 (0.025)	0.092 (0.017)	0.088 (0.011)	0.070 (0.010)	0.062 (0.009)	0.058 (0.011)	0.049 (0.014)	0.041 (0.021)
0.1	0.111 (0.037)	0.080 (0.022)	0.068 (0.014)	0.105 (0.012)	0.095 (0.010)	0.072 (0.011)	0.068 (0.012)	0.057 (0.014)	(0.0)
-0.5	0.086 (0.032)	0.097 (0.022)	0.072 (0.014)	0.092 (0.012)	0.093 (0.010)	0.072 (0.012)	0.070 (0.015)	0.036 (0.018)	(0.0)
-1.1		0.086 (0.018)	0.079 (0.013)	0.080 (0.010)	0.089 (0.010)	0.071 (0.008)	0.058 (0.014)	(0.0)	
-1.7	0.078 (0.021)	0.135 (0.019)	0.134 (0.016)	0.091 (0.013)	0.080 (0.012)	0.066 (0.012)	(0.0)	(0.0)	
-2.3			0.158 (0.036)	0.132 (0.023)	0.059 (0.031)	0.027 (0.035)			

Figure 37c. (continued)

3C144 - 6 COMPONENT FIT : RMS

	-2.5	-1.9	-1.3	-0.7	-0.1	0.5	1.1	1.7	2.3
2.5					******	******	******	******	
1.9				0.0370	0.0332	******	******	******	******
1.3			******	******	******	0.0187	0.0192	******	******
0.7		******	******	0.0198	0.0194	0.0178	0.0207	0.0248	******
0.1	******	******	******	0.0187	0.0184	0.0232	0.0242	0.0238	0.0384
-0.5	******	0.0356	0.0231	0.0172	0.0148	0.0227	0.0285	0.0317	0.0438
-1.1	******	******	0.0222	0.0157	0.0179	0.0150	0.0230	0.0368	
-1.7	******	0.0359	******	0.0253	******	0.0239	0.0320	0.0548	
-2.3		******	******	******	******	******			

Figure 38a. 3C144: Results of gaussian analysis — six-component solution — RMS (in optical depth)

3C144 - 6 COMPONENT FIT : DC OFFSET

	-2.5	-1.9	-1.3	-0.7	-0.1	0.5	1.1	1.7	2.3
2.5									
1.9				-0.011 (0.017)	-0.021 (0.011)				
1.3						0.033 (0.007)	0.035 (0.006)		
0.7				-0.003 (0.010)	0.022 (0.010)	0.014 (0.006)	0.015 (0.006)	0.078 (0.009)	
0.1				-0.002 (0.007)	0.022 (0.007)	0.035 (0.008)	0.047 (0.008)	0.081 (0.008)	0.115 (0.011)
-0.5		-0.053 (0.022)	-0.027 (0.012)	-0.008 (0.008)	0.003 (0.006)	0.024 (0.008)	0.038 (0.010)	0.059 (0.010)	0.084 (0.011)
-1.1			-0.034 (0.012)	-0.023 (0.008)	0.000 (0.008)	0.039 (0.005)	0.016 (0.008)	0.034 (0.012)	
-1.7		-0.048 (0.021)		-0.027 (0.013)		-0.012 (0.009)	0.034 (0.010)	0.071 (0.018)	
-2.3									

Figure 38b. 3C144: Results of gaussian analysis — six-component solution — DC offset (in optical depth).

3C144 - 6 COMPONENT FIT : CENTRAL OPTICAL DEPTH OF COMPONENT 1

	-2.5	-1.9	-1.3	-0.7	-0.1	0.5	1.1	1.7	2.3
2.5									
1.9				0.980 (0.035)	0.944 (0.076)				
1.3						0.929 (0.026)	0.984 (0.032)		
0.7				0.955 (0.024)	0.938 (0.020)	0.957 (0.028)	1.048 (0.049)	1.168 (0.029)	
0.1				0.994 (0.029)	1.058 (0.028)	1.090 (0.037)	1.168 (0.038)	1.172 (0.045)	1.094 (0.066)
-0.5		1.047 (0.065)	1.103 (0.021)	1.013 (0.036)	1.052 (0.066)	1.208 (0.062)	1.230 (0.047)	1.191 (0.086)	0.938 (0.184)
-1.1			1.121 (0.139)	1.065 (0.080)	1.009 (0.173)	1.187 (0.091)	1.294 (0.040)	1.240 (0.079)	
-1.7		0.814 (0.268)		1.378 (0.030)		1.213 (0.180)	1.259 (0.096)	1.229 (0.142)	
-2.3									

Figures 38c. 3C144: Results of gaussian analysis — six-component solution — central optical depths, central frequencies (KHz), and full widths at half maximum (KHz) of gaussian components, by component. For component 6, the central frequency and full width were held fixed at 40.0 and 50.0 KHz, respectively.

3C144 - 6 COMPONENT FIT : CENTRAL FREQUENCY OF COMPONENT 1

	-2.5	-1.9	-1.3	-0.7	-0.1	0.5	1.1	1.7	2.3
2.5									
1.9				-50.10 (0.10)	-50.36 (0.09)				
1.3						-50.46 (0.05)	-50.51 (0.05)		
0.7				-50.20 (0.06)	-50.22 (0.05)	-50.43 (0.05)	-50.55 (0.05)	-50.56 (0.05)	
0.1				-50.41 (0.06)	-50.50 (0.05)	-50.59 (0.06)	-50.63 (0.05)	-50.74 (0.05)	-50.87 (0.08)
-0.5		-51.29 (0.13)	-50.96 (0.06)	-50.60 (0.07)	-50.59 (0.07)	-50.82 (0.07)	-50.84 (0.06)	-50.86 (0.07)	-50.96 (0.12)
-1.1			-51.18 (0.15)	-51.01 (0.08)	-50.94 (0.09)	-51.04 (0.06)	-51.10 (0.05)	-50.97 (0.09)	
-1.7		-52.13 (0.20)		-51.44 (0.24)		-51.32 (0.07)	-51.29 (0.08)	-51.16 (0.14)	
-2.3									

Figure 38c. (continued)

3C144 - 6 COMPONENT FIT : FULL WIDTH OF COMPONENT 1

	-2.5	-1.9	-1.3	-0.7	-0.1	0.5	1.1	1.7	2.3
2.5									
1.9				9.64 (0.34)	8.57 (0.44)				
1.3						8.07 (0.19)	7.71 (0.20)		
0.7				9.20 (0.21)	8.84 (0.19)	8.27 (0.19)	8.08 (0.24)	8.03 (0.19)	
0.1				9.04 (0.21)	8.84 (0.18)	8.40 (0.22)	8.22 (0.21)	7.93 (0.22)	7.14 (0.34)
-0.5		10.11 (0.46)	10.09 (0.19)	8.97 (0.21)	8.59 (0.24)	8.70 (0.26)	8.16 (0.24)	7.78 (0.34)	6.85 (0.68)
-1.1			9.98 (0.48)	9.15 (0.28)	8.34 (0.45)	8.51 (0.25)	8.40 (0.19)	7.99 (0.34)	
-1.7		8.26 (1.02)		9.63 (0.38)		8.50 (0.46)	8.42 (0.36)	8.22 (0.57)	
-2.3									

Figure 38c. (continued)

3C144 - 6 COMPONENT FIT : CENTRAL OPTICAL DEPTH OF COMPONENT 2

	-2.5	-1.9	-1.3	-0.7	-0.1	0.5	1.1	1.7	2.3
2.5									
1.9				0.391 (0.279)	0.207 (0.210)				
1.3						0.349 (0.090)	0.441 (0.034)		
0.7				0.223 (0.136)	0.250 (0.181)	0.259 (0.068)	0.291 (0.040)	0.345 (0.047)	
0.1				0.197 (0.064)	0.243 (0.046)	0.237 (0.095)	0.206 (0.078)	0.287 (0.041)	0.420 (0.058)
-0.5		0.211 (0.305)	0.066 (0.018)	0.215 (0.053)	0.311 (0.064)	0.187 (0.065)	0.204 (0.076)	0.294 (0.078)	0.597 (0.176)
-1.1			0.139 (0.126)	0.247 (0.074)	0.370 (0.166)	0.270 (0.089)	0.227 (0.049)	0.294 (0.087)	
-1.7		0.534 (0.232)		0.122 (0.081)		0.277 (0.165)	0.296 (0.094)	0.336 (0.158)	
-2.3									

Figure 38c. (continued)

3C144 - 6 COMPONENT FIT : CENTRAL FREQUENCY OF COMPONENT 2

	-2.5	-1.9	-1.3	-0.7	-0.1	0.5	1.1	1.7	2.3
2.5									
1.9				-31.27 (21.9)	-46.02 (9.09)				
1.3						-44.19 (3.83)	-44.55 (1.72)		
0.7				-47.91 (6.76)	-42.03 (12.2)	-46.61 (3.27)	-48.98 (1.38)	-42.22 (5.08)	
0.1				-52.49 (2.12)	-48.76 (2.37)	-46.57 (5.34)	-48.25 (3.86)	-49.23 (1.24)	-48.71 (0.96)
-0.5		-51.84 (18.0)	-63.89 (0.85)	-52.25 (1.11)	-52.44 (0.49)	-52.17 (1.07)	-49.44 (3.12)	-50.69 (0.85)	-50.70 (0.40)
-1.1			-55.06 (4.53)	-52.42 (0.62)	-51.73 (0.40)	-52.12 (0.46)	-51.87 (1.10)	-52.52 (0.87)	
-1.7		-50.52 (1.22)		-57.80 (1.07)		-51.47 (0.56)	-51.61 (0.85)	-52.01 (1.08)	
-2.3									

Figure 38c. (continued)

3C144 - 6 COMPONENT FIT : FULL WIDTH OF COMPONENT 2

	-2.5	-1.9	-1.3	-0.7	-0.1	0.5	1.1	1.7	2.3
2.5									
1.9				43.5 (20.7)	24.0 (17.4)				
1.3						28.3 (4.6)	23.7 (2.3)		
0.7				33.2 (7.8)	36.3 (11.8)	26.8 (5.1)	21.2 (3.5)	30.5 (6.1)	
0.1				24.6 (3.7)	27.1 (4.2)	26.7 (7.8)	25.7 (7.6)	22.1 (3.2)	20.2 (2.5)
-0.5		33.4 (17.0)	7.7 (2.4)	21.1 (3.6)	15.8 (1.4)	18.6 (3.7)	24.5 (8.0)	18.7 (4.1)	14.5 (2.2)
-1.1			16.3 (4.7)	17.1 (2.6)	14.2 (2.3)	15.2 (2.0)	22.0 (3.1)	18.5 (3.1)	
-1.7		16.0 (4.2)		5.9 (2.0)		15.8 (4.7)	18.7 (3.8)	18.8 (5.1)	
-2.3									

Figure 38c. (continued)

3C144 - 6 COMPONENT FIT : CENTRAL OPTICAL DEPTH OF COMPONENT 3

	-2.5	-1.9	-1.3	-0.7	-0.1	0.5	1.1	1.7	2.3
2.5									
1.9				0.169 (0.035)	0.207 (0.087)				
1.3						0.201 (0.052)	0.324 (0.106)		
0.7				0.347 (0.048)	0.163 (0.026)	0.218 (0.059)	0.265 (0.043)	0.324 (0.061)	
0.1				0.373 (0.034)	0.321 (0.033)	0.287 (0.061)	0.324 (0.051)	0.305 (0.030)	0.262 (0.050)
-0.5		0.354 (0.137)	0.352 (0.023)	0.401 (0.031)	0.424 (0.014)	0.400 (0.021)	0.406 (0.048)	0.420 (0.042)	0.371 (0.059)
-1.1			0.388 (0.026)	0.404 (0.016)	0.401 (0.016)	0.415 (0.015)	0.440 (0.024)	0.472 (0.056)	
-1.7		0.192 (0.104)		0.419 (0.018)		0.412 (0.023)	0.453 (0.036)	0.491 (0.093)	
-2.3									

Figure 38c. (continued)

3C144 - 6 COMPONENT FIT : CENTRAL FREQUENCY OF COMPONENT 3

	-2.5	-1.9	-1.3	-0.7	-0.1	0.5	1.1	1.7	2.3
2.5									
1.9				-24.88 (0.42)	-23.63 (0.85)				
1.3						-24.18 (0.72)	-23.47 (1.76)		
0.7				-24.01 (0.35)	-24.16 (0.39)	-23.17 (0.93)	-23.11 (0.60)	-23.15 (0.55)	
0.1				-23.66 (0.38)	-24.36 (0.28)	-23.90 (0.52)	-23.28 (0.44)	-23.48 (0.25)	-23.33 (0.33)
-0.5		-24.59 (0.70)	-24.27 (0.41)	-23.83 (0.39)	-24.14 (0.17)	-24.12 (0.21)	-23.65 (0.32)	-23.17 (0.30)	-23.08 (0.34)
-1.1			-24.60 (0.39)	-24.59 (0.20)	-24.16 (0.22)	-24.21 (0.12)	-24.19 (0.16)	-23.47 (0.27)	
-1.7		-28.26 (2.26)		-24.75 (0.23)		-24.07 (0.26)	-24.23 (0.25)	-23.97 (0.36)	
-2.3									

Figure 38c. (continued)

3C144 - 6 COMPONENT FIT : FULL WIDTH OF COMPONENT 3

	-2.5	-1.9	-1.3	-0.7	-0.1	0.5	1.1	1.7	2.3
2.5									
1.9				4.69 (1.14)	7.93 (2.00)				
1.3						9.01 (1.42)	12.35 (2.86)		
0.7				9.24 (0.90)	6.55 (0.97)	9.54 (1.68)	9.22 (1.33)	8.15 (1.04)	
0.1				9.87 (0.94)	8.12 (0.70)	8.84 (1.21)	8.79 (1.06)	6.68 (0.64)	5.12 (0.96)
-0.5		11.03 (2.61)	9.51 (0.76)	10.48 (0.91)	8.79 (0.38)	8.04 (0.53)	8.27 (0.81)	7.75 (0.72)	6.46 (0.90)
-1.1			9.94 (0.85)	9.19 (0.48)	8.96 (0.48)	7.75 (0.29)	6.93 (0.40)	7.47 (0.71)	
-1.7		11.94 (3.73)		8.37 (0.50)		8.83 (0.63)	7.38 (0.60)	7.33 (1.05)	
-2.3									

Figure 38c. (continued)

3C144 - 6 COMPONENT FIT : CENTRAL OPTICAL DEPTH OF COMPONENT 4

	-2.5	-1.9	-1.3	-0.7	-0.1	0.5	1.1	1.7	2.3
2.5									
1.9				0.528 (0.098)	0.540 (0.119)				
1.3						0.570 (0.078)	0.538 (0.137)		
0.7				0.526 (0.042)	0.516 (0.047)	0.488 (0.043)	0.438 (0.029)	0.520 (0.093)	
0.1				0.495 (0.025)	0.500 (0.030)	0.507 (0.060)	0.490 (0.039)	0.441 (0.040)	0.436 (0.060)
-0.5		0.328 (0.074)	0.445 (0.022)	0.497 (0.022)	0.491 (0.015)	0.476 (0.027)	0.541 (0.040)	0.536 (0.048)	0.500 (0.092)
-1.1			0.382 (0.023)	0.473 (0.014)	0.485 (0.016)	0.461 (0.023)	0.483 (0.042)	0.563 (0.059)	
-1.7		0.413 (0.121)		0.431 (0.017)		0.509 (0.026)	0.478 (0.046)	0.530 (0.085)	
-2.3									

Figure 38c. (continued)

3C144 - 6 COMPONENT FIT : CENTRAL FREQUENCY OF COMPONENT 4

	-2.5	-1.9	-1.3	-0.7	-0.1	0.5	1.1	1.7	2.3
2.5									
1.9				-14.43 (0.28)	-13.60 (0.58)				
1.3						-14.09 (0.42)	-13.82 (0.92)		
0.7				-12.99 (0.28)	-14.30 (0.23)	-13.67 (0.54)	-13.02 (0.43)	-13.83 (0.48)	
0.1				-12.89 (0.33)	-13.89 (0.24)	-13.50 (0.38)	-12.60 (0.38)	-13.22 (0.30)	-14.76 (0.55)
-0.5		-12.52 (0.78)	-13.17 (0.38)	-13.08 (0.35)	-13.16 (0.18)	-12.81 (0.21)	-12.51 (0.34)	-12.45 (0.44)	-13.30 (0.69)
-1.1			-13.33 (0.47)	-13.29 (0.21)	-12.81 (0.22)	-12.59 (0.14)	-13.02 (0.25)	-13.08 (0.60)	
-1.7		-15.85 (2.21)		-12.99 (0.27)		-12.33 (0.26)	-13.24 (0.40)	-13.85 (1.04)	
-2.3									

Figure 38c. (continued)

3C144 - 6 COMPONENT FIT : FULL WIDTH OF COMPONENT 4

	-2.5	-1.9	-1.3	-0.7	-0.1	0.5	1.1	1.7	2.3
2.5									
1.9				12.36 (1.33)	12.42 (1.50)				
1.3						12.84 (1.04)	11.08 (1.30)		
0.7				11.58 (0.69)	12.59 (0.78)	11.34 (0.93)	10.65 (0.90)	11.14 (1.26)	
0.1				10.84 (0.68)	11.42 (0.64)	11.43 (0.93)	11.85 (0.96)	12.77 (1.06)	12.73 (1.85)
-0.5		11.19 (1.84)	11.51 (0.81)	10.88 (0.63)	10.91 (0.44)	10.90 (0.66)	12.76 (0.99)	13.77 (1.34)	14.59 (2.35)
-1.1			11.55 (0.97)	11.42 (0.49)	11.36 (0.52)	11.72 (0.50)	13.78 (0.98)	15.24 (1.76)	
-1.7		18.40 (4.40)		11.68 (0.69)		11.92 (0.74)	13.53 (1.34)	15.62 (2.96)	
-2.3									

Figure 38c. (continued)

3C144 - 6 COMPONENT FIT : CENTRAL OPTICAL DEPTH OF COMPONENT 5

	-2.5	-1.9	-1.3	-0.7	-0.1	0.5	1.1	1.7	2.3
2.5									
1.9				0.250 (0.499)	0.437 (0.163)				
1.3						0.398 (0.077)	0.385 (0.063)		
0.7				0.409 (0.089)	0.368 (0.164)	0.417 (0.054)	0.484 (0.033)	0.436 (0.101)	
0.1				0.453 (0.032)	0.422 (0.038)	0.384 (0.080)	0.415 (0.059)	0.522 (0.041)	0.621 (0.061)
-0.5		0.471 (0.227)	0.440 (0.017)	0.410 (0.027)	0.431 (0.013)	0.443 (0.025)	0.401 (0.052)	0.445 (0.043)	0.511 (0.090)
-1.1			0.422 (0.022)	0.415 (0.014)	0.422 (0.013)	0.443 (0.021)	0.455 (0.040)	0.421 (0.049)	
-1.7		0.302 (0.122)		0.426 (0.014)		0.425 (0.022)	0.439 (0.045)	0.397 (0.078)	
-2.3									

Figure 38c. (continued)

3C144 - 6 COMPONENT FIT : CENTRAL FREQUENCY OF COMPONENT 5

	-2.5	-1.9	-1.3	-0.7	-0.1	0.5	1.1	1.7	2.3
2.5									
1.9				-4.6 (19.1)	-15.2 (12.9)				
1.3						-10.3 (6.4)	-8.2 (4.7)		
0.7				-15.4 (7.0)	-12.0 (10.7)	-14.4 (4.2)	-16.6 (1.8)	-9.6 (5.6)	
0.1				-20.2 (2.4)	-16.0 (2.6)	-14.4 (6.7)	-17.1 (4.5)	-16.6 (1.3)	-14.5 (0.9)
-0.5		-19.5 (12.9)	-23.4 (1.0)	-21.0 (2.3)	-21.7 (0.8)	-20.0 (1.4)	-17.4 (4.6)	-17.7 (2.2)	-17.1 (1.5)
-1.1			-22.7 (1.5)	-21.2 (1.1)	-22.2 (1.0)	-21.2 (0.9)	-18.0 (1.5)	-18.2 (2.3)	
-1.7		-17.6 (7.1)		-23.8 (0.8)		-19.7 (1.6)	-17.0 (1.6)	-16.1 (3.0)	
-2.3									

Figure 38c. (continued)

3C144 - 6 COMPONENT FIT : FULL WIDTH OF COMPONENT 5

	-2.5	-1.9	-1.3	-0.7	-0.1	0.5	1.1	1.7	2.3
2.5									
1.9				33.1 (18.7)	48.8 (13.3)				
1.3						41.2 (7.1)	33.7 (5.2)		
0.7				44.9 (7.2)	40.4 (9.4)	42.7 (4.5)	41.6 (2.6)	33.0 (5.5)	
0.1				47.3 (3.8)	41.3 (3.1)	42.5 (7.0)	44.8 (5.7)	38.9 (2.7)	35.1 (2.4)
-0.5		43.3 (11.5)	54.4 (3.8)	52.3 (4.1)	49.5 (2.4)	46.1 (3.6)	47.5 (7.2)	46.7 (6.1)	41.2 (5.9)
-1.1			55.4 (4.4)	55.6 (3.1)	52.2 (2.8)	44.1 (2.5)	42.1 (3.6)	48.4 (7.1)	
-1.7		59.8 (10.4)		56.4 (2.9)		50.2 (4.4)	45.0 (5.0)	49.9 (11.9)	
-2.3									

Figure 38c. (continued)

3C144 - 6 COMPONENT FIT : CENTRAL OPTICAL DEPTH OF COMPONENT 6

	-2.5	-1.9	-1.3	-0.7	-0.1	0.5	1.1	1.7	2.3
2.5									
1.9				0.096 (0.026)	(0.0)				
1.3						0.063 (0.014)	0.075 (0.011)		
0.7				0.096 (0.015)	0.084 (0.015)	0.066 (0.011)	0.064 (0.011)	0.075 (0.014)	
0.1				0.097 (0.010)	0.104 (0.011)	0.075 (0.015)	0.066 (0.014)	0.063 (0.012)	0.028 (0.018)
-0.5		0.096 (0.028)	0.061 (0.011)	0.078 (0.009)	0.086 (0.007)	0.074 (0.011)	0.065 (0.017)	0.035 (0.017)	0.012 (0.021)
-1.1			0.072 (0.011)	0.074 (0.008)	0.084 (0.008)	0.069 (0.007)	0.058 (0.012)	(0.0)	
-1.7		0.104 (0.034)		0.093 (0.012)		0.065 (0.011)	0.022 (0.017)	0.004 (0.034)	
-2.3									

Figure 38c. (continued)

for the wings at both ends of the spectrum. This solution converges for all but 3 of the 64 spectra and the parameteters are found to show more reasonable spatial variations. Unfortunately, this solution has higher values of the RMS and frequently contains small non-random disagreements with the data.

In a last attempt to obtain a solution without extremely wide components, an eight-component solution was tried. This solution converges for only one of the spectra with the results listed in Table VIII and plotted in Figure 36. Although the fit is very good, there is still a wide component in the solution and several components have only marginal significance. We must conclude that, with the present signal-to-noise ratio, very wide components are necessary to fit the spectra. If these components were broadened solely by their temperature, one would expect brightness temperatures in the hydrogen emission around 1000 °K. Since the observed emission is less than 100 °K (Radhakrishnan, et al 1972c), the wide components must result from a blend of a great many small cold clouds or a considerable turbulence.

The first component which is strongest to the west is found at lower frequencies to the southeast of the source

TABLE VIII: 3C144 — 8 COMPONENT FIT

X = - 0.1

Y = + 0.1

RMS = 0.018

Constant = 0.021 ± 0.009

Component	Optical Depth τ_0	$\sigma(\tau_0)$	Frequency f_0	$\sigma(f_0)$	Full Width d_0	$\sigma(d_0)$
1	0.048	0.022	-63.08	0.89	7.83	3.37
2	1.125	0.027	-50.57	0.05	9.20	0.18
3	0.351	0.013	-35.56	3.09	38.45	5.63
4	0.405	0.080	-24.26	0.49	8.75	0.93
5	0.712	0.179	-13.97	0.79	11.96	1.92
6	0.210	0.324	-02.85	5.31	16.22	14.15
7	0.090	0.114	+11.33	25.80	26.23	32.38
8	0.097	0.021	+40.00	—	50.00	—

with a range in velocity across the source of 0.4 km/sec (see Figures 37). This component is also significantly wider toward the southeast. The second component is very weak over the northern parts of the source and is found to be narrower and to occur at higher frequencies toward the northwest. The third component is found at lower frequencies toward the east and is weaker just south of the center of the source. The widths of this broad component are quite uncertain and show no significant systematic trends. The peak optical depths of the fourth component have a spatial distribution similar to that seen in Figure 33i. This component tends to be wider where it is strongest and to occur at lower frequencies toward the northwest. The high frequency wing seems to be strongest on the eastern side of the source, but this is quite sensitive to the DC offsets. A single DC offset is used for all frequencies because of the considerable number of frequency shifts and the relatively high optical depths present. However, as may be seen in Figures 34, this approximation is not really very good.

E. Results — Noise

The spectrum of the spatially constant part of the noise, computed using equation (3B-1), is plotted in Figure 39a. This spectrum has a profile very similar to that of the short-spacing flux spectrum (Figure 31), although the different frequency shifts sometimes have quite different amounts of noise. The noise is essentially a linear function of the short-spacing flux with a slope about 0.28 or 0.45 °K/flux unit depending on frequency shift (see Figure 39b). The noise levels for Cassiopeia A, despite its higher flux, are lower and the slope is only 0.11 °K/flux unit. The higher noise for the Crab Nebula probably arises from the sparseness and poor calibration of the data at the shortest spacings. The spectrum of the upper limit to the spatially variable part of the noise is plotted in Figure 39c. Although the variable part of the noise is again much smaller than the constant part, the variable part for 3C144 is larger than for 3C461 in absolute as well as relative magnitude.

The Monte Carlo tests again give results in good accord with the theory although at - 94 KHz a large increase in noise during the deconvolution process was

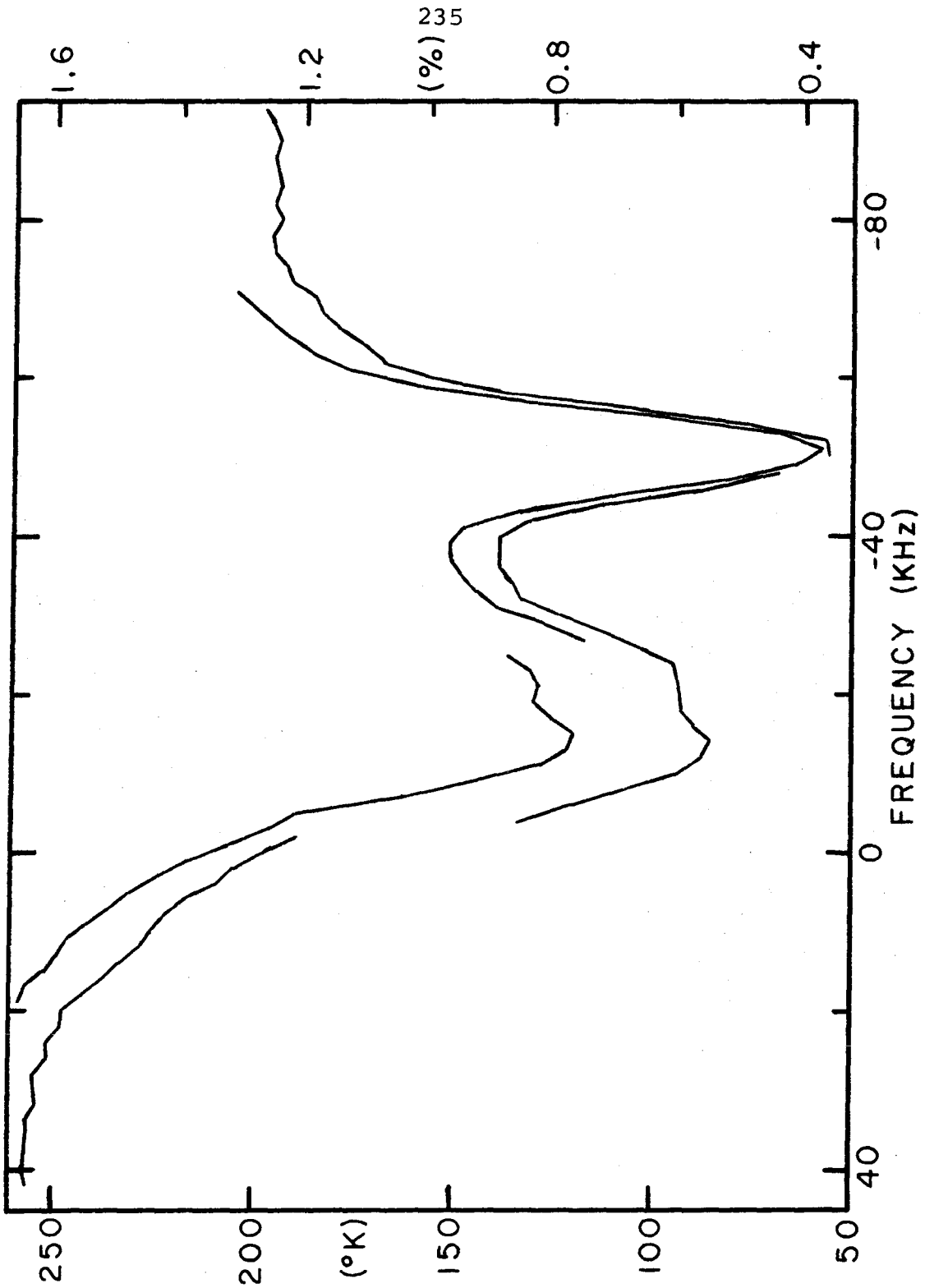

Figure 39a. 3C144: Spatially constant part of the noise as a function of frequency in °K (left hand scale) and in percent of the peak brightness on the continuum map (right hand scale). Each continuous line represents a different frequency shift.

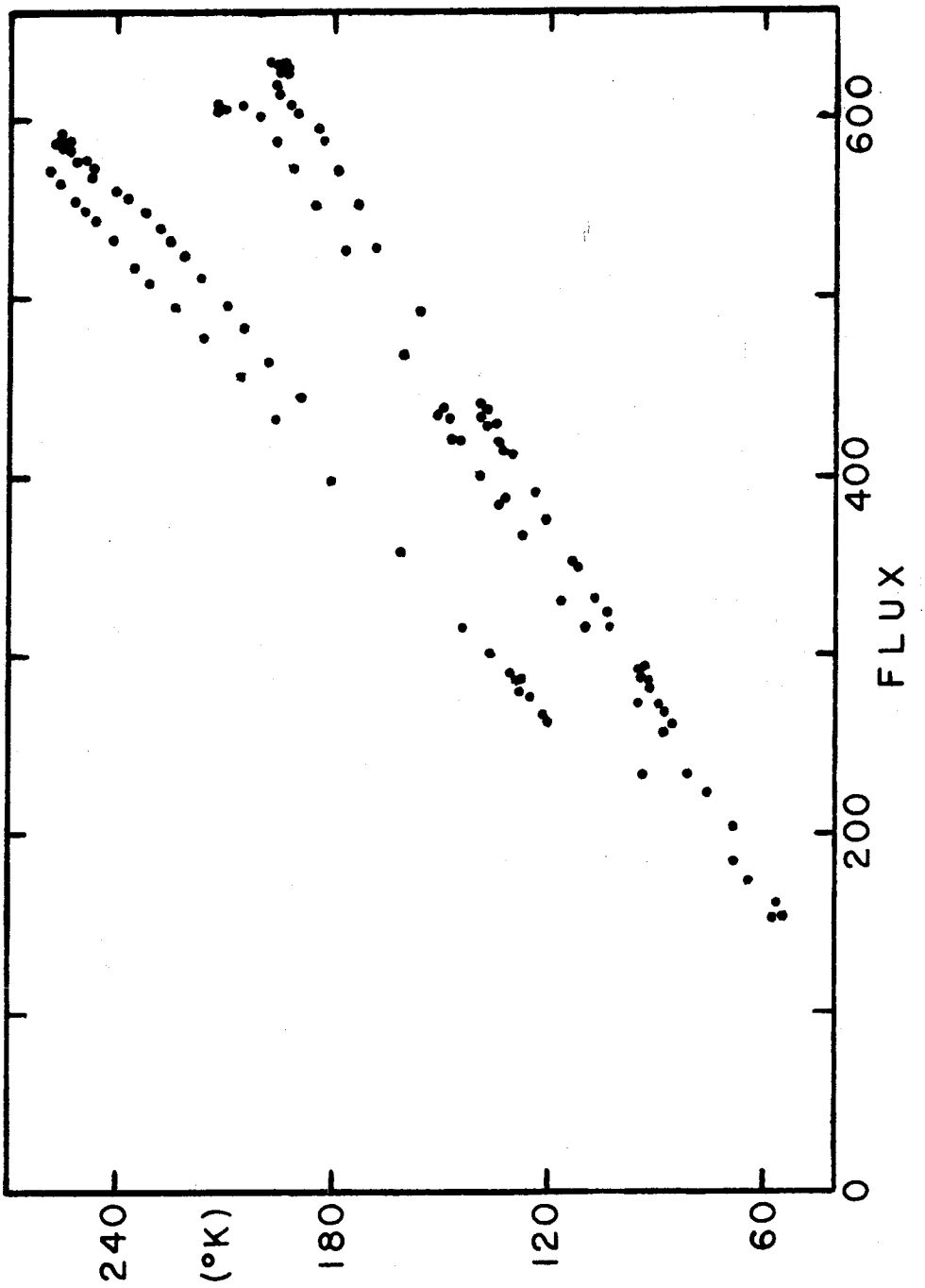

Figure 39b. 3C144: Spatially constant part of the noise in °K as a function of flux at 200 feet east-west.

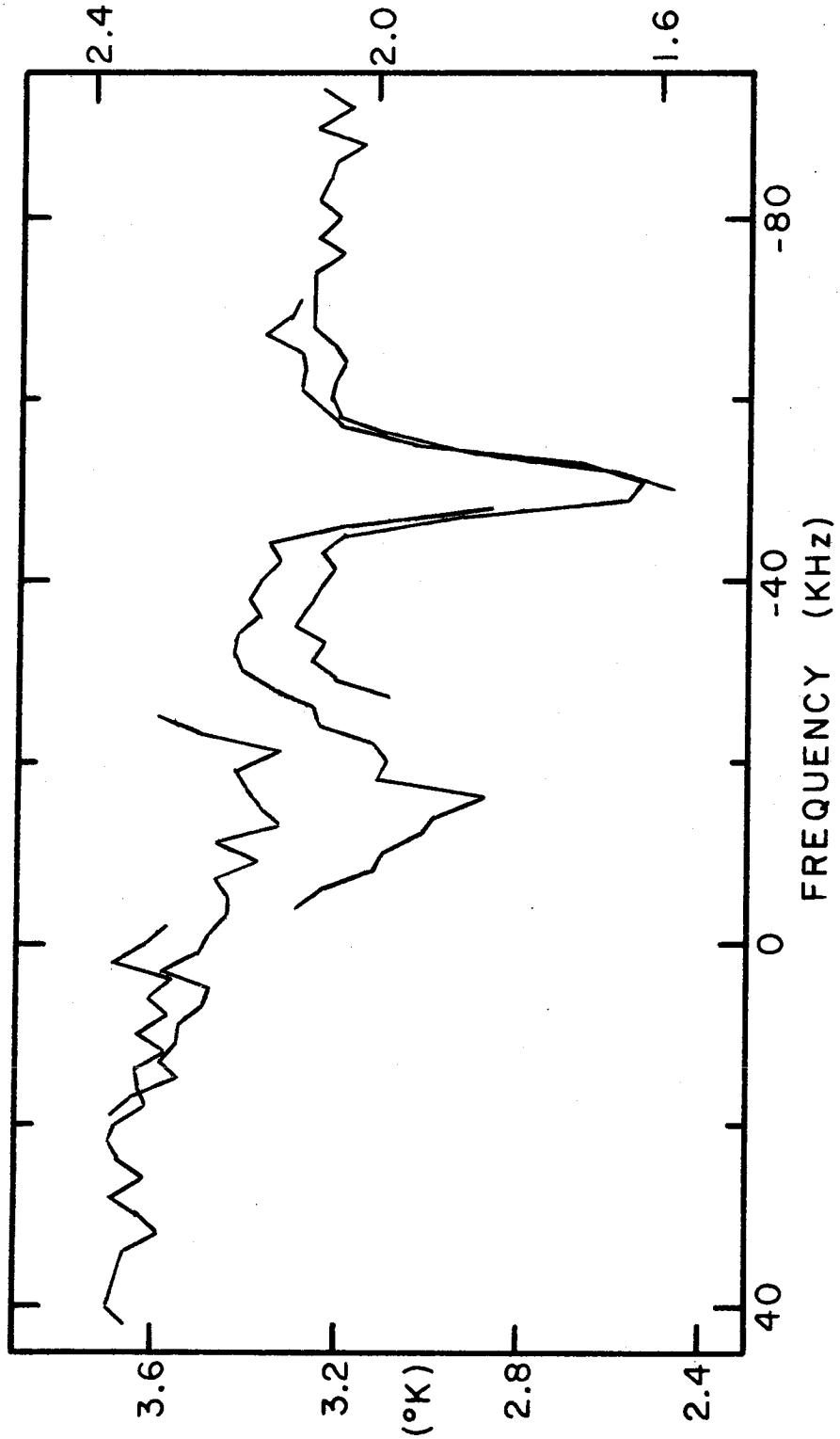

Figure 39c. 3C144: Upper limit to the spatially variable part of the noise as a function of frequency in °K (left hand scale) and relative to the peak brightness on the continuum map (times 10^4) (right hand scale). Each continuous line represents a different frequency shift.

needed to bring the results into accord (see Table V, Chapter 3B). On the dirty maps the noise is very nearly constant with a slight tendency at - 50 KHz for the noise to be larger off the source. However, on the clean maps, the noise is largest north and south of the source and in the southwest corner of the map area. These peaks are fairly well correlated with the major spurious responses seen in Figure 30.

F. Interpretation

The Crab Nebula is a much-studied supernova remnant. Trimble (1968) has measured the proper motions and radial velocities of a large number of filaments within the nebula. From her data and other considerations, she finds that the distance to the nebula is 2.02 Kpc. At this distance, the nebula is about 200 parsecs below the plane of the Galaxy. Since the Crab Nebula is near the galactic anti-center direction, the observed velocities of hydrogen clouds are poor indicators of their distances. Roberts (1972) has applied the TASS model of the Galaxy to the Perseus arm for the direction of the Crab Nebula. His results for the average gas density and radial velocity as a function of distance from the Sun are plotted in Figure 40.

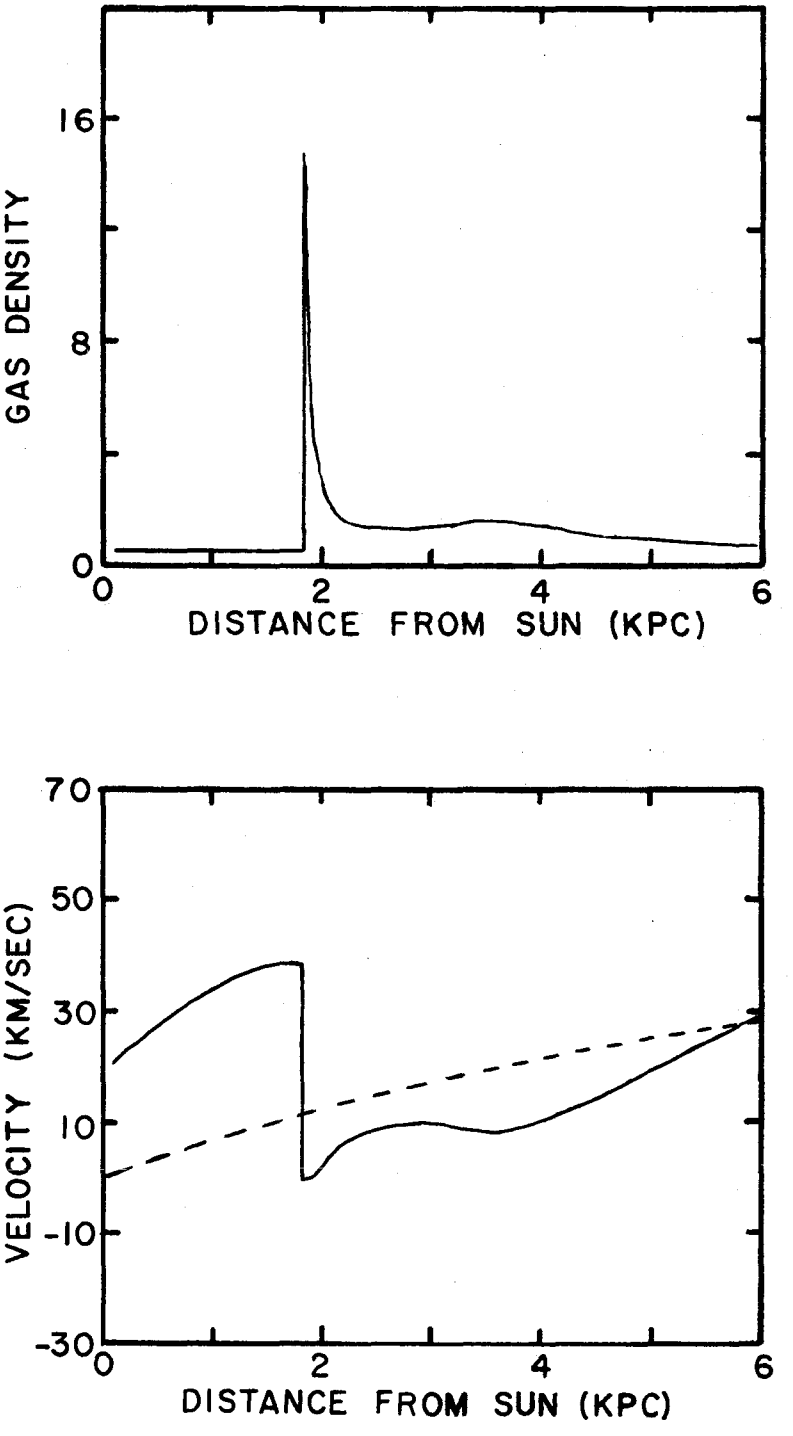

Figure 40. Predicted average gas density and line of sight velocity as functions of distance from the Sun in the TASS model for galactic longitudes 185°-195°, from Roberts (1972). Broken line from equilibrium model of Schmidt (1965).

At a distance of 1.8 Kpc, the shock front causes the radial velocity to drop abruptly to zero. Following the shock, the density drops rapidly and the velocity increases. The main arm is predicted to be at a velocity of 9 km/sec and a distance of 2.9 $\pm$ 0.3 Kpc.

Thus, we should expect to observe absorption features only from hydrogen near the Sun and within the post-shock region of the Perseus arm. Unfortunately, there are no spectral features at the predicted velocities (see Figure 30, for example). This negative result could have several explanations: (1) by chance, there might be no neutral hydrogen in the post-shock region in this direction; (2) the shock front may not be sustained to a height of 200 parsecs above the plane of the Galaxy although it is strong at a height of 100 parsecs in the direction of 3C461; (3) the source may be closer to us than given by Trimble; or (4) the TASS model may be wrong for this part of the Galaxy. We observe in the optical depth maps a considerable number of peaks and ridges within each of the spectral features. It would not be unreasonable to attribute these coincidences in velocity to the basic structure of the Galaxy (as we do for 3C461). However, we could also interpret the results as small concentrations within a few

large hydrogen clouds. Such an interpretation is supported by the large scale gradients found in the central velocities of the gaussian components.

The five-component solution of the spectra into gaussians allows us to deduce some reasonable values for the physical parameters of the hydrogen observed (see Figures 37). Component one has apparent temperatures ranging from 63 $\pm$ 3 °K to 105 $\pm$ 4 °K. (The six-component solution suggests apparent temperatures somewhat lower than these.) The second component has the lowest apparent temperatures with well-determined values less than 50 °K over the western half of the source. The fourth component has apparent temperatures around 150 °K. The computations of the physical parameters are summarized in Table IX. The parameters are computed for each component and the sum over the components at the maximum (H), average (A), and minimum (L) column densities. The column density divided by temperature, computed using equation (4-1), is given in the second column. The third column lists the column densities at an assumed temperature of 50 °K. If we assume a distance of 2.02 Kpc, we may express the column density as a mass observed per cell 0.6 arc minutes on a

TABLE IX: 3C144 — SAMPLE DENSITY AND MASS CALCULATIONS

Component	Parameter	Column Density $\frac{pc}{cm^3-^\circ K}$	Column Density $\frac{pc}{cm^3}$	Mass Per Cell $\frac{M_\odot}{cell}$	Total Mass $M_\odot$	Density $\frac{1}{cm^3}$
	H	1.99	100	0.30		113
1	A	1.48	74	0.23	13.9	84
	L	1.16	58	0.18		66
	H	0.56	28	0.09		32
2	A	0.31	15	0.05	2.9	18
	L	0.03	1.5	0.005		2
	H	6.47	324	0.99		368
3	A	3.74	187	0.57	35.0	213
	L	3.13	156	0.48		178
	H	1.40	70	0.22		80
4	A	0.88	44	0.14	8.2	50
	L	0.23	12	0.04		13
	H	1.15	58	0.18		65
5	A	0.43	22	0.07	4.0	24
	L	0	0	0		0
	H	8.88	444	1.36		505
TOTAL	A	6.84	342	1.05	64.0	388
	L	5.95	298	0.91		338

side (fourth column) and as a total mass (fifth column). If we assume the hydrogen to have a depth of one beam-width (0.88 pc at 2.02 pc), we obtain the densities in the sixth column.

The densities given in the table are quite substantial, but, at least for components 3, 4 and 5, almost certainly constitute upper limits. Since these three components most probably represent blends of several clouds, the use of a single beamwidth to represent a depth scale is improper. In fact, the lack of rapid spatial variations in these components suggests that they are considerably closer to us than the assumed 2.02 Kpc. The consistent behavior of all components across the source also suggests that the scale size is larger than a beamwidth. The total mass observed is only 64 solar masses and should be considered as an upper limit. Not only will beam-smearing effects cause this number to be too large, but also we assume in the computation a distance and a temperature which are themselves upper limits. Over half the mass observed is contained in the very broad component. That this component is real is established not only by the gaussian analysis, but also by the presence of details in

the spatial distribution of optical depth which remain over wide ranges of frequency. However, it is easy to establish that the width of this component is not representative of the temperature of the hydrogen.

We may ask if the optical image of the Crab Nebula shows any effects which might be due to interstellar absorption. Hogg, et al (1969) have observed the source at 11 cm wavelength and superposed their map on an optical print of the nebula. The radio contours show minima at some of the darker areas of the nebula suggesting that the lack of emission is due to local density minima in the source. However, the radio contours simply ignore some of the dark bays and spots visible on the optical plate. One is tempted to suggest that such dark spots are caused by intervening interstellar matter. Unfortunately, there is little, if any, correlation between the peaks in hydrogen density and these darker areas. In fact, since the radio source at 21-cm wavelength is larger than the optical source, most of the observed hydrogen peaks do not lie on the optical image.

CHAPTER 7

3C353

A. Results — Beam Patterns and Continuum Maps

3C353 is an extra galactic radio source at moderate galactic latitude and is considerably weaker than the three sources already discussed. In addition, it is at zero degrees declination, posing a severe challenge to the aperture synthesis technique. The distribution of data points obtained for one of the continuum frequency shifts is illustrated in Figure 41. The points lie along a set of parallel straight lines with a considerable density of points along the u-axis. To avoid conflict with observations of 3C461, observations of 3C353 were limited to five hours per day. However, only the north-south spacings lost any information as a result of this restriction.

The dirty beam which results from this distribution of data points is shown in Figure 42a. The principal pattern repeats in a north-south direction at intervals equivalent to the reciprocal of the 400-foot baseline interval. Secondary maxima of nearly 40 percent occur to the north and south at intervals equivalent to the reciprocal of the 1200-foot maximum spacing. The pattern is

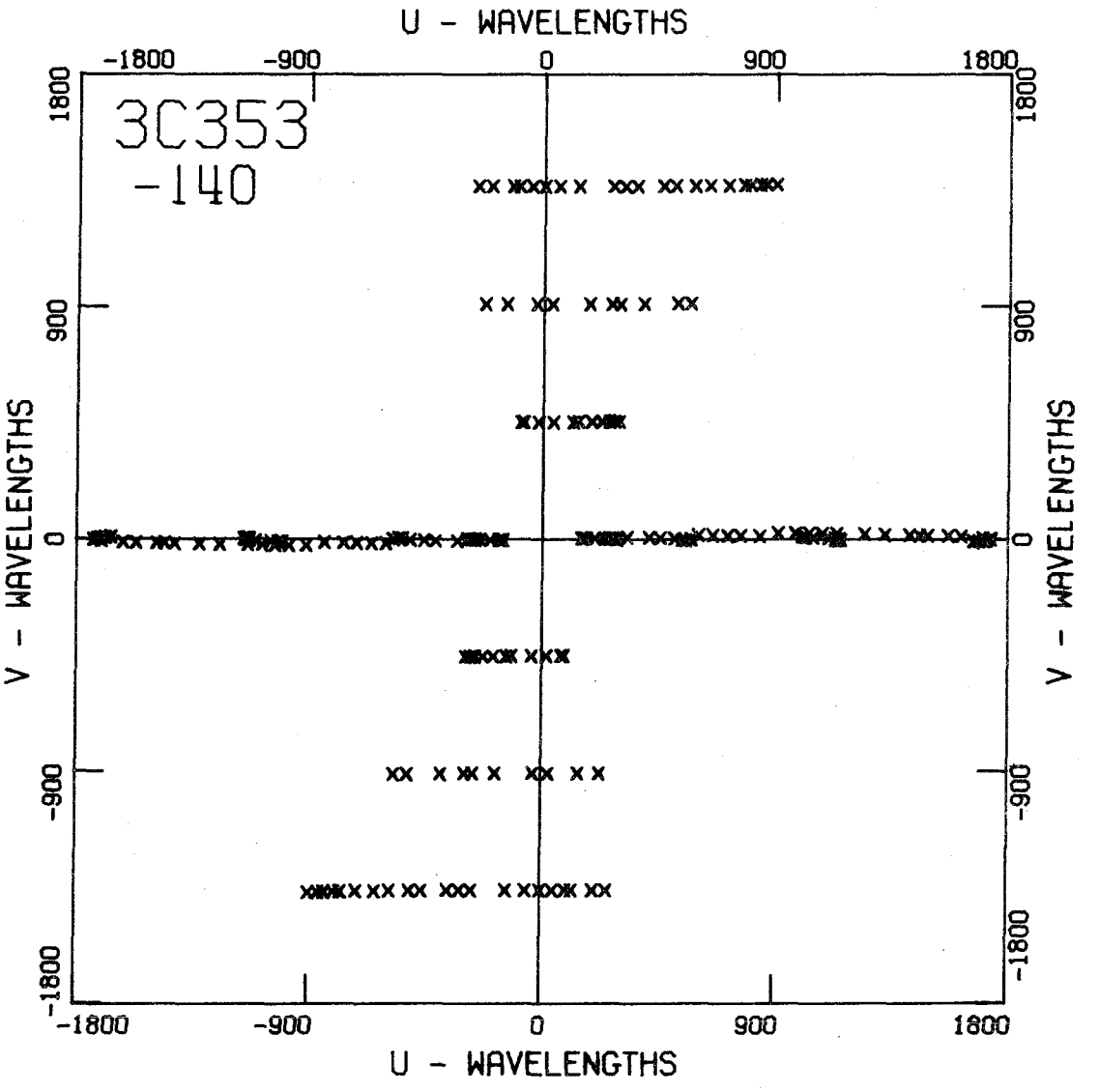

Figure 41. 3C353, continuum frequency shift: distribution of data points.

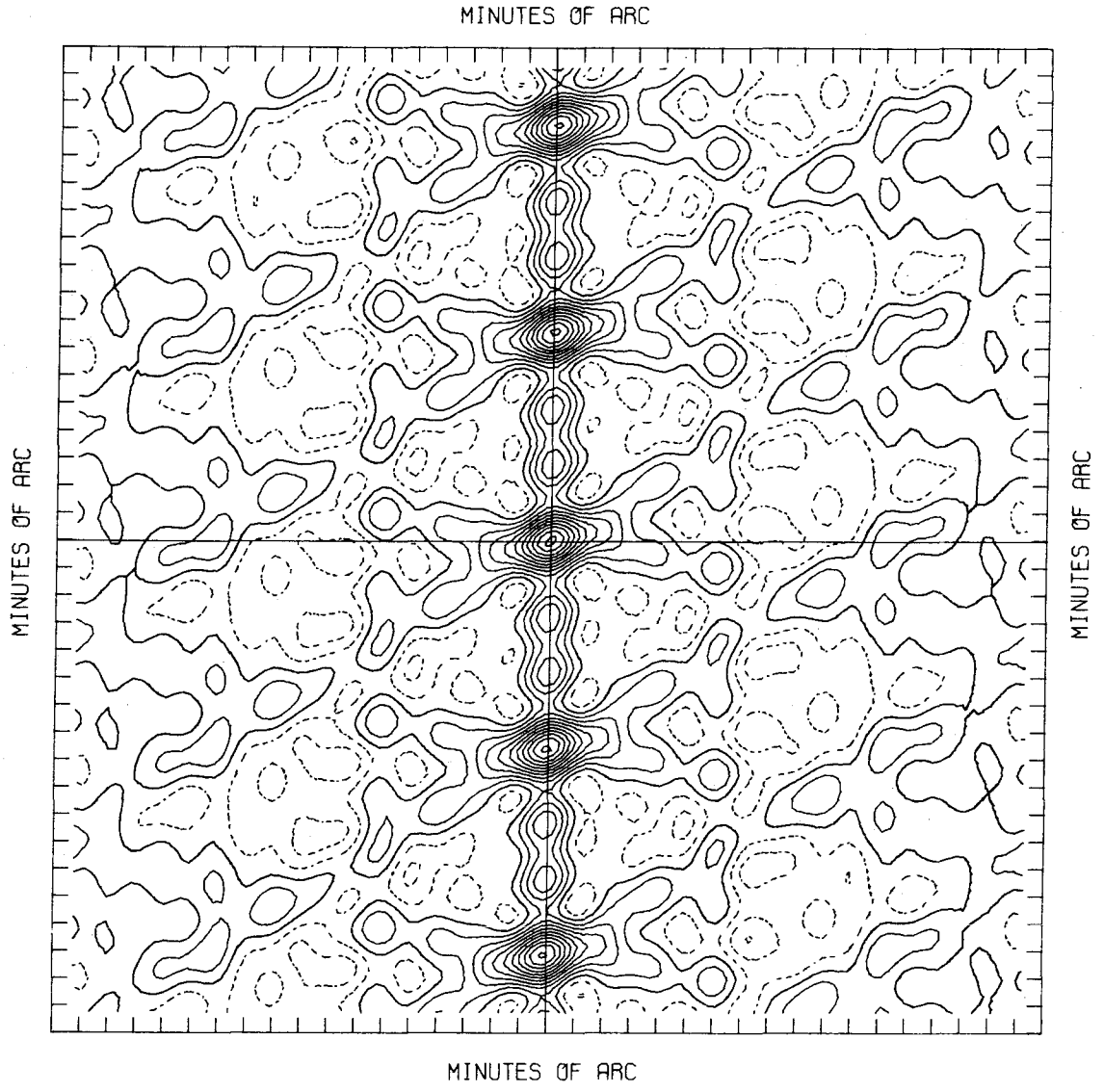

Figure 42a. 3C353, continuum frequency shift: dirty beam pattern, contour interval = 10%, large area.

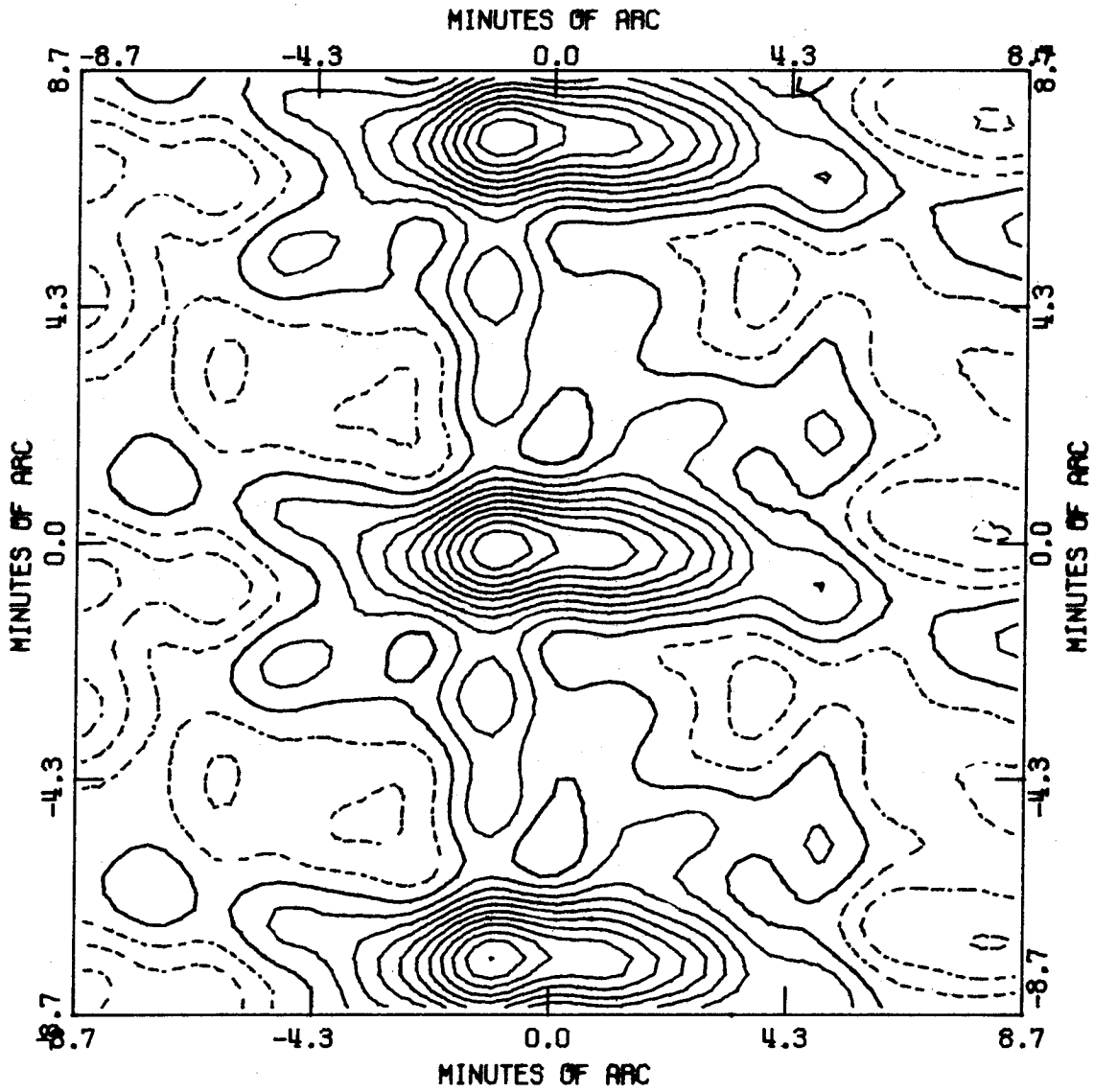

Figure 42b. 3C353, continuum frequency shift: dirty map, contour interval = 10%, large area.

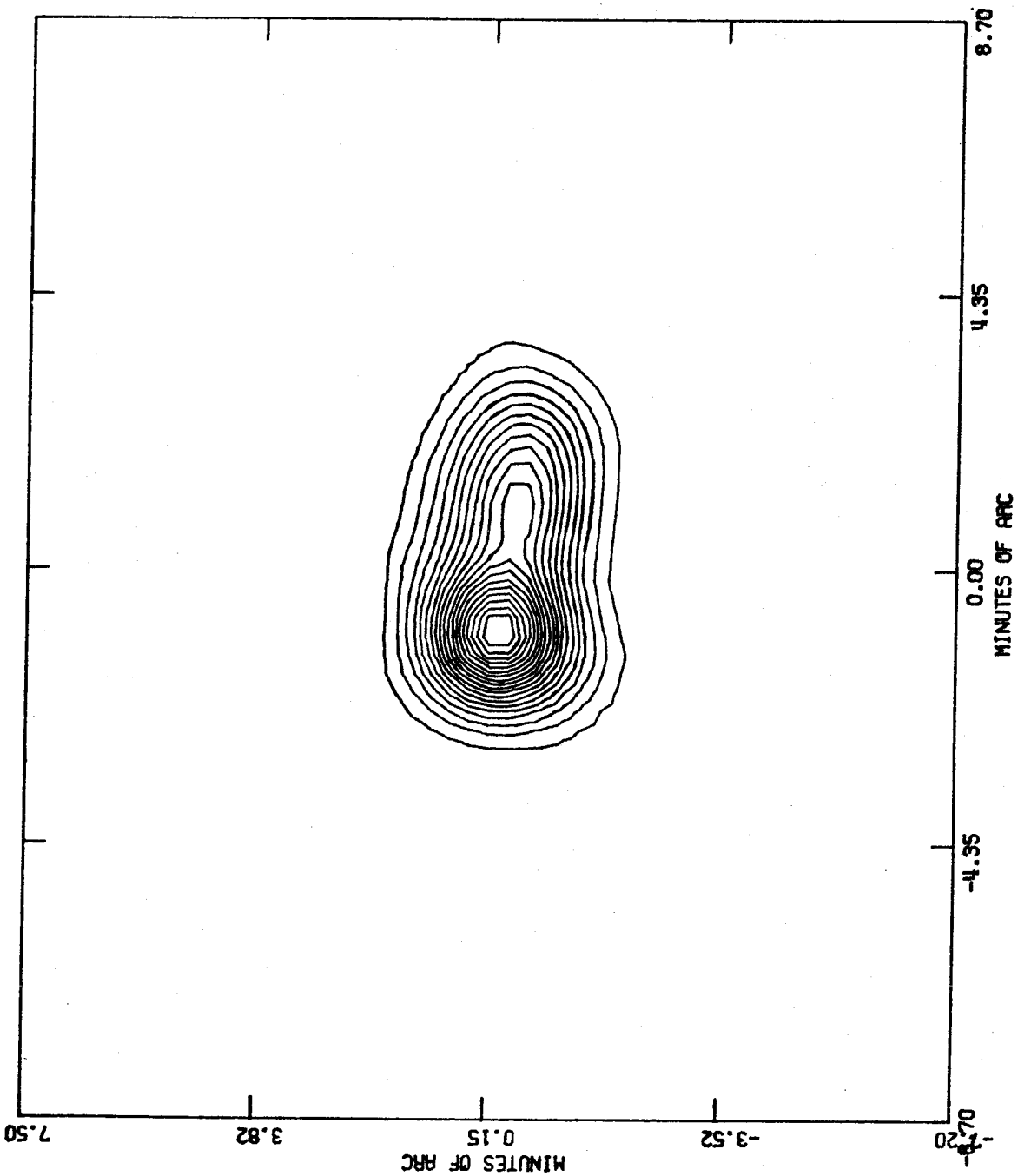

Figure 42c. 3C353, continuum frequency shift: clean map, contour interval = 5%, zero contour suppressed, large area.

tilted somewhat from the east-west direction as a result of the incomplete coverage on north-south baselines. The main beam is elliptical with an average width between half-power points about 1.58 arc minutes. The dirty map of the source reflects the lobe ambiguity. There appear to be three nearly identical sources along a north-south line. Spurious responses about 35 percent also occur. Because of the lobe ambiguity, a priori knowledge of the source position must be used to limit the area over which the deconvolution process is carried out. When this is done, the deconvolution works extremely well (Figure 42c). Spurious responses nowhere exceed about 3 percent and over most of the map area are one percent or less. The clean beam used was circular with a full width at half-maximum of 1.58 arc minutes.

The continuum map actually used to compute optical depth maps is displayed in Figure 43. The lines of constant galactic coordinates are drawn through the center of the map. Again we find that the spurious response level is increased when we perform the deconvolution over a small area. The source is a poorly-resolved double having a component ratio about 1.8 to 1.0. The stronger

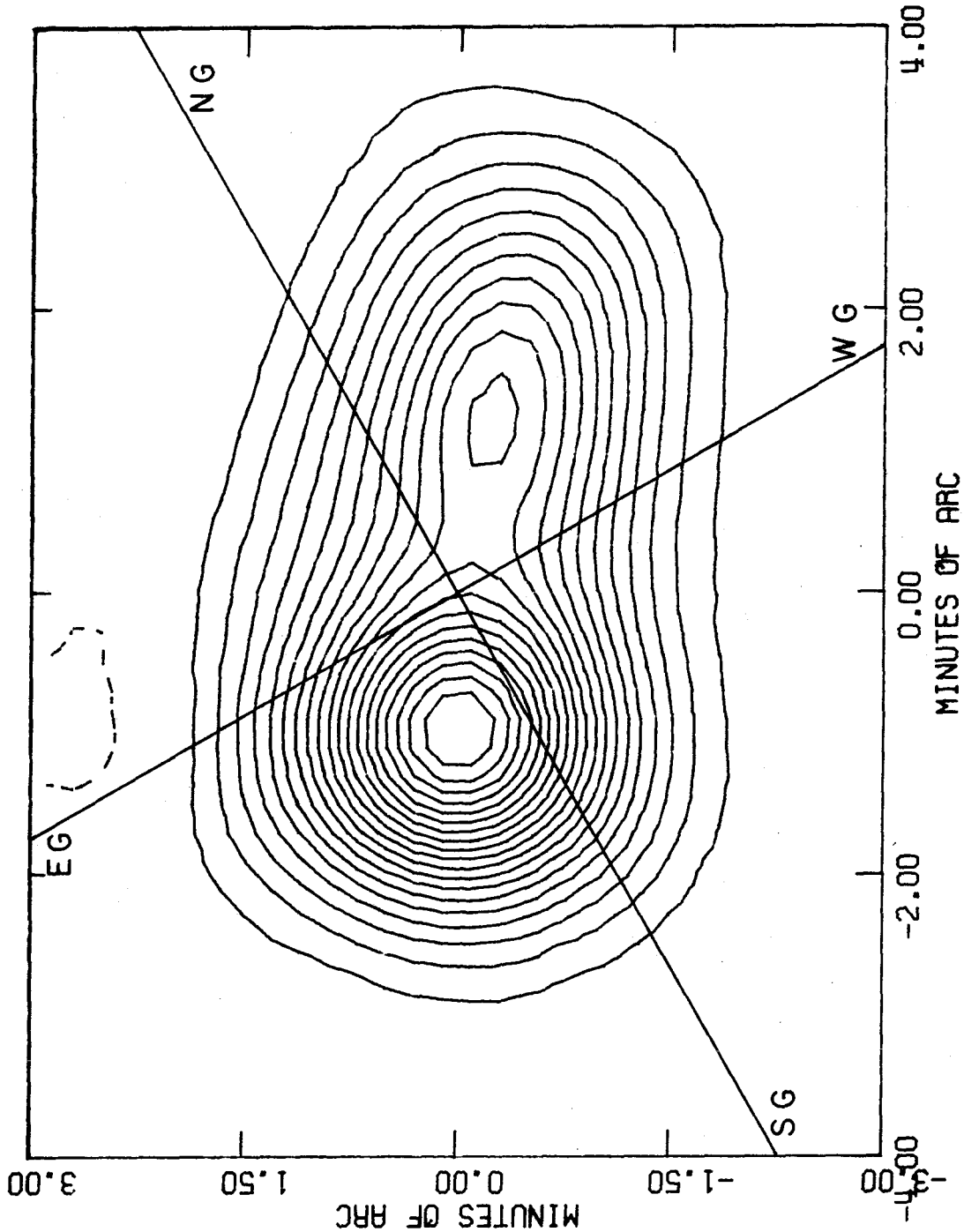

Figure 43. 3C353: continuum map, contour interval = 5% zero contour suppressed. Lines of constant galactic coordinates drawn with NG being galactic north and EG being galactic east (i.e. increasing longitude at constant latitude).

eastern component appears unresolved, but the weaker western component seems to be extended along the major axis of the source. As part of the tests described in Chapter 3B, maps made with smaller clean beams help establish this last point.

B. Results — Observed Spectra

About 110 minutes of observations at the short spacing were averaged to produce the spectrum of 3C353 plotted in Figure 44. The absorption feature contains two narrow lines of similar optical depth centered about 0 and 2 km/sec. The wings of the feature appear extended particularly at positive velocities. The spectrum observed at 1200 feet east-west is plotted in Figure 45 and represents a 70-minute integration. The upper portion of the figure contains the observed flux spectrum while the lower portion contains the observed phases. The two lines centered about 0.55 lobes represent the average phase uncertainty as a function of frequency. Since less than one third of the phase points lie outside these error bars, we must conclude that we have no significant evidence for structure in the absorbing medium. However, the gaussian analysis will be

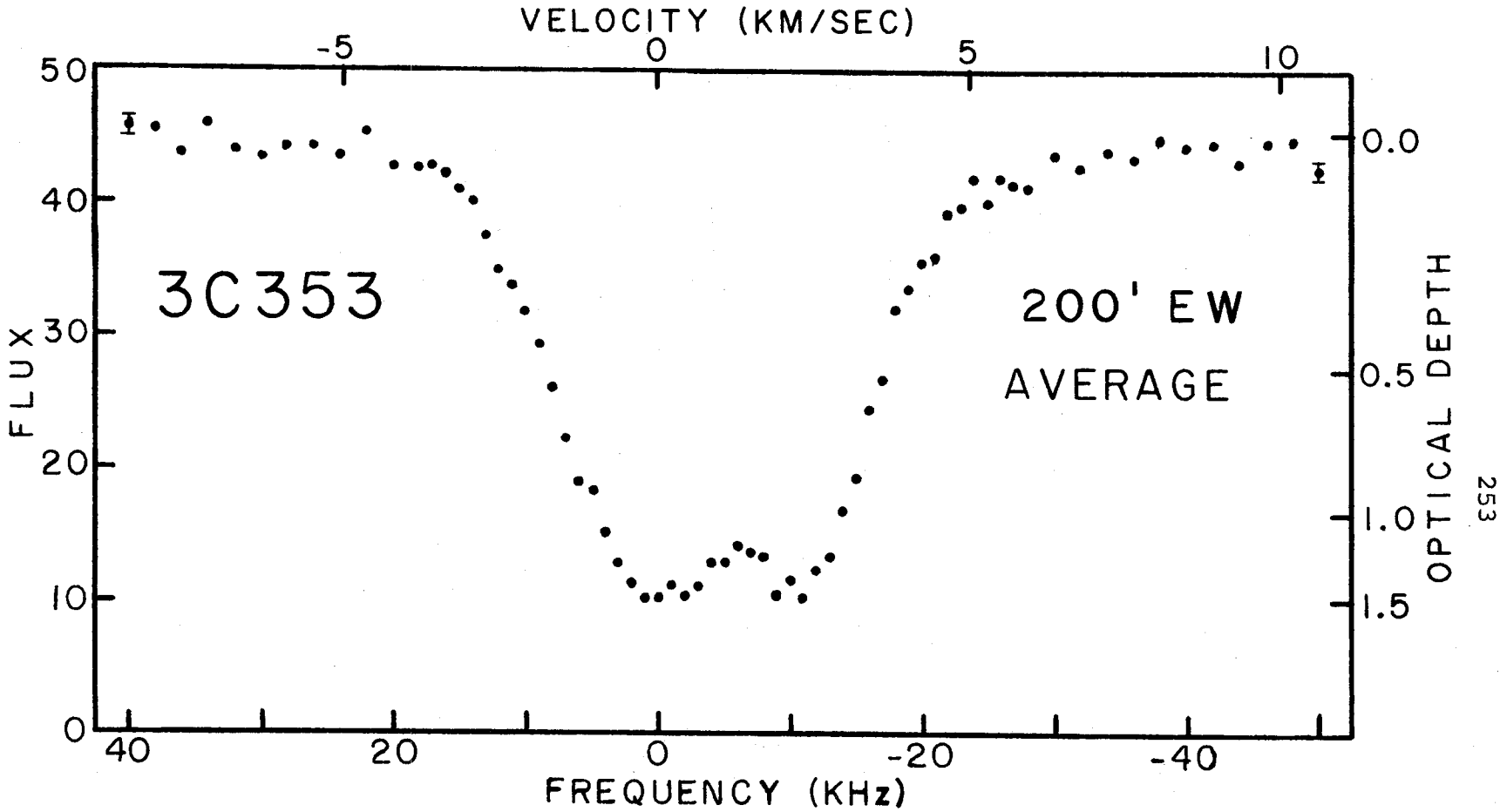

Figure 44. 3C353: flux spectrum at 200 feet east-west. Average of 110 minutes of observation.

Figure 45. (next page) 3C353: flux and phase spectra at 1200 feet east-west. Average of 70 minutes of observation. Light lines represent ± the phase uncertainty about 0.55 lobes as a function of frequency.

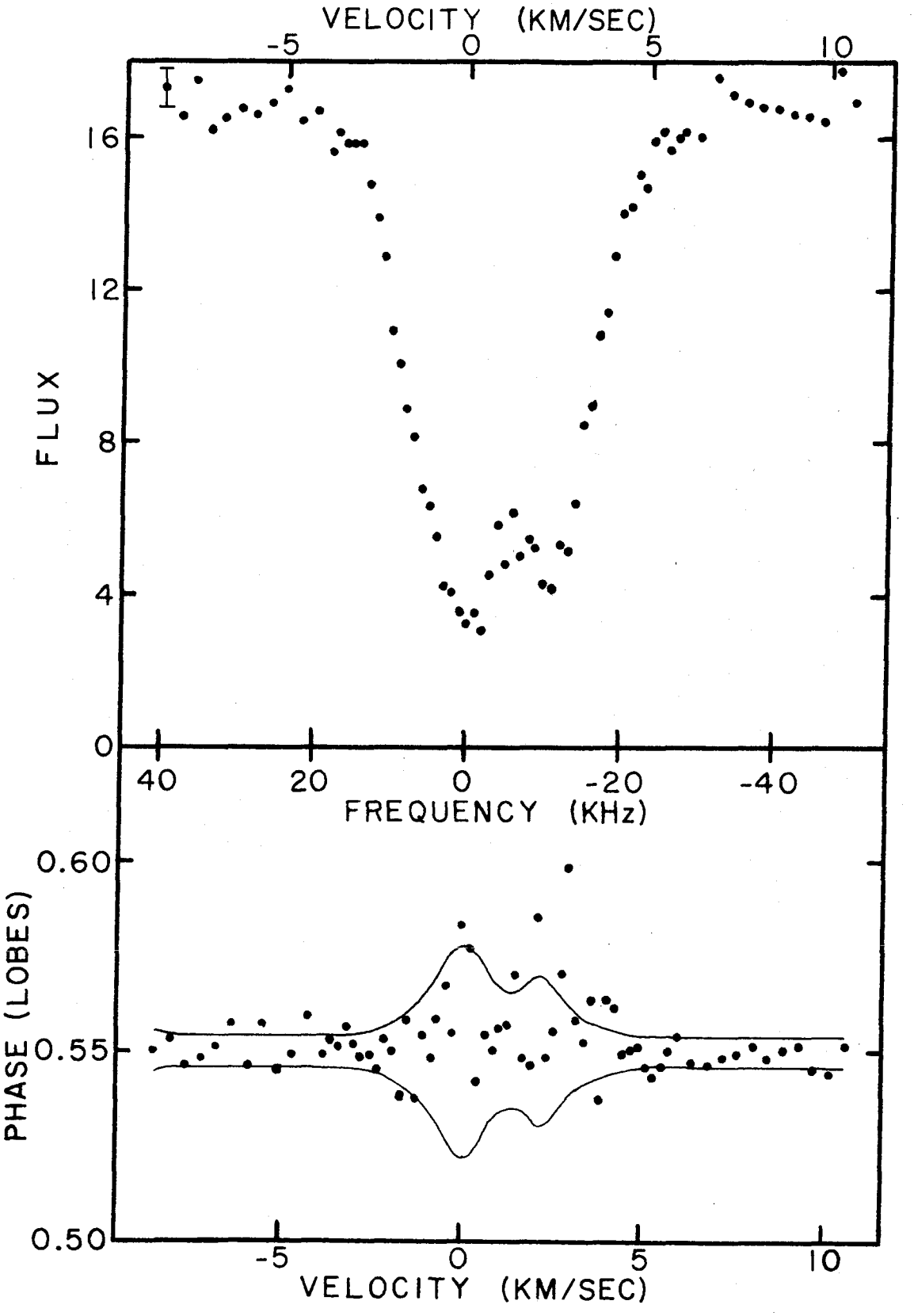
VELOCITY (KM/SEC)
-5
0
5
10
16
12
8
4
0
FLUX
40
20
0
-20
-40
FREQUENCY (KHz)
0.60
0.55
0.50
PHASE (LOBES)
-5
0
5
10
VELOCITY (KM/SEC)

seen to show the presence of some spatial structure particularly in the component at 2 km/sec.

C. Results — Optical Depth Maps

The optical depth maps also provide little evidence of spatial structure. Taken one at a time, they seem to show significant spatial structures, although the range of optical depths across maps within the line never exceeds a factor of two and is often quite a bit less. However, throughout the spectrum, it is unusual for two or three consecutive maps to indicate the same maxima and minima. We seem to be seriously limited by noise.

A small sample of the optical depth maps is given in Figures 46. The computation of optical depths is cut off at the 20 percent level of the continuum brightness. Since noise generally exceeded any systematic effects in the wings of the line, no corrections for the DC offsets are made in these figures. At - 11 KHz, in the first spectral feature, we see peaks typically to the southeast, southwest, and north of the source. Between the two spectral features, at 6 KHz, the peak to the north dominates most maps. In the second spectral feature, at 2 KHz, the maxima

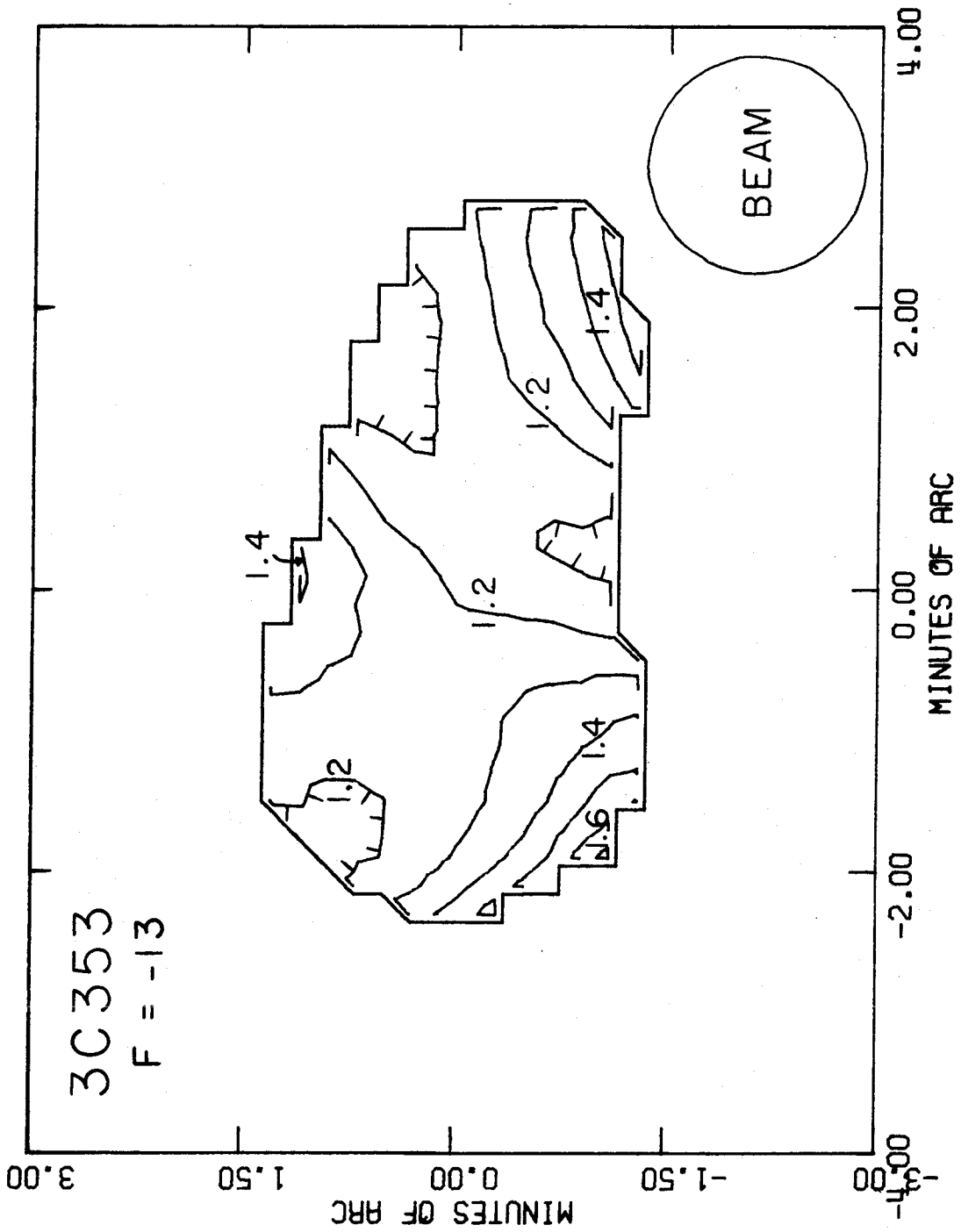

Figure 46a. 3C353: optical depth map at +2.8 km/sec, contour interval = 0.1. Illustrates beam size (full width at half maximum).

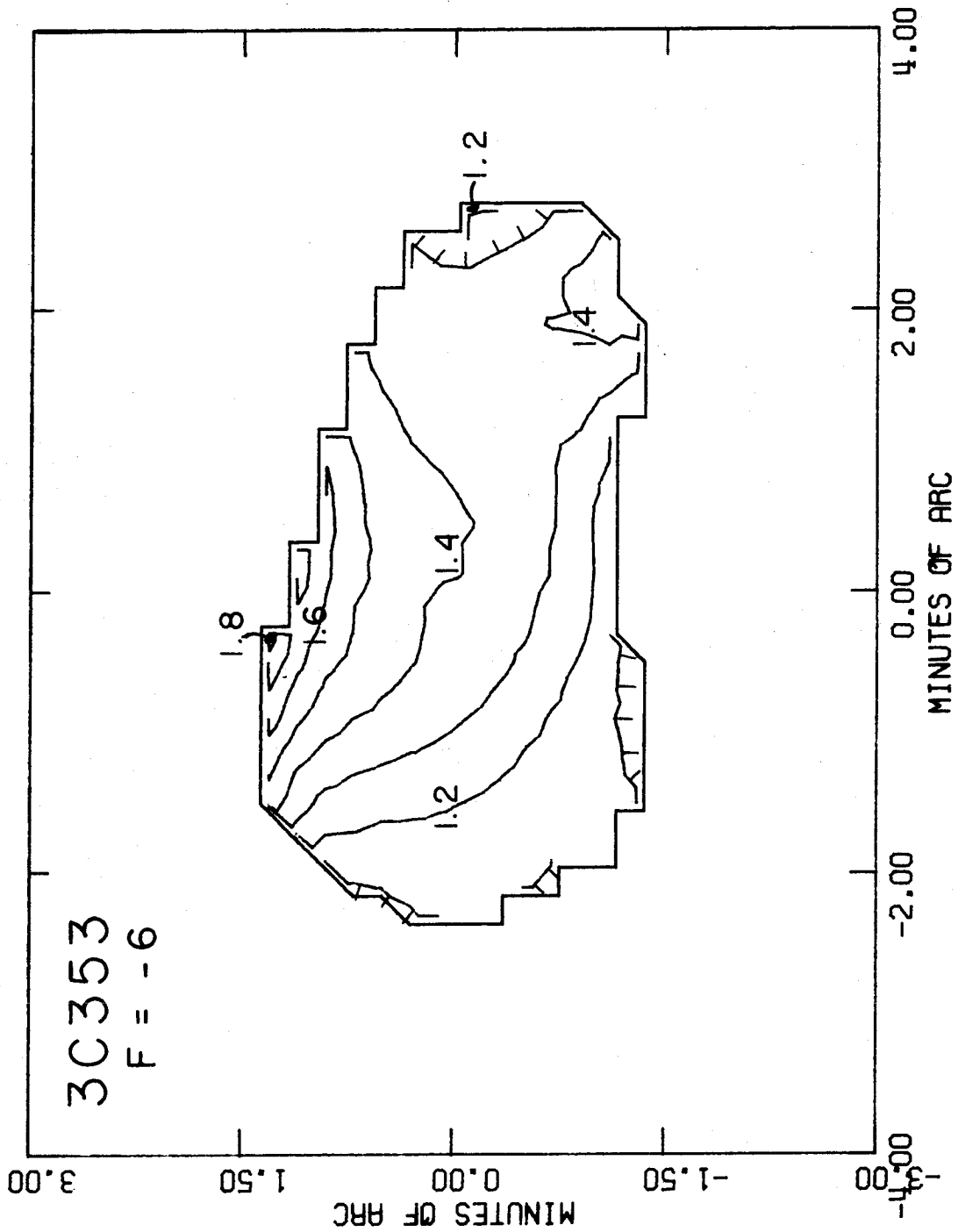

Figure 46b. 3C353: optical depth map at +1.3 km/sec, contour interval = 0.1.

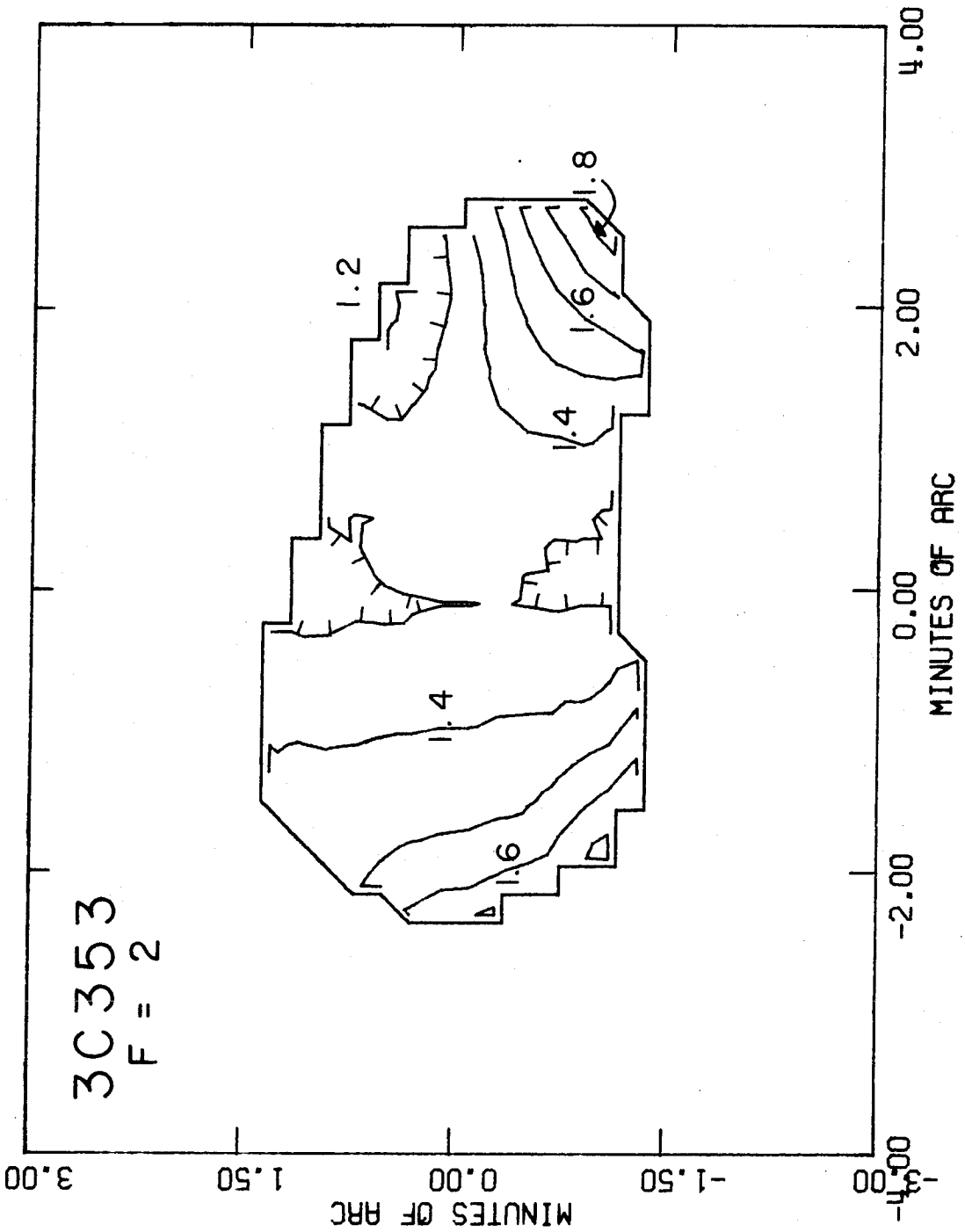

Figure 46c. 3C353: optical depth map at -0.4 km/sec, contour interval = 0.1.

to the southeast and southwest are usually most important. The southwestern peak in particular is at least partly the result of a serious DC offset.

D. Results — Spectra and Gaussian Fitting

Samples of the spectra with alternative gaussian fits are plotted in Figures 47 and 48. The two-component gaussian solution converged for all spectra with the results given in Figures 49. The first component is weakest just northwest of the center of the map. The central frequency of this component shows little significant variation although higher frequencies are preferred along the western edge of the source. A significant gradient in the width of this component does occur with the narrowest being toward the southeast. The second component also shows some variation in strength with a peak northeast of the coordinate origin. All center frequencies of this component are zero within the uncertainties except along the southwestern edge. The width of this components is larger toward the center of the source. The solutions at ($\pm$ 0.3, 1.3) are qualitatively different from the rest. Since optical depths are high between the two components there (see Figure 46b), the gaussian fit assigns a larger width and

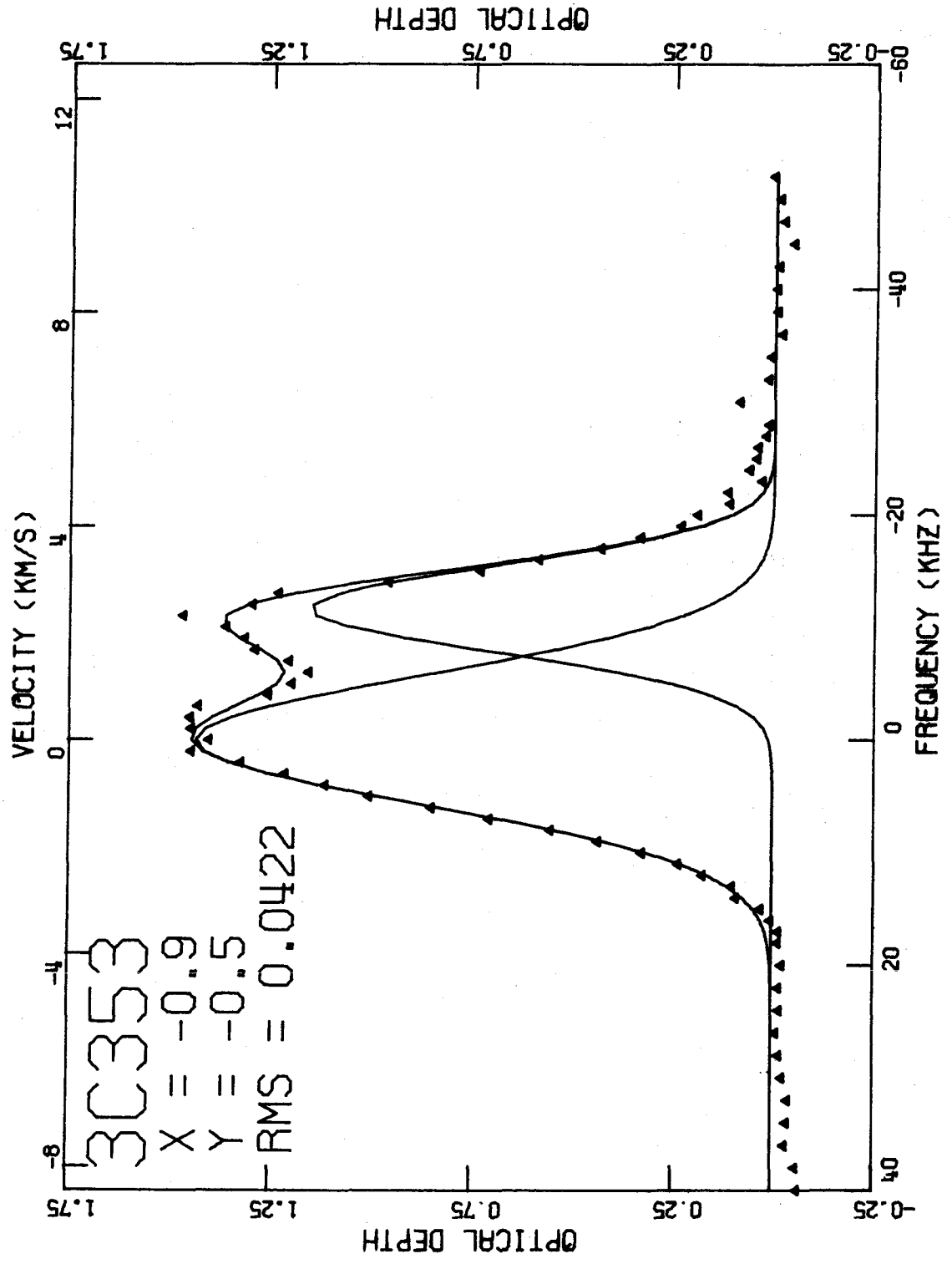

Figure 47a. 3C353: Spectrum at (-0.9, -0.5) with two-component gaussian fit.

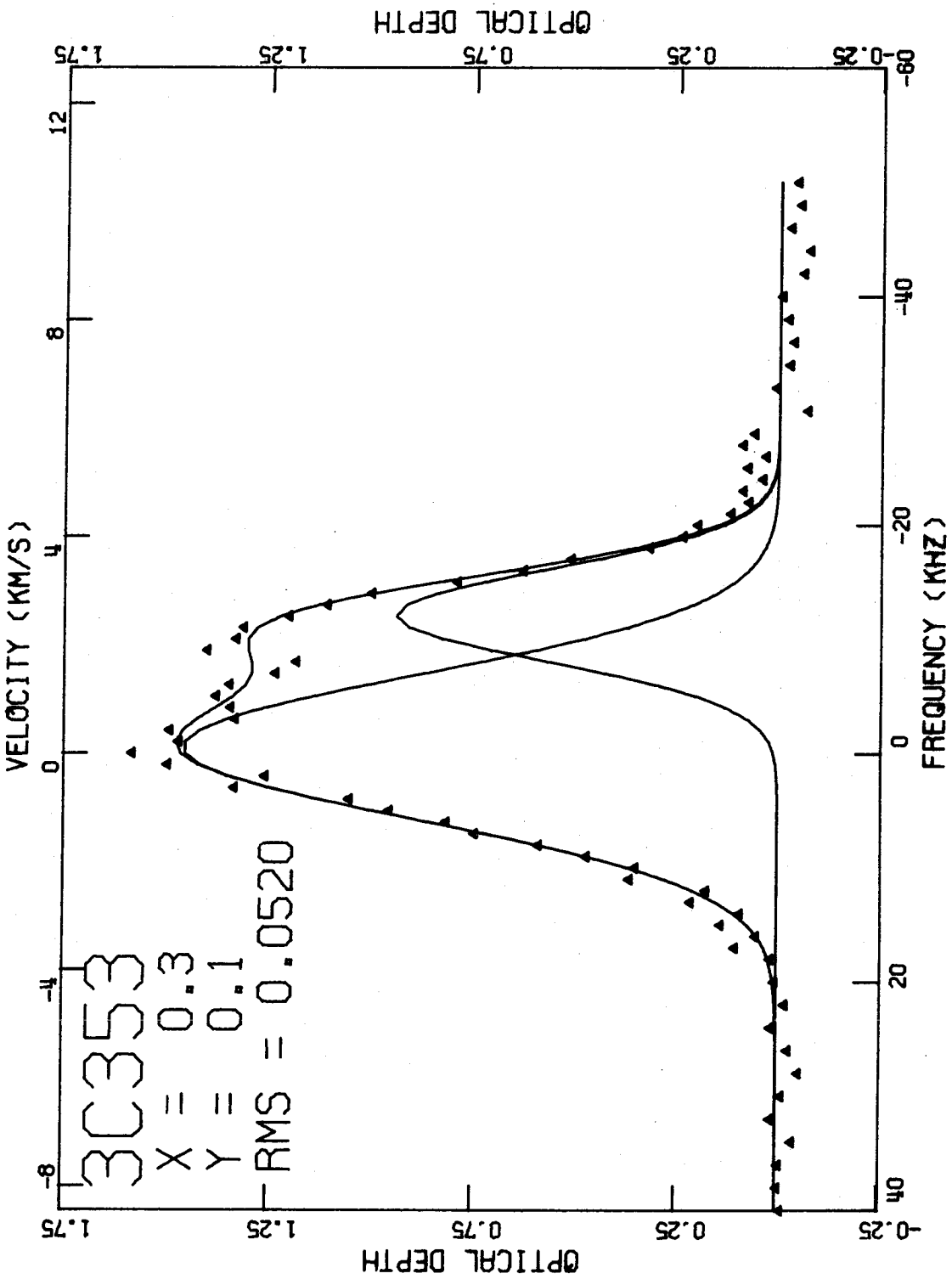

Figure 47b. 3C353: Spectrum at (0.3, 0.1) with two-component gaussian fit.

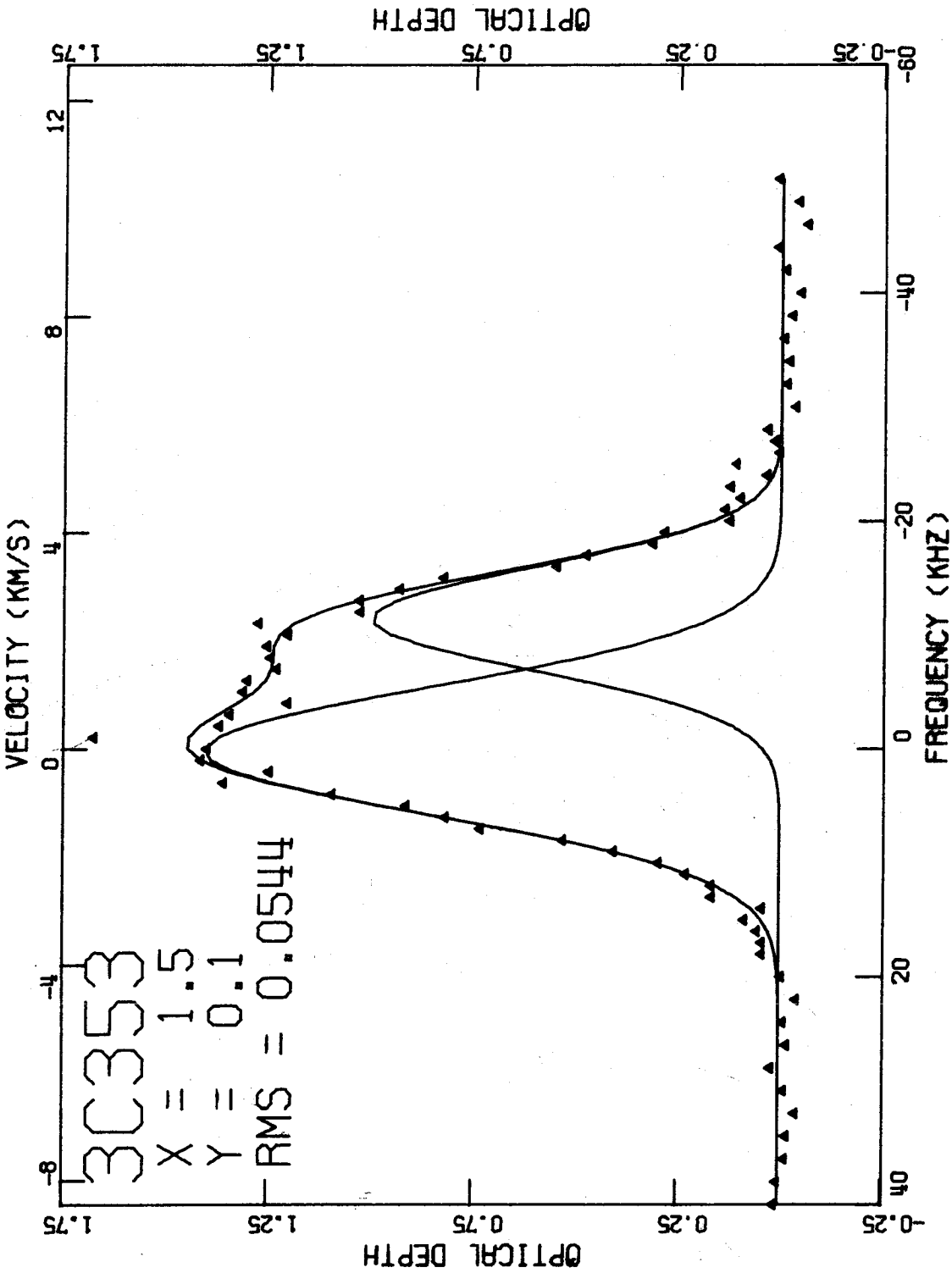

Figure 47c. 3C353: Spectrum at (1.5, 0.1) with two-component gaussian fit.

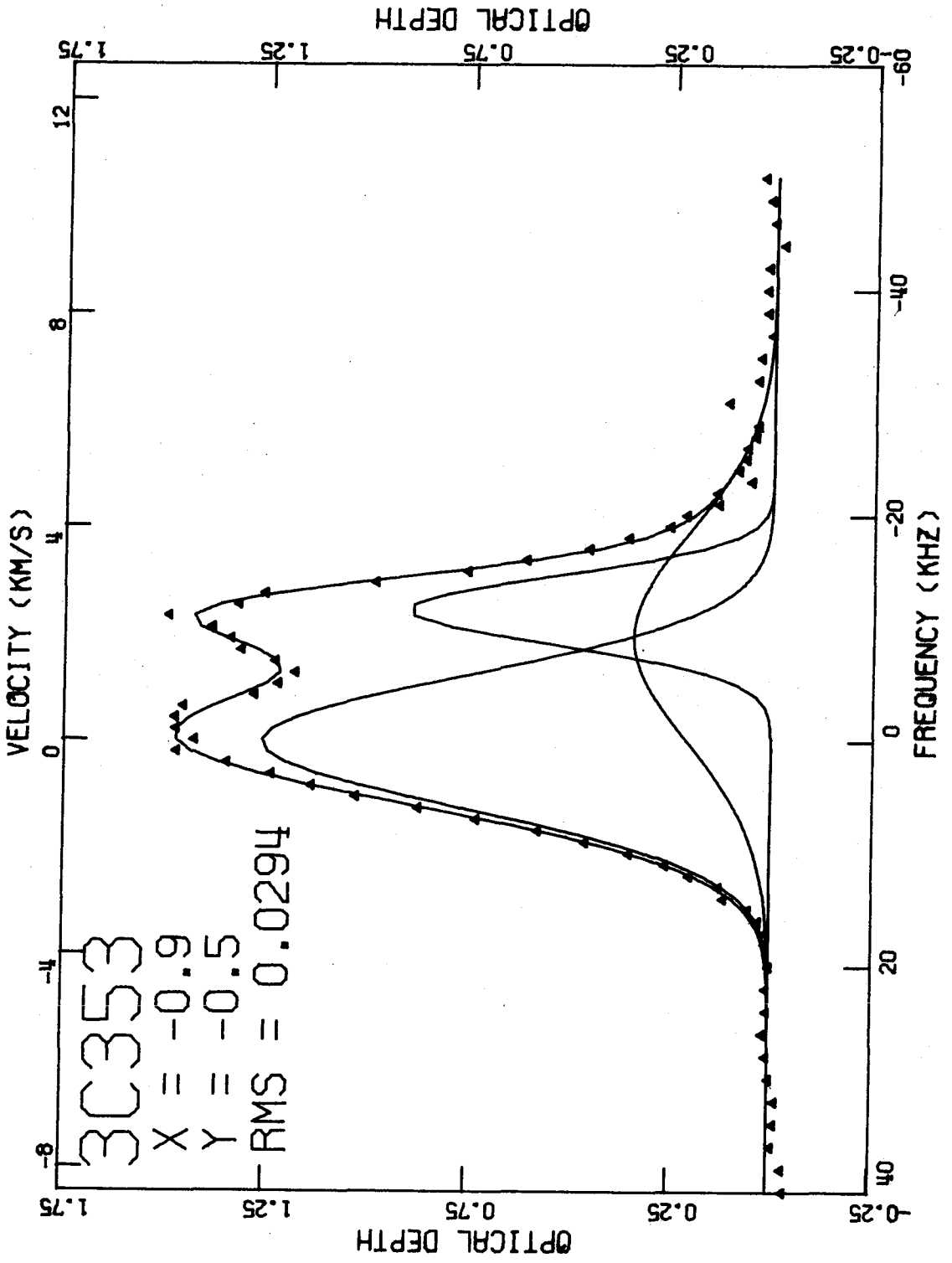

Figure 48a. 3C353: Spectrum at (-0.9, -0.5) with three-component gaussian fit.

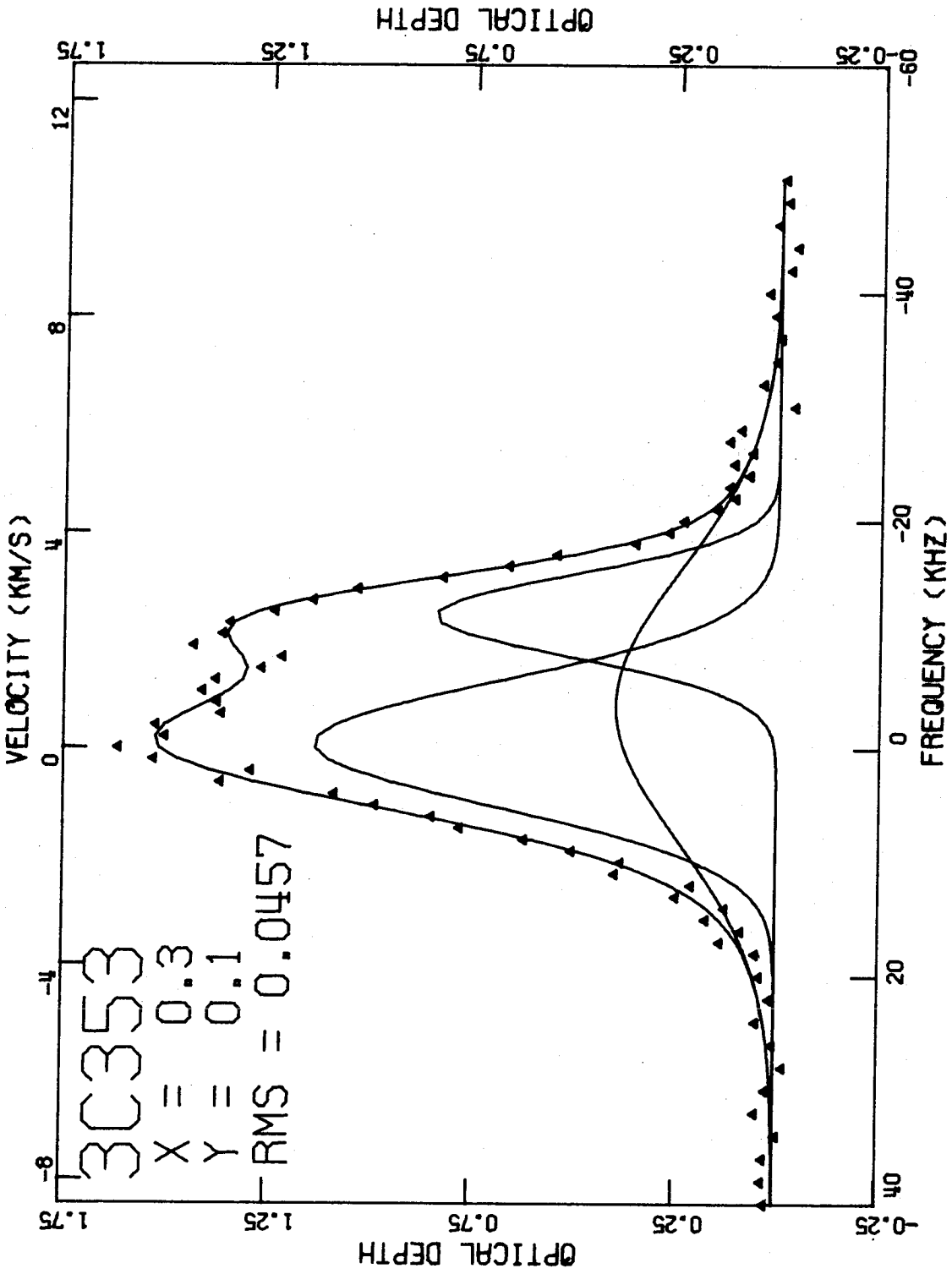

Figure 48b. 3C353: Spectrum at (0.3, 0.1) with three-component gaussian fit.

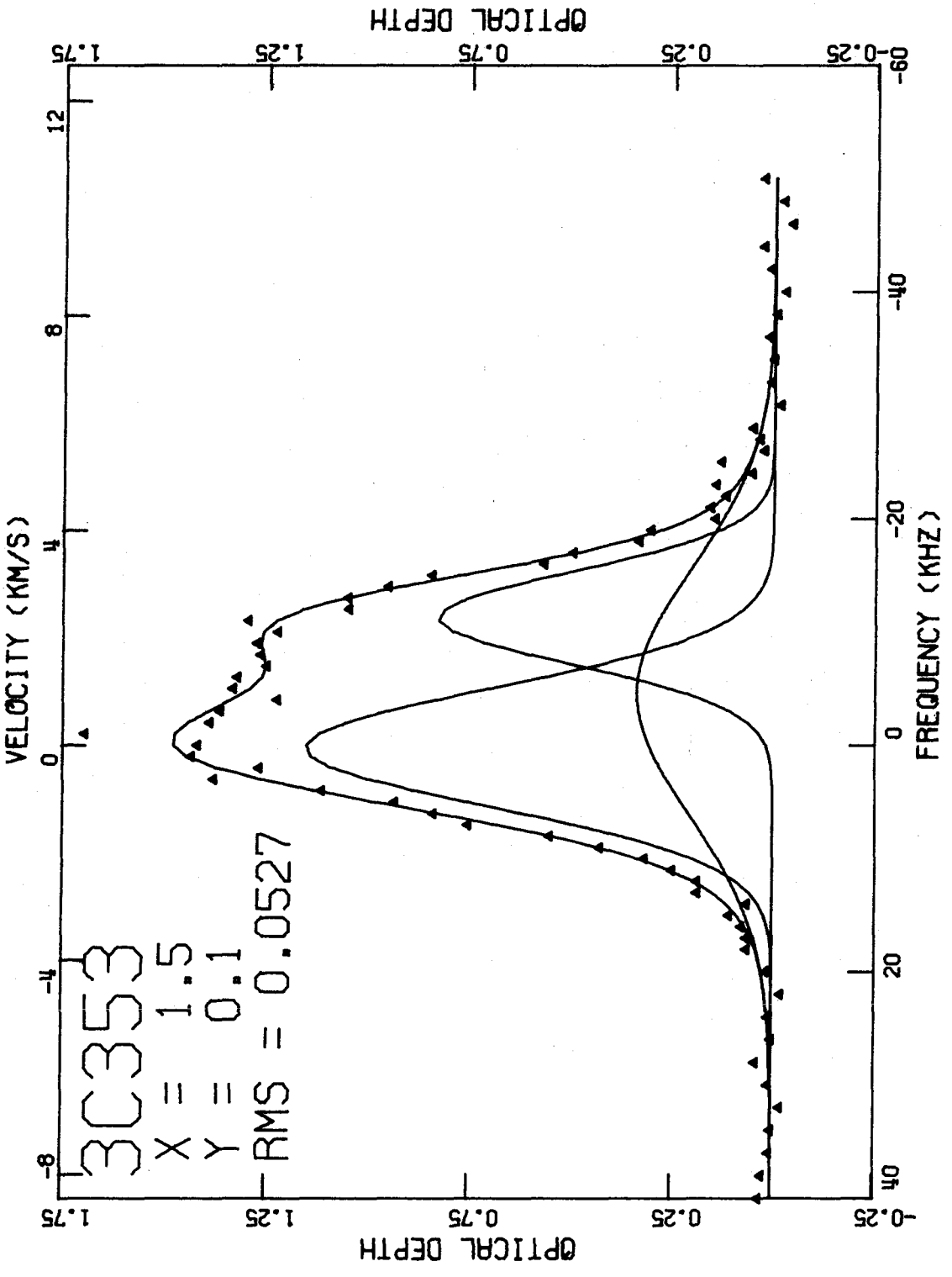

Figure 48c. 3C353: Spectrum at (1.5, 0.1) with three-component gaussian fit.

3C353 - 2 COMPONENT FIT : RMS

	-2.1	-1.5	-0.9	-0.3	0.3	0.9	1.5	2.1	2.7
1.3		0.0957	0.1015	0.1141	0.1402	0.1062			
0.7	0.0917	0.0578	0.0578	0.0766	0.0814	0.0620	0.0669	0.0953	
0.1	0.0806	0.0480	0.0433	0.0520	0.0520	0.0451	0.0544	0.0833	0.1041
-0.5	0.1019	0.0639	0.0422	0.0438	0.0545	0.0478	0.0596	0.0951	0.1159
-1.1	0.1595	0.1093	0.0724	0.0865	0.0905	0.0656	0.0817	0.1293	0.1654

Figure 49a. 3C353: Results of gaussian analysis — two-component solution — RMS (in optical depth).

3C353 - 2 COMPONENT FIT : DC OFFSET

	-2.1	-1.5	-0.9	-0.3	0.3	0.9	1.5	2.1	2.7
1.3		0.156 (0.017)	0.139 (0.018)	0.080 (0.024)	0.126 (0.029)	0.175 (0.019)			
0.7	0.126 (0.016)	0.095 (0.010)	0.081 (0.010)	0.074 (0.014)	0.107 (0.015)	0.106 (0.011)	0.071 (0.012)	0.065 (0.017)	
0.1	0.143 (0.014)	0.091 (0.008)	0.075 (0.008)	0.059 (0.009)	0.069 (0.009)	0.065 (0.008)	0.079 (0.010)	0.072 (0.015)	0.071 (0.019)
-0.5	0.112 (0.017)	0.085 (0.011)	0.079 (0.007)	0.059 (0.008)	0.043 (0.010)	0.065 (0.009)	0.122 (0.011)	0.151 (0.017)	0.130 (0.021)
-1.1	0.067 (0.027)	0.089 (0.019)	0.086 (0.012)	0.055 (0.015)	0.039 (0.016)	0.080 (0.012)	0.149 (0.014)	0.215 (0.023)	0.238 (0.029)

Figure 49b. 3C353: Results of gaussian analysis — two-component solution — DC offset (in optical depth).

3C353 - 2 COMPONENT FIT : CENTRAL OPTICAL DEPTH OF COMPONENT 1

	-2.1	-1.5	-0.9	-0.3	0.3	0.9	1.5	2.1	2.7
1.3		1.120 (0.100)	0.990 (0.151)	0.433 (0.109)	0.255 (0.124)	1.120 (0.234)			
0.7	1.131 (0.069)	1.098 (0.051)	1.058 (0.059)	0.946 (0.104)	0.824 (0.150)	0.937 (0.097)	1.032 (0.085)	1.059 (0.116)	
0.1	1.145 (0.060)	1.113 (0.041)	1.096 (0.041)	1.043 (0.058)	0.938 (0.066)	0.919 (0.057)	0.998 (0.063)	1.048 (0.084)	1.042 (0.079)
-0.5	1.224 (0.075)	1.163 (0.053)	1.152 (0.038)	1.125 (0.042)	1.029 (0.058)	0.966 (0.055)	1.052 (0.065)	1.124 (0.082)	1.097 (0.075)
-1.1	1.332 (0.118)	1.199 (0.094)	1.170 (0.063)	1.168 (0.069)	1.104 (0.078)	1.043 (0.068)	1.143 (0.082)	1.257 (0.091)	1.195 (0.092)

Figure 49c. 3C353: Results of gaussian analysis — two-component solution — central optical depths, central frequencies (KHz) and full widths at half maximum (KHz) of gaussian components, by component.

3C353 - 2 COMPONENT FIT : CENTRAL FREQUENCY OF COMPONENT 1

	-2.1	-1.5	-0.9	-0.3	0.3	0.9	1.5	2.1	2.7
1.3		-11.35 (0.66)	-12.13 (0.69)	-13.22 (0.48)	-13.29 (1.01)	-10.39 (1.69)			
0.7	-11.55 (0.38)	-11.63 (0.26)	-11.91 (0.28)	-12.36 (0.42)	-12.40 (0.60)	-11.58 (0.57)	-10.85 (0.70)	-10.74 (1.10)	
0.1	-11.64 (0.27)	-11.65 (0.19)	-11.74 (0.19)	-11.91 (0.26)	-12.06 (0.30)	-11.90 (0.29)	-11.39 (0.44)	-11.04 (0.78)	-11.14 (1.02)
-0.5	-11.86 (0.28)	-11.72 (0.22)	-11.60 (0.17)	-11.54 (0.21)	-11.72 (0.28)	-11.84 (0.27)	-11.35 (0.40)	-10.90 (0.72)	-10.89 (0.98)
-1.1	-12.17 (0.36)	-11.99 (0.32)	-11.61 (0.27)	-11.20 (0.39)	-11.34 (0.43)	-11.66 (0.32)	-11.17 (0.45)	-10.39 (0.79)	-10.02 (1.25)

Figure 49c. (continued)

30353 - 2 COMPONENT FIT : FULL WIDTH OF COMPONENT 1

	-2.1	-1.5	-0.9	-0.3	0.3	0.9	1.5	2.1	2.7
1.3		10.64 (1.00)	10.12 (1.08)	6.06 (1.69)	5.85 (3.33)	12.33 (1.97)			
0.7	9.04 (0.69)	9.16 (0.46)	9.28 (0.49)	9.40 (0.76)	9.84 (1.06)	10.57 (0.80)	11.43 (0.96)	12.04 (1.51)	
0.1	8.35 (0.53)	8.72 (0.35)	9.09 (0.34)	9.39 (0.45)	9.48 (0.52)	9.77 (0.48)	10.69 (0.64)	11.75 (1.14)	12.96 (1.60)
-0.5	7.91 (0.58)	8.44 (0.42)	8.98 (0.31)	9.38 (0.35)	9.39 (0.48)	9.52 (0.46)	10.39 (0.62)	11.41 (1.12)	12.95 (1.62)
-1.1	7.45 (0.78)	8.00 (0.66)	8.65 (0.50)	9.27 (0.67)	9.28 (0.74)	9.24 (0.56)	9.98 (0.73)	11.15 (1.30)	13.33 (2.17)

Figure 49c. (continued)

3C353 - 2 COMPONENT FIT : CENTRAL OPTICAL DEPTH OF COMPONENT 2

	-2.1	-1.5	-0.9	-0.3	0.3	0.9	1.5	2.1	2.7
1.3		1.393 (0.062)	1.481 (0.063)	1.649 (0.049)	1.706 (0.061)	1.270 (0.227)			
0.7	1.459 (0.041)	1.488 (0.026)	1.528 (0.027)	1.530 (0.039)	1.475 (0.054)	1.397 (0.050)	1.326 (0.069)	1.307 (0.114)	
0.1	1.506 (0.035)	1.489 (0.021)	1.501 (0.020)	1.491 (0.025)	1.458 (0.026)	1.437 (0.024)	1.403 (0.037)	1.392 (0.073)	1.400 (0.101)
-0.5	1.564 (0.043)	1.469 (0.027)	1.435 (0.019)	1.419 (0.021)	1.419 (0.026)	1.422 (0.023)	1.408 (0.035)	1.438 (0.069)	1.460 (0.105)
-1.1	1.650 (0.066)	1.495 (0.046)	1.382 (0.032)	1.323 (0.041)	1.326 (0.043)	1.347 (0.031)	1.357 (0.043)	1.412 (0.087)	1.423 (0.167)

Figure 49c. (continued)

3C353 - 2 COMPONENT FIT : CENTRAL FREQUENCY OF COMPONENT 2

	-2.1	-1.5	-0.9	-0.3	0.3	0.9	1.5	2.1	2.7
1.3		0.30 (0.66)	-0.70 (0.80)	-3.60 (0.48)	-4.35 (0.52)	0.16 (1.52)			
0.7	0.16 (0.39)	0.02 (0.28)	-0.27 (0.30)	-0.90 (0.51)	-1.33 (0.74)	-0.42 (0.56)	0.34 (0.60)	0.53 (0.88)	
0.1	0.05 (0.30)	0.00 (0.21)	-0.08 (0.22)	-0.27 (0.30)	-0.51 (0.35)	-0.37 (0.31)	0.21 (0.40)	0.71 (0.63)	1.02 (0.68)
-0.5	-0.12 (0.34)	-0.06 (0.27)	0.04 (0.21)	0.08 (0.24)	-0.11 (0.32)	-0.20 (0.30)	0.39 (0.40)	1.00 (0.61)	1.33 (0.64)
-1.1	-0.40 (0.48)	-0.40 (0.45)	-0.09 (0.35)	0.28 (0.45)	0.18 (0.49)	-0.05 (0.39)	0.49 (0.52)	1.32 (0.71)	1.77 (0.79)

Figure 49c. (continued)

3C353 - 2 COMPONENT FIT : FULL WIDTH OF COMPONENT 2

	-2.1	-1.5	-0.9	-0.3	0.3	0.9	1.5	2.1	2.7
1.3		12.94 (1.10)	14.80 (1.30)	19.90 (0.98)	20.07 (1.03)	12.50 (1.78)			
0.7	12.64 (0.80)	13.24 (0.54)	14.00 (0.58)	15.25 (0.90)	15.79 (1.19)	13.81 (0.86)	12.34 (0.87)	12.09 (1.21)	
0.1	13.03 (0.66)	13.45 (0.43)	13.82 (0.42)	14.37 (0.56)	14.94 (0.62)	14.43 (0.54)	13.26 (0.66)	12.42 (0.95)	11.74 (1.01)
-0.5	13.38 (0.78)	13.61 (0.58)	13.51 (0.41)	13.47 (0.45)	14.06 (0.60)	14.49 (0.56)	13.47 (0.69)	12.27 (0.98)	11.37 (0.99)
-1.1	13.80 (1.14)	14.07 (0.97)	13.37 (0.71)	12.42 (0.87)	12.86 (0.94)	14.05 (0.75)	13.30 (0.93)	11.39 (1.19)	10.30 (1.24)

Figure 49c. (continued)

lower center frequency than normal to component 2 and nearly eliminates component 1. Such a fit is not particularly meaningful.

The gaussian solution described above fits the two peaks in the spectra fairly well, but has problems with the wings. An alternative three-component solution converges for 32 of the 40 spectra with the results given in Figures 50. For a few map points this solution converges to a fit which is qualitatively different from the rest. Although where this solution converges the RMS is lower than in the two-component solution, the uncertainties in the parameters are significantly larger. As a result of the large uncertainties, there are no significant variations across the source in the peak optical depths of the three components. The widths of components 2 and 3 also show no significant variation, but component 1 is narrower to the east. All components tend to occur at slightly higher frequencies toward the west perhaps due to a slight slope in the spectral baseline (which was not determined by the fitting procedure).

E. Results — Noise

The results of the noise computations using equation (3B-1) are presented in Figures 51. The constant part of

3C353 - 3 COMPONENT FIT : RMS

	-2.1	-1.5	-0.9	-0.3	0.3	0.9	1.5	2.1	2.7
1.3		******	0.0933	0.1108	0.1392	0.1063			
0.7	******	******	0.0458	0.0674	0.0746	0.0607	******	******	
0.1	0.0743	0.0347	0.0288	0.0420	0.0457	0.0415	0.0527	0.0805	0.0968
-0.5	0.0908	0.0517	0.0294	0.0362	0.0533	0.0442	0.0549	0.0906	0.1111
-1.1	0.1440	0.1003	******	******	******	0.0640	0.0761	0.1253	0.1639

Figure 50a. 3C353: Results of gaussian analysis — three-component solution — RMS (in optical depth).

3C353 - 3 COMPONENT FIT : DC OFFSET

	-2.1	-1.5	-0.9	-0.3	0.3	0.9	1.5	2.1	2.7
1.3			0.058 (0.057)	0.045 (0.042)	0.089 (0.051)	0.144 (0.038)			
0.7			0.038 (0.015)	0.026 (0.023)	0.062 (0.024)	0.083 (0.019)			
0.1	0.111 (0.021)	0.066 (0.009)	0.042 (0.008)	0.020 (0.014)	0.036 (0.015)	0.041 (0.013)	0.059 (0.015)	0.043 (0.024)	0.023 (0.030)
-0.5	0.069 (0.024)	0.058 (0.013)	0.055 (0.007)	0.016 (0.019)	0.022 (0.019)	0.038 (0.016)	0.091 (0.017)	0.113 (0.026)	0.088 (0.031)
-1.1	-0.002 (0.037)	0.050 (0.024)				0.054 (0.021)	0.107 (0.025)	0.171 (0.055)	0.199 (0.043)

Figure 50b. 3C353: Results of gaussian analysis — three-component solution — DC offset (in optical depth).

3C353 - 3 COMPONENT FIT : CENTRAL OPTICAL DEPTH OF COMPONENT 1

	-2.1	-1.5	-0.9	-0.3	0.3	0.9	1.5	2.1	2.7
1.3			0.81 (0.14)	0.73 (0.19)	0.73 (0.33)	1.00 (0.36)			
0.7			0.88 (0.08)	0.84 (0.13)	0.80 (0.16)	0.86 (0.21)			
0.1	0.98 (0.10)	0.86 (0.07)	0.90 (0.06)	0.90 (0.08)	0.84 (0.11)	0.84 (0.13)	0.83 (0.27)	0.76 (0.33)	0.68 (0.26)
-0.5	0.98 (0.12)	0.89 (0.11)	0.90 (0.07)	1.04 (0.04)	0.94 (0.11)	0.92 (0.09)	0.91 (0.19)	0.76 (0.48)	0.57 (0.63)
-1.1	1.01 (0.20)	0.90 (0.19)				0.98 (0.15)	1.01 (0.18)	0.93 (0.46)	0.65 (0.90)

Figure 50c. 3C353: Results of gaussian analysis — three-component solution — central optical depths, central frequencies (KHz) and full widths at half maximum of gaussian components, by component.

3C353 - 3 COMPONENT FIT : CENTRAL FREQUENCY OF COMPONENT 1

	-2.1	-1.5	-0.9	-0.3	0.3	0.9	1.5	2.1	2.7
1.3			-12.20 (0.44)	-12.39 (0.66)	-11.88 (1.58)	-10.09 (1.62)			
0.7			-11.69 (0.19)	-11.78 (0.35)	-11.48 (0.56)	-11.18 (0.59)			
0.1	-11.54 (0.22)	-11.52 (0.11)	-11.59 (0.11)	-11.67 (0.19)	-11.62 (0.26)	-11.49 (0.29)	-11.21 (0.40)	-11.04 (0.61)	-11.30 (0.56)
-0.5	-11.63 (0.22)	-11.55 (0.14)	-11.52 (0.10)	-11.58 (0.16)	-11.64 (0.27)	-11.49 (0.28)	-10.89 (0.36)	-10.60 (0.68)	-11.06 (1.15)
-1.1	-11.75 (0.25)	-11.66 (0.24)				-11.36 (0.33)	-10.64 (0.40)	-10.03 (0.75)	-10.21 (2.42)

Figure 50c. (continued)

3C353 - 3 COMPONENT FIT : FULL WIDTH OF COMPONENT 1

	-2.1	-1.5	-0.9	-0.3	0.3	0.9	1.5	2.1	2.7
1.3			8.05 (1.10)	7.84 (1.52)	9.09 (2.58)	11.30 (2.61)			
0.7			7.64 (0.53)	8.03 (0.86)	8.81 (1.14)	9.85 (1.18)			
0.1	6.93 (0.64)	6.75 (0.40)	7.42 (0.34)	8.02 (0.51)	8.48 (0.66)	9.12 (0.69)	9.56 (1.23)	9.45 (1.92)	8.76 (1.93)
-0.5	6.06 (0.70)	6.56 (0.54)	7.10 (0.35)	8.51 (0.33)	8.64 (0.71)	9.07 (0.58)	9.62 (0.91)	9.58 (2.21)	9.13 (3.98)
-1.1	4.87 (0.92)	5.75 (0.94)				8.77 (0.78)	9.39 (0.96)	10.16 (2.16)	11.40 (5.48)

Figure 50c. (continued)

3C353 - 3 COMPONENT FIT : CENTRAL OPTICAL DEPTH OF COMPONENT 2

	-2.1	-1.5	-0.9	-0.3	0.3	0.9	1.5	2.1	2.7
1.3			1.40 (0.08)	1.19 (0.41)	1.12 (0.53)	1.10 (0.42)			
0.7			1.29 (0.12)	1.15 (0.27)	1.05 (0.33)	1.16 (0.38)			
0.1	1.40 (0.22)	1.29 (0.28)	1.26 (0.10)	1.26 (0.13)	1.14 (0.25)	1.15 (0.30)	1.15 (0.42)	1.14 (0.38)	1.14 (0.28)
-0.5	1.28 (0.24)	1.25 (0.58)	1.26 (0.29)	1.39 (0.03)	1.31 (0.17)	1.22 (0.21)	1.09 (0.31)	0.99 (0.55)	0.98 (0.64)
-1.1	0.99 (0.40)	0.94 (0.46)				1.13 (0.34)	1.04 (0.28)	1.00 (0.46)	0.97 (0.62)

Figure 50c. (continued)

3C353 - 3 COMPONENT FIT : CENTRAL FREQUENCY OF COMPONENT 2

	-2.1	-1.5	-0.9	-0.3	0.3	0.9	1.5	2.1	2.7
1.3			-1.23 (0.58)	-1.83 (0.79)	-1.98 (1.65)	0.10 (1.44)			
0.7			-0.33 (0.23)	-0.70 (0.40)	-0.81 (0.59)	-0.29 (0.58)			
0.1	0.06 (0.30)	0.23 (0.34)	-0.08 (0.18)	-0.30 (0.23)	-0.34 (0.32)	-0.19 (0.34)	0.24 (0.51)	0.47 (0.57)	0.53 (0.46)
-0.5	0.16 (0.48)	0.31 (0.68)	0.18 (0.34)	-0.12 (0.18)	-0.17 (0.32)	-0.08 (0.29)	0.54 (0.39)	1.05 (0.62)	1.15 (0.83)
-1.1	0.19 (0.89)	0.24 (1.09)				0.05 (0.42)	0.68 (0.44)	1.38 (0.53)	1.65 (0.57)

Figure 50c. (continued)

3C353 - 3 COMPONENT FIT : FULL WIDTH OF COMPONENT 2

	-2.1	-1.5	-0.9	-0.3	0.3	0.9	1.5	2.1	2.7
1.3			15.32 (1.50)	14.08 (2.56)	12.94 (4.00)	11.15 (2.55)			
0.7			13.39 (0.69)	12.87 (1.37)	12.19 (1.94)	12.32 (1.71)			
0.1	13.35 (1.21)	13.62 (1.02)	13.50 (0.49)	13.52 (0.70)	13.00 (1.13)	12.66 (1.24)	12.26 (1.43)	11.73 (1.52)	11.04 (1.33)
-0.5	13.13 (1.36)	13.76 (1.97)	13.80 (1.02)	13.89 (0.51)	13.78 (0.91)	12.94 (1.06)	11.45 (1.36)	10.03 (2.11)	9.47 (2.43)
-1.1	11.45 (2.42)	12.50 (2.47)				12.48 (1.64)	10.77 (1.53)	8.77 (2.02)	7.76 (2.42)

Figure 50c. (continued)

3C353 - 3 COMPONENT FIT : CENTRAL OPTICAL DEPTH OF COMPONENT 3

	-2.1	-1.5	-0.9	-0.3	0.3	0.9	1.5	2.1	2.7
1.3			0.24 (0.08)	0.50 (0.41)	0.56 (0.53)	0.28 (0.47)			
0.7			0.35 (0.14)	0.48 (0.28)	0.52 (0.35)	0.30 (0.42)			
0.1	0.23 (0.16)	0.37 (0.21)	0.35 (0.11)	0.33 (0.14)	0.40 (0.26)	0.34 (0.32)	0.34 (0.50)	0.42 (0.49)	0.52 (0.34)
-0.5	0.43 (0.24)	0.42 (0.41)	0.34 (0.21)	0.12 (0.03)	0.16 (0.18)	0.26 (0.22)	0.40 (0.34)	0.63 (0.70)	0.76 (0.85)
-1.1	0.83 (0.43)	0.70 (0.50)				0.28 (0.36)	0.41 (0.30)	0.58 (0.61)	0.77 (1.08)

Figure 50c. (continued)

3C353 - 3 COMPONENT FIT : CENTRAL FREQUENCY OF COMPONENT 3

	-2.1	-1.5	-0.9	-0.3	0.3	0.9	1.5	2.1	2.7
1.3			-11.5 (4.5)	-4.6 (1.9)	-4.2 (2.0)	-4.3 (3.4)			
0.7			-6.6 (1.5)	-4.4 (1.2)	-3.5 (1.2)	-3.7 (1.9)			
0.1	-10.8 (8.9)	-8.9 (5.5)	-6.9 (1.3)	-5.8 (1.4)	-3.8 (1.1)	-3.1 (1.2)	-4.7 (1.8)	-6.0 (2.3)	-6.9 (2.0)
-0.5	-8.2 (4.1)	-9.2 (9.9)	-9.2 (6.2)	-14.7 (4.2)	-6.3 (3.8)	-2.6 (1.5)	-3.1 (1.3)	-4.1 (1.3)	-5.2 (1.3)
-1.1	-5.6 (1.9)	-5.7 (2.4)				-2.6 (2.0)	-2.6 (1.6)	-3.1 (2.2)	-4.0 (3.2)

Figure 50c. (continued)

3C353 - 3 COMPONENT FIT : FULL WIDTH OF COMPONENT 3

	-2.1	-1.5	-0.9	-0.3	0.3	0.9	1.5	2.1	2.7
1.3			44.4 (16.9)	31.1 (12.5)	30.8 (14.0)	30.1 (22.5)			
0.7			29.8 (5.3)	29.4 (7.7)	28.5 (8.3)	27.4 (13.5)			
0.1	26.3 (11.0)	21.9 (4.6)	26.8 (3.1)	30.3 (6.0)	28.0 (7.2)	26.8 (8.3)	25.6 (11.5)	26.6 (10.9)	28.7 (8.5)
-0.5	25.3 (5.9)	21.2 (7.7)	21.9 (5.0)	43.4 (11.9)	30.9 (15.5)	30.1 (10.3)	27.3 (8.6)	25.3 (9.4)	25.1 (9.5)
-1.1	25.3 (5.1)	23.4 (4.9)				28.5 (13.8)	29.0 (9.5)	26.0 (10.4)	24.0 (11.2)

Figure 50c. (continued)

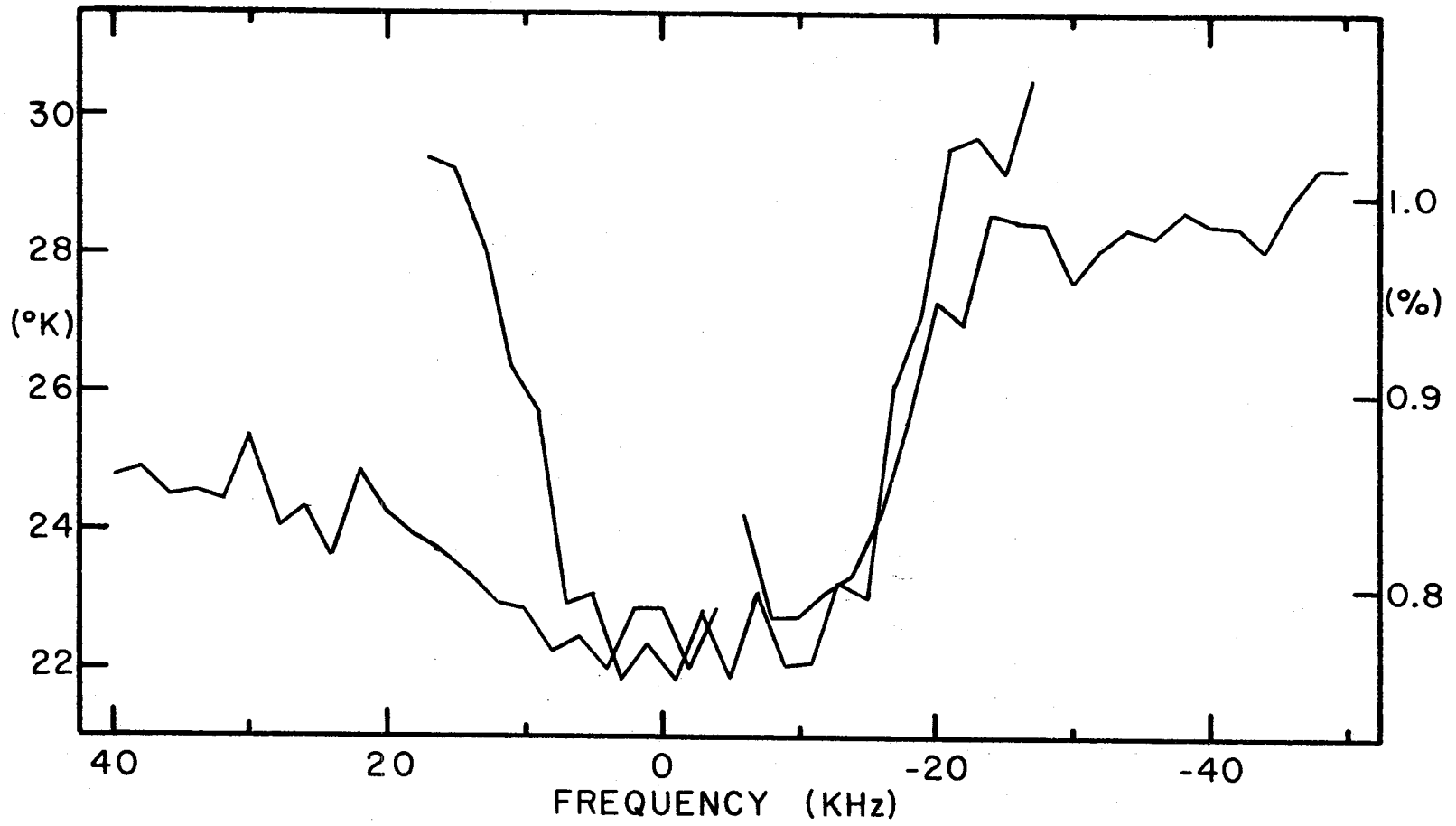

Figure 51a. 3C353: Spatially constant part of the noise as a function of frequency in °K and in percent of the peak brightness on the continuum map (right hand scale). Each continuous line represents a different frequency shift.

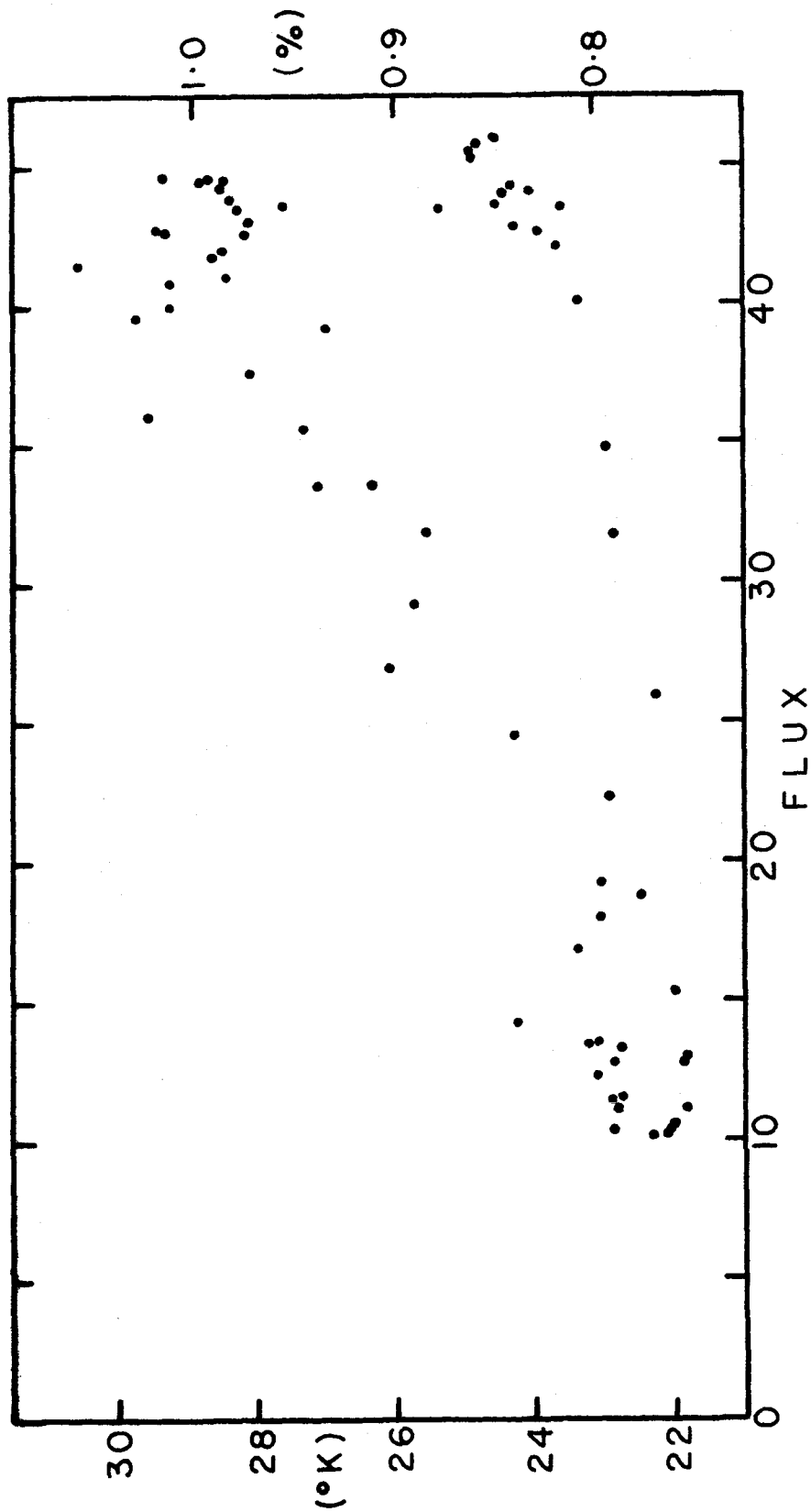

Figure 51b. 3C353: Spatially constant part of the noise as a function of flux at 200 feet east-west in °K and in percent of the peak brightness on the continuum map (right hand scale).

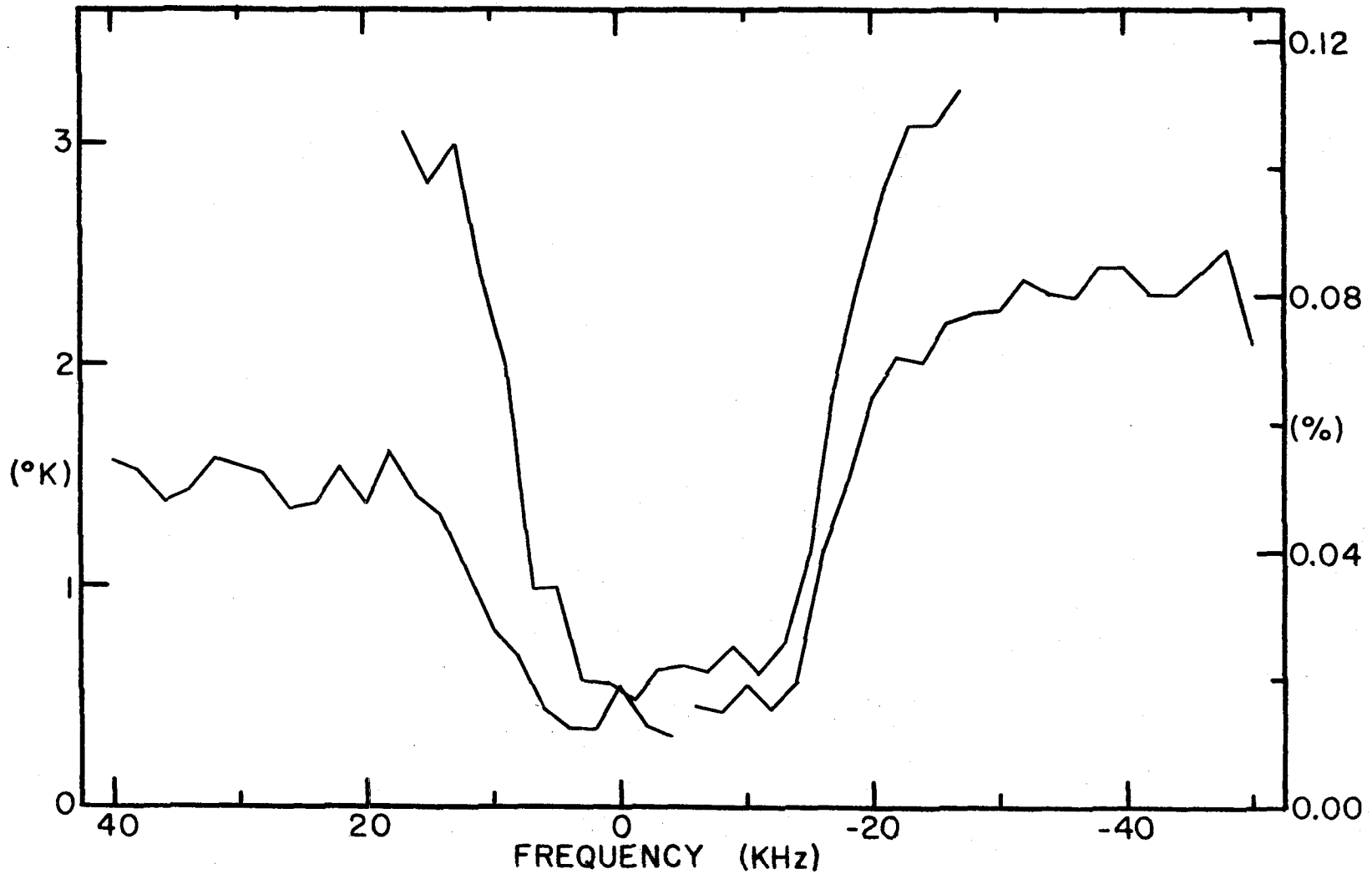

Figure 51c. 3C353: Upper limit to the spatially variable part of the noise as a function of frequency in °K and in percent of the peak brightness on the continuum map (right hand scale). Each continuous line represents a different frequency shift.

the noise is plotted as functions of frequency and short-spacing flux in Figures 51a and 51b, respectively. This part of the noise depends on the flux in the same manner as is found for the other sources. However, the + 018 frequency shift shows a surprisingly low noise with little dependence on flux. The upper limit to the variable part of the noise is plotted in Figure 51c as a function of frequency. This limit shows a stronger dependence on flux and is larger compared to the constant term than is found for the other sources. Again the agreement between the Monte Carlo tests and these noise calculations is very good (see Table V, Chapter 3B). The noise is found to be considerably higher on the source at 38 KHz, both before and after the deconvolution process. With such poor sampling of the (u, v) plane, such a result is not surprising and one wonders why it was not also found at - 4 KHz. At both frequencies used in these tests, the deconvolution process does cause an increase in the noise and, particularly, in the variance of the noise across the maps.

F. Interpretation

The standard model for the rotation of the Galaxy (Schmidt 1965) places the observed hydrogen within a few

hundred parsecs of the Sun or at a distance of about 19 Kpc. The latter possibility is ruled out by the high latitude of the source. The TASS model of the Galaxy has not been applied in detail to the local (Orion) arm although a major absorption feature seen over a wide range of longitudes about the galactic center has been suggested as arising from the shock front of the local arm (see Figure 1b; Riegel and Jennings 1969 and Riegel and Crutcher 1972). Stellar absorption spectra have placed the distance to this feature at less than 150 parsecs (Crutcher, R. M. 1972, private communication). Unfortunately, this feature, at a velocity of 6 km/sec, is not seen in spectra in the general direction of 3C353 although it is seen at both higher and lower longitudes (Radhakrishnan, et al 1972c). Since it is reasonable to presume that the hydrogen observed is part of the local arm and, hence, closer to us than the shock front, a distance of 100 parsecs will be assumed.

In the two-component solution, the average column density of component 1 is 1.38 $pc/cm^3/^\circ K$ and of component 2 is 2.66 $pc/cm^3/^\circ K$. Apparent temperatures as low as 50 $^\circ K$ and lower are found by the gaussian analysis for component

1. Taking this as the actual temperature, we find average column densities of 69 and 133 pc/cm^3. At the assumed distance, the source subtends a length of 0.14 pc. Since the gaussian analysis turned up some significant variation across the source, a reasonable lower limit to the depth of the clouds would be 0.14 pc. Substituting we find upper limits to the densities of 500 and 950 cm^{-3}. If the scale lengths of the clouds are around 1 pc, we find densities of 69 and 133 cm^{-3} which are similar to those found for Cassiopeia A and the Crab Nebula. Thus, we again find rather high densities in the absorbing medium. The total mass observed is only 0.08 solar masses due to the proximity of the hydrogen.

CHAPTER 8

OTHER SOURCES

In addition to the synthesis observations already discussed, a number of absorption spectra were measured at only one or two spacings. The frequency shifts used in these measurements are listed in Table X. Tables I and IV give position information for these sources.

A. W12 (3C147.1)

The HII region 3C147.1 was originally one of the synthesis sources in this program. Because of its large size and the very high optical depths found it was too weak for a proper synthesis. The vector average of about 100 minutes of data at the 200-foot east-west spacing is plotted in Figure 52. Despite the high galactic latitude, the absorption line is very deep and complex. The spectrum contains a broad feature about 0 km/sec, deep features at 7.4 and 9.5 km/sec, and a narrow feature near 13.7 km/sec. The phase spectrum reveals considerable structure in the absorbing medium particularly about 12.7 km/sec. Although the errors are very large at the bottom of the line, the presence of large positive phases about 9.5 km/sec seems well established. That there is also spatial structure in

TABLE X: FREQUENCY SHIFTS FOR THE OTHER SOURCES

W12 (3C147.1)	3C147	3C405	NGC5128*
+ 125 c	+ 200 c	+ 240 c	- 2375 c
+ 016 c	+ 094	+ 130	- 2560
- 003	+ 048	+ 084	- 2636
- 030	+ 002	+ 038	- 2744
- 049	- 044	- 034	- 2820
- 064	- 150 c	- 080	- 3025 c
- 180 c		- 200 c	

* 4-KHz filters

c Continuum frequency shift

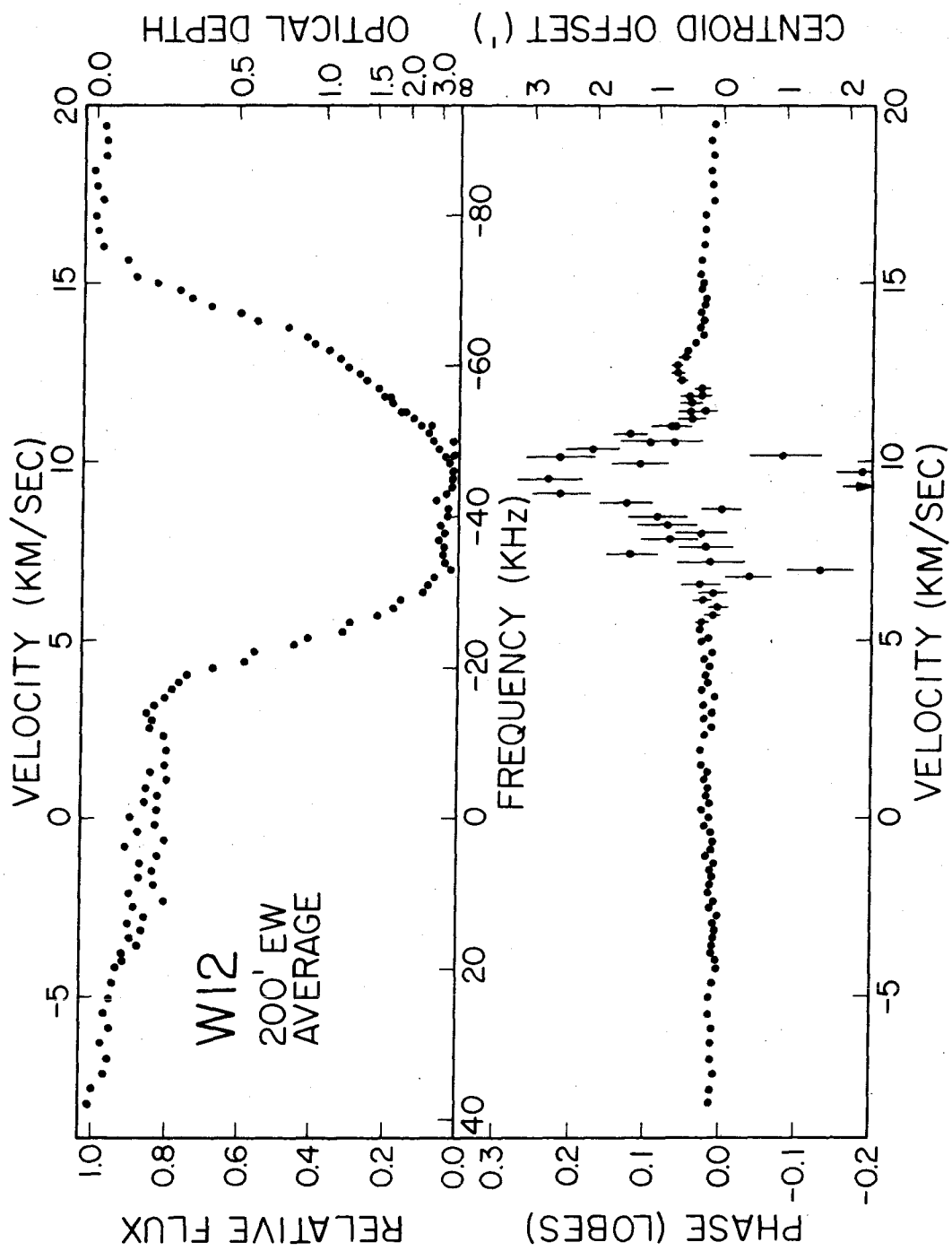

Figure 52. W12 (3C147.1): relative flux and phase spectra at 200 feet east-west. Average of 100 minutes of observation.

the absorbing medium around 0 km/sec is suggested not only by the small positive phases but also by the systematic disagreement in line shape of the two frequency shifts there. Such disagreement can arise when observations of a partially resolved feature are averaged over different sets of hour angles.

There is considerable interest in the absorption spectrum of this source, which is usually referred to in the literature by its other names: W12, NGC2024, and G206.5-16.4. Goss (1968) discovered absorption in the spectrum of this source in all four OH lines. At 1667 MHz, the optical depth observed at 9.3 km/sec is roughly a factor of four greater than for any other source in his survey. Since the line shapes are similar for all four lines (Manchester, et al 1970), a thermal interpretation of the OH absorption seems quite reasonable. However, the relative line strengths observed in OH are not those expected from an optically thin region in thermal equilibrium. Hence, it is suggested that the structure of the absorbing medium has an angular size smaller than that of the source. The data in Figure 52 would certainly support such a conclusion, although at 7 to 9.5 km/sec the optical depths must be high over the entire source. The

principal OH absorption features occur at 9.33 km/sec (1612 and 1667 MHz) and 9.54 km/sec (1665 and 1720 MHz) with a lesser feature around 12.5 km/sec.

Formaldehyde absorption at 6-cm wavelength has also been observed in the spectrum of this source (Whiteoak and Gardner 1970 and Zuckerman, et al 1970). With a line profile not unlike those found in OH, the principal formaldehyde feature occurs at 8.65 km/sec with a broad feature around 12.4 km/sec and a possible feature at 24.8 km/sec. Clearly this source is of considerable interest since it represents a probable association of neutral hydrogen with both OH and formaldehyde. Another problem raised by the absorption spectra is the distance to the source. Photometric observations of the presumed exciting star place the HII region at a distance of 0.4 Kpc (Johnson 1967). The velocity of the H109α recombination line from the source suggests a similar distance, about 0.5 Kpc. However, the velocities seen in the absorption lines would place the source at a distance greater than 1 Kpc according to the standard model of galactic rotation. We may be observing a considerable peculiar velocity or some non-equilibrium effects in the galactic rotation.

B. 3C147

There has also been some interest generated in the absorption spectrum of the quasi-stellar source 3C147. Shuter, Pulley and Rogstad (1967) reported a 28 ± 8 percent absorption feature at a velocity of - 44.3 km/sec (+ 209 KHz). This feature, corresponding to the far arm of the Galaxy, would require that the distance to the source be at least 9.2 Kpc. However, the observations at 800 feet east-west with the 4-KHz filters fail to confirm this result. After nearly two hours of integration no absorption feature is found at these frequencies with an uncertainty around 2 percent. Hughes, Thompson, and Colvin (1971) report a similar finding.

The spectrum of the source was observed with the 1-KHz filters at the 1200-foot east-west baseline. Due to the low flux of the source as well as pressures on observing time, the spectrum was observed only every two KHz. The vector average of about 135 minutes of data is plotted in Figure 53. The flux spectrum is given at the top and the phase spectrum at the bottom of the figure. The presence of non-zero phase in the spectrum of a point source would indicate that galactic hydrogen emission is affecting the observations. However, no significant phase

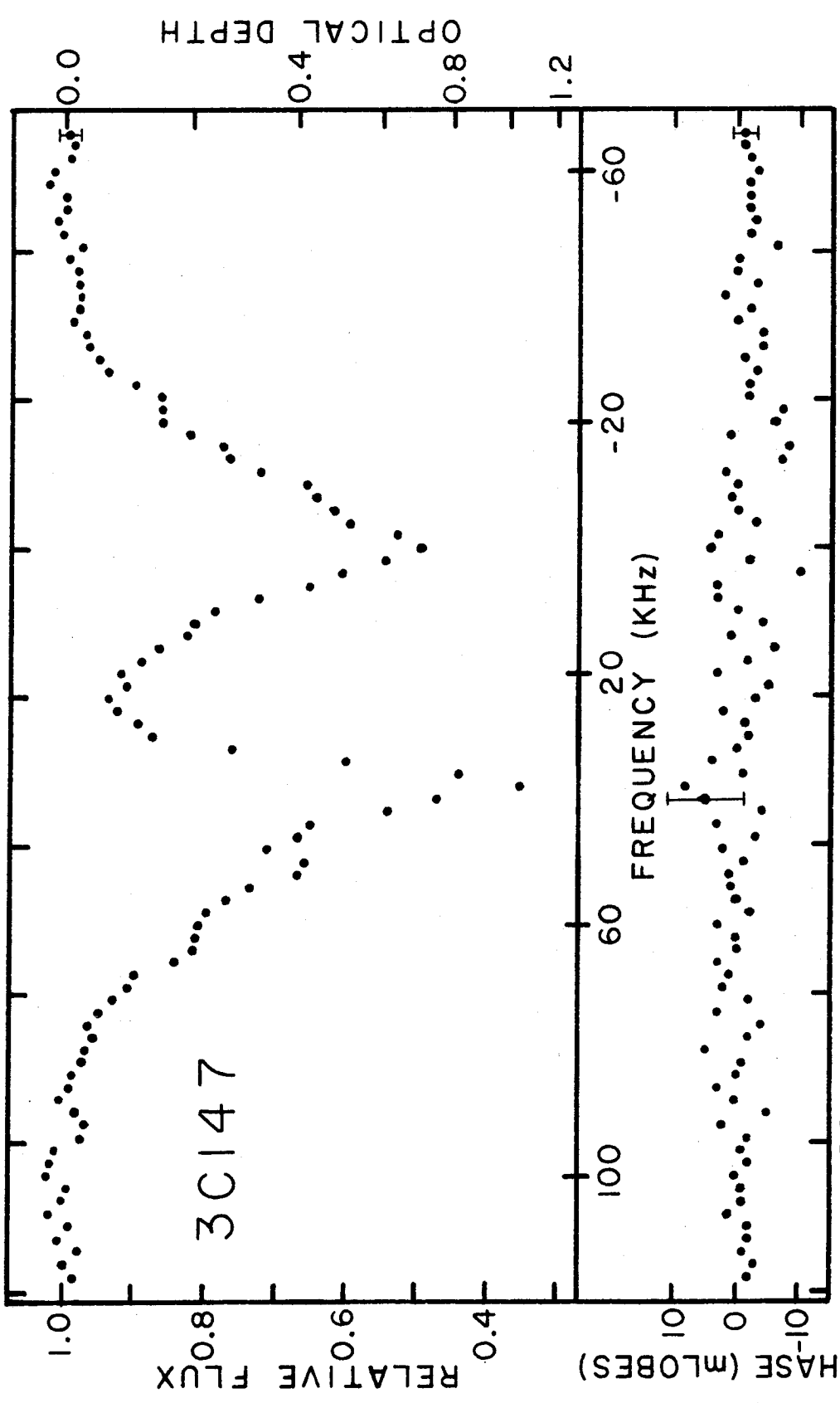

Figure 53. 3C147: relative flux and phase (milli lobes) spectra at 1200 feet east-west. Average of 135 minutes of observation.

is seen. The flux spectrum is quite complicated. Local hydrogen causes a line at 0 km/sec with a long wing toward higher velocities and at least one significant bend in the spectrum at 4.6 km/sec. The Perseus arm causes a narrow feature at - 8.0 km/sec and lesser features about - 10.8 and - 13.1 km/sec. The narrow feature, by its width and depth, certainly suggests a density-wave shock region with the broad and complicated feature arising in the main part of the Perseus arm. A more detailed examination of this spectrum in the light of the TASS model would be interesting. Unfortunately, Roberts (1972) does not present his calculations for this longitude range.

C. Cygnus A (3C405 (Zero Velocity))

The spectrum of Cygnus A at frequencies around 0 KHz was observed at the 200-foot east-west spacing. The results after 50 minutes of integration are presented in Figure 54. Again the pressure for observing time and the considerable width of the spectrum caused the data to be obtained only at intervals of 2 KHz. Since the absolute phase was not well calibrated, to produce this figure it was necessary to apply a DC offset in phase to each frequency shift separately. This brings the frequency shifts into agreement, but adds some further uncertainty. Nevertheless,

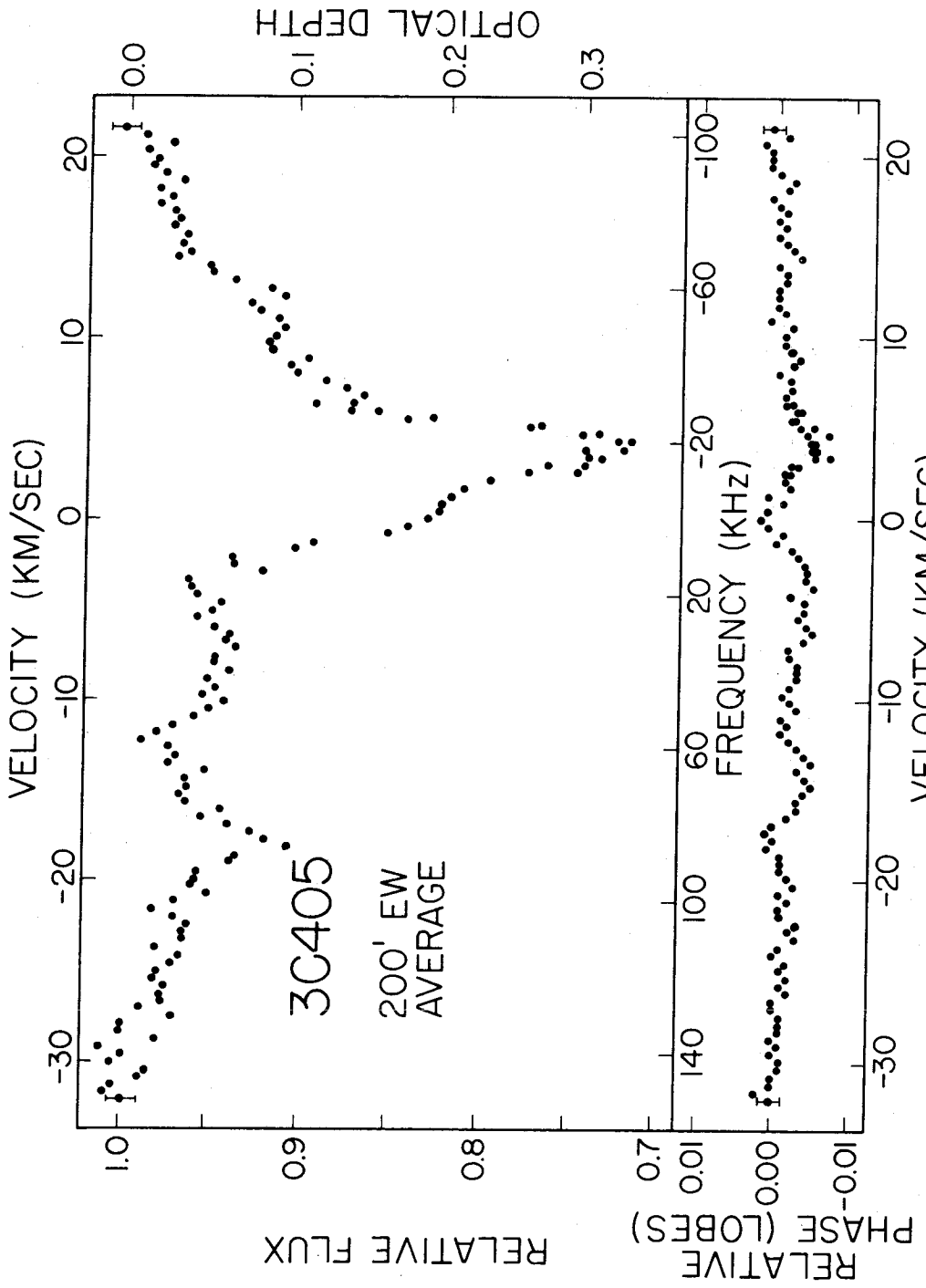

Figure 54. 3C405: relative flux and phase spectra at 200 feet east-west. Average of 50 minutes of observation.

the presence of some structure in the absorbing medium appears to be well-established, particularly around 4.0, 0.0, - 11.4, and - 17.8 km/sec. The flux spectrum shows absorption over most of the frequency range observed. Features at 12.3, 4.0, 0.0, - 6.3, - 14.8, and - 18.2 km/sec are quite obvious. The large number of features is caused by the fact that the line of sight to the source lies directly along the local (Orion or Carina-Cygnus) arm for a considerable distance. In fact, using the standard rotation model (Schmidt 1965), the feature at - 18.2 km/sec is caused by hydrogen nearly 7 Kpc from the Sun. In this equilibrium model, the feature at 12.3 km/sec is forbidden without a peculiar velocity of at least 4 km/sec.

D. Centaurus A (NGC5128)

In an attempt to confirm Roberts' (1970) observation of an extragalactic absorption line, the absorption spectrum of Centaurus A was observed with the 4-KHz filters. Roberts reports a peak optical depth of 0.02 averaged over his 22-minute of arc beam. Since considerably higher optical depths could be expected over parts of the source, interferometric observations were conducted at the 400- and, particularly, 800-foot east-west spacings. The

visibility function of a double source, such as the central parts of Centaurus A, is quite sensitive to a variation of optical depth across the source. The observations at the redshift of the galaxy NGC5128 show no spectral features even at the minimum in the visibility function of the continuum source. The noise ranged from about 3 percent to at least 10 percent at this minimum. Thus, the data suggest that the hydrogen is fairly uniformly distributed at least over the central parts of the radio source and are not inconsistent with Roberts' results.

SUMMARY AND CONCLUSIONS

This thesis has presented the results of an aperture synthesis program on interstellar neutral hydrogen as seen in absorption in the spectra of four strong radio sources. The receiving equipment and methods of calibration are discussed in some detail. The unusual method of Fourier transformation used in this program is discussed in Chapter 3 and compared to other transform methods in Appendix D. The noise on the final maps is moderately well understood and is evaluated using both a Monte Carlo method and a theoretical formulation. The spectra obtained are analyzed as sums of gaussians using a least-squares method. In the appendices, the basic principles of aperture synthesis and hydrogen line formation are presented and the problem of detector law failure is discussed.

Cygnus A is found to have two major absorption features both of which have spatial structure within the absorbing medium. The complex and broad feature due to hydrogen in the local or Carina-Cygnus arm of the Galaxy was observed only at short spacing. However, the narrow, apparently simple feature due to hydrogen in the Perseus arm was observed with a complete synthesis and is found to

have four components. The strongest component is heavily concentrated toward the eastern edge of the source and has a peak optical depth two to three times that seen at short spacings. The apparent temperature of this component is 70 °K, half that deduced from short-spacing observations. Such changes with improved resolution are important in discussions of general models for the interstellar medium. The hydrogen can be interpreted as a shell expanding at 2 km/sec, with an outer radius about 9.7 parsecs, a thickness about 1.1 parsecs, a density of 6 cm^{-3}, and a total mass around 175 solar masses. The origin or cause of such a shell is unknown.

Cassiopeia A was observed with full synthesis within the broad, complex absorption feature associated with the Perseus arm. The absorption feature separates into two major features each of which has considerable spatial structure within the absorbing medium, but of qualitatively different types. On the low frequency side of the absorption feature, the optical depth maps reveal a bewildering variety of peaks, ridges, and minima which vary fairly rapidly with frequency. Optical depths as great as four occur but the contrast in optical depths across the source

never exceeds factors of two or three. At higher frequencies, the optical depth maps generally have only one or two peaks. Optical depths of six or more are common and the contrast in optical depths across the source can exceed factors of seven. The higher frequency part of the absorption feature is interpreted as arising in regions immediately following a density-wave shock front at the leading edge of the Perseus arm while the lower frequency part arises in the main body of the Perseus arm. The spectra do not seem to vary across the source by as much as one would expect from the complicated spatial structure. This result suggests that considerably better spatial resolution is required in order to separate the spectral components. Support for this statement is also provided by the fact that only a few of the spectra could be satisfactorily fit with sums of gaussians. Cloud diameters about a parsec (the beamwidth) or less and cloud densities on the order of 50 cm^{-3} within the arm and 300 cm^{-3} within the post-shock region are suggested by the data. One unusual cloud is seen to be rotating with a maximum period of three million years. However, there does not appear to be sufficient mass to prevent this cloud from rather rapidly disintegrating.

The absorption spectrum of the Crab Nebula is also found through a full aperture synthesis to reveal significant structure in the interstellar medium. Although the optical depth maps contain a number of apparently unresolved peaks, the contrasts in optical depth across the source are small and all spectral components are found at each point on the source. The principal component has a significant velocity gradient across the source and appears to contain several condensations within a large, less dense cloud. Apparent temperatures around 50 °K are well determined for one of the components while cloud densities as great as 100 cm^{-3} are suggested. Over half the hydrogen observed occurs in a very wide component having peak optical depth about 0.45 and apparent temperature around 3000 °K. Since hydrogen emission temperatures in this direction are not on the order of 1000 °K, this component must represent the superposition of a large number of small, cold, and probably turbulent clouds.

A full synthesis was also performed on the absorption feature in the spectrum of 3C353. The poor signal-to-noise ratio on the maps prevents any reliable determination of spatial structure in the absorbing medium. However,

gaussian analysis of the spectra suggests that such structure does exist at least in the form of a gradient in the width of one of the two main components. The distance to the hydrogen is very poorly determined but a reasonable estimate indicates that this gradient occurs over a distance of only 0.14 parsecs! The apparent temperature of this component becomes as low as 50 °K while reasonable estimates of the densities of both components are on the order of 100 cm^{-3}. Again a rather wide component having optical depth about 0.4 and apparent temperature about 700 °K was necessary to obtain the best fits to the spectra. Since the brightness temperature in emission in this direction is only about 50 °K (Radhakrishnan, et al 1972d), this broad component must also represent a superposition of many cold and perhaps turbulent clouds.

The distribution of hydrogen absorption features should reflect in part the large-scale motions and structure of the Galaxy. The TASS model of the Galaxy predicts the occurence of shock fronts at the leading edges of the spiral density wave pattern. In the post-shock region a narrow deep absorption feature should arise while in the main part of the spiral arm a broader, shallower, more complicated feature should arise. This pattern of

absorption is seen in the spectra of Cassiopeia A, the Crab Nebula, and 3C147. A detailed examination of the TASS model by Roberts (1972) shows good qualitative agreement with the data presented here for Cassiopeia A (with the proviso that the Perseus arm is 0.25 Kpc closer to us than taken by Roberts). For the Crab Nebula and 3C147 the absorption features do not occur at the velocities predicted by Roberts for the Perseus arm. Considering the latitudes of these two sources, it is likely that the hydrogen observed is closer to us than the Perseus arm and that the shock wave is not sustained at distances from the plane of the Galaxy greater than 170 parsecs or so (although it is still strong at a distance of 100 pc).

As described in the Introduction, the two-phase model of the interstellar medium is well-founded on theoretical grounds, but the observational evidence is shaky. The data reported here only make the observational evidence appear even more uncertain. Scale lengths in the interstellar medium of a parsec (or possibly even 0.14 pc) are found to be common. The moderate improvement in resolution obtained by this program is seen to cause a significant decrease in observed line widths. This decrease is just the result of

the improved resolution of blended clouds and velocity gradients. Thus it is clear that the difference in the observed widths of hydrogen emission and absorption profiles is due at least partly to the difference in the spatial resolution in the two types of observations. Radhakrishnan, et al (1972d) regard the presence of very wide components in emission spectra as very significant since they do not see them in their corresponding absorption profiles. However, with the improved signal-to-noise ratio of this program, wide components are found in the spectra of all the synthesis sources except Cygnus A. Since the absorption measurements directly determine the optical depth, it is easy to establish that these wide components do not arise in a diffuse, hot gas, but result, instead, from the superposition of many cold clouds.

APPENDIX A

APERTURE SYNTHESIS

The method of interferometric aperture synthesis is best understood by first considering the analogy with the single-dish telescope. The voltage V produced at the horn of this telescope by an element of area of the dish dudv due to radiation at frequency ω from an element of sky dxdy may be written as

$$V(u,v,x,y,t)=V(x,y)W(u,v)e^{i[\omega t+\xi(x,y,t)]}\,e^{i2\pi[u(x-x_0)+v(y-y_0)]}$$

where the telescope is pointed at (x_0, y_0), u and v are measured in wavelengths, ξ is a random function which varies rapidly in all coordinates, and W is a weighting function which accounts for taper introduced by the horn and which is zero outside the dish area. The total voltage at the horn is the integral of this voltage over the dish and the sky. This voltage is then detected by a system which responds to the time average of the power. Thus

$$R(x_0, y_0) =$$

$$\beta^2 \int_{-\infty}^{\infty} dudv \int_{-\infty}^{\infty} du'dv' \int_{-\infty}^{\infty} dxdy \int_{-\infty}^{\infty} dx'dy' \; T^{\frac{1}{2}}(x,y)$$

$$T^{\frac{1}{2}}(x',y')W(u,v)W(u'v')\exp\left[2\pi i\{u(x-x_0)-u'(x'-x_0)+v(y-y_0)\right.$$

$$\left.-v(y'-y_0)\}\right] \langle \exp\left[i(\xi(x,y,t)-\xi(x',y',t)\right] \rangle$$

where we introduce the brightness temperature of the sky $T(x, y)$, where $T(x, y)$ is proportional to $V^2(x, y)$. Since

$$\langle e^{i\left[\xi(x,y,t)-\xi(x',y',t)\right]} \rangle = {}^2\delta(x-x', y-y')$$

by our assumption of a random noise signal, the response simplifies to

$$R(x_0, y_0) = \beta^2 \int_{-\infty}^{\infty} dudv \int_{-\infty}^{\infty} du'dv' e^{-2\pi i\left[(u-u')x_0+(v-v')y_0\right]}$$

$$W(u, v)\, W(u', v')$$

$$\times \int_{-\infty}^{\infty} dxdy \; T(x,y) e^{i2\pi\left[(u-u')x+(v-v')y\right]} .$$

(A-1)

Transforming coordinates we obtain finally

$$R(x_0,y_0)= \int_{-\infty}^{\infty}\int dudv\ F(u,v)A(u,v)e^{-2\pi i(ux_0+vy_0)} \tag{A-2}$$

where the complex fringe visibility function is defined as

$$F(u,v) \equiv \beta^2\iint dxdy\ T(x,y)e^{i2\pi(ux+vy)}$$

and the autocorrelation of the weighting function is

$$A(u,v) \equiv \int_{-\infty}^{\infty}\int du'dv'\ W(u+u',\ v+v')\ W(u',v').$$

Thus, the single dish responds to the Fourier transform of the visibility function weighted by a sampling function.

Let us now consider the standard sampling theorem (Bracewell 1958). We sample the visibility function at regular intervals in u of $1/2\ x_c$ and v of $1/2\ y_c$. The sampled visibility function may be written as

$$V'(u,v) = {}^2III(2x_c m\Delta u,\ 2y_c n\Delta v)\ V(u,v)$$

where the III (sha) function is defined as

$${}^2III(x,y) = \sum_{\mu=-\infty}^{\infty}\ \sum_{\nu=-\infty}^{\infty}\ {}^2\delta(x-\mu,\ y-\nu).$$

If we Fourier transform the sampled visibility function we obtain a map given by

$$R(x, y) = {}^{2}III(x/2x_c, y/2y_c) * T(x, y)$$

where $T(x, y)$ is the true brightness distribution and $*$ denotes a convolution. In other words, we now have the desired map repeated at intervals of $2x_c$ in x and $2y_c$ in y. If

$$T(x, y) = 0 \text{ for } |x| > x_c \text{ or } |y| > y_c$$

then the repetition does not cause the maps to overlap and hence causes no error. Therefore, we must sample the visibility function at intervals smaller than the inverse diameter of the source being observed.

Since this sampling interval is about 400 feet (for the sources in this program at 21 cm) which is larger than the diameter of almost all single-dish telescopes, all information collected by the elements of a single dish is redundant for such sources. We may remove this redundancy or lack of resolution at reasonable cost if we sacrifice collecting area. We use one small telescope as the central surface element of the aperture to be synthesized while another movable telescope provides other surface elements of the synthesized aperture (Figure A1). If the voltages

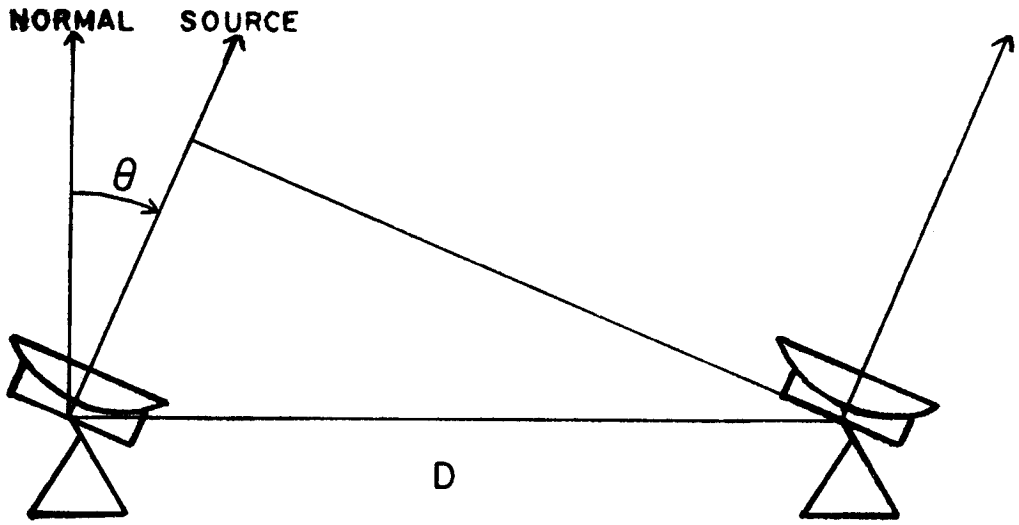

Figure A1. Geometry of two-element interferometer.

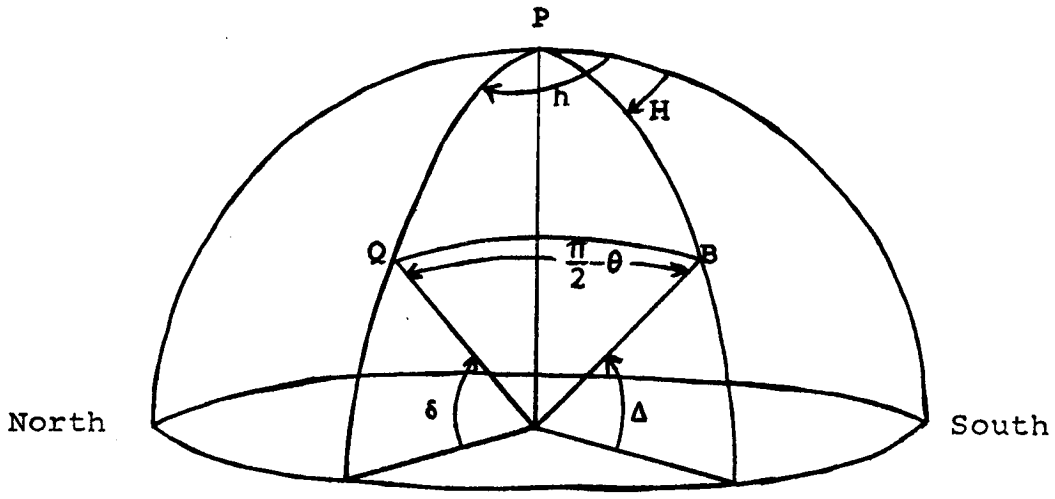

Figure A2. Celestial sphere with source (Q) and pole of baseline (B).

from the two telescopes are multiplied together and smoothed the output is

$$R(x, y) = V_0^2 \, e^{i\tau(x, y)} \qquad \text{(A-3)}$$

where $\tau(x, y) = \frac{2\pi D}{\lambda} \sin\theta(x,y)$ and V_0 is the voltage produced by the source at each telescope. As the earth rotates, $\sin\theta$ varies producing an approximately sinusoidal output called fringes. The phase τ may be expanded about some angle θ_0 as

$$\tau = \frac{2\pi D}{\lambda} \sin\theta_0 + \frac{2\pi D}{\lambda} \cos\theta_0 \Delta\theta \qquad \text{(A-4)}$$

where the first term is the "expected fringe" which is removed during reduction and the second term is the "fringe phase". For an extended source, the total response of the interferometer is just the integral of the separate responses of equation (A-3) to produce

$$R(u,v) = \int_{-\infty}^{\infty}\int dxdy \; T(x,y) e^{i2\pi(ux+vy)}$$

where the expected fringe has been removed and the phase $\frac{D}{\lambda} \cos\theta_0 \Delta\theta$ has been expressed in rectangular coordinates. In other words, the interferometer directly measures the visibility function.

The formulae for $\sin\theta_0$, u, and v may be derived as follows. The three points indicated on the celestial sphere in Figure A2 are the north celestial pole P, the pole of the extended baseline B and the source Q. The hour angle and declination of the source are h and δ, respectively, while the corresponding quantities for the baseline are H and Δ. The angle between Q and B is $\pi/2-\theta$. The law of cosines is used on the triangle PQB to give

$$\sin\theta = \sin\delta\sin\Delta + \cos\delta\cos\Delta\cos(h-H) .$$

The projection of the baseline along constant longitude is

$$v=-\frac{D}{\lambda}\frac{\partial\sin\theta}{\partial\delta} =-\frac{D}{\lambda}\left\{\cos\delta\sin\Delta-\sin\delta\cos\Delta\cos(h-H)\right\}$$

and the projection of the baseline along constant latitude is

$$u = \frac{D}{\lambda}\frac{1}{\cos\delta}\frac{\partial\sin\theta}{\partial h} = -\frac{D}{\lambda}\cos\delta\sin(h-H).$$

The choice of signs for u and v is a matter of convention while the factor $(1/\cos\delta)$ enters the equation for u so that x may be expressed in units of angle rather than time. As the source changes hour angle, the values of u and v describe an ellipse in the (u, v) plane. To fully sample the visibility function, we observe the source through the

available range of hour angle at a number of discrete antenna separations D.

The Hermitian property of the visibility function is quite useful and easily derived. Since the visibility function and the source brightness are a Fourier-transform pair we may write

$$T(x,\ y)=\alpha \int_{-\infty}^{\infty}\int dudv\ \underset{\sim}{V}(u,v)e^{-i2\pi(ux+vy)} .$$

Writing the visibility function as the sum of a real and imaginary part we obtain the imaginary part of T as

$$Im\big(T(x,\ y)\big) =$$

$$\alpha \int_{-\infty}^{\infty}\int dudv\big[I(u,v)\cos 2\pi(ux+vy)-R(u,v)\sin 2\pi(ux+vy)\big] .$$

Since this must be zero we may use the symmetry properties of sines and cosines and the independence of R and I to show that

$$R(u,\ v) = R(-u,\ -v)$$

$$I(u,\ v) = -\ I(-u,\ -v)$$

or

$$V(u,\ v) = V^*(-u,\ -v) .$$

Therefore we need sample the visibility function over only one-half of the (u, v) plane. This formalism is only a more elegant way to express the fact that the only

difference between say an east-west and a west-east baseline is the sign convention for the phase.

We should now relax the implicit assumption of monochromatic emission and discuss the real antenna system illustrated in Figure A3 (due to Read 1963). Let x, y, and z be the electrical lengths of the cables associated with telescope 1 and $x + \Delta x$, $y + \Delta y$, and $z + \Delta z$ be the corresponding electrical lengths for telescope 2. Let ω_{LO} be the angular frequency of the local oscillator, ω_{IF} be the angular frequency (or frequencies) to which the IF amplifiers respond and $V(\omega_{LO} + \omega_{IF})$ be the amplitude of the signal following the RF stages. Then the voltages are given by:

at (a) $\quad V(\omega_{LO} + \omega_{IF}) \sin (\omega_{LO} + \omega_{IF})t$

at (b) $\quad V(\omega_{LO} + \omega_{IF}) \sin \left[(\omega_{LO} + \omega_{IF})(t - x/c)\right]$

at (c) $\quad \cos \omega_{LO}(t - y/c)$

and at (d)

$$V(\omega_{LO} + \omega_{IF})\sin\left[(\omega_{LO} + \omega_{IF})(t - x/c)\right]\cos\left[\omega_{LO}(t - y/c)\right].$$

Rewriting this last expression using trigonometric identities we have at (d)

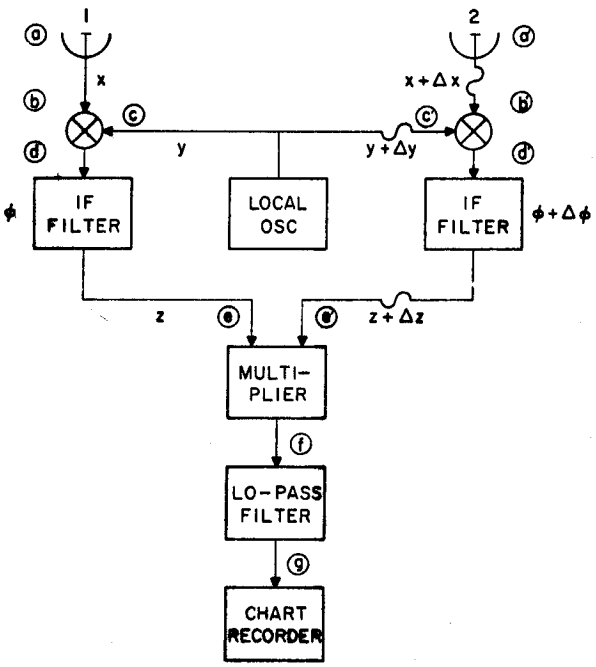

Figure A3. Receiver logic from Read (1963).

$$0.5\ V(\omega_{LO} + \omega_{IF})\Big\{\sin\big[(2\omega_{LO} + \omega_{IF})t - \omega_{LO}(x/c + y/c) - \omega_{IF}\ x/c\big] + \sin\big[\omega_{IF}t + \omega_{LO}(y/c-x/c) - \omega_{IF}\ x/c\big]\Big\} .$$

The IF filter will introduce a phase shift φ and a gain function g. Assuming that $g(2\omega_{LO} + \omega_{IF}) = 0$, we obtain at (e)

$$0.5\ g_1(\omega_{IF})V(\omega_{LO}+\omega_{IF})\sin\big[\omega_{IF}(t-x/c-z/c)+\varphi+\omega_{LO}(y/c-x/c)\big] .$$

The signal reaching the second telescope is delayed by τ seconds with respect to that reaching the first telescope. With this exception, the derivation of the voltages from the second telescope is identical to that given above. The result at (e') is

$$0.5\ g_2(\omega_{IF})V(\omega_{LO}+\omega_{IF})\sin\big[\omega_{IF}(t-x/c-\Delta x/c-z/c-\Delta z/c-\tau) +\varphi+\Delta\varphi+\omega_{LO}(y/c+\Delta y/c-x/c-\Delta x/c)\big] .$$

We take the product of these two voltages and simplify the result to obtain

$$0.125\ g_1(\omega_{IF})g_2(\omega_{IF})V^2(\omega_{LO}+\omega_{IF})$$

$$x\Big\{\cos\big[\omega_{IF}(\tau+\Delta x/c+\Delta z/c) - \Delta\varphi + \omega_{LO}(\tau+\Delta x/c-\Delta y/c)\big] - \cos\big[\omega_{IF}(2t-\tau-2x/c-\Delta x/c-2z/c-\Delta z/c) + 2\varphi + \Delta\varphi + \omega_{LO}(-\tau+2y/c+\Delta y/c-2x/c-\Delta x/c)\big]\Big\} .$$

The second term is rejected by the low-pass filter leaving at (g)

$$R(\tau)=0.125\int_{-\infty}^{\infty} d\omega_{IF}\; g^2(\omega_{IF})V^2(\omega_{LO}+\omega_{IF})\cos\left[(\omega_{IF}+\omega_{LO})\tau + \omega_{IF}(\Delta x/c+\Delta z/c) - \Delta\varphi + \omega_{LO}(\Delta x/c-\Delta y/c)\right]$$

where we now explicitly show the integral over all ω_{IF}.[1] Thus the response is the Fourier transform of the bandpass shape times the source power spectrum.

Two special cases of this formula are of interest. In double sideband operation where one assumes that

$$g^2(\omega_{IF})\; V^2(\omega_{LO} + \omega_{IF}) = g^2(-\omega_{IF})\; V^2(\omega_{LO} - \omega_{IF})$$

the formula becomes

$$R(\tau)=\tfrac{1}{4}\left[\cos\;\omega_{LO}(\tau+\Delta x/c-\Delta y/c)-\Delta\varphi\right]\int_0^{\infty} d\omega_{IF}\; g^2(\omega_{IF})V^2(\omega_{LO}+\omega_{IF})\cos\left[\omega_{IF}(\tau+\Delta x/c+\Delta z/c)\right] .$$

---

1 The integrals over all frequencies should really be shown prior to the multiplication step. However, the low-pass filter removes all signals except those where $\omega_{IF}(1)=\omega_{IF}(2)$ and $\omega_{IF}(1)=-\omega_{IF}(2)$. The latter signal is multiplied by $V(\omega_{LO}+\omega_{IF})V(\omega_{LO}-\omega_{IF})$ which is zero on average because of the assumption of a random noise signal.

It is common practice to maximize the Fourier transform and hold it constant by "tracking delay" i.e. by forcing

$$\frac{\Delta z}{c} = - \tau - \frac{\Delta x}{c} \quad .$$

In single sideband operation, such as was used in this program, it is assumed that

$$V^2(\omega_{LO} + \omega_{IF}) = 0 \qquad \text{for } \omega_{IF} < 0.$$

Then the response becomes

$$R(\tau) = \frac{1}{8} \int_0^\infty d\omega_{IF}\, g^2(\omega_{IF})\, V^2(\omega_{LO} + \omega_{IF})$$

$$\cos\left[(\omega_{IF} + \omega_{LO})\tau + \omega_{IF}(\Delta x/c + \Delta z/c)\right.$$

$$\left. - \Delta\varphi + \omega_{LO}(\Delta x/c - \Delta y/c)\right] \quad .$$

The delay may again be tracked which causes the fringes to enter with a frequency proportional to ω_{LO}. However, since delay is tracked in discrete steps at the OVRO which cause small jumps in fringe phase, this procedure has not normally been followed. Instead the delay is held fixed for each record causing the fringes to enter with a frequency proportional to $\omega_{LO} + \omega_{IF}$. In the reduction, the measured phases must be carefully corrected for the delay employed and the value of ω_{IF} used must be fairly accurate.

This development has implicitly assumed that the signal has come from a point source. The generalization to a source of finite size may be written as

$$R(\tau)= \frac{1}{8} \int_{-\infty}^{\infty}\int dxdy \int_{0}^{\infty} d\omega_{IF}\; g^2(\omega_{IF})V^2(\omega_{LO}+\omega_{IF},\, x,\, y)$$

$$\cos\left[(\omega_{IF}+\omega_{LO})\tau_0+\omega_{IF}(\Delta x/c+\Delta z/c)-\Delta\varphi+\omega_{LO}(\Delta x/c-\Delta y/c)\right.$$

$$\left. + (\omega_{IF} + \omega_{LO})\, \Delta\tau(x,\, y)\right]$$

where x and y are here used as space coordinates. Therefor, whether or not delay is tracked, the phase departure from the expected fringe is determined by the observing frequency.

APPENDIX B

HYDROGEN LINE FORMATION

This appendix contains the basic equations of radiative transfer and line formation assumed in the main text to be known by the reader.

Let us first consider a gas in thermodynamic equilibrium at an effective temperature T called the spin temperature. Let us also assume that the atoms of this gas can exist in one of two states. We may write the number of photons emitted by spontaneous emission as n_2A_{21} and by stimulated emission as $I_\nu n_2 B_{21}$ where n_i is the number of atoms in state i, I_ν is the radiation density and A_{21} and B_{21} are the spontaneous and stimulated emission coefficients respectively, for the atom. The number of photons absorbed is given by $n_1 I_\nu B_{12}$ where B_{12} is the absorption coefficient for the atom. Since no net energy is emitted by the gas

$$n_1 I_\nu B_{12} = n_2 A_{21} + n_2 I_\nu B_{21}$$

or

$$\frac{A_{21}}{B_{12}} = \frac{n_1}{n_2} I_\nu \left[1 - \frac{n_2}{n_1} \frac{B_{21}}{B_{12}} \right] .$$

Since the gas in in thermodynamic equilibrium we substitute the relations

$$\frac{n_2}{n_1} = \frac{g_2}{g_1} e^{-h\nu/kT} \tag{B-1}$$

and

$$I_\nu = \frac{8\pi h\nu^3}{c^2(e^{h\nu/kT} - 1)} \tag{B-2}$$

to obtain

$$\frac{A_{21}}{B_{12}} = \frac{g_1}{g_2} \frac{8\pi h\nu^3}{c^2(1 - e^{-h\nu/kT})} \left[1 - \frac{g_2}{g_1} \frac{B_{21}}{B_{12}} e^{-h\nu/kT}\right]$$

where g_i is the statistical weight of state i and $h\nu$ is the energy difference between the two states. Since the coefficients are intrinsic properties of the atom independent of temperature, this equation states that

$$g_2 B_{21} = g_1 B_{12}$$

and

$$\frac{A_{21}}{B_{12}} = \frac{8\pi g_1}{g_2} \frac{h\nu^3}{c^2} .$$

Now consider a slab of this gas of spin temperature T_s having thickness dz illuminated by radiation at temperature T(z). Then

$$\frac{dI_\nu}{dz} = h\nu[n_2 A_{21} + n_2 I_\nu B_{21} - n_1 I_\nu B_{12}]$$

or

$$\frac{dI_\nu}{dz} = h\nu\, n_2 A_{21}\left[1 - I_\nu\left(1 - \frac{g_2 n_1}{g_1 n_2}\right)\frac{c^2}{8\pi h\nu^3}\right]$$

where the units of density are atoms per cm^3 per Hertz. Using (B-1) and (B-2) and the Rayleigh-Jeans approximation ($h\nu << kT$) and noting that the total number of atoms n is given by

$$n = n_1 + n_2 = n_2\left(1 + \frac{g_1}{g_2}\, e^{h\nu/kT_s}\right)$$

we find

$$dT = -\,(T - T_s)d\tau$$

where

$$d\tau = \frac{c^2\, A_{21}}{8\pi\, \nu^2}\,\frac{h\nu}{k}\left(\frac{g_2}{g_1 + g_2}\right)\frac{n}{T_s}\,dz \quad .$$

We may now consider the particular case of the hydrogen atom. Each of the orbital angular momentum states is split in "fine-structure" states by the interaction of the electron spin $\underset{\sim}{\sigma}_e$ with the orbital angular momentum $\underset{\sim}{L}$. Each of these states is split into "hyperfine" states by the interaction of the proton spin $\underset{\sim}{\sigma}_p$ with the total electronic angular momentum $\underset{\sim}{J} = \underset{\sim}{\sigma}_e + \underset{\sim}{L}$. State 1 in the above discussion occurs when the two spins are anti-parallel resulting in a total spin of zero and a single eigenstate ($g_1 = 1$).

State 2 occurs when the two spins are parallel resulting in a total spin of one and three eigenstates ($g_2 = 3$). It has been shown (Bethe and Salpeter 1957) that the energy of a given hydrogen state is

$$E = \frac{h\nu_0}{n^3}\left[\frac{F(F+1) - \sigma_p(\sigma_p+1) - J(J+1)}{J(J+1)(2L+1)}\right]$$

where F is the total angular momentum, n is the principal quantum number, and ν_0 is $\alpha^2 gm/m_p$ in Rydbergs. For the ground state of hydrogen, n = 1, L = 0, and σ_p and J are one-half. Then the transition between F values of one and zero has energy difference

$$\Delta E = h\nu = \frac{8}{3} h\nu_0 \ .$$

This energy difference is 5.873×10^{-6} electron volts which is equivalent to a temperature ($h\nu/k$) of 6.816×10^{-2} °K. With respect to the cesium frequency standard, the frequency of this transition has been found to be 1, 420, 405, 751· 768 ± 0.002 Hz (Hellwig et al 1970). The spontaneous transition rate for this magnetic dipole radiation is 2.85×10^{-15} per second. This very low transition rate means that the intrinsic line width due to the uncertainty

principle is negligibly small. However, because of doppler shifts, the line will be observed to have a finite width. Bearing this in mind we substitute numbers to obtain

$$d\tau = 5.45 \times 10^{-19} \frac{dN_v(z)}{T_s(z)} \qquad \text{(B-3)}$$

where $dN_v(z)$ is the column density of hydrogen atoms between z and z + dz having velocity between V and V + dV in units of atoms per cm^2 per km/sec.

Let us consider a simple case in which $T_s(z)$ is constant through some cloud of hydrogen. The observed brightness temperature will be given by

$$T_{obs}(\nu) = Te^{-\tau_\nu} + T_s(1 - e^{-\tau_\nu}).$$

where

$$\tau_\nu = \int d\tau_\nu = 5.45 \times 10^{-19} \frac{N_v}{T_s} \quad .$$

In the high optical depth case,

$$T_{obs}(\nu) \approx T_s$$

while in the very low optical depth case

$$T_{obs}(\nu) \approx T + (T_s - T)\tau_\nu.$$

In the latter case, in the absence of a background source,

$$T_{obs}(\nu) \approx T_s\tau_\nu = 5.45 \times 10^{-19} N_v$$

independent of temperature.

As described in the Introduction, it is thought that the interstellar medium consists of both hot (low optical depth) and cold (high optical depth) regions. In absorption, we can only observe moderately high optical depths and hence will observe only the distribution of optical depths of the cold clouds. However, as the equations above reveal, we will observe in emission the combined distribution of the column density of the hot medium and the temperature of the cold medium. With the enormous quantities of hydrogen in the Galaxy, it is very hard to use the two types of observations to determine separately the density and temperature distributions of the hot and cold regions.

APPENDIX C

A DISCUSSION OF DETECTOR LAW

In this experiment a very wide range of power levels obtained. Contributing to these levels were the receiver noise (90 to 150 °K), the antenna temperature due to sources (frequency and source dependent, 0 to 200 °K), and the antenna temperature due to the general galactic hydrogen emission (frequency dependent, perhaps 0 to 100 °K). In order to properly evaluate the results of this experiment, we must consider the response of a correlation interferometer without a priori assumptions about the detector law.

The important elements of the correlation interferometer are illustrated in Figure C1. The random signals s from the source or sources are received at the two telescopes where each receiver adds a random noise r. One detector is used to detect the sum of the two signals while a second detector is used to detect the difference. The output of the system is the difference of the outputs of the two detectors smoothed by some time constant. If we assume that the output of a detector may be written as

$$G_i(|v|^2)\ |v|^2$$

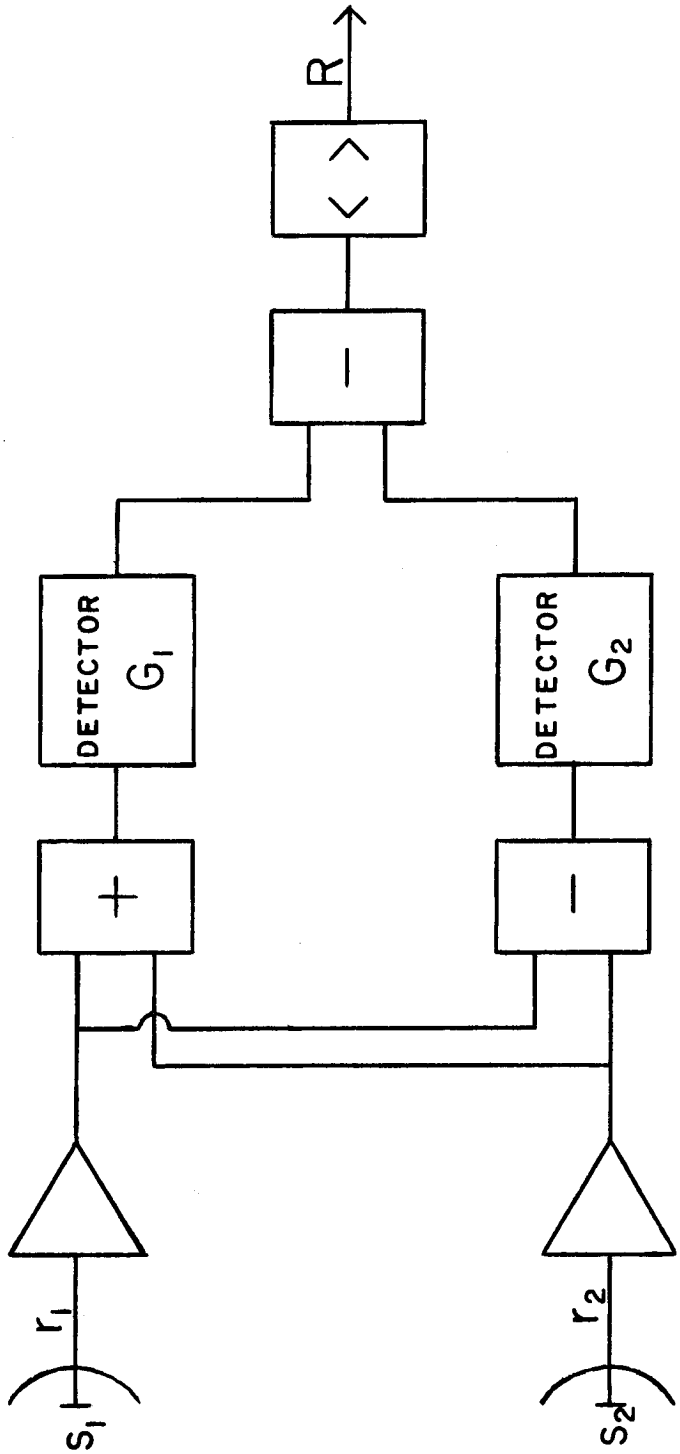

Figure C1. Correlator logic.

where v is the input voltage, then the output of the system is

$$R = \langle G_1(|v_1 + v_2|^2)|v_1 + v_2|^2 - G_2(|v_1 - v_2|^2)|v_1 - v_2|^2 \rangle \tag{C-1}$$

Thus, if the detectors are square-law (G = 1), then the system is a true multiplier.

It is common to attempt to evaluate (C-1) using a Taylor series expansion of the form

$$\langle G(P)P \rangle \approx G_0 P_0 + \dot{G}_0 \langle \Delta P^2 \rangle + \frac{\ddot{G}_0}{2} \langle \Delta P^2 \rangle + \ldots$$

about the average power P_0. The validity of such an expansion depends on ΔP being small at all times. To show in detail that this is not the case, let us evaluate the variance of P using

$$\langle \Delta P^2 \rangle = \langle P^2 \rangle - P_0^2 .$$

We assume that all four signals are random noise voltages oberying gaussian statistics and that none of the signals are correlated except for a partial correlation of s_1 and s_2. We may write

$$|v_1 \pm v_2|^2 \equiv P_{\pm} = |s_1 + r_1 \pm s_2 \pm r_2|^2$$

to obtain

$$P_{0\pm} = \langle|s_1|^2\rangle + \langle|s_2|^2\rangle + \langle|r_1|^2\rangle + \langle|r_2|^2\rangle \pm \langle[s_1 s_2]\rangle$$

and

$$\langle\Delta P^2\rangle = \left(\langle|s_1|^4\rangle - \langle|s_1|^2\rangle^2\right) + \left(\langle|s_2|^4\rangle - \langle|s_2|^2\rangle^2\right)$$

$$+ \left(\langle|r_1|^4\rangle - \langle|r_1|^2\rangle^2\right) + \left(\langle|r_2|^4\rangle - \langle|r_2|^2\rangle^2\right)$$

$$+ 4\langle|r_1|^2\rangle\langle|r_2|^2\rangle + 4\langle|r_1|^2\rangle\langle|s_1|^2\rangle + 4\langle|r_1|^2\rangle\langle|s_2|^2\rangle$$

$$+ 4\langle|r_2|^2\rangle\langle|s_1|^2\rangle + 4\langle|r_2|^2\rangle\langle|s_2|^2\rangle$$

$$+ \left(\langle[s_1 s_2]^2\rangle - \langle[s_1 s_2]\rangle^2\right) + 2\left(\langle|s_1|^2|s_2|^2\rangle - \langle|s_1|^2\rangle\langle|s_2|^2\rangle\right)$$

$$\pm 2\Big(\langle(|s_1|^2 + |s_2|^2)[s_1 s_2]\rangle$$

$$- \left(\langle|s_1|^2\rangle + \langle|s_2|^2\rangle\right)\langle[s_1 s_2]\rangle\Big)$$

where the notation $[\quad]$ means

$$[f_1 f_2] = f_1^* f_2 + f_1 f_2^* \ .$$

Since the noise voltages have the probability distribution[1]

$$p(v) = \frac{1}{\sqrt{2\pi T}} e^{-v^2/2T}$$

we note that

$$\langle |v_i|^2 \rangle = T_i$$

and

$$\langle |v_i|^4 \rangle = 3T_i^2 .$$

For simplicity, assume that we are observing a point source so that

$$s_1 = s_2 e^{i\theta}$$

where θ is the phase delay between the signals reaching the two antennas. Then, we may evaluate the averages to find that

$$P_{0\pm} = T_T \pm T_v \cos\theta$$

and

$$\langle (\Delta P)^2_{\pm} \rangle = 2T_T^2 + 2T_v^2 \cos^2\theta \pm 4(T_{s_1} + T_{s_2}) T_v \cos\theta$$

where

---

1 For simplicity we ignore the effects of the bandpass shape on the voltage distribution and treat the voltages as real numbers accounting for phase only when necessary.

$$T_T \equiv T_{r_1} + T_{r_2} + T_{s_1} + T_{s_2}$$

is the total system temperature and

$$T_v = 2\sqrt{T_{s_1} T_{s_2}}$$

is the correlated system temperature. These equations show that the variance of P is nearly $\sqrt{2}$ larger than P_0 making any attempt at a Taylor series expansion meaningless.

In December 1969 a number of tests were conducted in order to measure the detector law. Since the experimental set-up (see Figure C2) was less complex than the normal observing situation, we will analyze the experiment first. Uncorrelated noise voltages n_1 and n_2 arrive from the two telescopes and are allowed to mingle through a variable attenuator β. A variable delay is inserted which allows the phase of the mingled or correlated signals to be varied to generate the equivalent of fringes. The "fringe amplitude" is measured from a chart recorder at the output of the correlator.

We first compute the correlation coefficient ρ defined by

$$\rho = \frac{\langle v_1 v_2 \rangle}{\left[\langle v_1 v_1^* \rangle \langle v_2 v_2^* \rangle\right]^{\frac{1}{2}}}$$

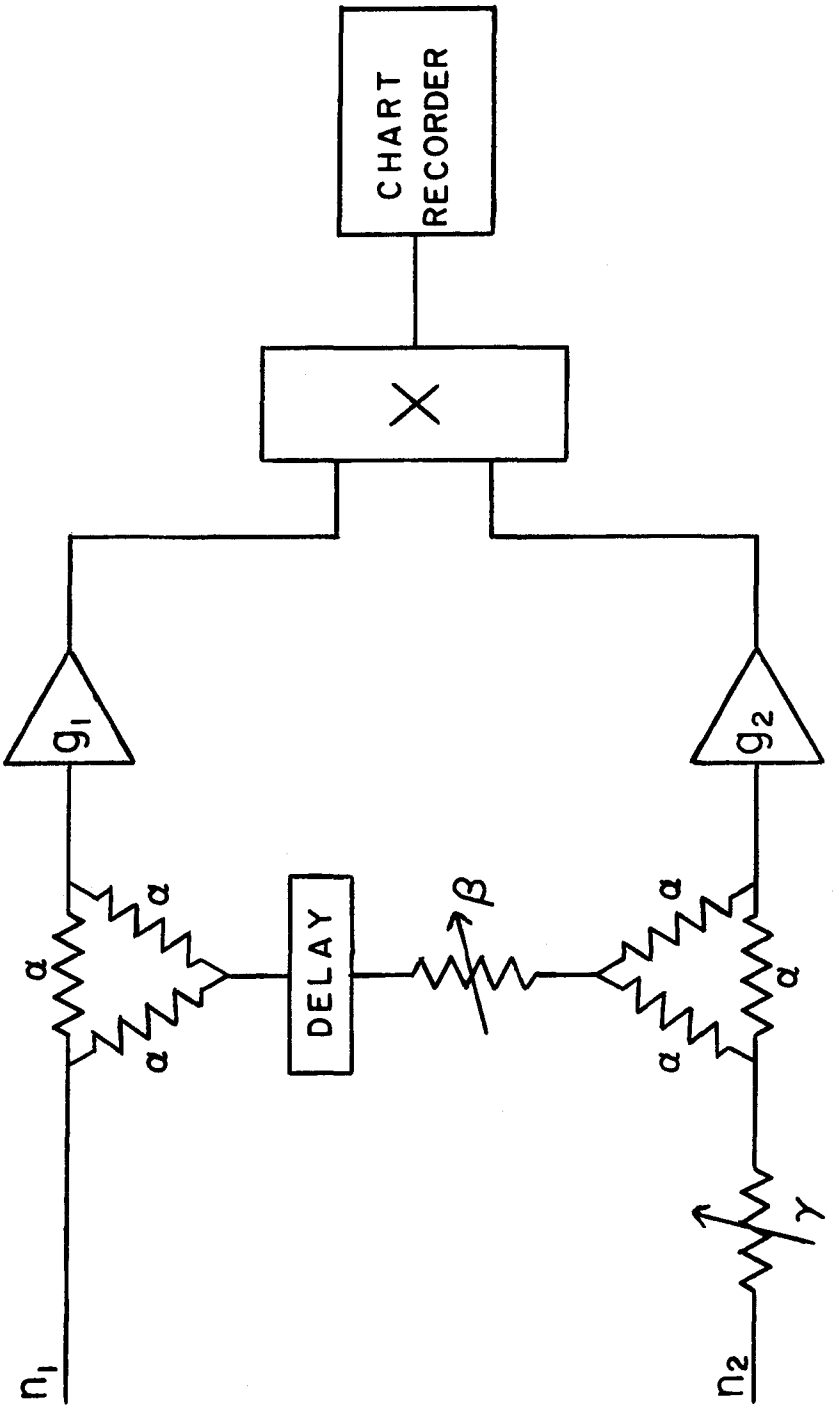

Figure C2. Block diagram of experiment to measure detector law.

Using

$$v_1 = g_1(\alpha n_1 + \alpha^2\beta\gamma n_2)$$

$$v_2 = g_2(\alpha\gamma n_2 + \alpha^2\beta n_1)$$

we obtain

$$\rho = \frac{\alpha\beta\left[T_1 + \gamma^2 T_2\right]}{\left[(\alpha\beta)^2(T_1^2 + \gamma^4 T_2^2) + \gamma^2 T_1 T_2(1 + \alpha^4\beta^4)\right]^{\frac{1}{2}}} \qquad \text{(C-2)}$$

where

$$T_1 \equiv \langle |n_1|^2 \rangle$$

$$T_2 \equiv \langle |n_2|^2 \rangle \quad .$$

The powers at the detectors are given by

$$P_{\pm} = \alpha^2 \left| (g_1 \pm \alpha\beta g_2)n_1 + (\alpha\beta g_1 \pm g_2)\gamma n_2 \right|^2 \quad . \qquad \text{(C-3)}$$

We will make a number of assumptions to simplify the analysis. For most of the experiment, T_1 equalled T_2, γ was 1, and the gains were set on AGC at the same level. This least assumption means that $\langle |v_1|^2 \rangle$ and $\langle |v_2|^2 \rangle$ were constants or

$$g_1 = k_1\left[T_1 + \alpha^2\beta^2\gamma^2 T_2\right]^{-\frac{1}{2}}/\alpha$$

and

$$g_2 = k_2\left[\alpha^2\beta^2 T_1 + \gamma^2 T_2\right]^{-\frac{1}{2}}/\alpha \quad .$$

Substituting these assumptions in (C-2) and (C-3) we find

$$\rho = \frac{2\alpha\beta}{1 + \alpha^2\beta^2}$$

and

$$P_{\pm} = k^2 \frac{(1 \pm \alpha\beta)^2}{(1 + \alpha^2\beta^2)} \frac{|n_1 \pm n_2|^2}{T} \quad .$$

Note, since $\alpha = 0.5$ and β is less than 1,

$$0 \leq \rho \leq 0.8$$

with our assumptions.

Since we may not use a Taylor expansion, we must assume a detector law in order to apply equation (C-1). It is reasonable to presume that the detector will be somewhere between a square-law detector (G = 1) and a "voltage"-law detector $G(P) = P^{-\frac{1}{2}}$. Thus we shall assume

$$G_1(P) = G_2(P) = \frac{1}{1 + \kappa\sqrt{P}} \qquad \text{(C-4)}$$

which yields an output

$$R = \frac{k^2}{\left[(1 + \alpha^2\beta^2)T\right]^{\frac{1}{2}}}$$

$$\left\langle \frac{(1+\alpha\beta)^2|n_1+n_2|^2}{\sqrt{(1+\alpha^2\beta^2)T} + \kappa k(1+\alpha\beta)|n_1+n_2|} - \frac{(1-\alpha\beta)^2|n_1-n_2|^2}{\sqrt{(1+\alpha^2\beta^2)T} + \kappa k(1-\alpha\beta)|n_1-n_2|} \right\rangle .$$

To evaluate the time average, we must evaluate integrals like

$$\frac{1}{2\pi T} \int_{-\infty}^{\infty}\int dn_1 dn_2 \, \frac{|n_1 \pm n_2|^2}{1 + a_{\pm}|n_1 \pm n_2|} e^{-(n_1^2 + n_2^2)/2T} .$$

A coordinate transformation is suggested producing

$$\frac{1}{2\pi T} \int_0^{2\pi} d\theta \int_0^{\infty} dr \, \frac{r^3(1 \pm \cos 2\theta)}{1 + a_{\pm}|\cos\theta \pm \sin\theta|r} e^{-r^2/2T} .$$

Unfortunately it appears that this integral may only be done numerically.

Thus we must consider two more specialized cases. Let

$$k_1 = k_2 = \sqrt{T}\, k \quad .$$

Then, for a purely square-law detector,

$$R = \frac{k^2}{(1+\alpha^2\beta^2)} \langle (1 + \alpha\beta)^2 |n_1 + n_2|^2 - (1 - \alpha\beta)^2 |n_1 - n_2|^2 \rangle$$

$$R = \frac{4\alpha\beta k^2}{(1 + \alpha^2\beta^2)} \langle |n_1|^2 + |n_2|^2 \rangle$$

or, finally,

$$R = (4k^2T)\rho \quad .$$

For a voltage law detector having a gain given by

$$G = \frac{1}{\kappa\sqrt{P}}$$

we have an output given by

$$R = \frac{k}{\kappa\sqrt{1 + \alpha^2\beta^2}} \langle (1 + \alpha\beta)|n_1 + n_2| - (1 - \alpha\beta)|n_1 - n_2| \rangle \ .$$

The probability integrals are now easily evaluated using the coordinate transformation suggested above to obtain

$$R = \frac{4k\sqrt{T}}{\sqrt{\pi}\ \kappa} \frac{\alpha\beta}{(1 + \alpha^2\beta^2)^{\frac{1}{2}}}$$

or

$$R = \frac{2k\sqrt{T}}{\sqrt{\pi}\ \kappa} \sqrt{1 + \alpha^2\beta^2}\ \rho \quad .$$

In terms of the response of a square-law detector

$$R(\text{voltage}) = R(\text{square}) \frac{\sqrt{1 + \alpha^2\beta^2}}{2k\kappa\sqrt{\pi T}} . \qquad \text{(C-5)}$$

Since all terms in this proportionality factor are constant in this experiment except for β, the deviation from the ideal response will never exceed about 12 percent. Note that this deviation is actually an increase in the fringe amplitude over that expected for high degrees of correlation. It is interesting to note that in this experiment the deviation from an ideal response curve for voltage law detectors is due solely to the use of the AGC. Equation (C-5) may be rewritten as

$$R(\text{voltage}) = R(\text{square}) \frac{1}{2ag\kappa\sqrt{\pi T}} .$$

Since T is assumed constant and, if AGC is not used, g is a constant, the ratio of the two responses is constant.

The results of the measurements are plotted in Figure C3. As expected, the output is very close to a linear function of the correlation coefficient with the only obvious departures occuring for $\rho > 0.8$ (where $\gamma < 1$ and there are serious calibration difficulties). These results are expressed as relative gains in Figure C4. It

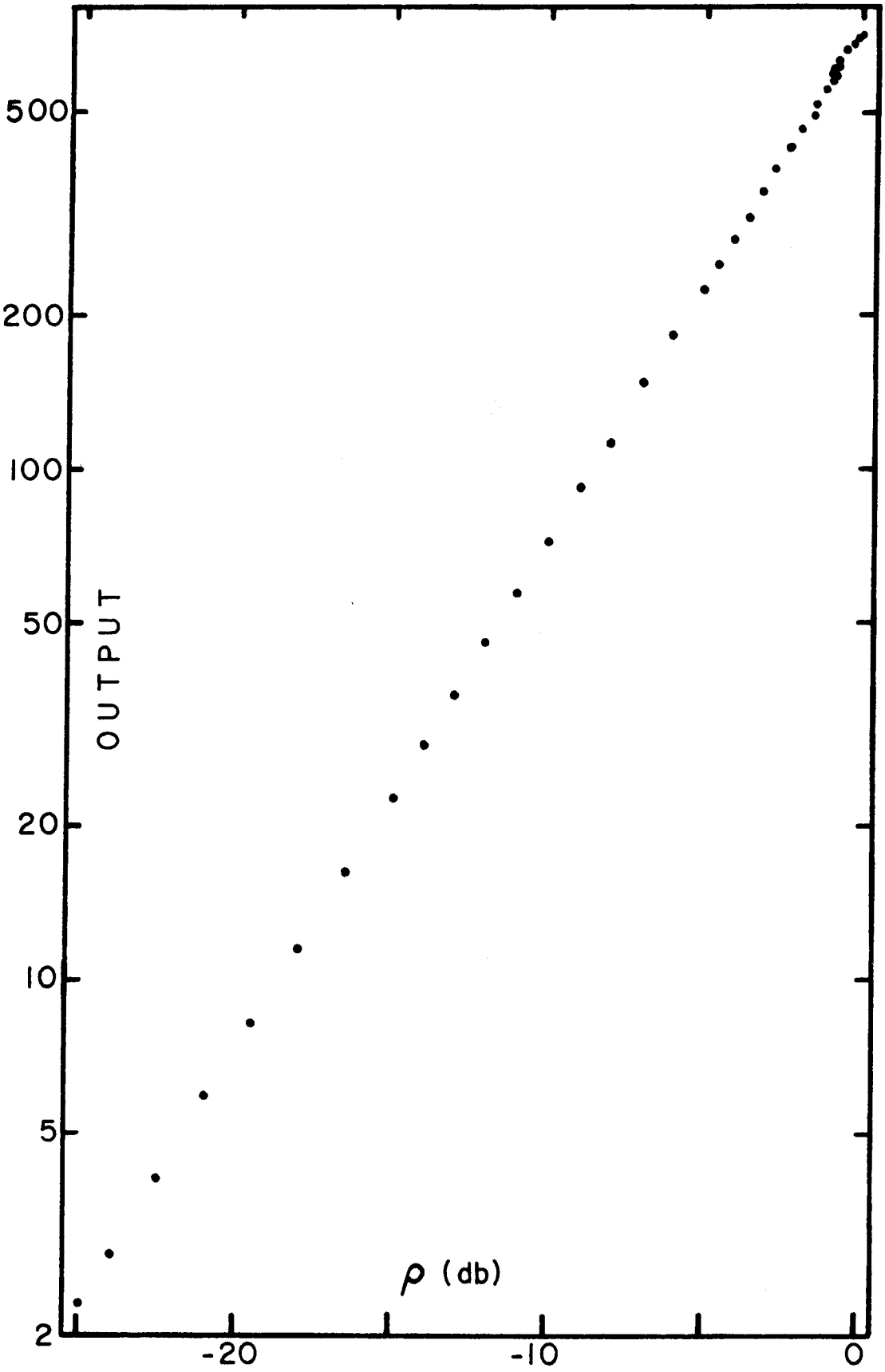
500
200
100
50
20
10
5
2
OUTPUT
ρ (db)
-20
-10
0

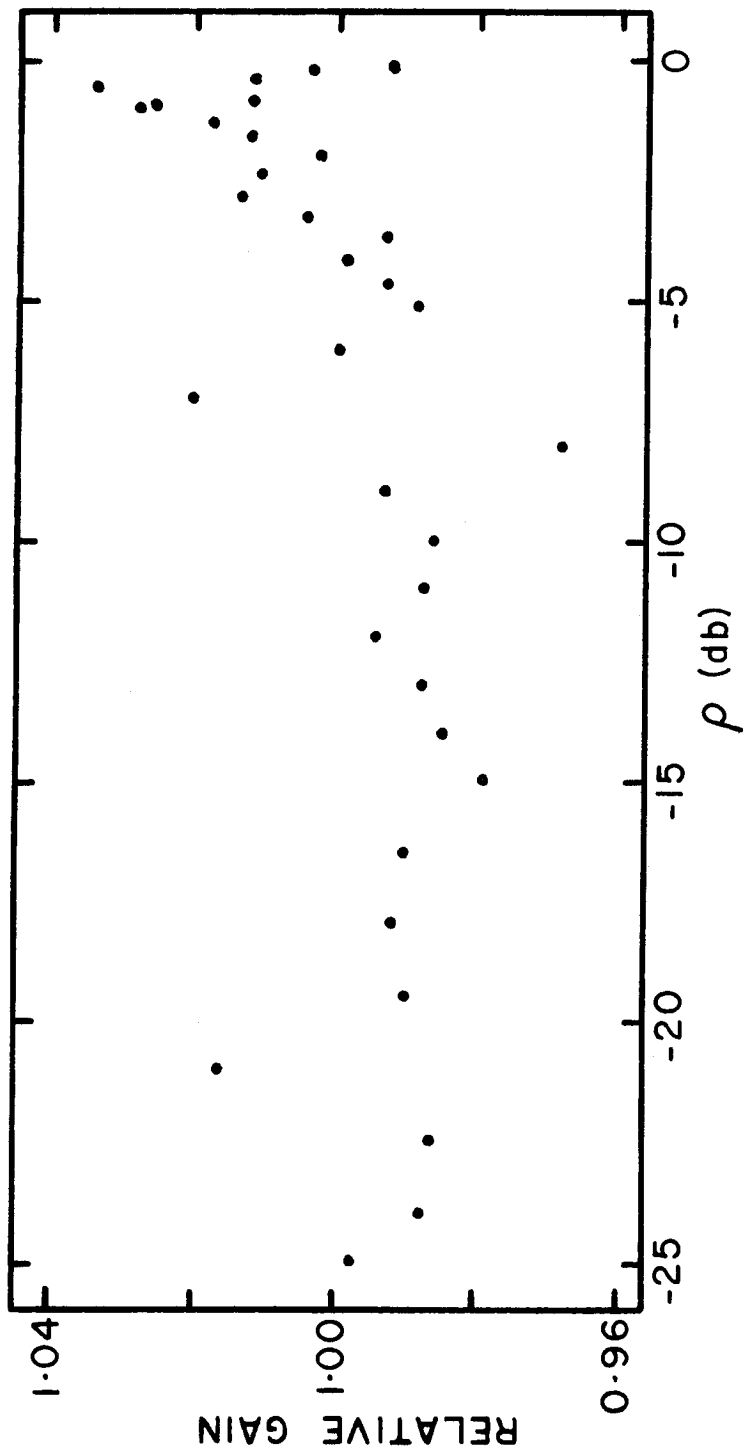

Figure C4. Output of correlator divided by the correlation coefficient (expressed as relative gain) as a function of the correlation coefficient.

Figure C3. (previous page) Output of correlator at AGC level 10 as a function of the correlation coefficient.

may be seen that the gain is approximately constant for $\rho < 0.3$. The gain increases as ρ goes from 0.3 to 0.87 or so and then appears to drop rapidly. This increase is about 3.6 ± 0.9 percent. The output of the system was also measured as a function of the AGC level. Although the results were those expected with square-law detectors, an uncertainty around $\pm$ 3 percent was unavoidable due to inaccuracies in setting the AGC levels. The response in the narrowband channels was observed throughout the program by measuring the gains of the narrowband channels relative to the broadband for a variety of sources. A systematic difference in the two detector laws was occasionally seen, but it was never greater than about one percent.

The results illustrated in Figure C4 indicate that the detector law is certainly not a pure voltage law and is probably not a pure square law. Unfortunately, the general detector law given by equation (C-4) results in a probability integral which is qualitatively different from that of either of the "pure" detector laws. Under the general detector law, the most probable instantaneous power ($P \sim 0$) enters following a square law while large powers enter with a voltage law.

We should now reconsider the actual observing situation. The powers reaching the two detectors are

$$P_{\pm} = |r_1 + s_1 \pm r_2 \pm s_2|^2$$

or

$$P_{\pm} = |r_1 \pm r_2|^2 + 2s_1(s_1 + r_1 \pm r_2)(1 \pm \cos\theta) \ .$$

For a pure square law detector, the response is given by

$$R = \langle P_+ - P_- \rangle$$

or

$$R = 4T_s \cos\theta \ .$$

For a pure voltage-law detector, the response depends on integrals of the form

$$\frac{1}{\left[(2\pi)^3 T_{r_1} T_{r_2} T_s\right]^{\frac{1}{2}}} \int_{-\infty}^{\infty}\iint dr_1 dr_2 ds \ e^{-r_1^2/2T_{r_1}} e^{-r_2^2/T_{r_2}} e^{-s^2/2T_s}$$

$$\left[|r_1 \pm r_2|^2 + 2s(s + r_1 \pm r_2)(1 \pm \cos\theta)\right]^{\frac{1}{2}} \ .$$

Unfortunately there does not seem to be any way to carry out this integral analytically.

Thus, the analysis of the detector law turns out to be very frustrating. The measurements show a departure from the square-law response having the general nature,

but not the magnitude, expected for a pure voltage-law detector. At high input levels, the instantaneous output of a voltage-law detector is less than that of a square-law detector. Nevertheless, voltage law detectors in the experimental set-up will give outputs which are the ideal response curves when AGC is not used and which exceed the ideal response curves at high degrees of correlation when AGC is used. In the experimental set-up, each part of the signal from one telescope is completely correlated with at least part of the signal from the other telescope. Since the signals do not have this property in the actual observing situation, the measured fringes are affected by voltage-law detectors in a somewhat different manner which is not directly calculable. Due to the failure to find analytic solutions to a number of integrals, we are simply unable to predict what effects a realistic detector law would have on the response either in the experimental or the normal observing situations. Although it seems likely that these effects are only a few percent for this experiment, the uncertainty in the detector law should be considered in any evaluation of the results of this experiment.

APPENDIX D

ALTERNATE FOURIER INVERSION METHODS

The Fourier inversion method used in this program involves a brute-force inversion of the data followed by a deconvolution procedure. Since the computation time necessary to invert irregularly spaced data is at least $\sqrt{N}$ times longer than for data obtained on a rectangular grid, most observers smooth their data to a rectangular grid. This smoothing may be written as a convolution with some convolving function C followed by a multiplication by the sha function:

$$V'(u, v) = III\ C * (VS).$$

Since most observers do not apply weights to their data prior to the smoothing, they multiply by a function inversely proportional to the number of data points contributing to a grid point to obtain

$$V'(u, v) = III\ R[C * (VS)]$$

where

$$R(u, v) = 1/(C * S) \quad \text{where} \quad C * S \neq 0$$

$$R(u, v) = 0 \quad \text{where} \quad C * S = 0 .$$

The function R may also contain a tapering of the data. The Fourier transform of V' produces the dirty map

$$T_D(x, y) = \overline{III} * \overline{R} * [\overline{C}(T * B_D)]$$

where B_D is the dirty beam of Chapter 3 ($\overline{S}$) and T is the true brightness distribution. The response to a point source at the origin is

$$T_D(\text{point}) = \overline{III} * \overline{R} * (\overline{C}\ B_D)$$

which points up a serious flaw in the method: the response to an extended source is not the true source brightness convolved with the response to a point source.

This response is sufficiently complicated that we should discuss each of the functions which enters into it. The Fourier transform of the sha function is another sha function. If the intervals of the III function are sufficiently small, then the intervals of $\overline{III}$ will be so large that we may ignore this convolution and study only the central part of the map. The function R is normally evaluated only at grid points and little can be said about its behavior in general other than that it will contain discontinuities. If the data were continuously and uniformly distributed over the (u, v) plane to a

maximum spacing d_0, then $\overline{R}$ will consist approximately of the sum of two functions having the forms

$$d_0^2 \frac{J_1(2\pi d_0 r)}{(2\pi d_0 r)}$$

and

$$d_0 J_0(2\pi d_0 r)$$

where the J's are Bessel functions of the first kind and $r = \sqrt{x^2 + y^2}$. If the data are not so well distributed, R will be full of bumps and even discontinuities which will introduce even more complex behavior into $\overline{R}$. The function R effectively assigns different weights to the same data point depending on the various grid points to which it was smoothed. If we assign a unique weight to each data point in the manner described in Chapter 3, then there is no need to introduce the function R. Then, if the $\overline{III}$ function may also be ignored, we have

$$T_D = \overline{C}(T * B)$$

and

$$T_D(\text{pt source}) = \overline{C}\ B\ .$$

Since $\overline{C}$ is a known and well-behaved function, we may remove the affects of $\overline{C}$ and then carry out the deconvolution.

The function C is usually chosen to be either a gaussian or a pill box so that $\bar{C}$ is a gaussian or a sinc function, respectively. The sinc function goes rapidly through zero but continues to have significant value for a considerable distance. With the gaussian, there are no problems with division by zero and the effects of the convolution with the sha function are reduced.

Let us assume that we wish to map an area 2d on a side completely containing some source. In order to perform the deconvolution we must compute the beam pattern over an area 4d on a side. To avoid any effect of the gridding on the maps we must take a grid interval of 1/4d. This apparent contradiction to the sampling theorem results from the assumption in the derivation of the sampling theorem that the measurements were made at the grid points. Such an assumption is equivalent to a uniform sampling for which the dirty beam would be a delta function. The fact that the beam pattern is not a delta function forces us to the more extreme gridding requirement. A reasonable choice for the width of $\bar{C}$ would be 2d making the width of C be about 1/2.26d. With this width, the convolving function centered on one grid point has a value nearly 0.5 at the adjacent grid points. Thus, a reasonable choice for

the convolving function indicates that the observations need not be made at baseline intervals as small as the gridding interval.

Most earlier attempts to perform the deconvolution have involved some sort of model-fitting procedure. I did attempt one of these schemes, described by Shostak (1972), but found that it did not sufficiently remove the effects of the beam pattern.

APPENDIX E

THE SOLUTION OF THE SPHERICAL SHELL PROBLEM

Let R_1 be the outer radius and R_2 the inner radius of a uniform spherical shell. If r is the ratio of the depth through the shell at some displacement y to the depth through the center, then

$$r = \frac{\sqrt{R_1^2 - y^2} - \sqrt{R_2^2 - y^2}}{(R_1 - R_2)} \qquad (|y| \leq R_2)$$

$$r = \frac{\sqrt{R_1^2 - y^2}}{(R_1 - R_2)} \qquad (R_2 \leq |y| \leq R_1)$$

$$r = 0 \qquad (|y| \geq R_1).$$

The maximum value of r occurs at $|y| = R_2$. Since the maximum optical depths occur to the east of Cygnus A (Figure 12e, Chapter 4C), we consider the solution of the case $|y| \leq R_2$ only. Defining

$$\kappa = (R_1 - R_2)/R_1$$

and

$$x = y/R_1$$

we solve

$$\kappa r = \sqrt{1 - x^2} - \sqrt{(1 - \kappa)^2 - x^2} \qquad \text{(E-1)}$$

obtaining

$$\kappa = \frac{2(r\sqrt{1 - x^2} - 1)}{r^2 - 1} \quad .$$

This solution is valid only when it satisfies equation (E-1). Testing the solution we find the requirement that

$$(r^2 + 1)\sqrt{1 - x^2} - 2r = - \left| (r^2 + 1)\sqrt{1 - x^2} - 2r \right|$$

or

$$2r \geq (1 + r^2)\sqrt{1 - x^2} \quad . \qquad \text{(E-2)}$$

Since κ is positive we also have the limit

$$r\sqrt{1 - x^2} > 1 \quad . \qquad \text{(E-3)}$$

These formulas allow us to set upper and lower limits on x and R_1 as

$$\frac{1}{r} < \sqrt{1 - x^2} \leq \frac{2r}{1 + r^2}$$

or

$$\frac{|y|r}{\sqrt{r^2 - 1}} < R_1 \leq \frac{|y|(r^2 + 1)}{(r^2 - 1)} \quad . \qquad \text{(E-4)}$$

For Cygnus A, we find in Chapter 4 that

$$\int \tau \, d\nu = 0.609 \, \frac{pc}{cm^3 \, ^\circ K} \text{ at } (-0.975, -0.675)$$

and

$$\int \tau \, d\nu = 0.193 \, \frac{pc}{cm^3 \, ^\circ K} \text{ at } (1.275, \; 0.225).$$

Substituting the parameters

$$r = 3.156$$

$$y = 8.5 \text{ pc}$$

$$T = 70 \, ^\circ K$$

we find

$$9.0 < R_1 \leq 10.4 \text{ parsecs}$$

and

$$0 < \kappa \leq 0.183 \; .$$

The density in the shell is given by

$$n_H = \frac{\left[T \int \tau \, d\nu \right]_0}{2 \kappa R_1}$$

which yields

$$\infty > n_H \geq 3.5 \text{ cm}^{-3}.$$

The mass of the shell is given by

$$M = \frac{2\pi}{3} \left[T \int \tau \, d\nu \right]_0 R_1^{\,2} (3 - 3\kappa + \kappa^2)$$

which yields

$$160 < M < 190 \text{ solar masses.}$$

At an "average" value of R_1 these values become

$$R_1 = 9.7 \text{ pc}$$

$$R_2 = 8.56 \text{ pc}$$

$$\kappa = 0.116$$

$$n = 6 \text{ cm}^{-3}$$

$$M = 175 \, M_\odot \quad .$$

APPENDIX F

CASSIOPEIA A - OPTICAL DEPTH MAPS

A summary of the optical depth maps of Cassiopeia A (3C461) is given in Chapter 5C, but the detailed description is deferred to this appendix. Representative samples of the optical depth maps are given in Figures 22 (for frequencies < 212 KHz) and Figures 23 (for frequencies > 212 KHz). The maps are presented in the same manner as those for Cygnus A (see Chapter 4C) with the exceptions that the computation of optical depths is cut off at the 20 percent level of the continuum brightness and that there are no corrections for possible "DC offsets". The reader is also referred to Chapter 5D for spectra at a number of interesting map points. To avoid long sets of direction words, I will use in the following discussion the (x, y) coordinates of the map features expressed in minutes of arc.

As may be seen in Figure 20 of Chapter 5B, there is a significant optical depth in the wings of the absorption. Unfortunately, because of the presence of significant DC offsets, it is impossible to determine which of the features seen on the optical depth maps in the wings are real. By

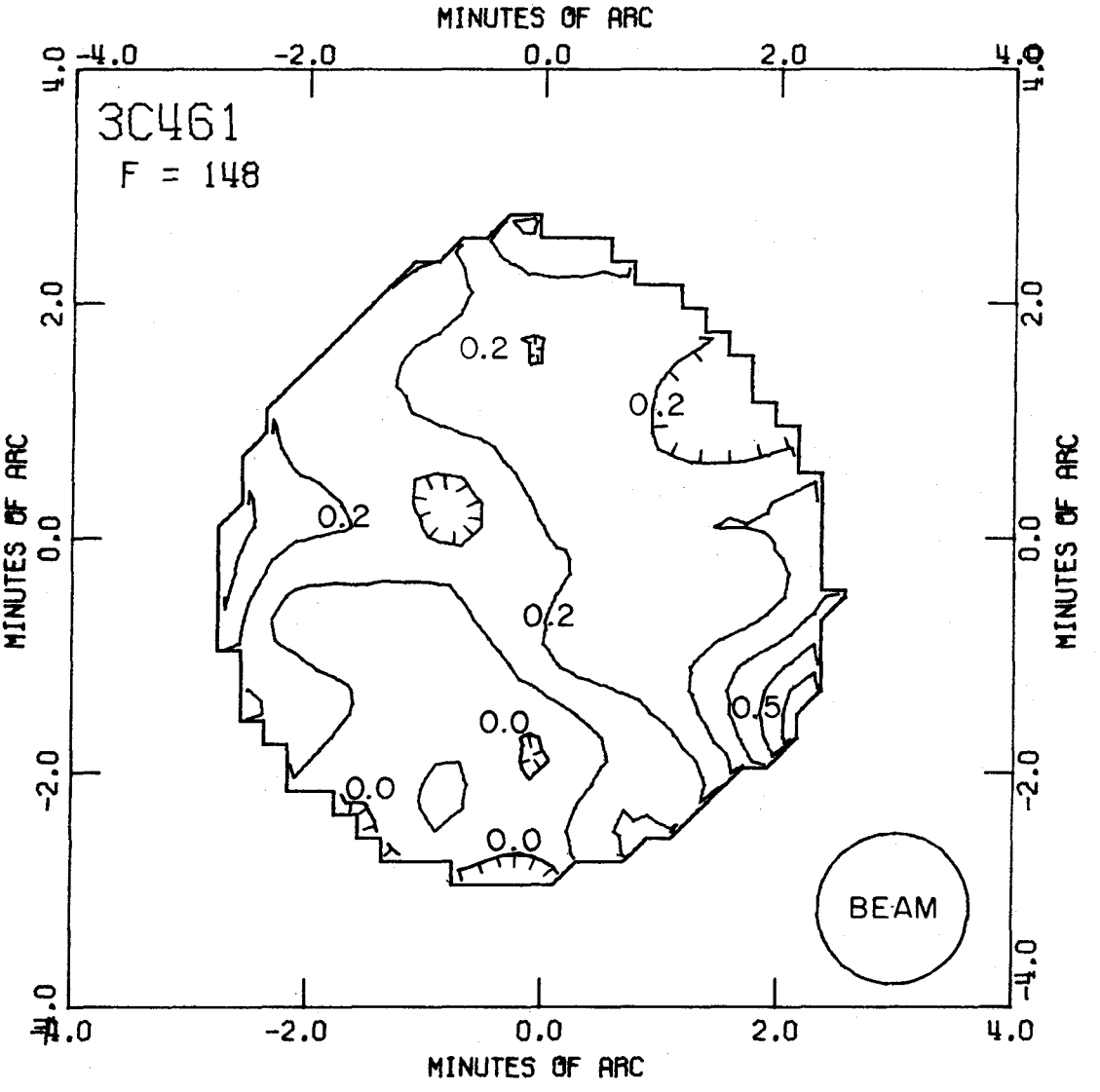

Figure 22a. 3C461: optical depth map at -31.3 km/sec, contour interval = 0.1. Illustrates beam size (full width at half maximum).

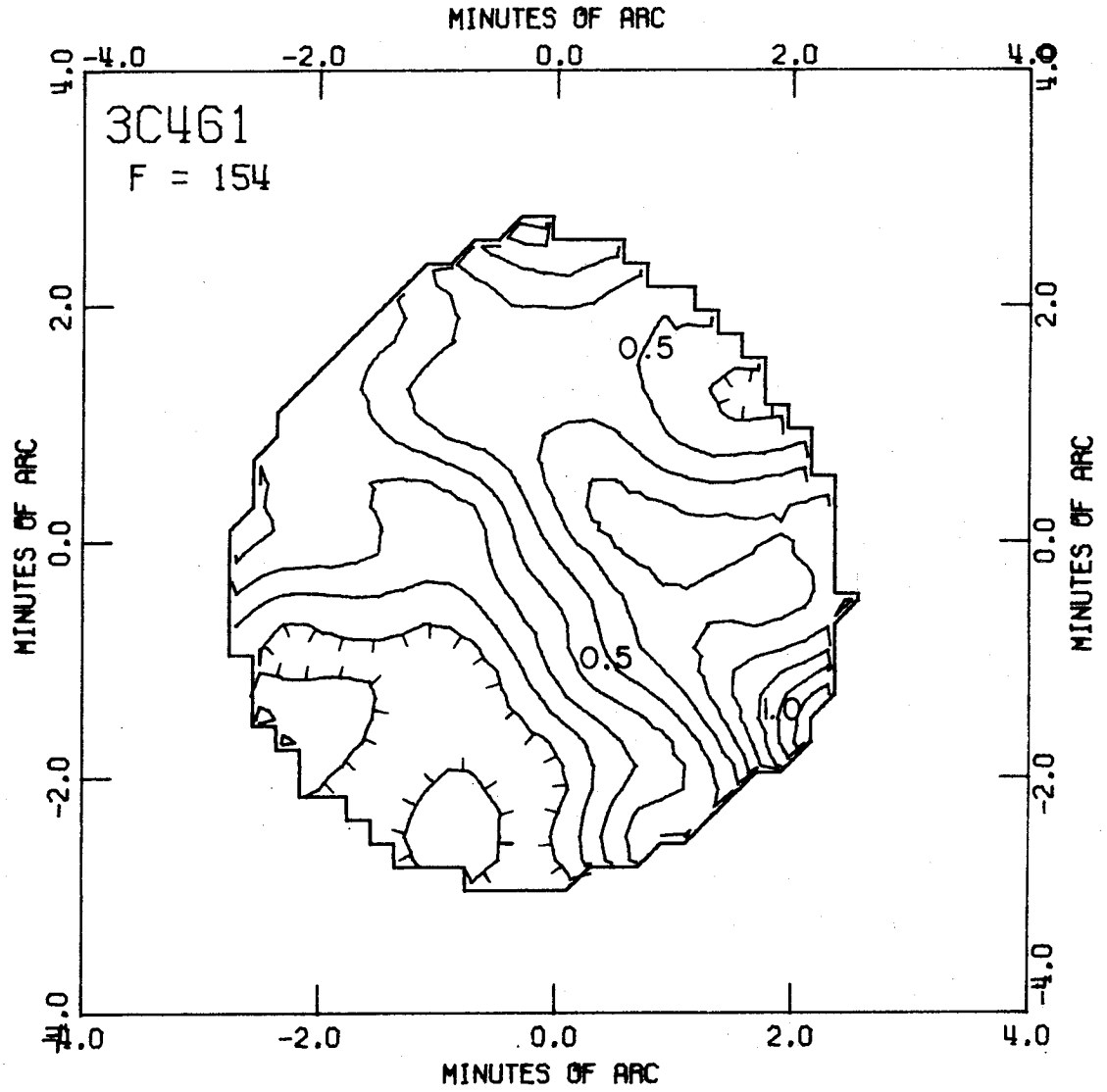

Figure 22b. 3C461: optical depth map at -32.6 km/sec, contour interval = 0.10.

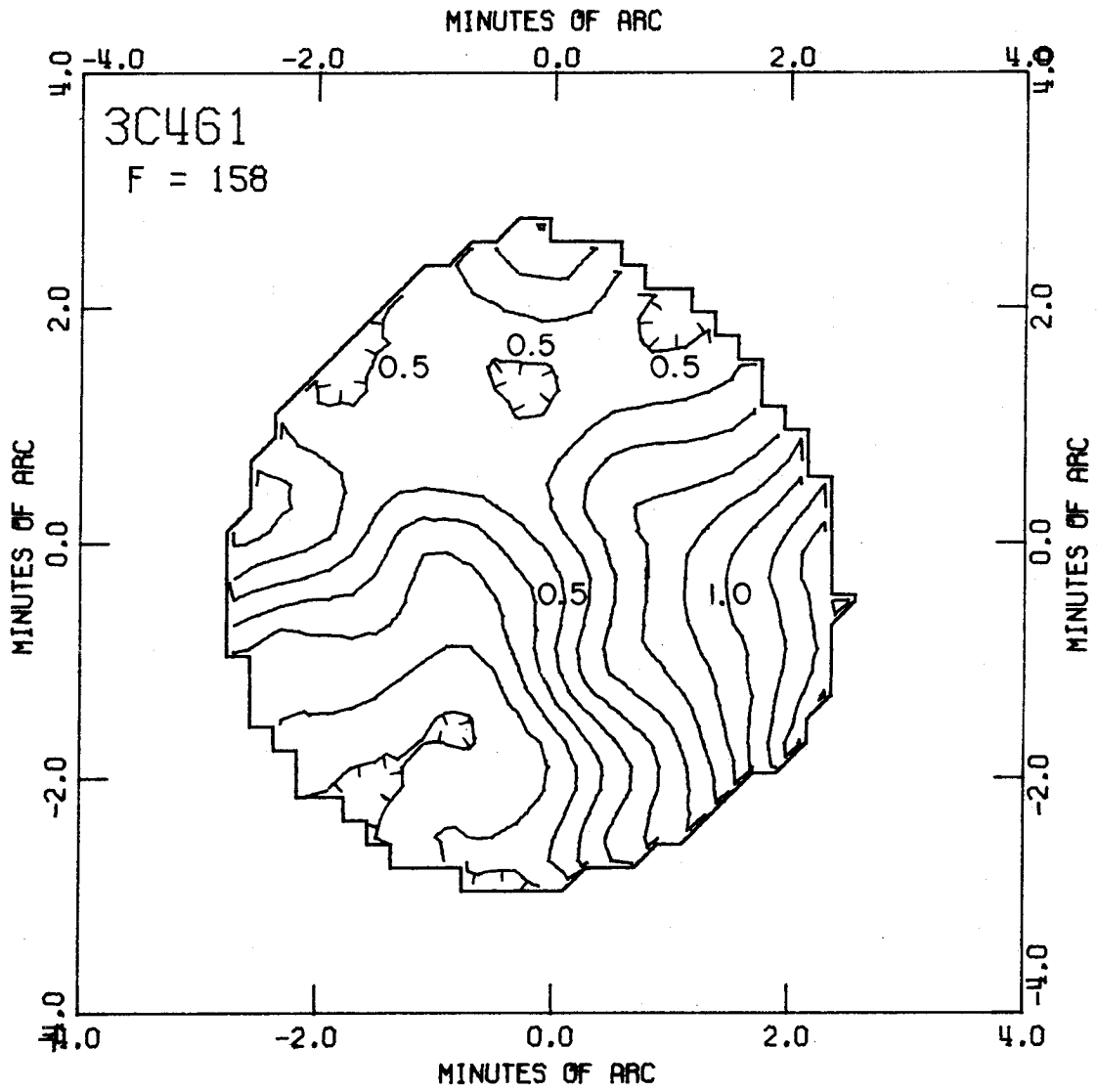

Figure 22c. 3C461: optical depth map at -33.4 km/sec, contour interval = 0.10.

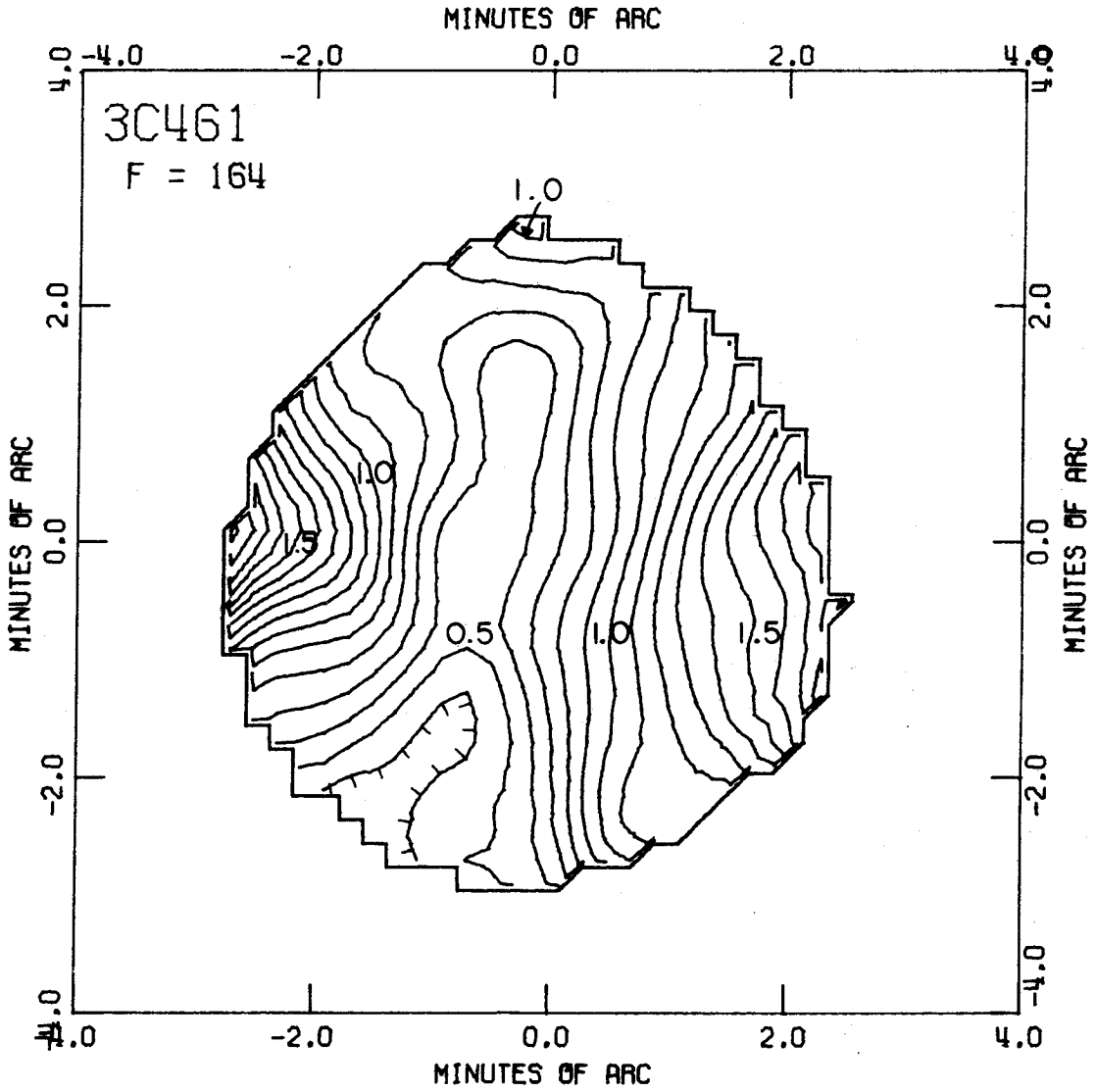

Figure 22d. 3C461: optical depth map at -34.7 km/sec, contour interval = 0.10.

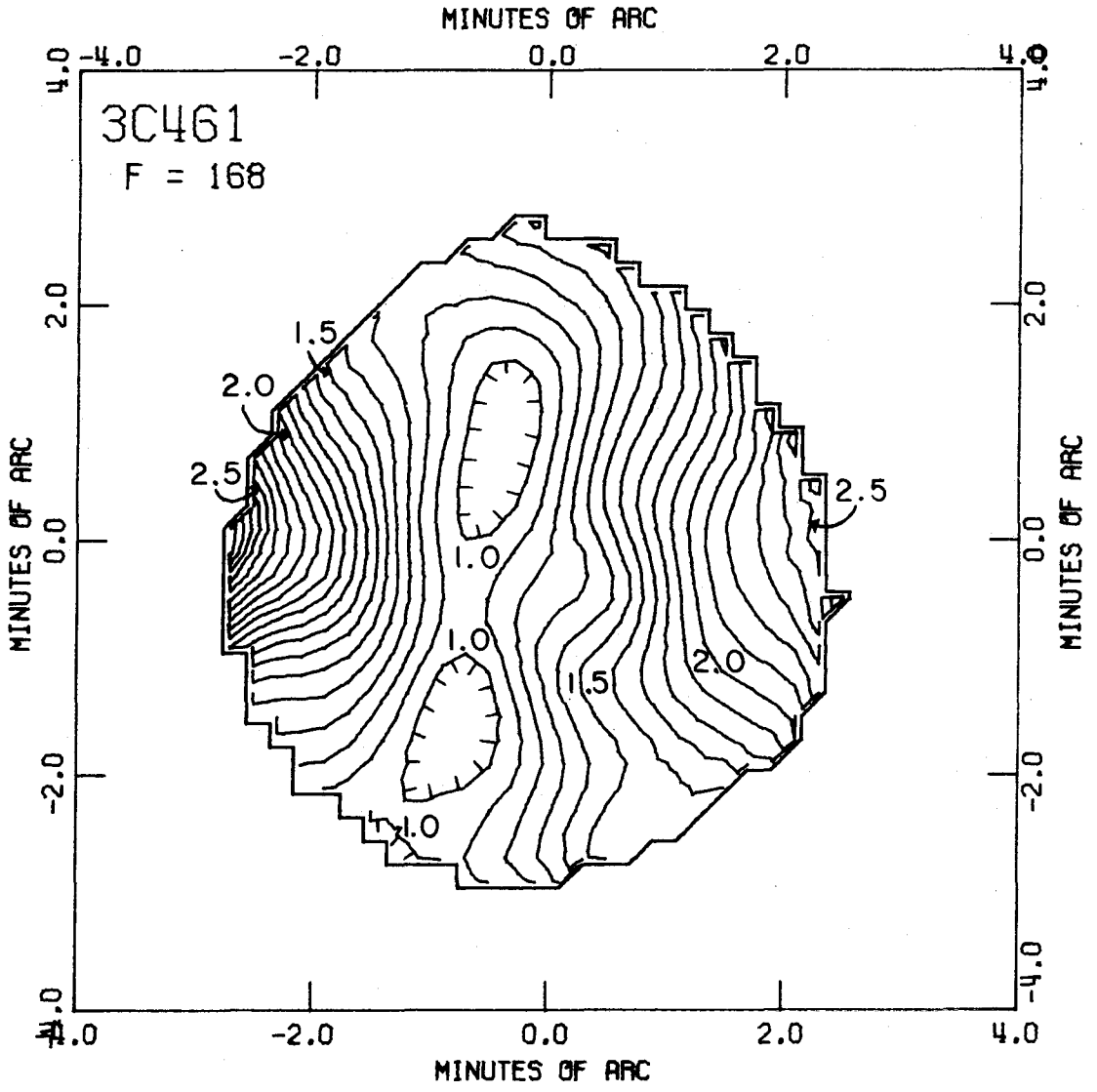

Figure 22e. 3C461: optical depth map at -35.6 km/sec, contour interval = 0.10.

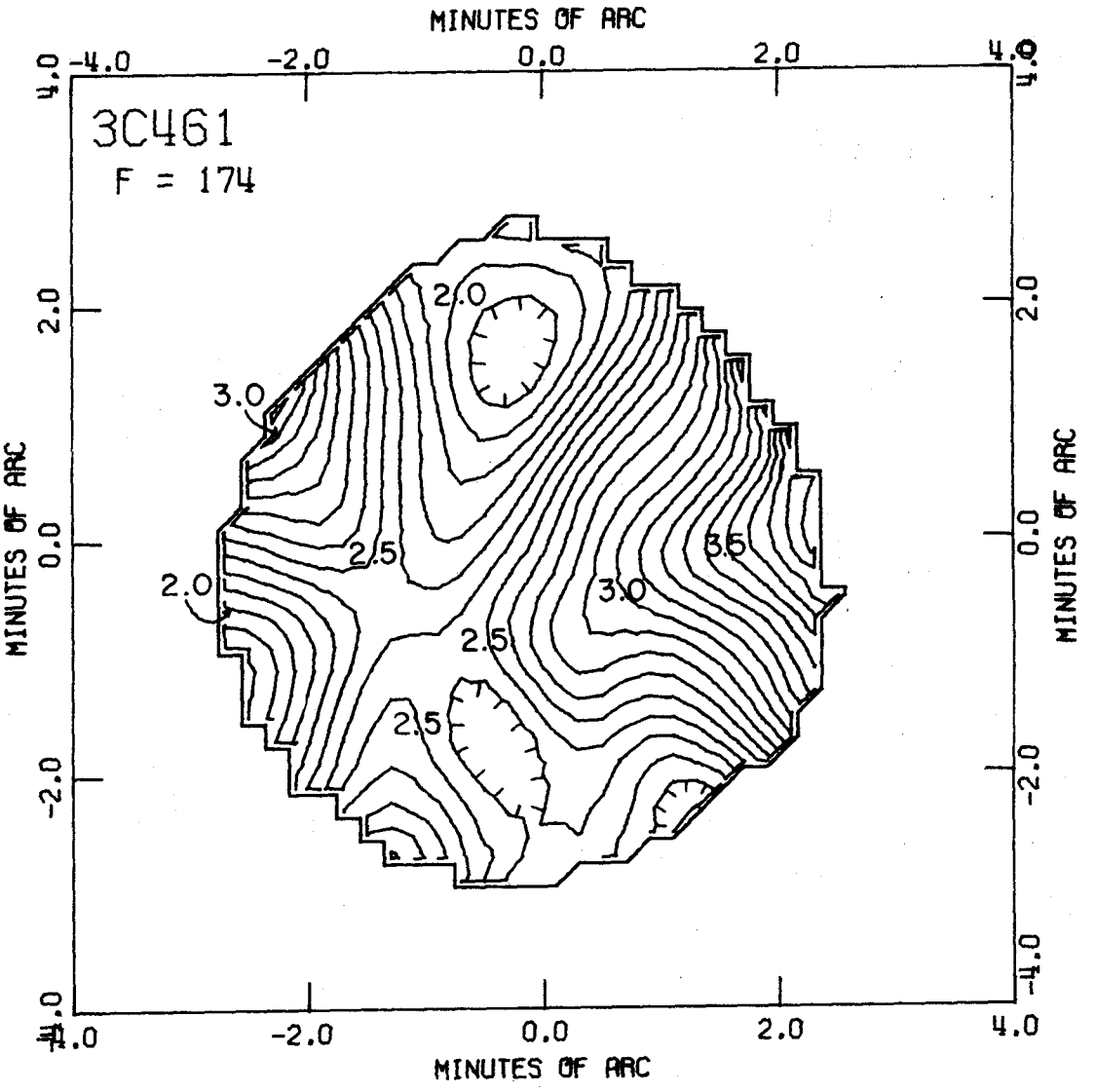

Figure 22f. 3C461: optical depth map at -36.8 km/sec, contour interval = 0.10.

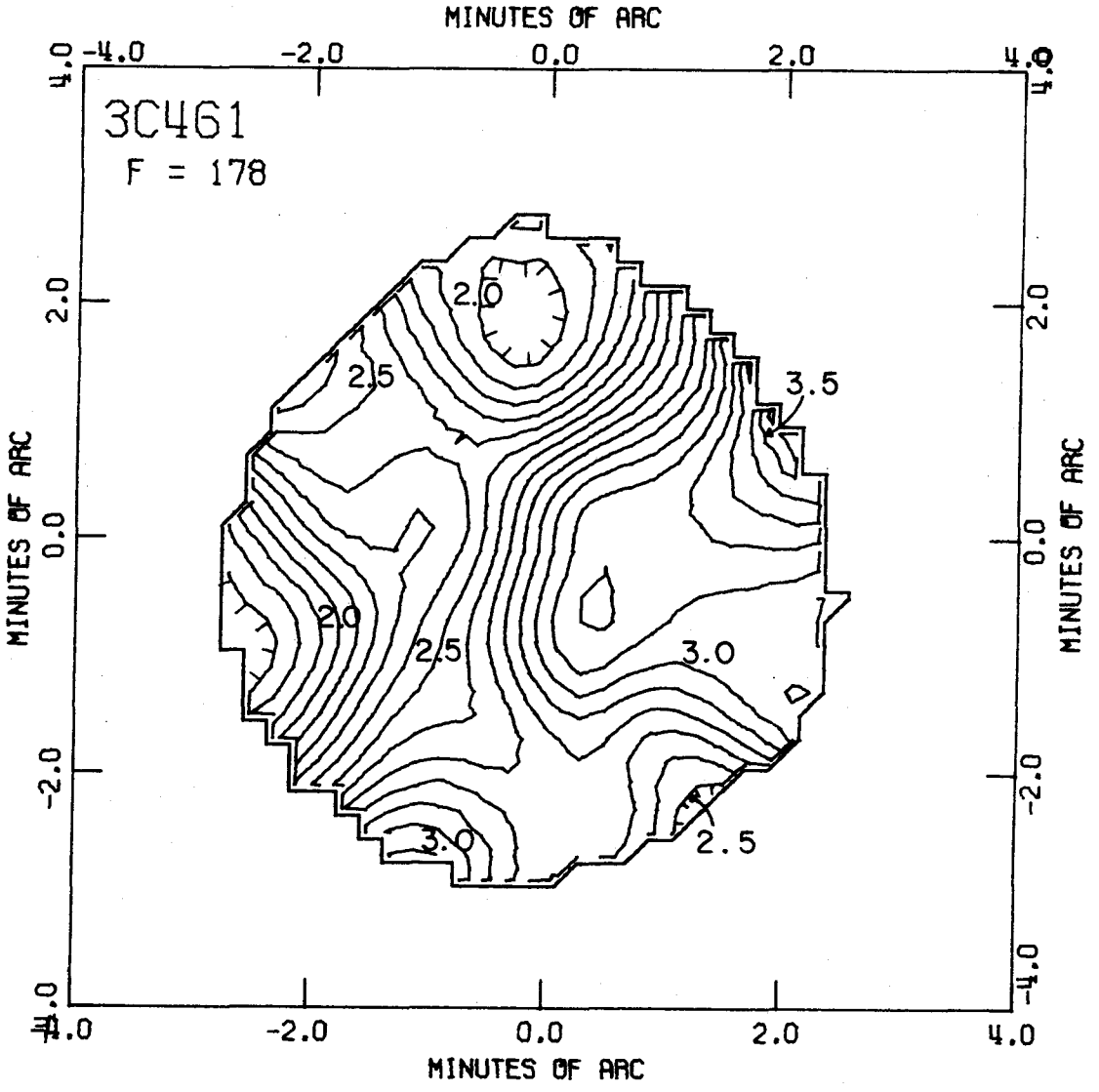

Figure 22g. 3C461: optical depth map at -37.7 km/sec, contour interval = 0.10.

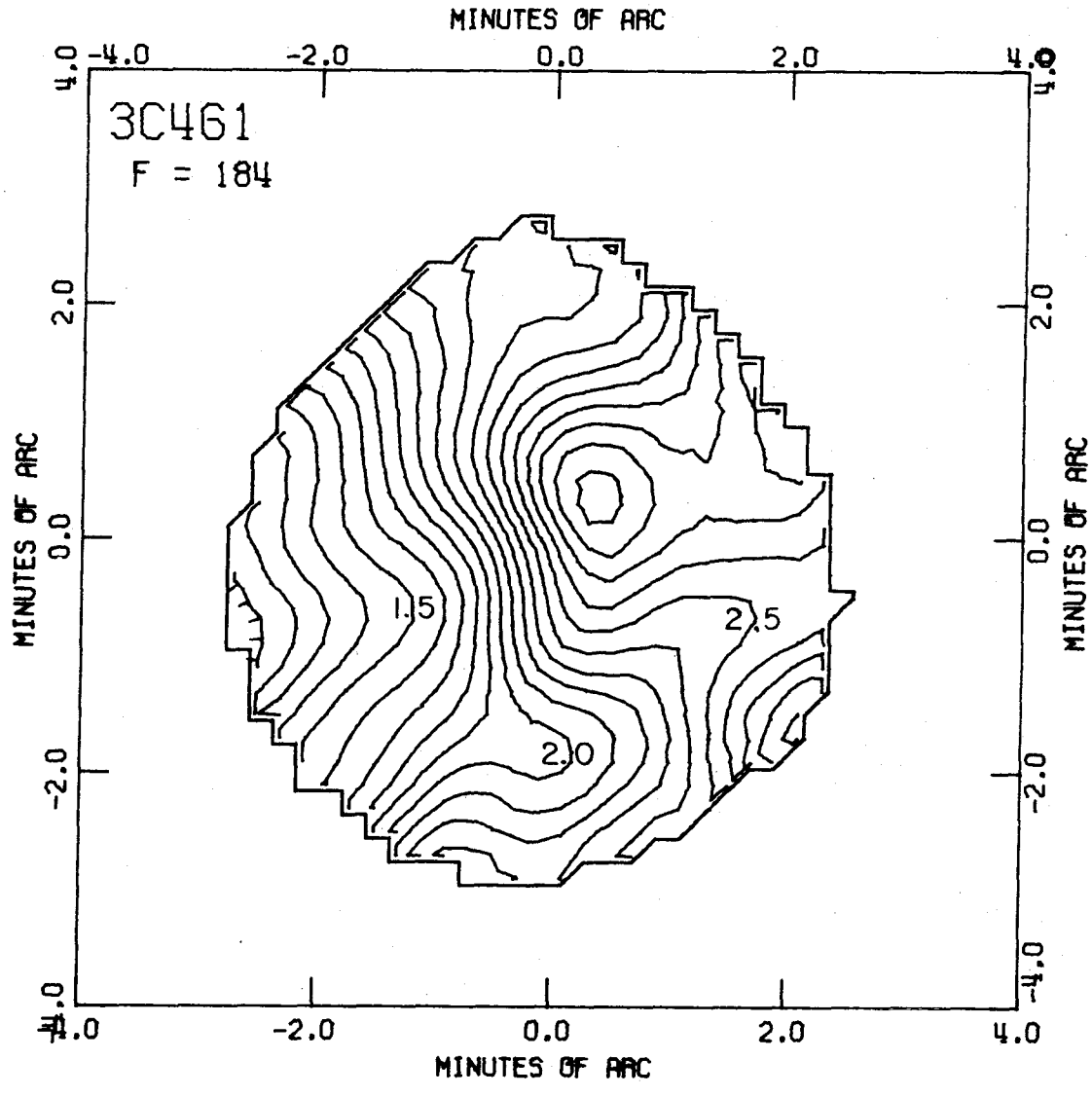

Figure 22h. 3C461: optical depth map at -39.0 km/sec, contour interval = 0.10.

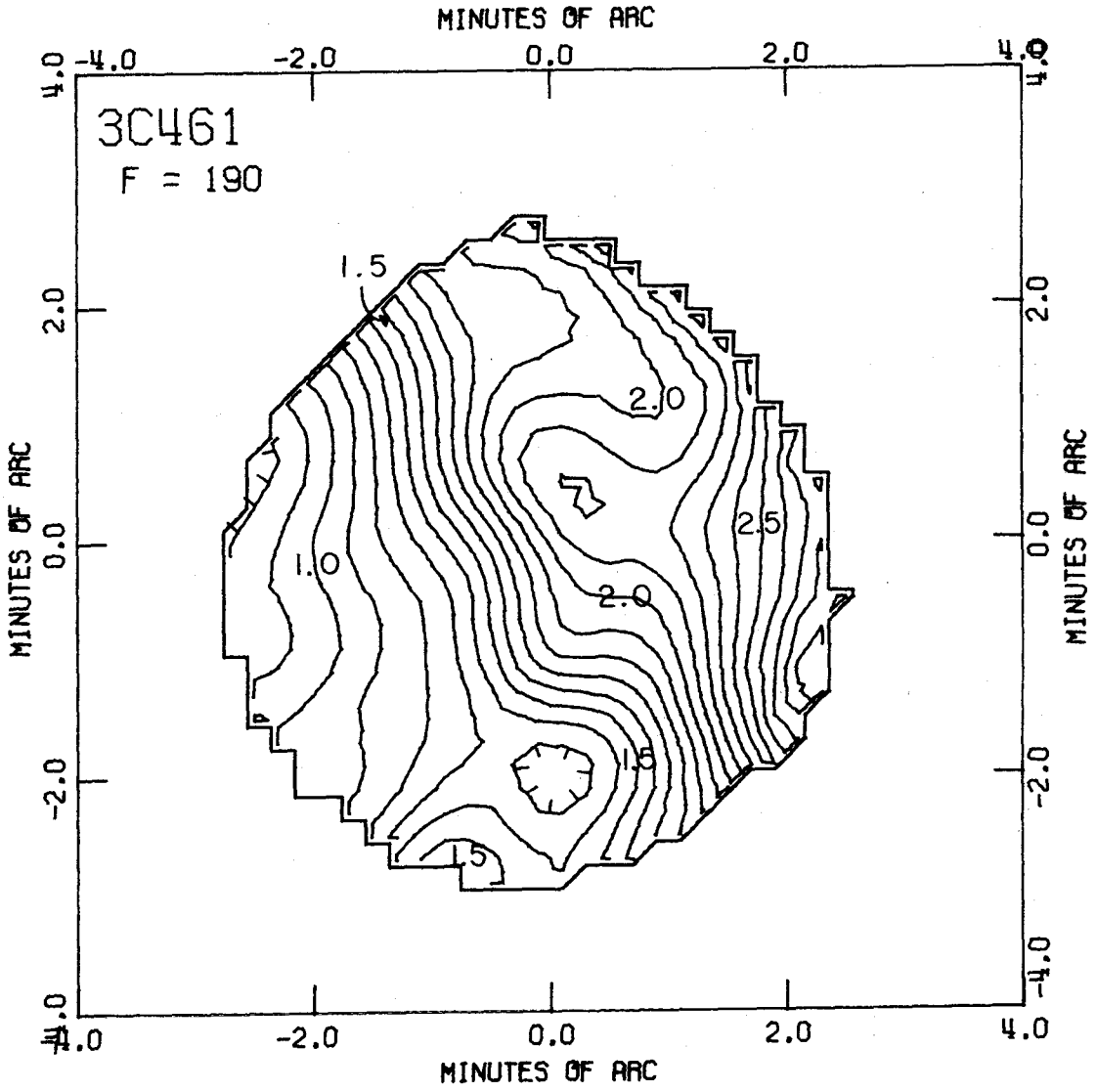

Figure 22i. 3C461: optical depth map at -40.2 km/sec, contour interval = 0.10.

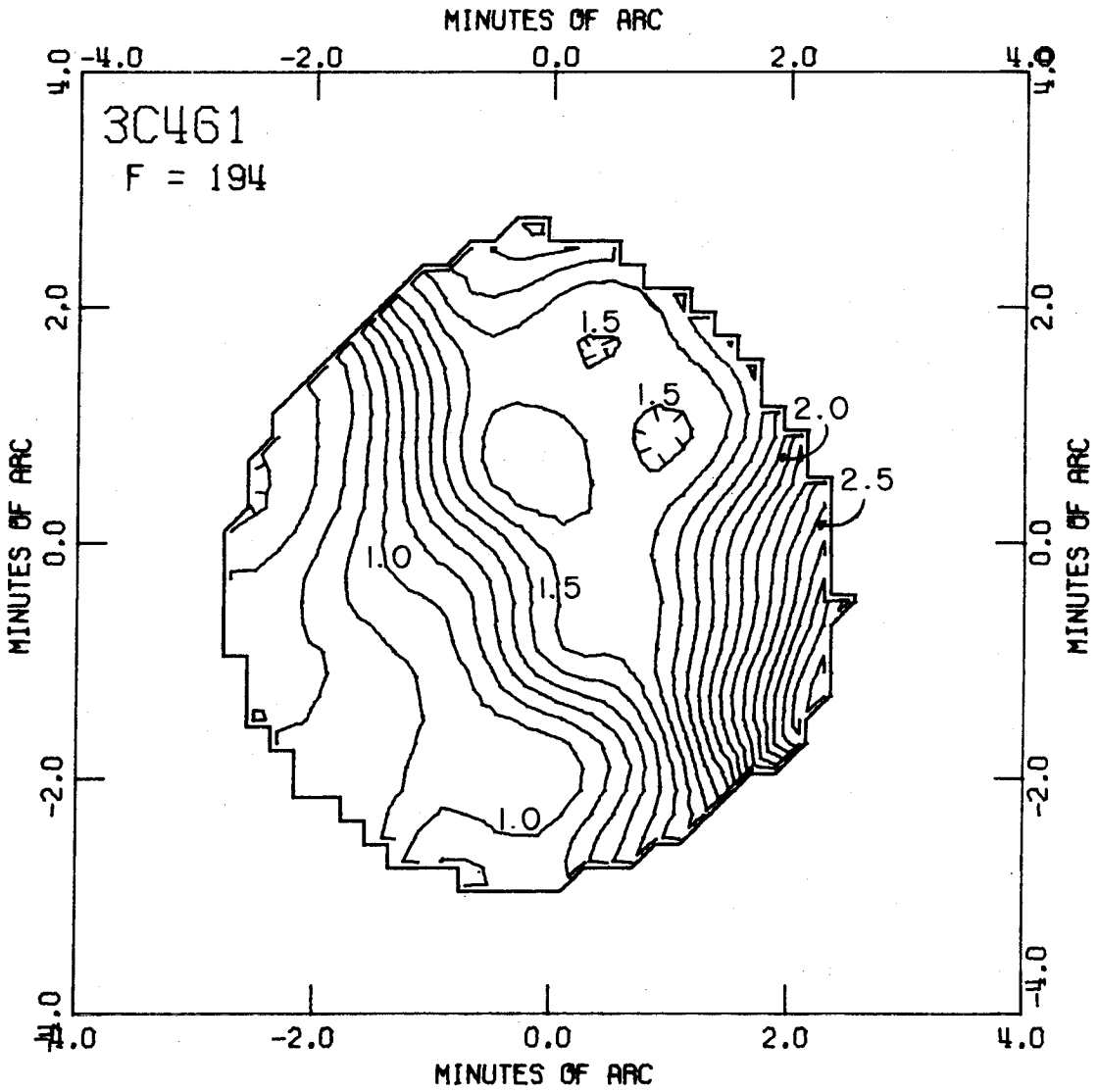

Figure 22j. 3C461: optical depth map at - 41.0 km/sec, contour interval = 0.10.

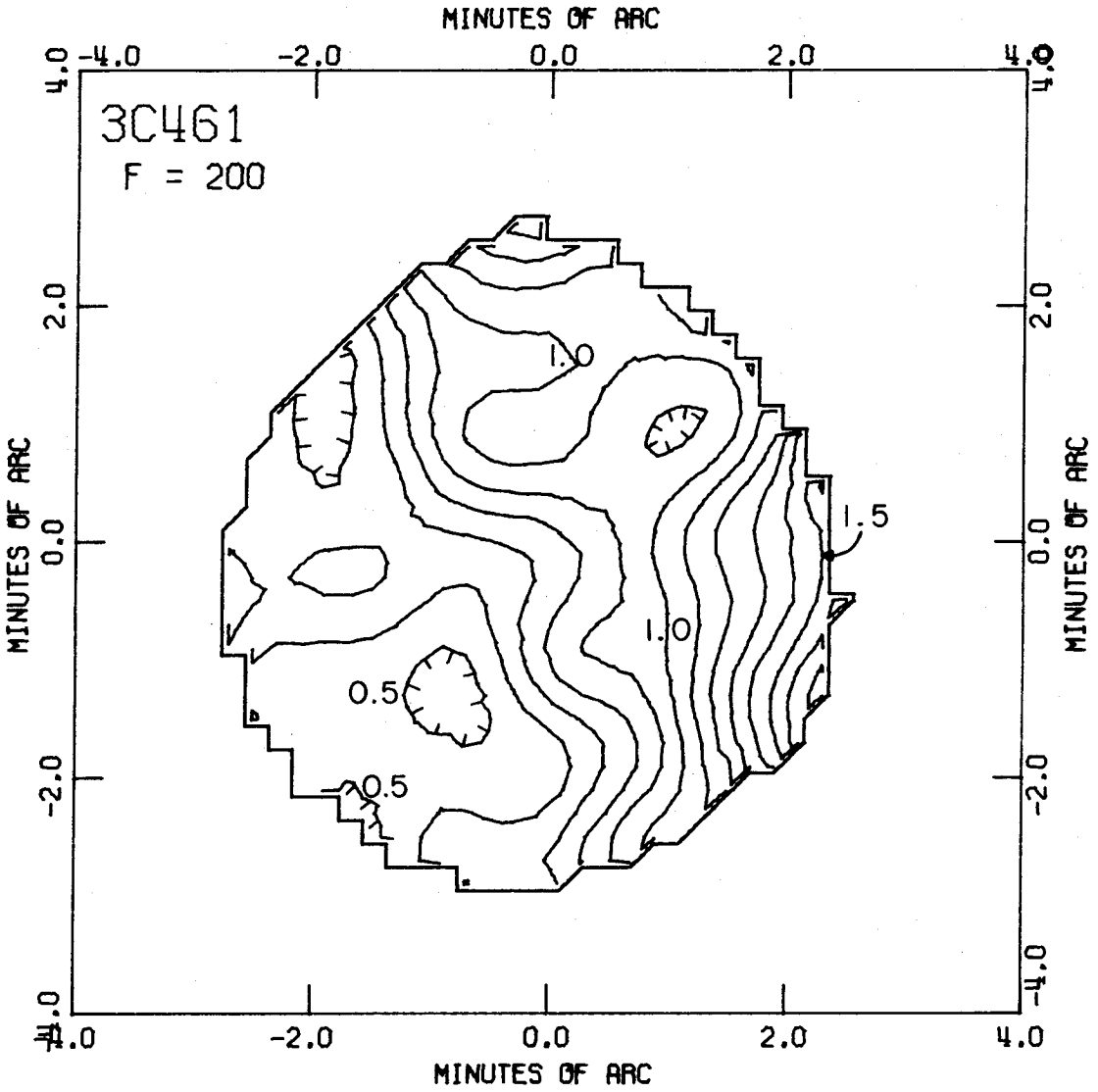

Figure 22k. 3C461: optical depth map at -42.3 km/sec, contour interval = 0.10.

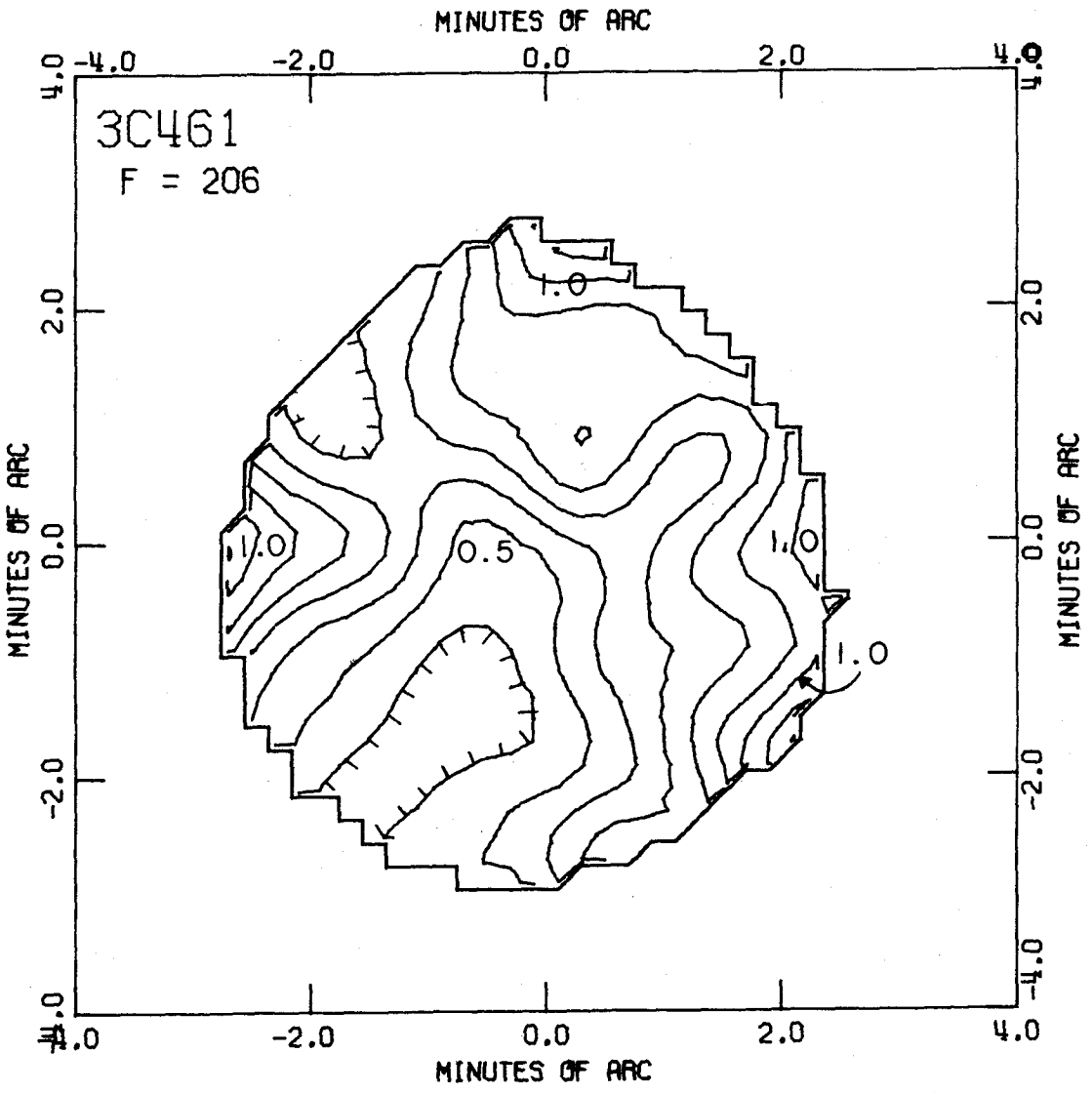

Figure 221. 3C461: optical depth map at -43.6 km/sec, contour interval = 0.10.

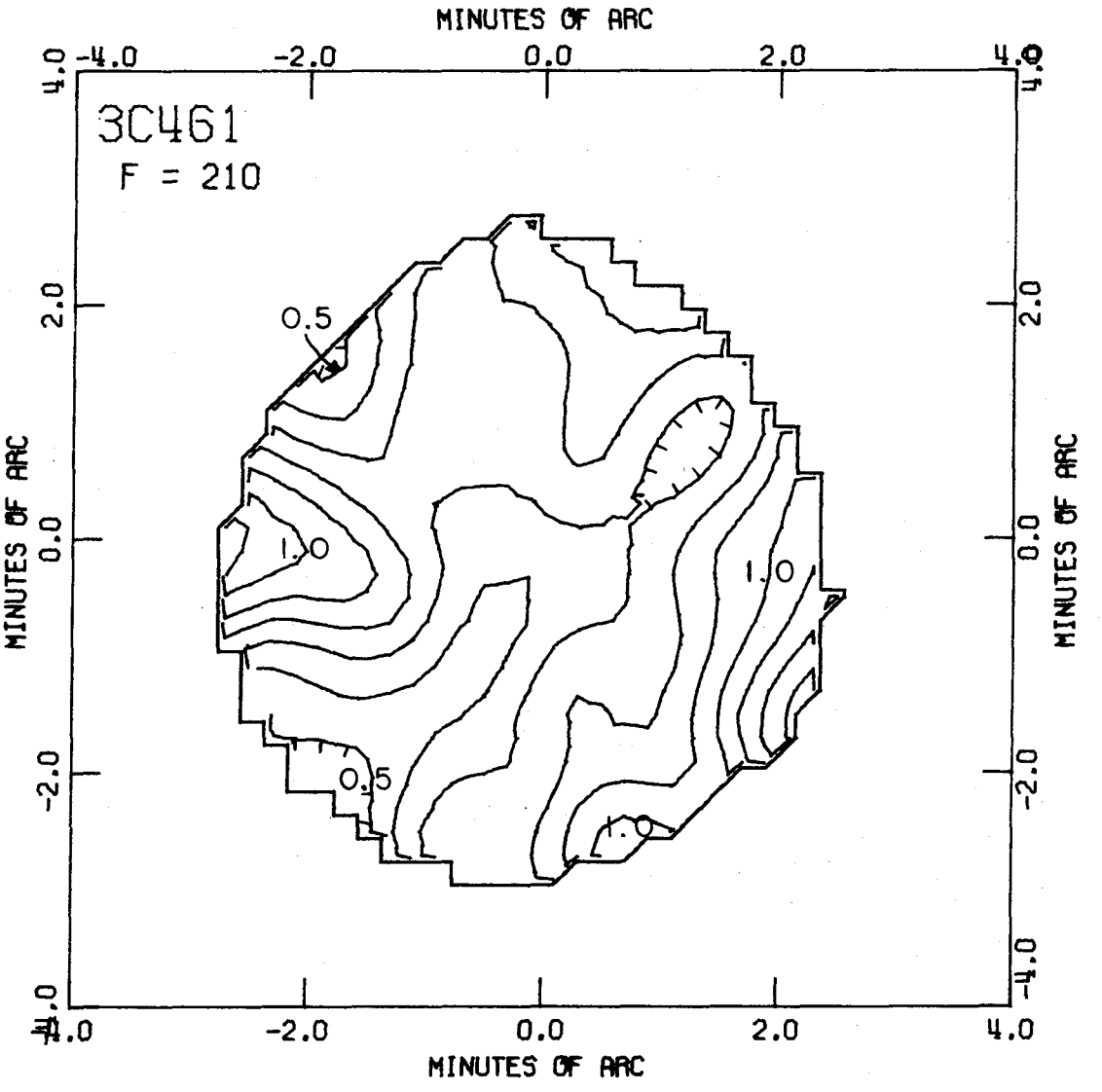

Figure 22m. 3C461: optical depth map at -44.5 km/sec, contour interval = 0.10.

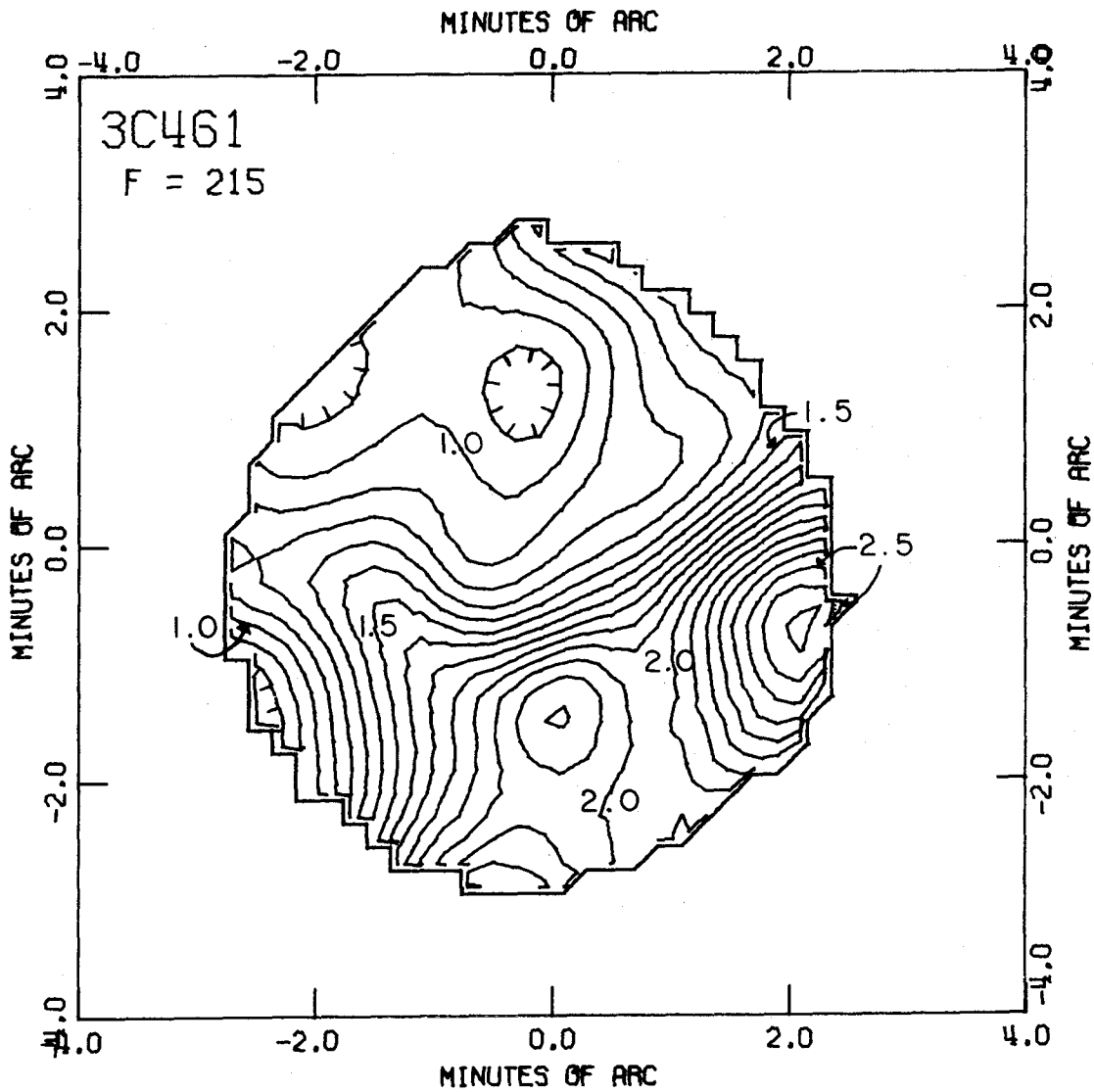

Figure 23a. 3C461: optical depth map at -45.5 km/sec, contour interval = 0.10.

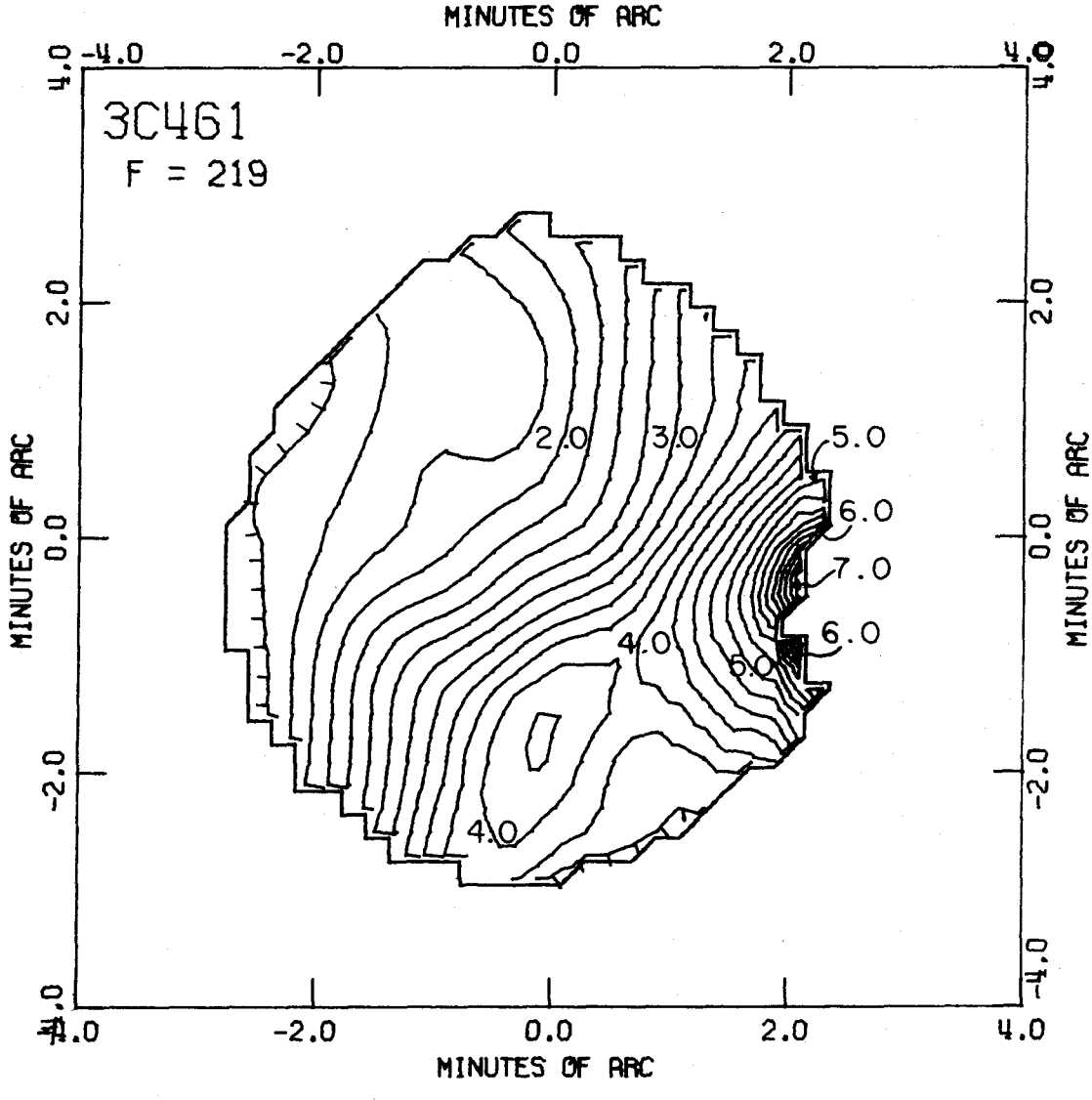

Figure 23b. 3C461: optical depth map at -46.4 km/sec, contour interval = 0.25.

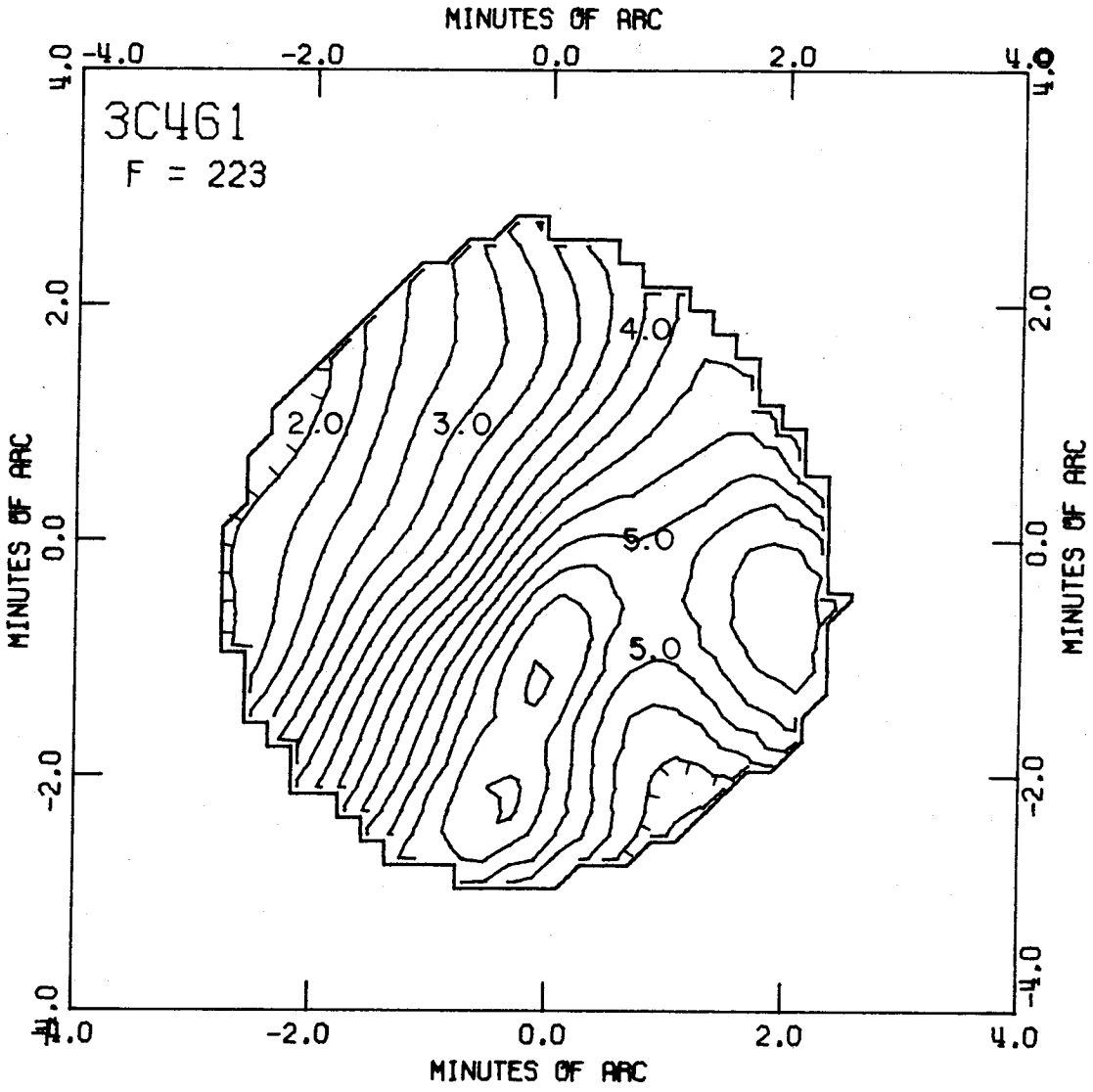

Figure 23c. 3C461: optical depth map at -47.2 km/sec, contour interval = 0.25.

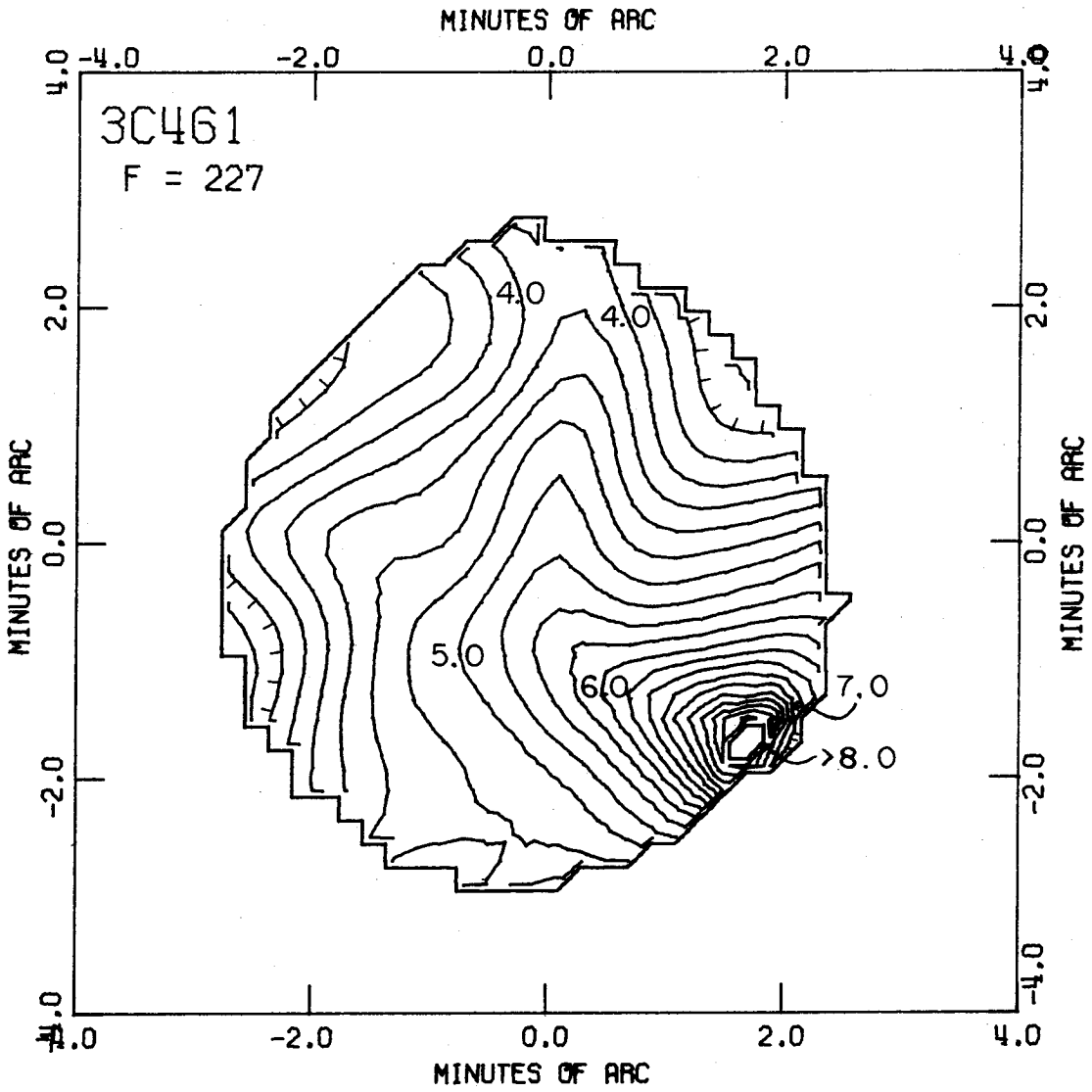

Figure 23d. 3C461: optical depth map at -48.0 km/sec, contour interval = 0.25.

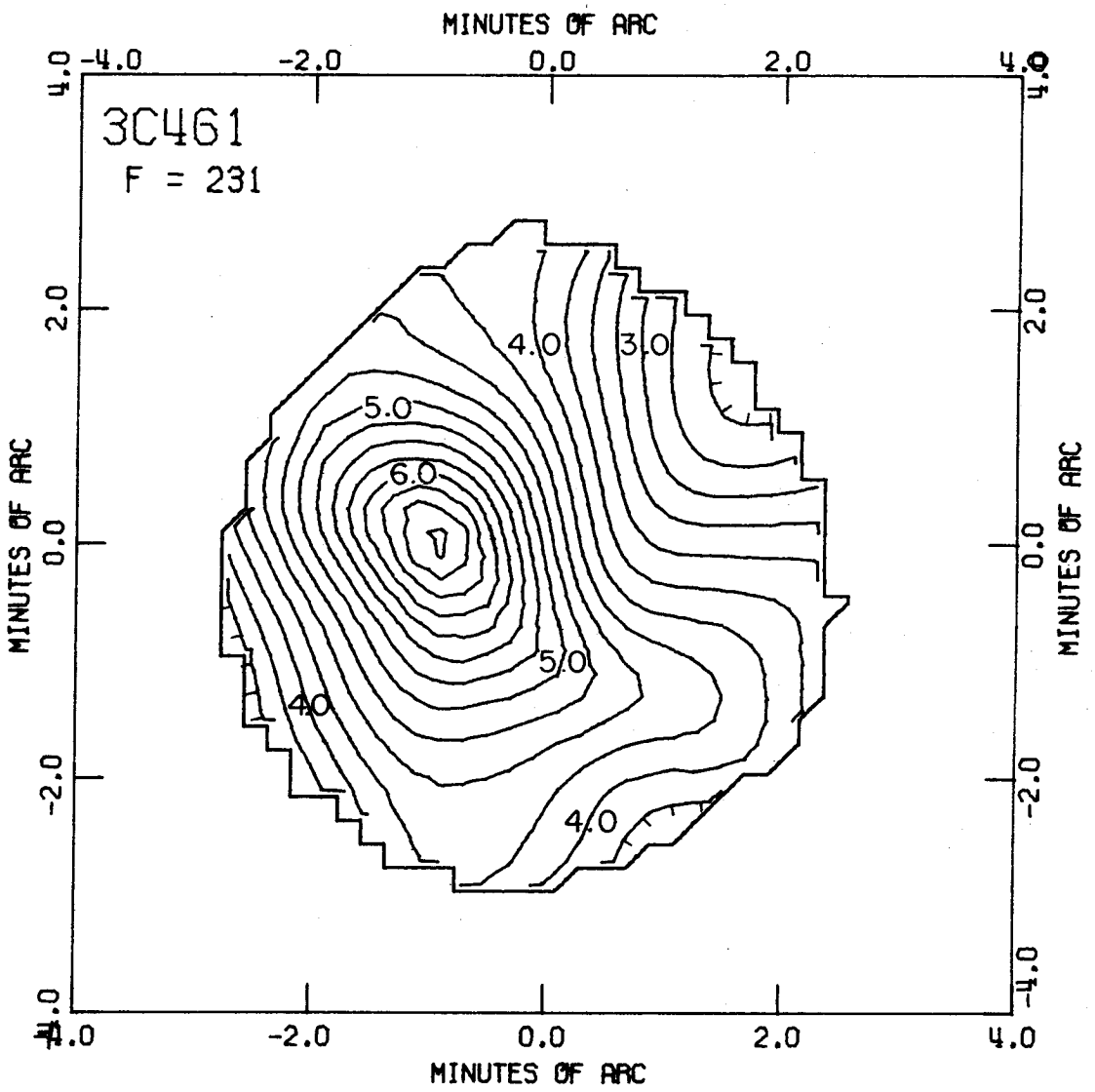

Figure 23e. 3C461: optical depth map at -48.9 km/sec, contour interval = 0.25.

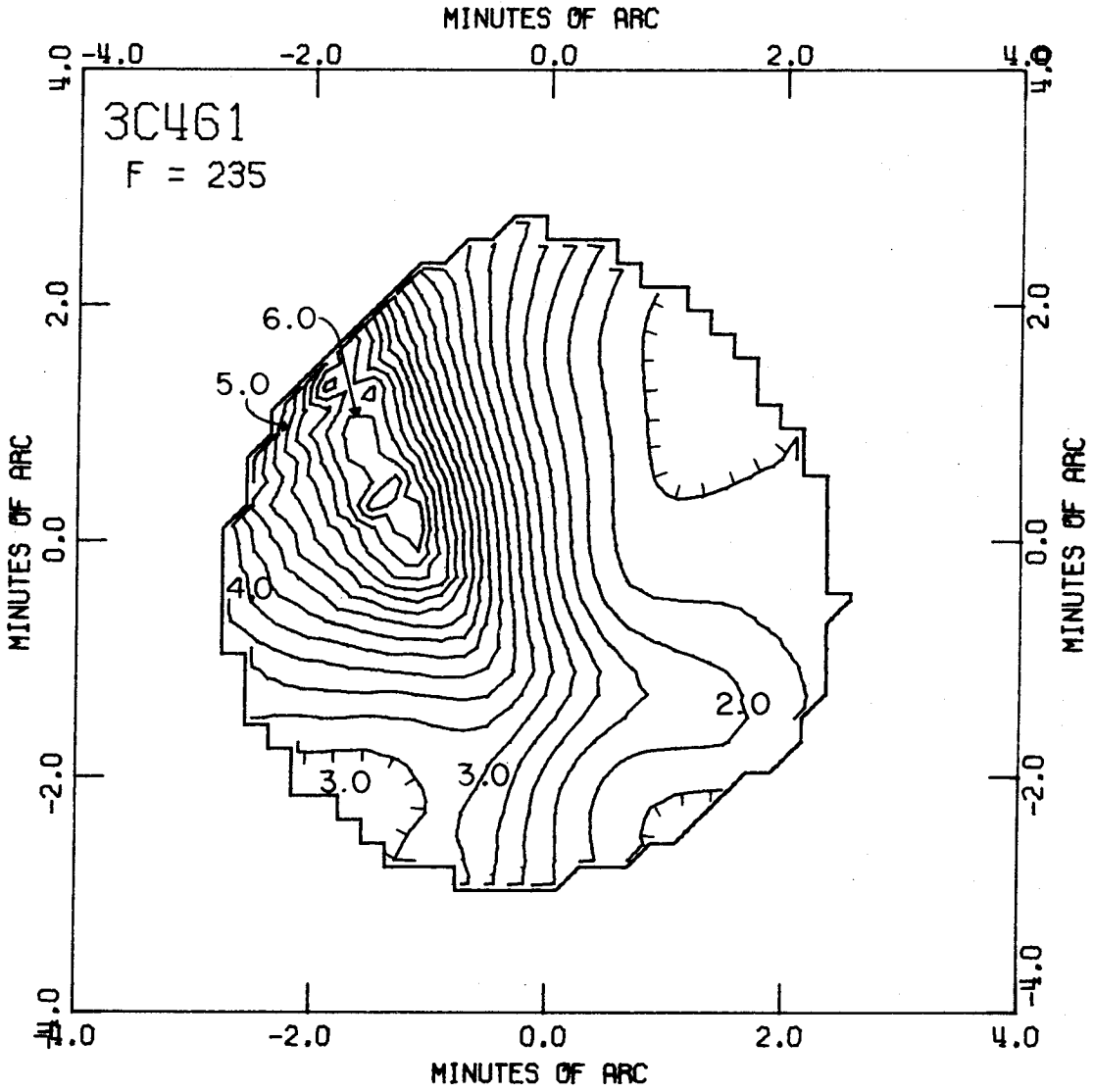

Figure 23f. 3C461: optical depth map at -49.7 km/sec, contour interval = 0.25.

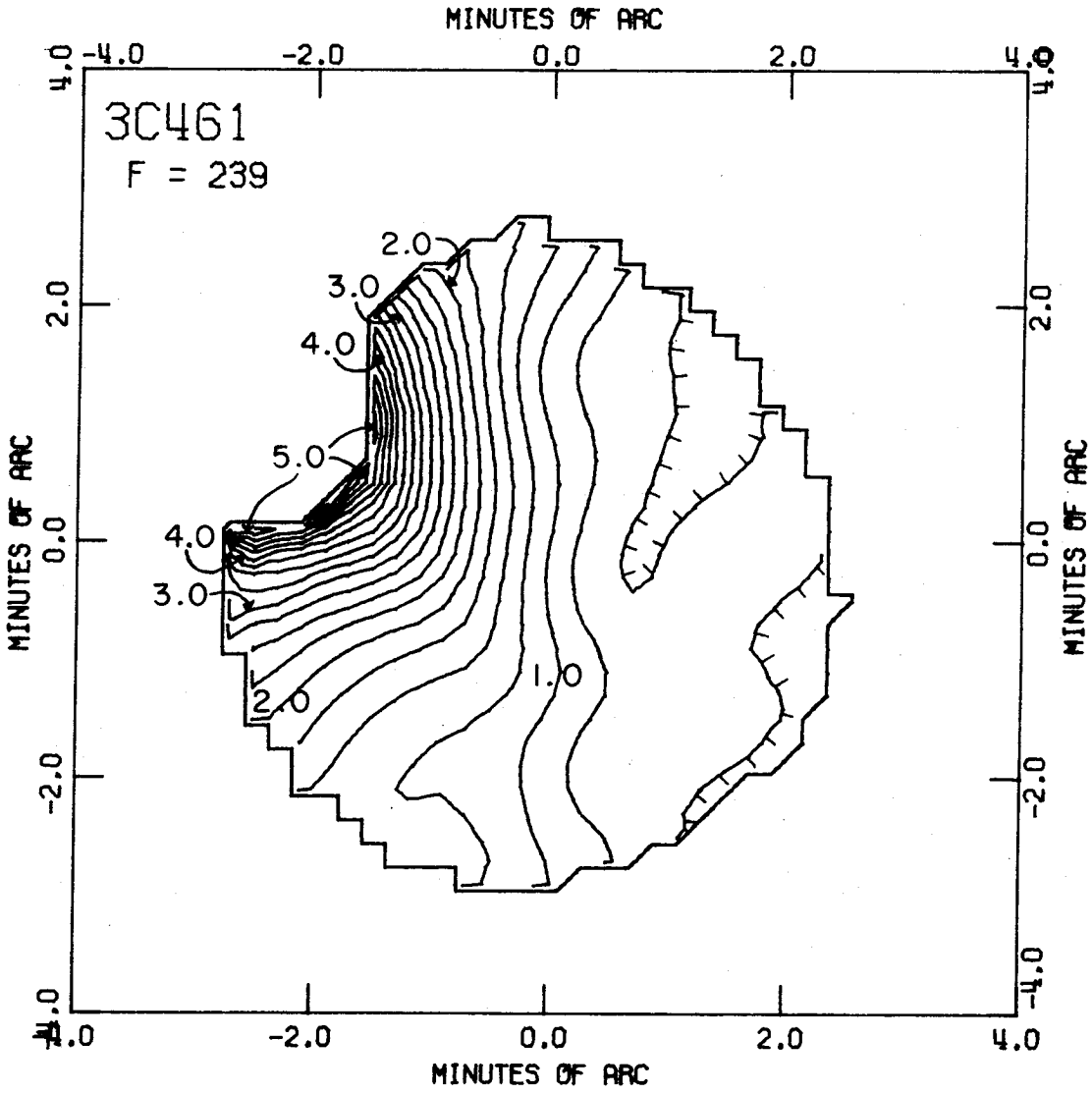

Figure 23g. 3C461: optical depth map at -50.5 km/sec, contour interval = 0.25.

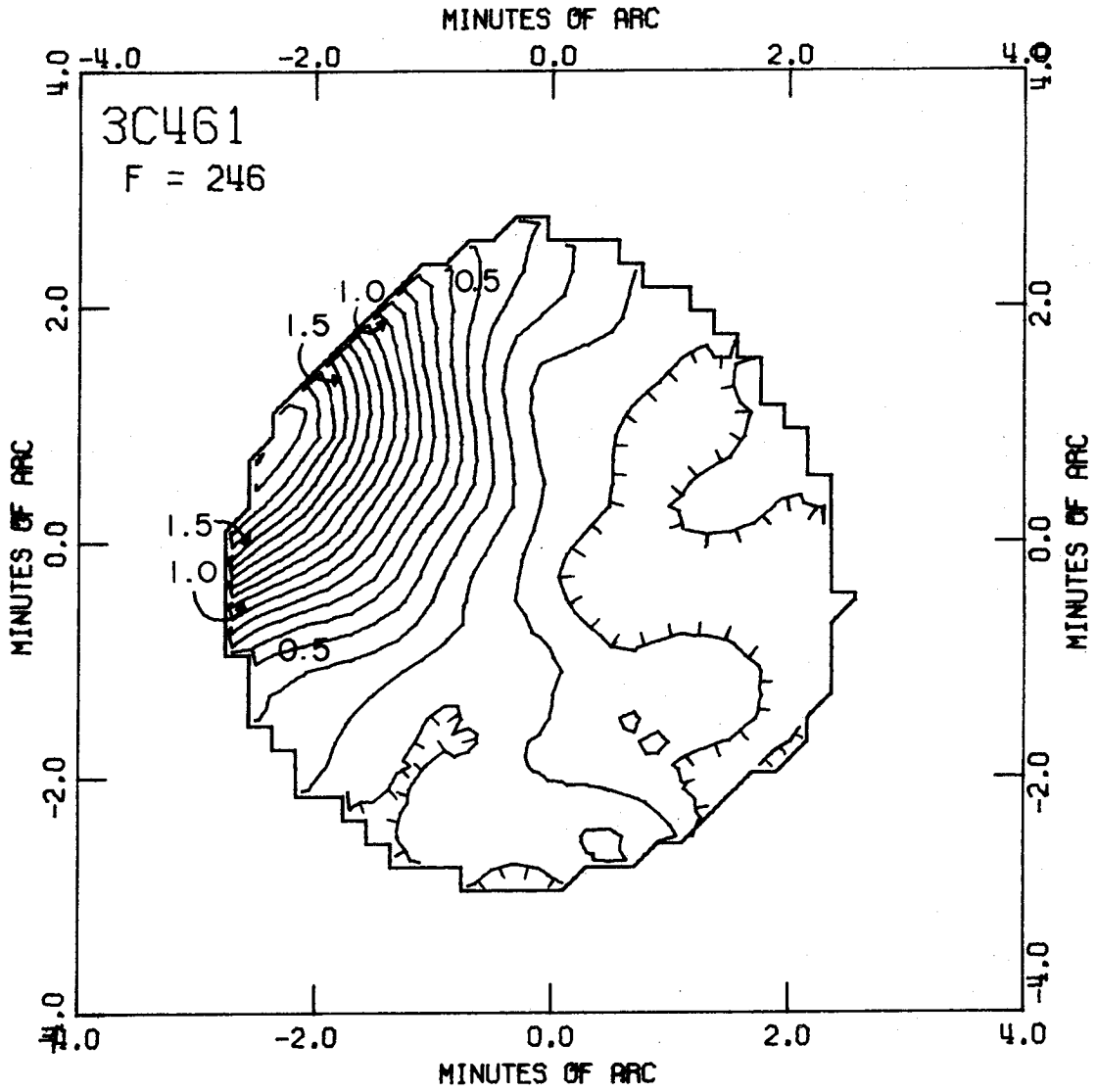

Figure 23h. 3C461: optical depth map at -52.0 km/sec, contour interval = 0.10.

148 KHz (Figure 22a), some features which are almost certainly real begin to develop. The principal peak off the source from (2.1, -1.5) is the beginning of the very broad wing of a spectral feature which attains maximum optical depth (τ) around 174 KHz (see Figure 24k, Chapter 5D). The peak to the north of (-0.1, 2.7) is the beginning of a spectral feature centered near 155 KHz (see Figure 24e). On the 148 KHz map, there is also a ridge in τ running between minor peaks at (2.3, 0.1), (0.2, 0.7), and (-0.7, 1.3). The peak at the eastern edge of the source is probably the result of the DC offsets. By 154 KHz, the two peaks and the ridge are more prominant and all optical depths have increased. The middle bump along the ridge is now centered at (0.7, 0.1).

Although most optical depths have increased by 158 KHz and some new peaks are present, the northern peak has a slightly lower τ. The major ridge is still quite obvious, but is now dominated by high τ's off the western edge of the source. A peak has developed to the east of (-2.5, 0.4) and there is evidence for a peak to the southwest. A minor ridge running to the southeast from (2.3, -0.5) is also seen. It is worth noting that the odd frequency shift

(+ 171) places the major western peak on the source about (2.3, -0.1) at these frequencies. By 164 KHz, the map is completely dominated by peaks having τ around 1.9 just east and west of the source and by a weaker peak well to the north of the source. A valley runs north-south through the center of the source with τ's less than 0.6. The weaker peaks and ridges mentioned above are probably still present but they are somewhat obscured by the steep gradients. At 168 KHz all optical depths have increased but the spatial distribution is not much changed. The eastern peak and the minima have gained relative strength and the northern peak is less prominent. Two ridges are seen and a peak to the southwest is strongly suggested.

By 174 KHz, the τ distribution has changed significantly. The eastern peak reached a maximum τ around 172 KHz and has, by 174 KHz, shifted northward to (-2.3, 1.1). The western peak off (2.3, 0.2) has optical depth near 4 and, with a ridge extending from this peak toward (0.5, -0.7), dominates the map. A peak off (-1.3, -2.7) has developed while the peak to the southwest has disappeared. A striking minimum at (-0.3, 1.7), which has been visible on many of the maps so far discussed, is no longer

well explained by the peaks seen on the map. A significant concentration of optical depth well to the north of the source is suggested by this minimum although there might be some agent (e.g. HII or H_2 region) acting to remove the neutral hydrogen from this particular line of sight.

By 178 KHz, the peak at (-2.3, 1.1) has dropped in relative strength while the western peak has moved northward to (2.0, 1.0). The ridge is quite prominent with a secondary peak now seen at (0.5, -0.6). The peak at (-1.3, -2.7) attains maximum τ at 176 KHz and drops off rapidly at higher frequencies (see Figure 24c). By 184 KHz, almost all traces of this peak and the peak off (-2.3, 1.1) have vanished and all τ's have decreased. Two new peaks have appeared at (0.3, 0.3) and off (2.1, -1.7). The peaks at (2.0, 1.0) and (0.5, -0.6) can still be seen, but no longer dominate the maps. Although the western edge of the source retains a τ around 3 at 190 KHz, the optical depths over the rest of the source continue to drop. Peaks are seen at (2.1, -1.7), (0.3, 0.3), and (-0.7, - 2.9). Extensions of the contours hint at peaks near (-0.1, 0.7) and (0.3, -0.7). There is apparently considerable optical depth northwest of the source.

At 194 KHz, the western edge still shows a τ near 3. Lesser peaks are found off (-0.1, 2.7) and at (-0.1, 0.7), (0.3, -0.6), and (-0.7, -2.9). From 194 KHz to 200 KHz the optical depths drop over the full map area. A ridge develops from (-2.7, -0.3) to (-1.5, -0.3) and the western peak appears somewhat double. The northern peak off (-0.1, 2.7) is more prominent and several lesser peaks are present.

Most of the spectra across the source have a minimum optical depth between 200 and 210 KHz. At 206 KHz we find major peaks off (-2.7, 0.0), (0.5, 2.5), (2.3, 0.1) and (2.2, - 1.5) and lesser peaks off (0.7, - 2.7) and at (-0.9, 1.1) and (0.3, 0.9). A similar spatial distribution occurs at 210 KHz with the only changes being a relative decrease in the peak off (2.3, 0.1) and a motion of the northern peak westward.

By 215 KHz (Figure 23a) all optical depths have increased sharply with major peaks appearing at (2.1, -0.8) and (0.1, -1.4) and off (-0.6, -2.9). The contours clearly show the effects of the peak which moved from (-2.7, 0.0) at 210 KHz to (-1.6, -0.3) at 213 KHz before beginning to lose its identity. A local minimum is seen as a striking circular feature at (-0.3, 1.3) and a peak in τ northwest

of the source is suggested. The optical depths at the western edge of the source become uncomputably high by 219 KHz. A second peak occurs at (-0.1, -0.8). The even frequency shift (+ 226) places both peaks somewhat farther south but with poorer signal-to-noise ratio at these frequencies. The great contrast in τ across the source tends to obscure any minor peaks which might be present. The western peak reaches a maximum in optical depth around 222 KHz and then falls off appearing near (1.9, -0.6) at 223KHz. The other major peak is seen as two peaks at (-0.3, -2.2) and (-0.1, -1.2). The contrast in optical depth across the source has decreased due to a sharp increase in τ on the eastern side of the source. However, no minor peaks are seen. By 227 KHz, only one unresolved peak of very high optical depth and two ridges are found. The peak centered at (1.7, - 1.7) appears to be the major western peak with its centroid shifted southward since the 225 KHz map places the peak at an intermediate position.

At 229 KHz a new major peak appears at (-0.8, -0.2) while the western peak drops considerably. At 231 KHz the new peak is centered at (-0.9, 0.0) with contours extending to the southwest and northeast. The western peak, at a τ

around 4, is now seen only as an extension of the contour lines and continues to drop rapidly as the frequency increases. By 235 KHz, the optical depths across the western half of the source have dropped sharply. The major peak has moved to (-1.3, 0.5). At 239 KHz, the peak has moved near the northeast edge of the source where optical depths around 6 are no longer computable. Minor peaks are suggested around (1.9, 0.0) and (1.2, - 1.5) and off (-0.7, -2.5). By 246 KHz, the peak has moved off the source and all τ's have dropped considerably. Several minor peaks are seen but they are now at levels which could be due to the DC offsets.

In the preceeding descriptive paragraphs I have emphasized the features visible in the maps of Figures 22 and 23, but have tried to take into account the attributes of the maps not presented here. In general, maps at adjacent frequencies which are obtained using different frequency shifts are somewhat different in appearance. I have tried to add appropriate comments above for the few places at which such differences might be significant. For simplicity in the above description I occasionally refer to the motion of some peak with

changing frequency. There are some cases, particularly from 229 to 239 KHz, where the assumption of a velocity gradient across the feature is probably correct. However, for most cases, it is at least equally likely that the apparent motion is due to a change in the relative strengths of two or more separate, but not fully resolved, peaks.

APPENDIX G

THE CRAB NEBULA - OPTICAL DEPTH MAPS

A summary and general discussion of the optical depth maps is presented in Chapter 6C with a detailed description and a representative sample (Figures 33) of the maps being deferred to this appendix. Again the computation of optical depths is cut off at the 20 percent level of the continuum brightness and no correction for possible DC offsets is made. These offsets are quite visible in the maps (not shown here) at the low frequency end of the spectrum. Negative offsets covering the southeast portion of the source may actually represent the local increase in hydrogen emission suggested by the spectrum in Figure 31 (Chapter 6B). The negative offsets reach a peak at (0.3, -2.1) and the positive offsets have a peak at (2.3, 0.9). These offsets have values somewhat larger than the noise levels suggested by the various noise computations. By -76 KHz or so, some of the optical depths on the map are real. The distribution is similar to that seen at - 64 KHz (Figure 33a). Quite a few peaks are present on this map including peaks off (2.3, 0.9), (-1.7, 0.7), and

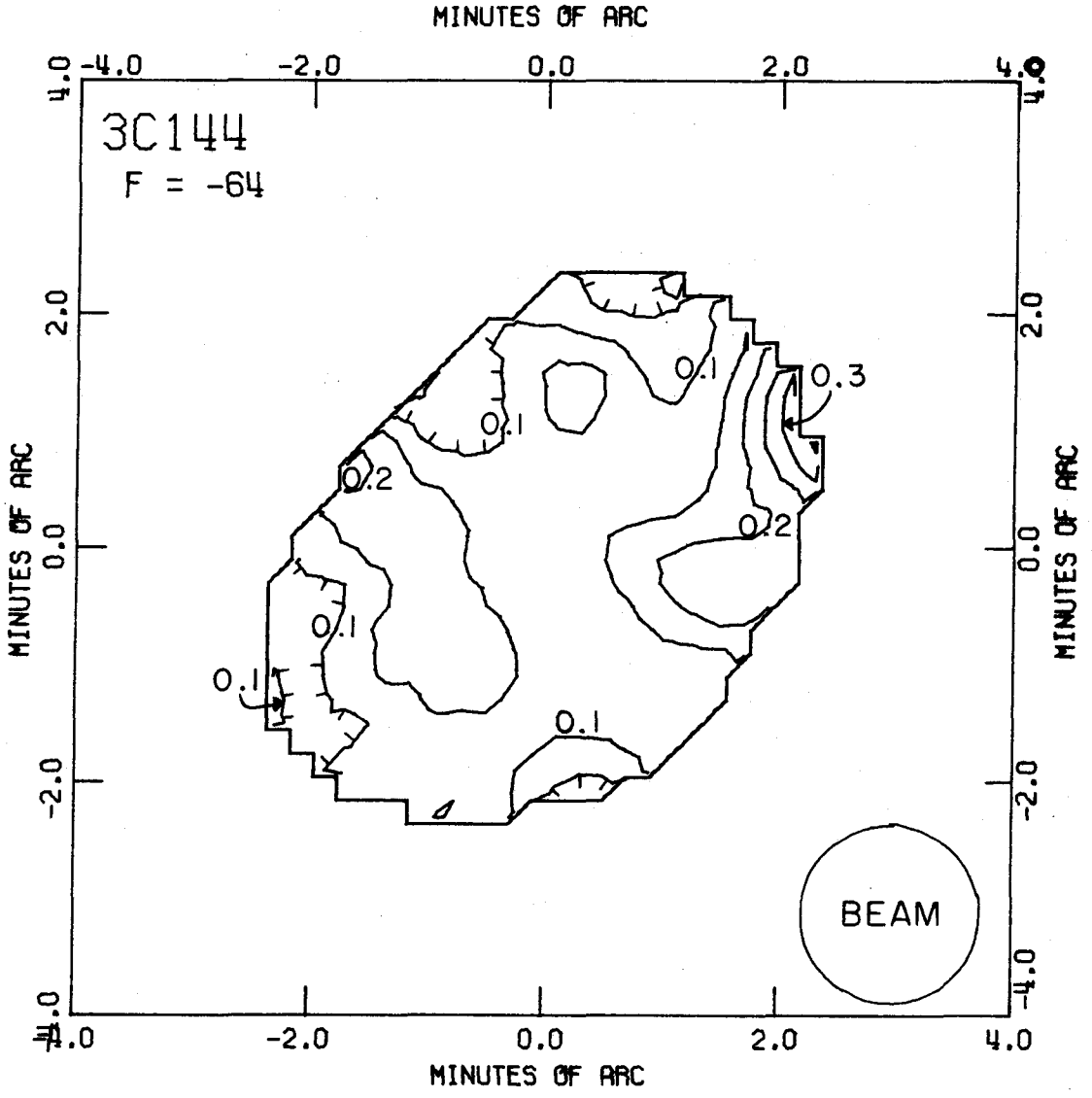

Figure 33a. 3C144: optical depth map at +13.5 km/sec, contour interval = 0.05. Illustrates beam size (full width at half maximum).

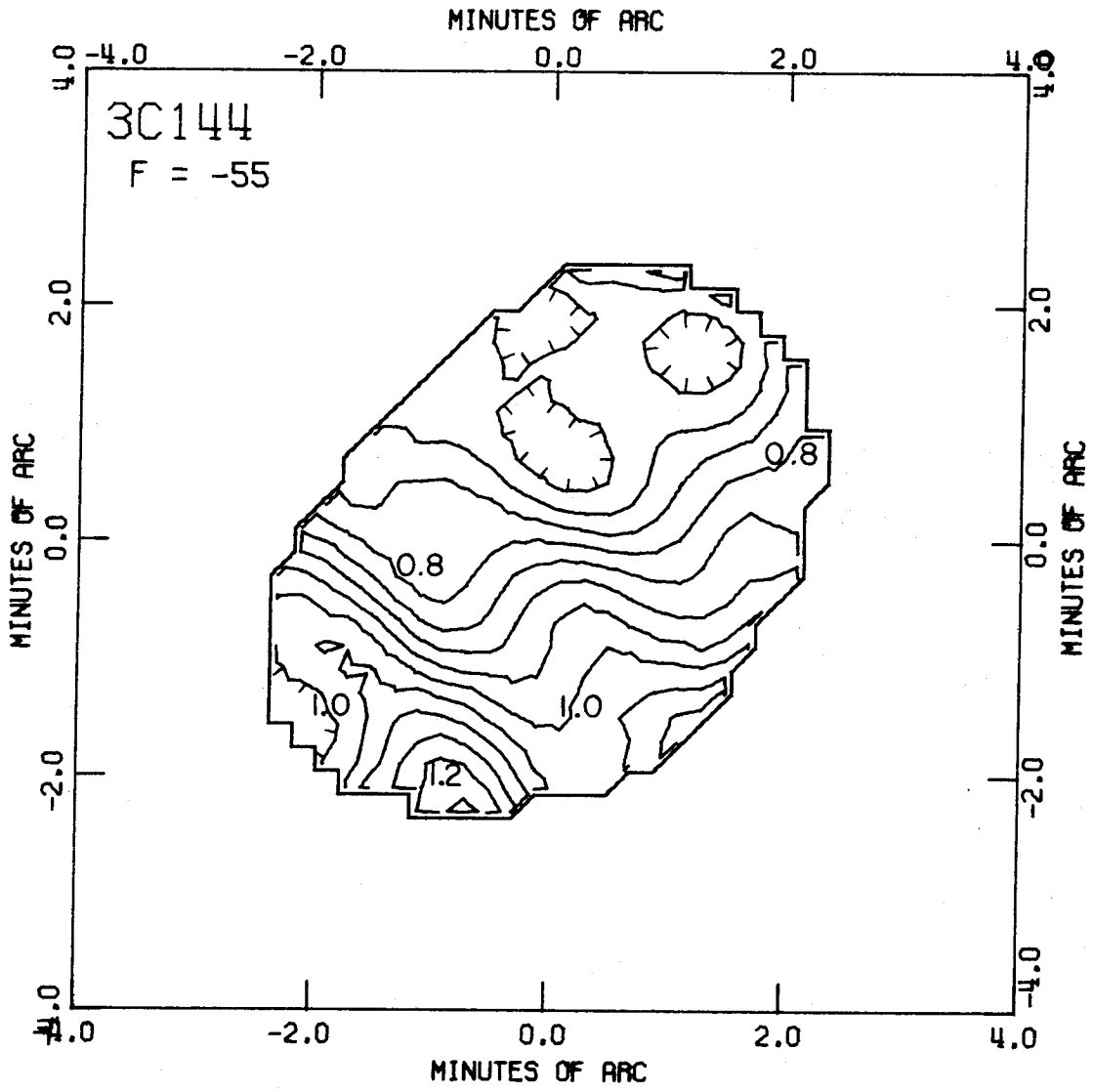

Figure 33b. 3C144: optical depth map at +11.6 km/sec, contour interval = 0.05.

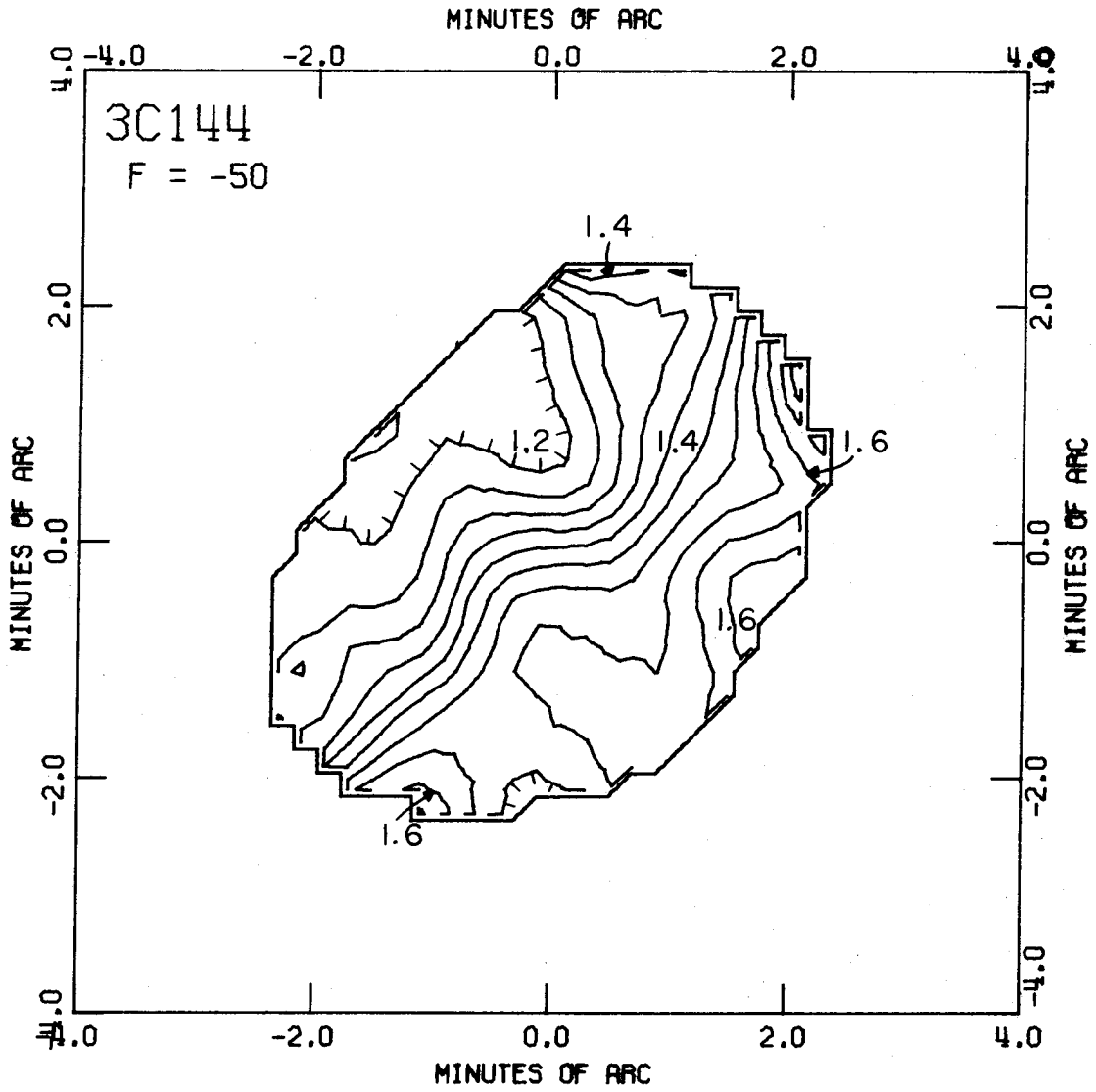

Figure 33c. 3C144: optical depth map at +10.6 km/sec, contour interval = 0.05.

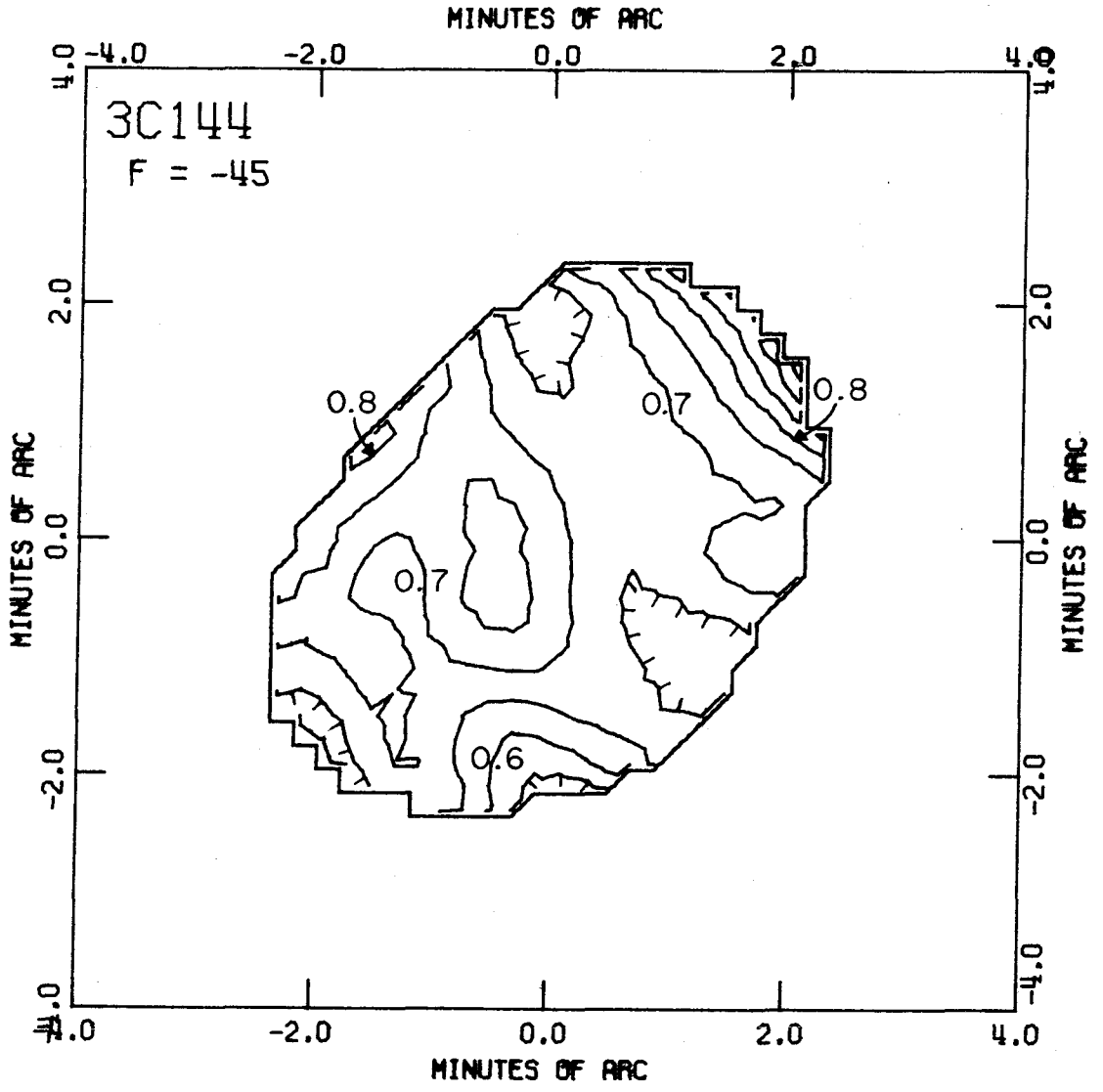

Figure 33d. 3C144: optical depth map at +9.5 km/sec, contour interval = 0.05.

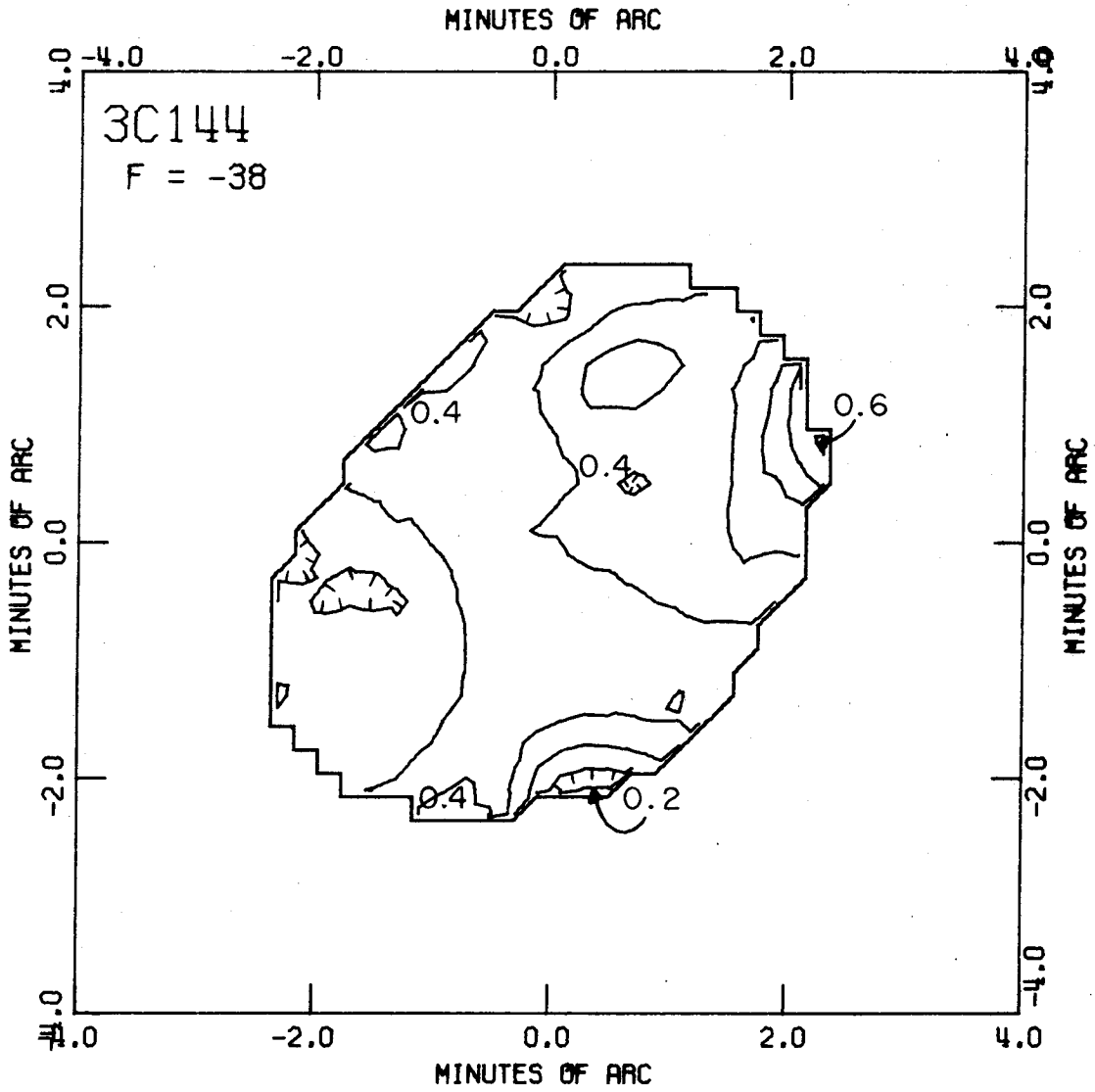

Figure 33e. 3C144: optical depth map at +8.0 km/sec, contour interval = 0.05.

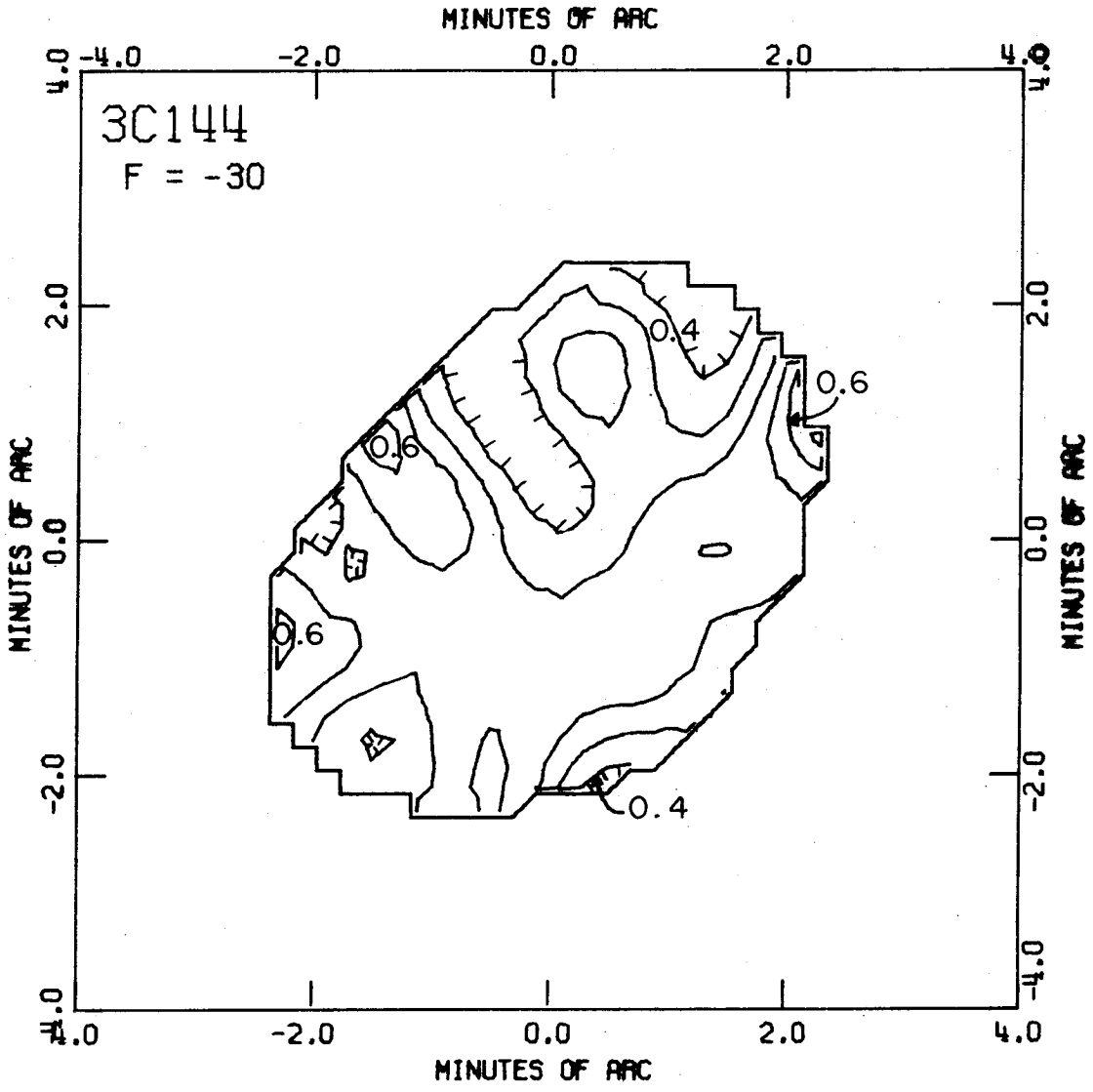

Figure 33f. 3C144: optical depth map at +6.4 km/sec, contour interval = 0.05.

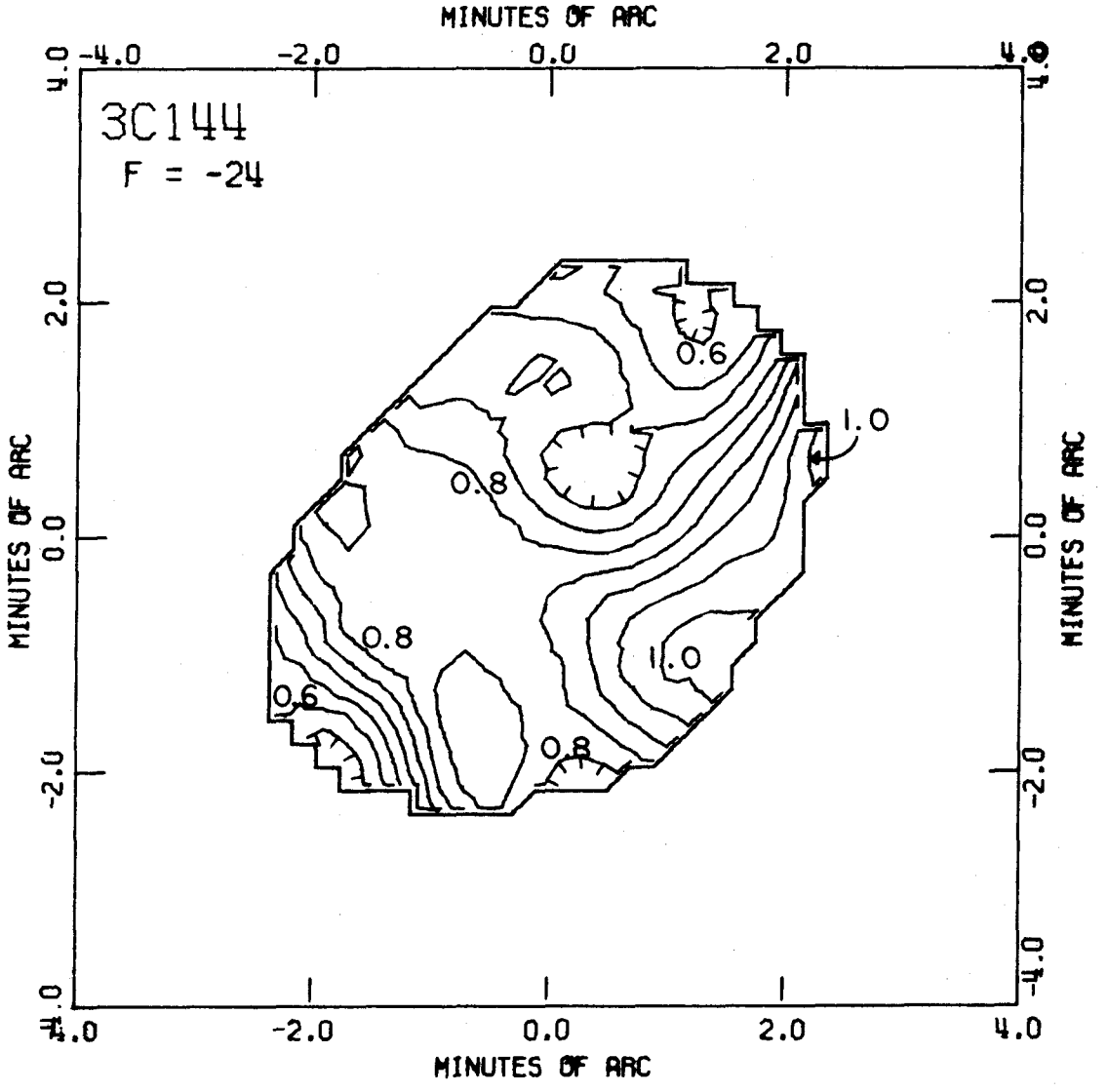

Figure 33g. 3C144: optical depth map at +5.1 km/sec, contour interval = 0.05.

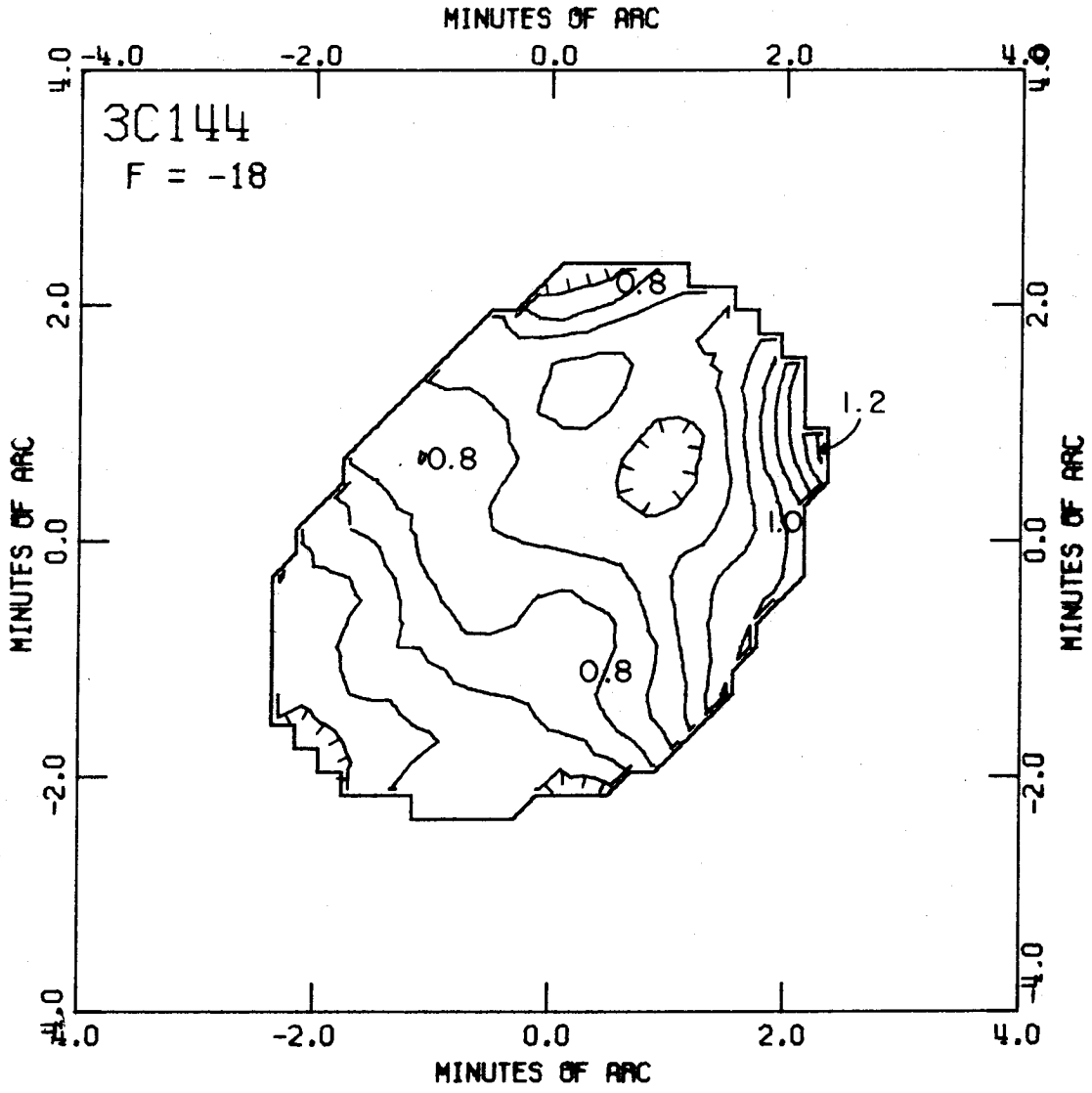

Figure 33h. 3C144: optical depth map at +3.8 km/sec, contour interval = 0.05.

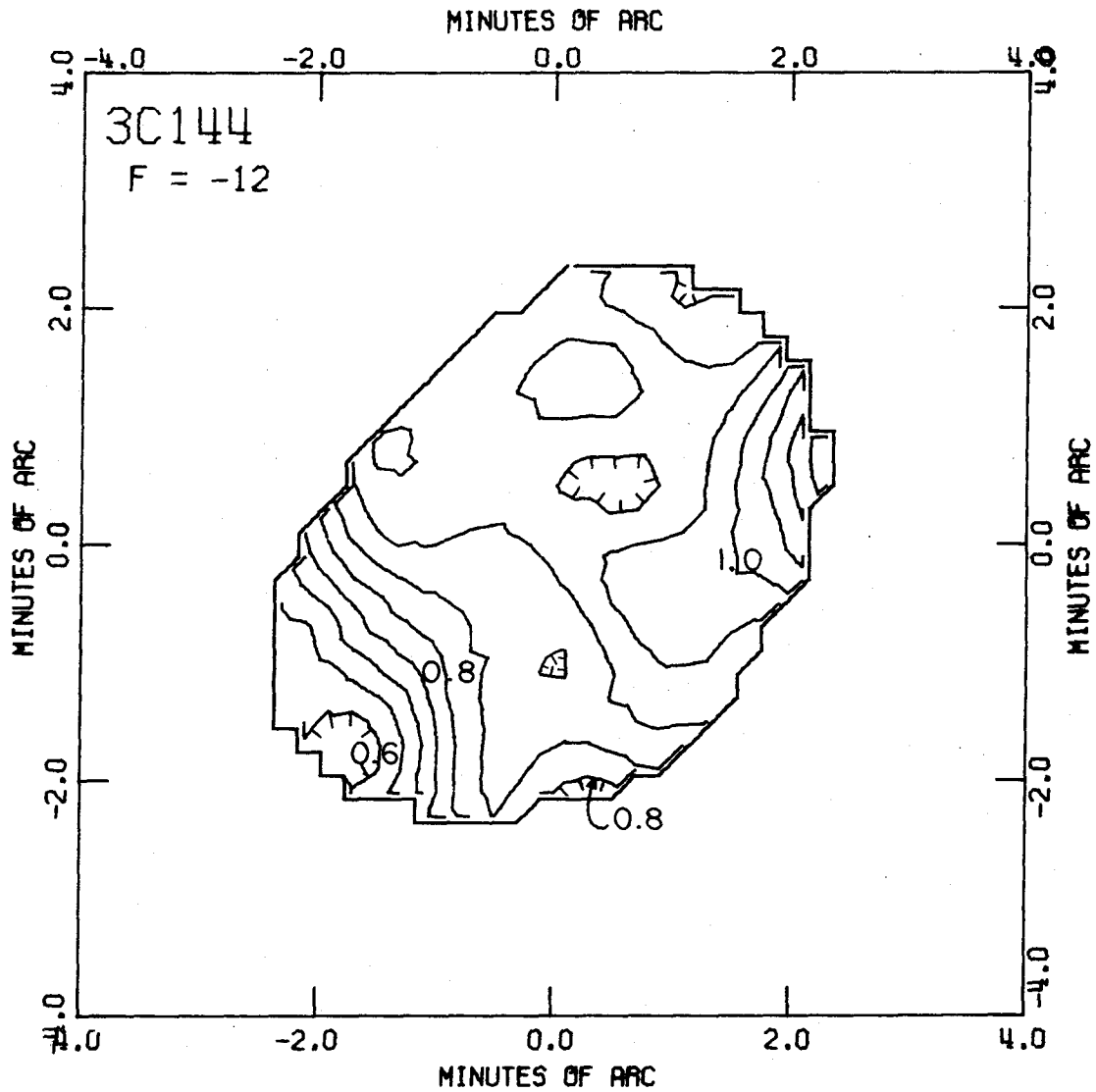

Figure 33i. 3C144: optical depth map at +2.5 km/sec, contour interval = 0.05.

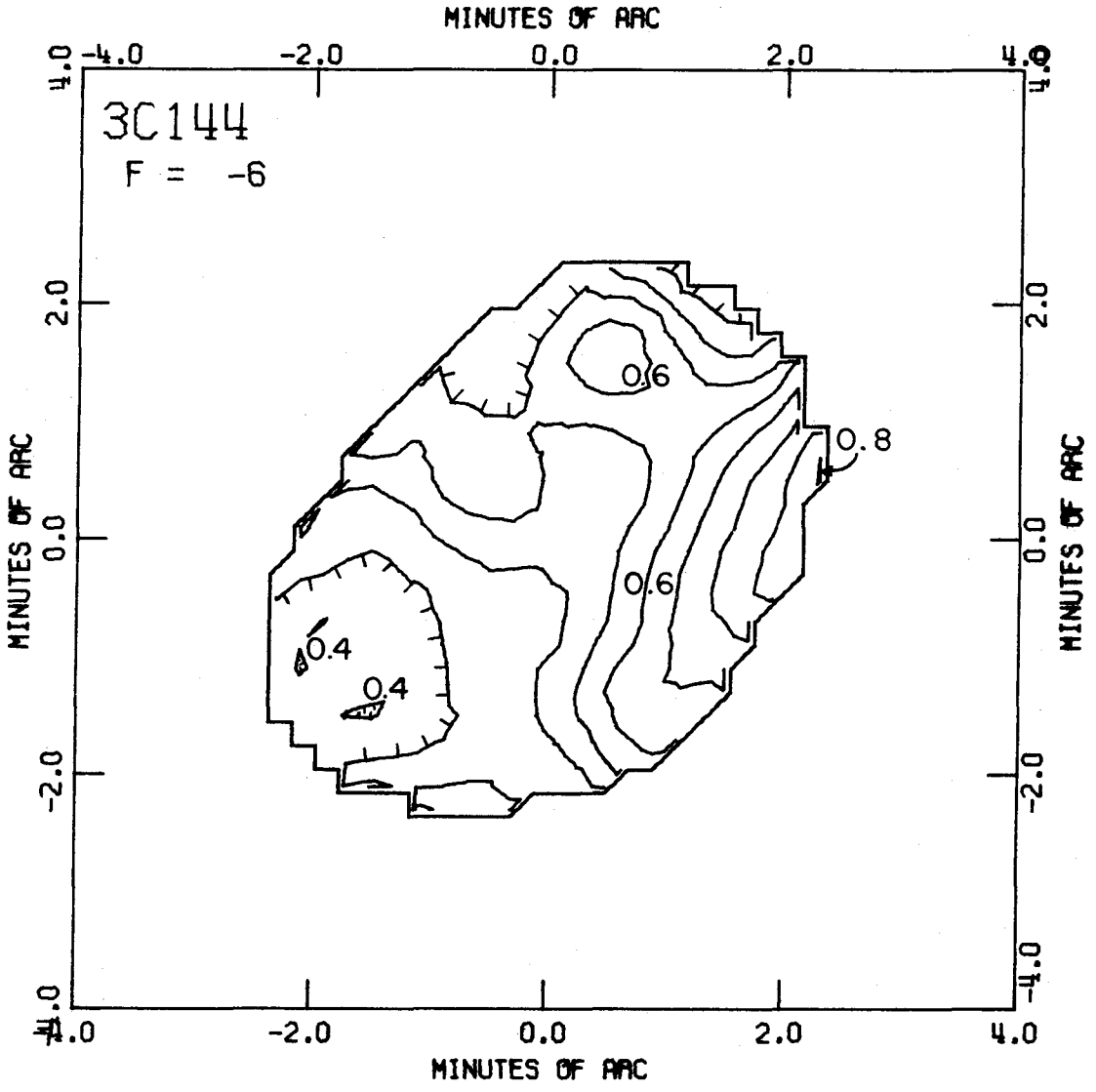

Figure 33j. 3C144: optical depth map at +1.3 km/sec, contour interval = 0.05.

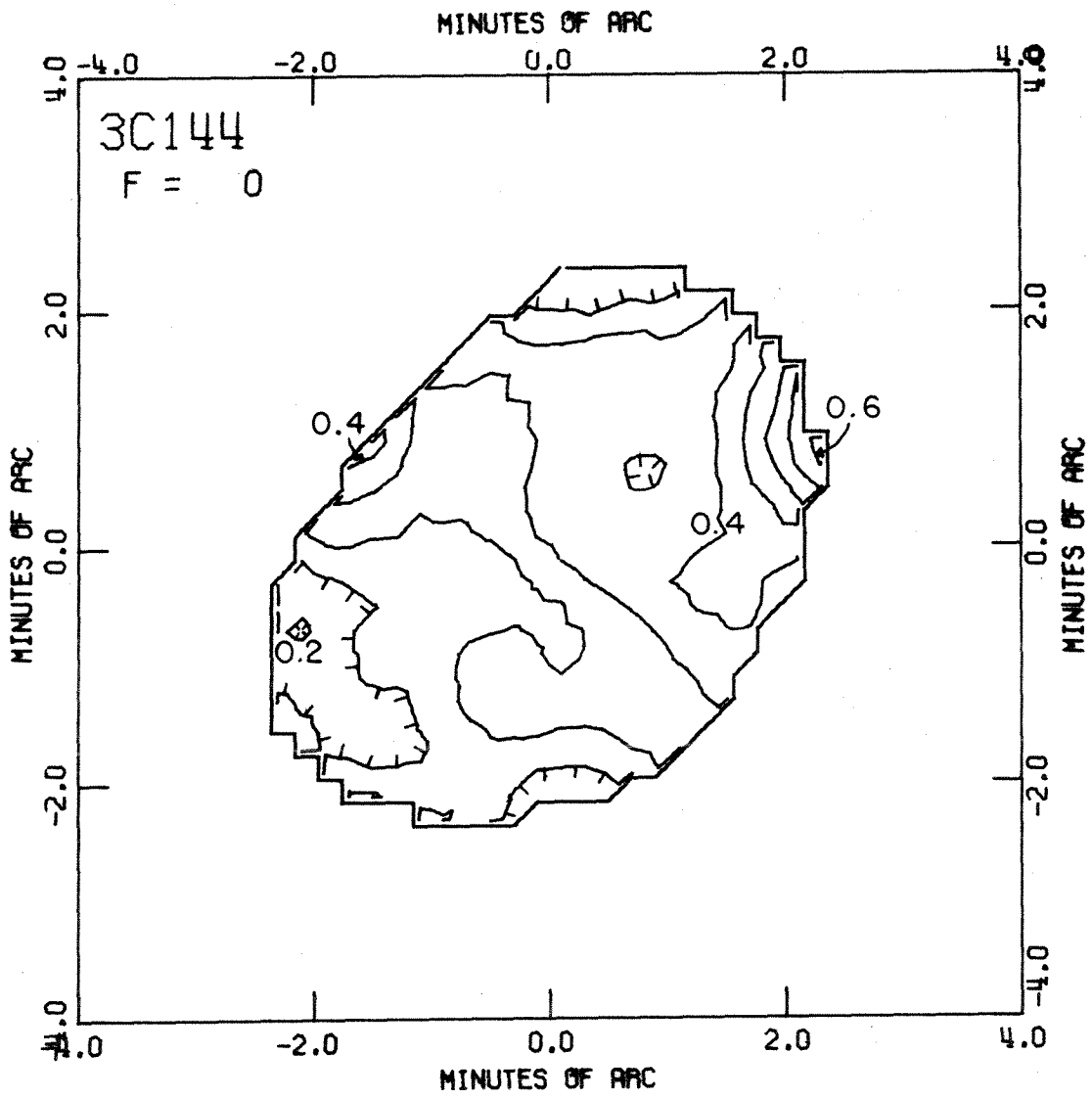

Figure 33k. 3C144: optical depth map at 0.0 km/sec, contour interval = 0.05.

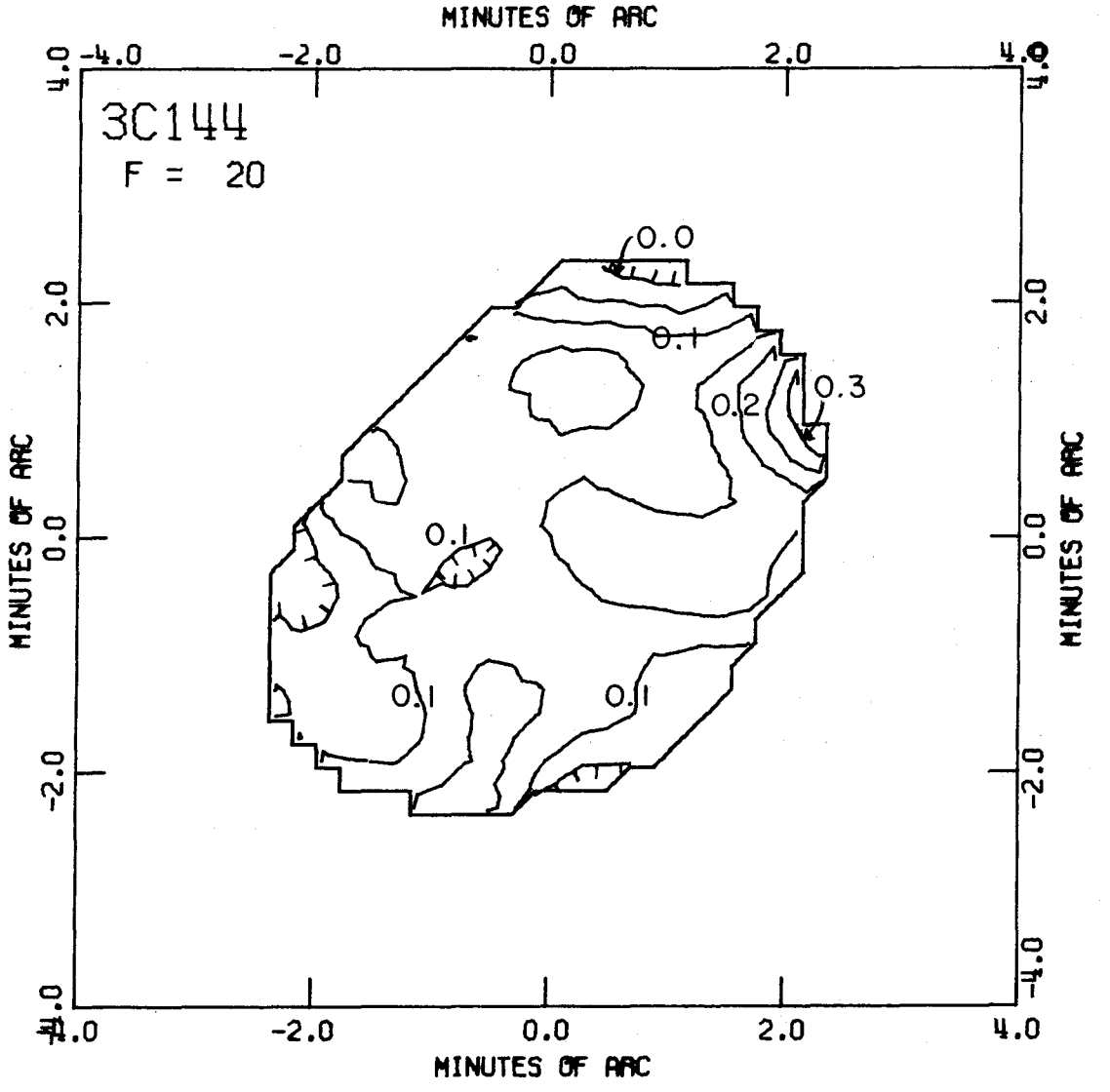

Figure 331. 3C144: optical depth map at -4.2 km/sec, contour interval = 0.05.

(-0.9, - 2.3) and peaks at (1.5, -0.3), (-0.7, -1.0) and (0.2, 1.4). Complicated patterns of this sort are found on most of the optical depth maps of this source.

The next three maps trace the changes in the hydrogen distribution through the narrow absorption feature. At -55 KHz, the optical depth (τ) is greatest in the southern parts of the source with peaks at (-0.7, -2.3) and (1.2,-1.6) and a ridge from the main peak toward (-1.9, -0.9). The contours also suggest the presence of several lesser features. As the frequency increases the peak at (1.2, -1.6) becomes more prominent, but by - 50 KHz the map is dominated by peaks to the west and northwest: (1.9, -0.5) and (2.1, 1.5), respectively. The peak near (-1.1, -2.3) now is still prominent but the peak at (1.2,-1.6) is seen more as a ridge between (0.9, -1.7) and (-0.1, -0.9). A maximum off the source to the north and other features are also suggested. By -45 KHz, the peak optical depths are along the northwest edges of the source, with only a few traces of the other peaks mentioned above. All optical depths are lower and new peaks appear to the east around (-1.7, 0.7), (-0.5, -0.3), and (-1.5, -1.1).

At - 38 KHz the optical depths are near a minimum between the two main spectral features. Optical depths are generally quite low although the peak at (2.3, 0.9) is prominent and lesser peaks are seen around (0.6, 1.4), (-0.9, -2.3), (-0.9, 1.5), and (-1.5, 0.9). Most of the major peaks seen on the previous three maps still show some traces at - 38 KHz.

The next five maps (Figures 33f-j) trace the changes in the distribution of optical depth through the broad absorption feature. By - 30 KHz all optical depths have increased and a number of peaks are seen. The peak at (2.3, 0.9) dominates this map and all maps at higher frequencies. Another long-lived peak is located around (0.3, 1.5). The peak off (-2.3, -0.8) is particularly prominent from - 36 to - 26 KHz, but drops off at higher frequencies. A broad high region between peaks at (2.3, 0.9), (1.5, -1.1), (-0.5, -2.1), and (-1.6, 0.6) dominates the map at - 24 KHz, but is also seen at - 30 KHz. The low optical depth region to the north of the source at - 24 KHz will be seen to have a striking effect on the appearance of the spectra. By - 18 KHz, this region becomes one of higher optical depths although the

principal peaks are still along the western edge of the source. By - 12 KHz, peaks are found at (2.3, 0.8), (1.1, -0.5), (-1.3, 0.9) and (0.3, 1.4). A new peak develops around (1.9, -0.5) gaining considerable prominence by - 9 KHz and remaining visible at - 6 KHz. By - 6 KHz all optical depths have dropped and (-0.5, 0.5) appears briefly as a local maximum.

The optical depth maps in the long high-frequency tail of the spectrum show surprisingly similar spatial structure over a wide range of frequency. Although the optical depths are real (see Figure 31), it is hard to determine how much of the apparent structure is due solely to the DC offsets. The peak at (2.3, 0.9) is most prominent. At 0 KHz, we find peaks also at (0.5, 1.4), (-1.5, 0.9), (1.5, -0.2) and (-0.4, -1.1). At 20 KHz the minor peaks are found at (1.0, -0.3), (0.3, 1.3), (-1.5, 0.7), (-0.5, -1.3) and (-0.9, -2.3).

REFERENCES

Berge, G. L. and Greisen, E. W. 1969, Ap. J., 156, 1125.

Bracewell, R. N. 1958, Proc. IRE, 46, 97.

Clark, B. G. 1965, Ap. J., 142, 1398.

Clark, B. G., Radhakrishnan, V., and Wilson, R. W. 1962, Ap. J., 135, 151.

de Jager, G. 1970, Nature, 225, 622.

de Jager, G., Lyne, A. G., Pointon, L., and Ponsonby, J.E.B. 1968, Nature, 220, 128.

de Jager, G. and Neven, L. 1966, B. A. N., 18, 306.

Ewen, H. I. and Purcell, E. M. 1951, Nature, 168, 356.

Field, G. B., Goldsmith, D. W. and Habing, H. J. 1969, Ap. J. (Letters), 155, L149.

Fomalont, E. B. 1967, Publ. Owens Valley Radio Obs., 1, No. 3.

Goldsmith, D. W., Habing, H. J., and Field, G. B. 1969, Ap. J., 158, 173.

Gordon, K. J. and Gordon, C. P. 1970, Ap. Letters, 5, 153.

Goss, W. M. 1968, Ap. J. Supp., 15, 131.

Goss, W. M., Radhakrishnan, V., Brooks, J. W., and Murray, J. D. 1972, Ap. J. Supp., 24, 123.

Hagen, J. P., Lilley, A. E. and McClain, E. F. 1955, Ap. J., 122, 361.

Hagen, J. P. and McClain, E. F. 1954, Ap. J., 120, 368.

Heiles, C. 1967, Ap. J. Supp., 15, 97.

Heiles, C. and Verschuur, G. L. 1969, Ap. Letters, 3, 21.

Hellwig, H., Vessot, R. F. C., Levine, M. W., Zitzewitz, P. W., Allan, D. W. and Glaze, D. J. 1970, IEEE Trans. Instrum. Meas., IM-19, 200.

Hogg, D. E., MacDonald, G. H., Conway, R. G., and Wade, C.M. 1969, A. J.. 74, 1206.

Hughes, M. P., Thompson, A. R. and Colvin, R. S. 1971, Ap. J. Supp., 23, 323.

Johnson, H. L. 1967, Ap. J. (Letters), 150, L39.

Kaper, H. G., Smits, D. W., Schwarz, U., Takakubo, K. and Van Woerden, H. 1966, B. A. N., 18, 465.

Kepner, M. 1970, A. and Ap., 5, 444.

Kerr, J. F., Hindman, J. V. and Gum, C. S. 1959, Aust. J. Ph., 12, 270.

Lin, C. C. and Shu, F. H. 1964, Ap. J., 140, 646.

_____ 1966, Proc. Nat. Acad. Sci., 55, 229.

Manchester, R. N., Robinson, B. J. and Goss, W. M. 1970, Aust. J. Ph., 23, 751.

Muller, C. A. 1957, Ap. J., 125, 830.

Muller, C. A. and Oort, J. H. 1951, Nature, 168, 357.

Muller, C. A. and Westerhout, G. 1957, B. A. N., 13, 151.

Pawsey, J. L. 1951, Nature, 168, 358.

Radhakrishnan, V., Brooks, J. W., Goss, W. M. , Murray, J.D. and Schwarz, U. J. 1972a, Ap. J. Supp., 24, 1.

Radhakrishnan, V. and Goss, W. M. 1972b, Ap. J. Supp., 24, 161.

Radhakrishnan, V., Goss, W. M., Murray, J. D. and Brooks, J. W., 1972c, Ap. J. Supp., 24, 49.

Radhakrishnan, V., Murray, J. D., Lockhart, P. and Whittle, R. P. J. 1972d, Ap. J. Supp., 24, 15.

Read, R. B. 1963, Ap. J., 138, 1.

Riegel, K. W. and Crutcher, R. M. 1972, Astr. Astrophys., 18, 55.

Riegel, K. W. and Jennings, M. C. 1969, Ap. J., 157, 563.

Roberts, M. S. 1970, Ap. J. (Letters), 161, L9.

Roberts Jr., W. W. 1969, Ap. J., 158, 123.

_____ 1972, Ap. J., 173, 259.

Ryle, M., Elsmore, B. and Neville, A. C. 1965, Nature, 205, 1259.

Schklovsky, I. S. 1949, Astronomicheskii Zhurnal, 26, 10.

Schmidt, M. 1965, Galactic Structure, ed. Blaauw, A. and Schmidt, M., (Chicago and London, The University of Chicago Press), 513.

Shostak, G. S. 1972, unpublished thesis, California Institute of Technology.

Shu, F. H., Milione, V., Gebel, W., Yuan, C., Goldsmith, D. W., and Roberts Jr., W. W. 1972, Ap. J., 173, 557.

Shuter, W. L. H. 1967, Radio Astronomy and the Galactic System, ed Van Woerden, H., (London and New York, Academic Press), 47.

Shuter, W. L. H., Pulley, H. C. and Rogstad, D. H. 1967, Ap. J., 150, 711.

Shuter, W. L. H. and Verschuur, G. L. 1964, M. N. R. A. S., 127, 387.

Spitzer Jr., L. 1968, Nebulae and Interstellar Matter, ed. Middlehurst, B. M. and Aller, L. H., (Chicago and London, The University of Chicago Press), 1.

Spitzer Jr., L. and Savedoff, M. P. 1950, Ap. J., 111, 593.

Spitzer Jr., L. and Scott, E. H. 1969, Ap. J., 158, 161.

Stone, E. M. 1970, Ap. J., 159, 293.

Takakubo, K. and Van Woerden, H. 1966, B.A.N., 18, 488.

Thompson, A. R., Colvin , R. S., and Hughes, M. P. 1969, Ap. J., 158, 939.

Trimble, V. 1968, A. J., 73, 535.

Van de Hulst, H. C. 1945, Nederl. Tijdschi. Naturkunde, 11, 201.

_____ 1958, R. M. P., 30, 913.

Van de Hulst, H. C., Muller, C. A. and Oort, J. H. 1954, B. A. N., 12, 117.

Van den Bergh, S. 1971, Ap. J., 165, 259.

Van den Bergh, S. and Dodd, W. W. 1970, Ap. J., 162, 485.

Verschuur, G. L. 1969, Ap. Letters, 4, 85.

_____ 1970, Interstellar Gas Dynamics, ed. Habing, H. J., (Dordrecht-Holland, D. Reidel Publishing Company), 150.

Verschuur, G. L. and Knapp, G. R. 1971, A. J., 76, 403.

Westerhout, G. 1967, Radio Astronomy and the Galactic System, ed. Van Woerden, H., (London and New York, Academic Press), 173.

Whiteoak, J. B. and Gardner, F. F. 1970, Ap. Letters, 5, 5.

Williams, D. R. W. and Davies, R. D. 1954, Nature, 173, 1182.

_____ 1956, Phil. Mag., Series 8, 1, 622.

Zuckerman, B., Buhl, D., Palmer, P. and Snyder, L. E. 1970, Ap. J., 160, 485.